Microwave Kinetic Inductance Detectors

Thesis by

Benjamin A. Mazin

In Partial Fulfillment of the Requirements

for the Degree of

Doctor of Philosophy

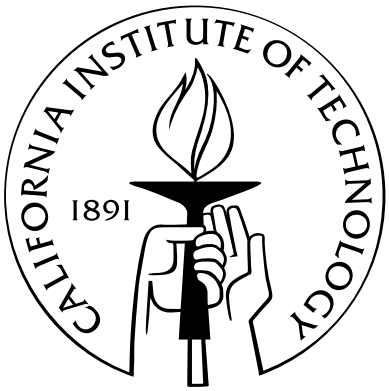

California Institute of Technology

Pasadena, California

2004

(Defended August 18, 2004)

Acknowledgements

This work would have been impossible without the patient help of this technology's inventors, Professor Jonas Zmuidzinas and Dr. Rick LeDuc. Professor Zmuidzinas unparalleled understanding of the issues involved in all stages of the project is remarkable, and I am grateful for the time and effort he has patiently put into helping me understand this complex field. It seems that many successful efforts in low temperature detectors depend not only on cleverness of concept but also in actually fabricating the devices you envision; I am very glad we had Dr. LeDuc's expert hand guiding the mask design and fabrication process.

Dr. Peter Day has greatly contributed to both the data and theory efforts, running a parallel effort at JPL. Many of the good ideas dealing with the cryogenics and thinking about the data are his. Also involved were Anastasios Vayonakis, who developed the 50 GHz low-pass filters and calculated the radiation loss, and Dr. Peter Mason, who has helped out with the cryogenics. Professor Sunil Golwala has helped me to understand the intricacies of dark matter detection. Jiansong Gao and Shwetank Kumar have helped with the simulation and design of the etched CPW devices. Professor Chris Martin and Dr. Brian Kern have contributed vital astronomical background.

I would also like to thank my parents, who have always steered me right, and my friends, who at times even feign interest in what I do at work.

Funding for this project has been provided by NASA, JPL DRDF, and the generous contributions of Alex Lidow, Caltech Trustee.

Abstract

Low temperature detectors have been a subject of intense interest to the scientific community over the last decade. These detectors work at very low temperatures, often well below 1 Kelvin, to minimize the noise in the measurement of photons. This leads to very powerful detectors applicable to a broad wavelength range.

Since these detectors are so sensitive even single pixels and small arrays (up to several hundred pixels) enable deeper explorations of the cosmos than ever before. Instruments based on these technologies have been used at submillimeter, optical, and X-ray wavelengths. The scientific prospects for these detectors increase as they grow in pixel count. For some applications, especially for Cosmic Microwave Background (CMB) polarization work, a large focal plane will not only increase efficiency but will also enable new and vital science.

Current superconducting technologies, such as Transition Edge Sensors (TESs), can currently deliver extremely high sensitivity in the submillimeter and read-noise free imaging spectroscopy at Optical/UV and X-ray wavelengths, but the largest arrays contain less that 100 pixels. In order to make real progress these arrays must contain many thousands of pixels. This is a formidable technical challenge.

This thesis will explore a promising emerging technology called Microwave Kinetic Inductance Detectors (MKIDs). MKIDs make use of the change in the surface impedance of a superconductor as incoming photons break up Cooper pairs. This is accomplished by making the strip of superconductor part of a microwave resonant circuit, and monitoring the phase of a signal transmitted through (or past) the resonator. The primary advantage of this technology is that by using resonant circuits with high quality factors, passive frequency domain multiplexing will allow up to thousands of resonators to be read out through a single coaxial cable and a single HEMT amplifier. This eliminates the cryogenic electronics (SQUIDS) and wiring problems associated with current superconducting devices. Inexpensive and powerful room-temperature readout electronics can leverage the microwave integrated circuits developed for wireless communications.

When this project started four years ago MKIDs were just a concept. In this thesis I will recount the progress we have made in taking this concept and turning it into a detector technology, building on the work we published in *Nature* in 2003. I will demonstrate that we have overcome

the major technical obstacles and shown conclusively that MKIDs work, and should provide much larger arrays than are possible with other technologies. Due to our work at Caltech and JPL, MKIDs are considered one of the leading technologies to reach the ambitious goals set for future ground and space missions. The noise performance is already good enough for sky-limited, ground-based, submillimeter astronomy.

Despite MKIDs acceptable noise performance for ground-based astronomy, there are many applications which require lower detector noise. The simple MKIDs we measure in Chapter 7 still exhibit a noise higher than theory would predict which could limit their usefulness for some applications.

In Chapters 7–9 we perform several experiments which identify the source of the excess noise as the substrate.

1. The noise roll-off frequency seems to match the resonator bandwidth fairly well, which scales linearly with the resonator quality factor Q. Any noise source associated with quasiparticles would be expected to have a roll-off associated with the quasiparticle lifetime and be independent of Q. Readout noise sources should also be independent of Q. More details are in Section 7.1.4.

2. Thick and thin aluminum films of the same lateral geometry, but with phase responses per quasiparticle different by a factor of 100, show similar noise at the same readout power. This is strong evidence that quasiparticles are not involved in the noise. For more details, see Section 7.3.

3. Changing the substrate from silicon to sapphire reduces the noise dramatically. This is strong evidence that the substrate is the cause of the noise, as shown in Chapter 8.

4. We designed a device with the substrate removed from areas where there are strong electromagnetic field concentrations. This also dramatically reduced the noise, as shown in Chapter 9.

   In the course of these experiments to characterize and identify the noise, we successfully demonstrate two distinct approaches which dramatically reduce the noise excess.

Taken together these experiments are conclusive evidence that the noise excess originates in the substrate. We will continue to improve the noise performance of MKIDs as our program to eliminate the substrate noise matures. The combination of our multiplexing technique and sensitive detectors will be an extremely powerful tool for astronomy from the submillimeter to the X-ray.

Contents

List of Figures

List of Tables

Chapter 1

Introduction

1.1 Introduction to Low Temperature Detectors

Low temperature detectors have been a subject of intense interest to the scientific community over the last decade. These detectors work at very low temperatures, often well below 1 Kelvin, to minimize the noise in the measurement of photons. This leads to very powerful detectors applicable to a broad wavelength range.

Since these detectors are so sensitive, even single pixels and small arrays (up to several hundred pixels) enable deeper explorations of the cosmos than ever before, and instruments based on these technologies have been used at submillimeter, optical, and X-ray wavelengths. The scientific prospects for these detectors increase as they grow in pixel count. For some applications, especially for Cosmic Microwave Background (CMB) polarization work, a large focal plane will not only increase efficiency but will also enable new and vital science.

There are several categories of low temperature detectors. Conventional bolometers [1] measure the temperature change that a single photon (or stream of photons) causes by measuring a change in the resistance of a thermistor. This technology powers millimeter and submillimeter cameras like SCUBA [2] and BOLOCAM [3]. It also provides imaging spectroscopy in the X-ray for AstroE-2 [4]. It is the most mature low temperature detector technology, but reading out large arrays is difficult. Arrays of several hundred pixels are achieved by brute force, putting many JFET amplifiers near the focal plane. This poses a technical challenge since JFET amplifiers need to operate around 100 Kelvin, and heat dissipation from the amplifiers and the heat load on the cold detector from the many read out wires can cause problems.

Magnetic microcalorimeters (MMCs) contain a metallic matrix doped with paramagnetic ions. In an applied magnetic field, an X-ray hitting the material will cause a change in the magnetization of the sensor which can be read out with a superconducting quantum interference device (SQUID). These devices have shown excellent X-ray resolution in the lab, but are still single pixel devices [5].

The remaining detectors technologies are based on low temperature superconductors. These are

materials whose electrical resistance vanishes at a critical temperature, T_c. This occurs because the crystal lattice of the material can cause an attractive force between electrons, causing them to condense into pairs (called Cooper pairs) which can carry a DC current without resistance. The number of electrons not bound together in Cooper pairs (quasiparticles) goes down exponentially as the temperature of the material is decreased.

Transition edge sensors [6] (TESs) maintain a small strip of superconductor at an intermediate resistance between its normal and superconducting state. This is accomplished by voltage biasing the superconductor with a circuit that provides negative electrothermal feedback. The power of this approach comes from the sharp variation of the resistance of the superconductor as a function of temperature near T_c. When a photon is absorbed in the superconductor the current necessary to maintain the elevated temperature of the strip drops. This current deficit pulse is read out with a SQUID amplifier. Various groups are developing TESs for submillimeter, optical/UV, and X-ray work [7, 8, 9].

It is possible to multiplex TESs in the time or frequency domains in order to increase the number of detectors [10, 11] that can be read out through a SQUID amplifier. These schemes require complex, custom superconducting electronics (including one SQUID per pixel for time domain multiplexing or one passive filter per pixel for frequency domain multiplexing) located close to the detector array. This requires many wires going between the SQUID multiplexer and TES. In the submillimeter this can be realized by bump-bonding a multiplexer wafer to a detector wafer since the pixel size and the SQUID size are comparable. This approach may not work in the optical/UV and X-ray where the SQUIDs are much larger than the detector pixels. Another issue is the complexity and heat transfer associated with the wiring of large multiplexed arrays.

Superconducting tunnel junctions [12, 13] (STJs) are a class of quasiparticle detectors which use a superconducting-normal-superconducting (SIS) junction with a very thin insulating tunnel barrier to measure the quasiparticles created when a photon breaks Cooper pairs. STJ detectors are being developed for submillimeter [14] and optical/UV and X-ray work [15, 16, 17, 18].

Superconducting tunnel junctions are difficult to fabricate. Making high quality barriers and maintaining the uniformity of the barrier across the wafer is a challenge. A magnetic field must be applied to STJs to suppress the Josephson current. Suppressing all the junctions simultaneously in a large array is difficult since the junctions may require different field levels for adequate suppression. The most commonly discussed multiplexing schemes for STJs [19, 20] use radio-frequency single electron transistors (RF-SETs) as pre-amplifiers, which are complex devices themselves. RF-SET multiplexing of STJs has not yet been demonstrated in the lab.

These low temperature detectors can currently deliver extremely high sensitivity in the submillimeter [14, 21], and read-noise free imaging spectroscopy in the optical/UV and X–ray [8, 9, 22, 23, 24], but the array sizes are small. In order to make real progress, these arrays must con-

Device	NEP	ΔE_{X-ray} (eV) at 6 keV	$R_{optical}$	Pixel Count	Theoretical δE
STJ	10^{-19}	12	10	36	$2.355\sqrt{\eta E(F+1+\frac{1}{<b>})/\Delta}$
TES	10^{-19}	4.5	20	25	$2.355\sqrt{4k_bT^2C\sqrt{n/2}/\alpha}$
MMC	-	3.6	-	1	$2.355\sqrt{8k_bT^2C}(\frac{\tau_0}{\tau})^{1/4}$
MKID	10^{-17}	?	-	?	$2.355\sqrt{\eta EF/\Delta}$

Table 1.1: A comparison of the current state-of-the-art superconducting detectors. The concept of noise equivalent power (NEP), a measure of the sensitivity of the detector, will be discussed extensively in Section 7.1.4.6. $R = E/\delta E$ is the energy resolution of the detector. The last column, Theoretical δE, shows how the energy resolution of the device scales for single photon detection. In these equations, the gap parameter is Δ, η is the conversion efficiency for creating quasiparticles, F is the Fano factor (.2), $< b >$ is the mean number of backtunnels, T is the device temperature, C is the absorber heat capacity near T_c, $n = 5$ for electron-phonon limited conductance, and $\alpha = (d\ln R/d\ln T)_{V=const}$. For the magnetic microcalorimeter (MMC) case, the relaxation time τ_0 of the spins is roughly 1 μs, and τ is the thermal relaxation time to the bath. While we have designed and fabricated a device that could contain up to 1024 pixels (Chapter 10) it has yet to demonstrate this spatial resolution. We will show our best estimates of energy resolution for MKIDs in Chapter 7.1-9.

tain many thousands of pixels. The technical challenges of building and reading out large arrays ($>\sim$ 1000 pixels) with any of the technologies mentioned are formidable.

1.2 Microwave Kinetic Inductance Detectors

This thesis will explore a promising emerging technology developed at Caltech and JPL, the Microwave Kinetic Inductance Detector (MKID) [25, 26, 27]. In these previous papers we have discussed the concepts behind MKIDs and made measurements of some simple devices. In our last paper, Day *et al.* [27], we measure the properties of a simple MKID and detect a mysterious excess noise. This thesis will provide more detailed background on all aspects of design and measurement of MKIDs and provide an identification of the excess noise as originating in the substrate. This identification has allowed us to design and test devices with significantly lower noise than previously demonstrated. This work is detailed in Chapters 7–9.

In a MKID, quasiparticles created by incident radiation are sensed by measuring the change in the surface impedance of a strip of superconductor. This change is caused by quasiparticles blocking the Cooper pairs from occupying some of the electron states (through the exclusion principle), which modifies the effective pairing energy and reduces the density of pairs. The relevant theory will be discussed extensively in Chapter 2.

This change in surface impedance is measured by making the strip of superconductor part of a microwave resonant circuit, and by monitoring the phase of a microwave signal transmitted through (or past) the resonator. Figure 1.1 gives an overview of this process. In Figure 1.1 panel (a) a photon

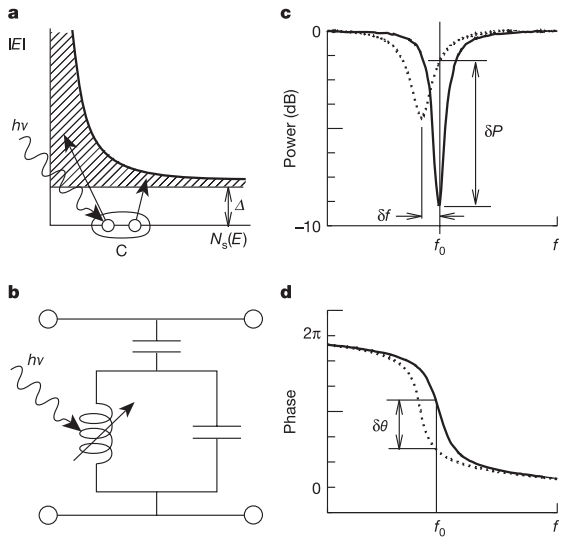

Figure 1.1: An illustration of the detection principle.

with energy $h\nu > 2\Delta$ (Δ is the superconducting gap energy) is absorbed in a superconducting film cooled to $T \ll T_c$, breaking Cooper pairs and creating a number of quasiparticle excitations $N_{qp} = \eta h\nu/\Delta$. The efficiency of creating quasiparticles η will be less that one since some of the energy of the photon will end up as vibrations in the lattice called phonons. In this diagram, Cooper pairs (C) are shown at the Fermi level, and the density of states for quasiparticles [28], $N_s(E)$, is plotted as the shaded area as a function of quasiparticle energy E.

Panel (b) shows that the increase in quasiparticle density changes the (mainly inductive) surface impedance $Z_s = R_s + i\omega L_s$ of the film (represented as the variable inductor), which is used as part of a microwave resonant circuit. The resonant circuit is depicted schematically here as a parallel LC circuit which is capacitively coupled to a through line. The effect of the surface inductance L_s is to increase the total inductance L, while the effect of the surface resistance R_s is to make the inductor slightly lossy (adding a series resistance).

Panel (c) shows that on resonance, the LC circuit loads the through line, producing a dip in its transmission. The quasiparticles produced by the photon increase both L_s and R_s, which moves the resonance to lower frequency (due to L_s) and makes the dip broader and shallower (due to R_s). Both of these effects contribute to changing the amplitude (c) and phase (d) of a microwave probe signal transmitted past the circuit. The amplitude and phase curves shown in this illustration are actually the data measured for a test device described in Day *et al.* at 120 mK (solid lines) and 260 mK (dashed lines). This choice of circuit design, which has high transmission away from resonance, is very well suited for frequency-domain multiplexing, since multiple resonators operating at slightly different frequencies could all be coupled to the same through line.

While ideas for kinetic inductance detectors have been discussed in the literature [29, 30, 31, 32, 33, 34, 35, 36], most of these devices operated close to T_c in a fashion similar to a TES, and in some cases used impractical readout schemes. The idea of reading out the change in kinetic inductance with a microwave resonant circuit while operating far below T_c was originated by our group. This approach has several advantage:

- High Q resonant circuits allow passive frequency-domain multiplexing of up to thousands of resonators through a single coaxial cable and a single HEMT amplifier. The best way to understand this is to think of each resonator as a radio station — it is not hard to listen to one specific station despite there being many stations at nearby frequencies. A single amplifier can boost the signal from an antenna, boosting the reception of all the stations simultaneously. This is exactly what happens in frequency domain multiplexing — each resonator in an array is fabricated with a different resonant frequency, and is excited and read out with a sine wave at its unique resonant frequency. One amplifier boosts the signal from all the resonators. The readout electronics do the work of separating out the signals from the individual resonators. See Figure 1.2 for an illustration of the readout process.

- The theoretical sensitivity (NEP) of an MKID scales as $\exp\left[-\Delta/k_bT\right]$ at temperatures well below the superconducting transition temperature (Section 3.4.1).

- This concept takes advantage of the recent dramatic advances in the performance of cryogenic microwave HEMT (High Electron Mobility Transistor) amplifiers, which provide noise temperatures below 10 K across multi-gigahertz bandwidths, and now operate at frequencies up to several hundred gigahertz [37].

- These devices are simple to fabricate, requiring no Josephson junctions or tuned bilayers, so fabricating large, uniform arrays should present no problems.

- An array readout of synthesizers and quadrature receivers at room temperature is readily implemented using miniature, low-cost, low-power integrated circuits developed for wireless communications, as shown in Section 5.6.1.

- The materials used in these devices are typically aluminum, tantalum, silicon, and sapphire. These are very resistant to shock, thermal cycling and radiation, so the devices are rugged and are ideal for the space environment.

- There is tremendous flexibility in the microwave circuit layout (microstrip lines, coplanar wave guides, striplines, slotlines, filters, etc.), in superconducting material selection (aluminum, tantalum, niobium, titanium, zirconium, etc.), and in substrates (sapphire, silicon, germanium, etc.). Separating the functions of radiation absorption and quasiparticle detection using

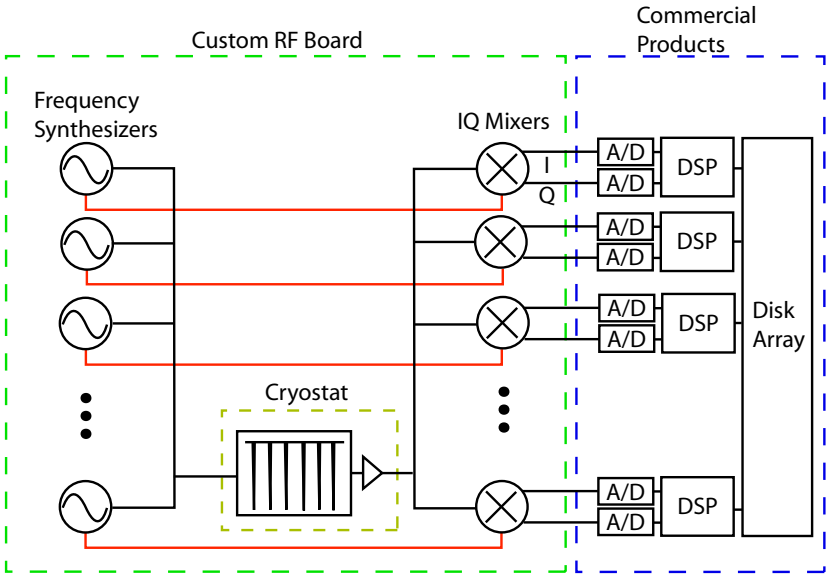

Figure 1.2: A block diagram of a frequency multiplexed readout based on the homodyne detection scheme described in Chapter 5.

bandgap engineering (trapping), diffusion, phonon coupling, or other techniques allows a wide diversity of solutions to engineering problems. Design issues will be discussed extensively in Chapter 3.

This thesis will explain in detail all the aspects of making and measuring MKIDs. It will also detail four important experimental results that have shown conclusively that the source of the excess noise reported in Day *et al.* [27] is due to the substrate.

1. The noise roll-off frequency seems to match the resonator bandwidth fairly well, which scales linearly with the resonator quality factor Q. Any noise source associated with quasiparticles would be expected to have a roll-off associated with the quasiparticle lifetime and be independent of Q. Readout noise sources should also be independent of Q. More details are in Section 7.1.4.

2. Thick and thin aluminum films of the same lateral geometry but with phase responses per quasiparticle different by a factor of 100 show similar noise at the same readout power. This is strong evidence that quasiparticles are not involved in the noise. For more details, see Section 7.3.

3. Changing the substrate from silicon to sapphire reduces the noise dramatically. This is strong evidence that the substrate is the cause of the noise, as shown in Chapter 8.

4. We designed a device with the substrate removed from areas where there are strong electromagnetic field concentrations. This also dramatically reduced the noise, as shown in Chapter 9.

Taken in combination, these experiments allow us to both identify the source of the excess noise as the substrate and to demonstrate two distinct techniques for lowering it.

1.3 Scientific Motivation

Superconducting detectors are niche devices — they are limited by their cold operating temperatures (often below 0.2 Kelvin) and their limited count rates (likely below 10 kHz) at optical/UV/X-ray wavelengths. They are not likely to replace room temperature photon detectors in daily use. However, for certain applications, mainly in astronomy, these disadvantages are outweighed by their advantages. MKIDs are applicable to a broad number of wavelength ranges, and in the following sections we will discuss their utility for each range.

1.3.1 Astronomy

1.3.1.1 Millimeter and Submillimeter Wavelengths

Between the radio and the far infrared lies one of the most important and poorly explored parts of the spectrum. It contains most of the energy of the Cosmic Microwave Background (CMB), which has proven to be an exceptional tool for studying the early universe [38, 39]. CMB polarization measurements (see Figure 1.3 and Figure 1.4) are of special interest because they may allow detection of gravitational waves in the early universe. This could provide proof of inflation and allow us to probe farther back in time towards the Big Bang.

Future CMB missions like Planck [41] will advance our knowledge, but missions 100 times more sensitive [42] are needed to get the polarization data [43, 40] that may prove so crucial to our understanding of inflation and dark energy [44]. This will not happen without dramatic advances in large detector arrays.

This wavelength region also contains a significant fraction of the Cosmic Infrared Background (CIB) [46], which is likely the integrated light from ultra-luminous infrared galaxies (ULIRGs) at high redshifts. Resolving this background may allow us to understand how and where the bulk of the star formation in the universe occurred.

Closer to home, the submillimeter band also contains most of the energy emitted from cool molecular clouds. These clouds are the birthplace of new stellar systems. Understanding star and planet formation is one of NASA's most important scientific goals for the coming decades.

Many of the detector goals in this wavelength range are called out in the NASA Infrared, Submillimeter, and Millimeter Detector Working Group (ISMDWG) report [42]. For most applications,

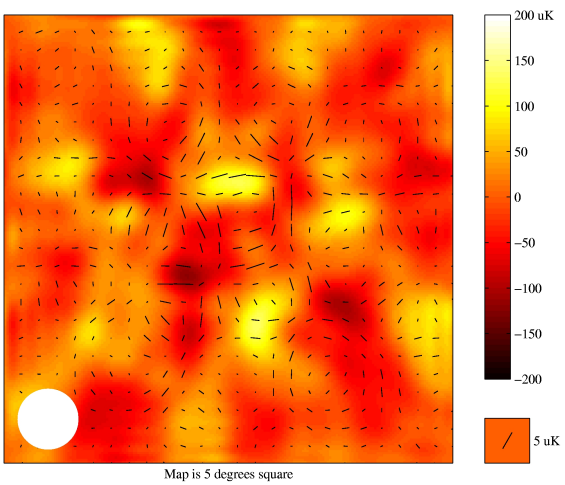

Figure 1.3: An image of the intensity and polarization of the cosmic microwave background radiation made with the Degree Angular Scale Interferometer (DASI) [40]. The polarization at each spot in the image is shown by a black line. The length of the line shows the strength of the polarization and the orientation of the line indicates the direction in which the radiation is polarized. Figure courtesy of the DASI website, http://astro.uchicago.edu/dasi/.

current state-of-the-art low temperature detectors in this wavelength range are usually limited not by their intrinsic sensitivity, but by other factors such as sky-noise, the black body emission of the atmosphere. This means that increases in the sensitivity of instruments must come by increasing pixel count. The IRSMDWG believes that "the need for high performance polarimetry with arrays of $> 10^3$ detectors in each of many wavelength bands is inescapable". This is an ideal application for large arrays of MKIDs.

Bolometers in the submillimeter can reach noise equivalent powers (NEPs) of $\sim 10^{-18}$ W Hz$^{-1/2}$ with several hundred pixels. However, future missions like the single aperture far-infrared observatory (SAFIR) will require noise equivalent powers (NEPs), the minimum amount of power a detector can measure in one second, around 10^{-20} W Hz$^{-1/2}$ with several thousand pixels for background-limited spectroscopy [47]. A figure showing the estimated required sensitivity of SAFIR is shown in Figure 1.5. While Transition Edge Sensors (TESs) are pushing into this sensitivity range, current multiplexing schemes [10] do not show an easy path to the required number of pixels. A very large effort is currently being put into developing a $\sim 1 \times 10^4$ pixel camera called SCUBA-2 [48, 7]. Many of the techniques used for SCUBA-2, such as indium bump bonding of a SQUID readout wafer to the detector array, are very expensive, and may not be applicable to optical/UV/X-ray wavelengths due to the size mismatch between the pixels and the SQUID readout. The approach taken by SCUBA-2 is a brute force solution to multiplexing, using thousands of wires and SQUIDs, and requiring a very

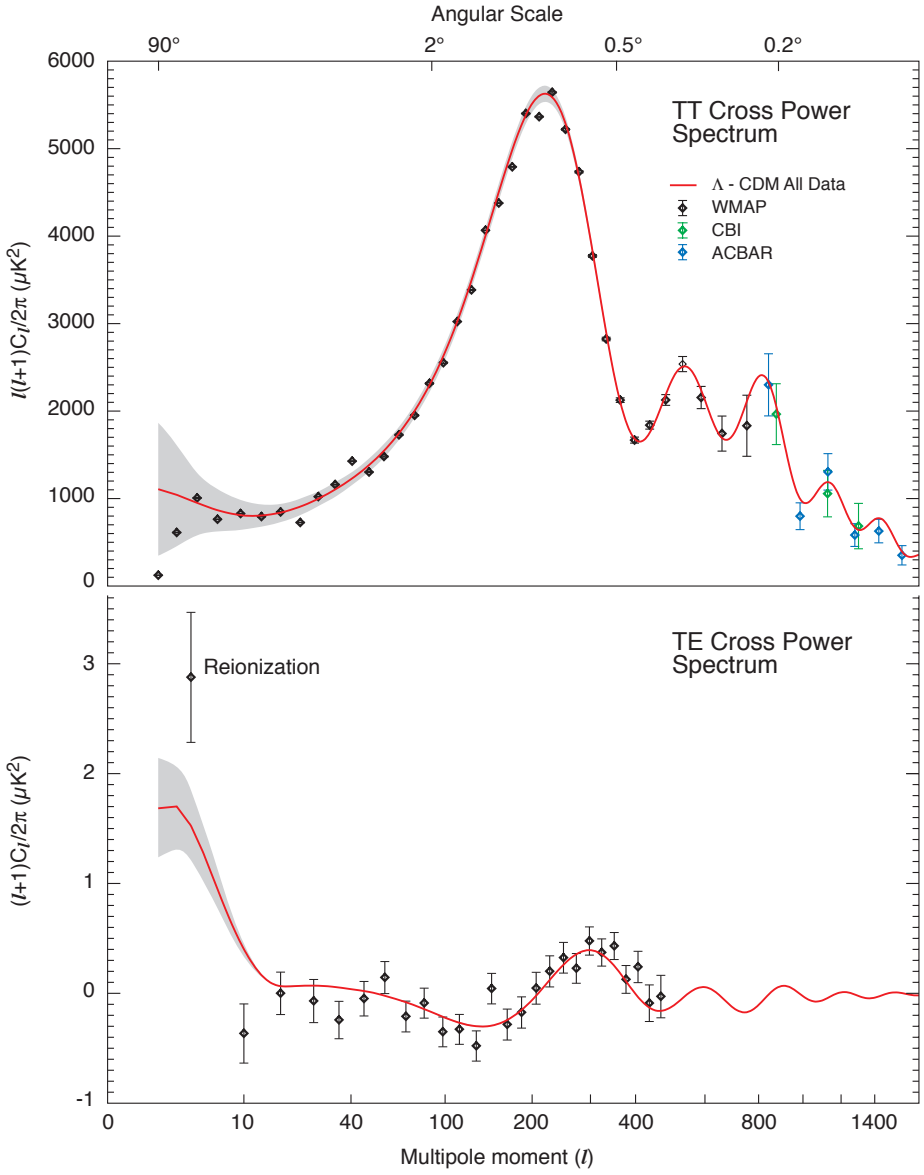

Figure 1.4: The current best CMB angular power spectrum from WMAP, COBE, ACBAR, and CBI data by Hinshaw *et al.* [45]. The bottom panel, the TE cross power spectrum, is the angular correlation between the temperature and E-mode polarization. The WMAP best fit model is also shown. Courtesy of the WMAP Science Team.

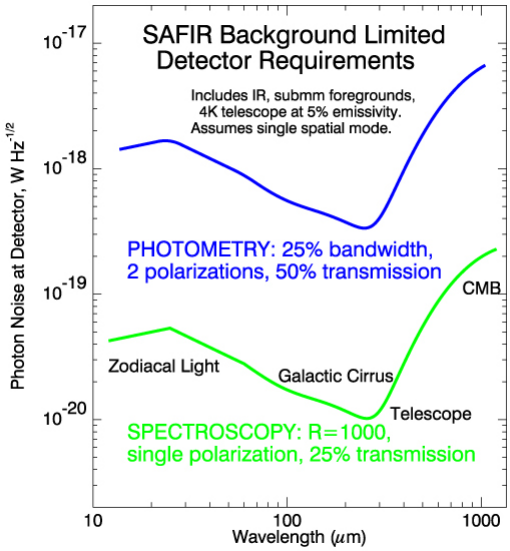

Figure 1.5: The estimated sensitivity requirements of SAFIR as a function of wavelength. The y-axis shows the minimum power the detector needs to be able to measure in one second. Spectroscopy requires significantly more sensitive detectors than photometry. The astrophysical background which sets the limits on sensitivity is noted on the figure. Figure courtesy of the SAFIR website [47].

large budget. Extending this technology to larger arrays would be difficult.

1.3.1.2 Optical

Optical astronomy deals with visible light from the atmospheric cutoff around 300 nm to the near infrared at 1 micron. The commercial and military applications of optical detectors are obvious, and significant effort has been put into developing powerful array detectors like charged coupled devices (CCDs). The Sloan Digital Sky Survey (SDSS) [49] contains 30 2048x2048 pixel detectors — over 125 million pixels! Superconducting detectors will not be able to compete in pixel count with conventional optical detectors in the foreseeable future.

The real advantages of superconducting detectors for optical astronomy are energy resolution ($R = E/\Delta E \approx 50$), read noise free output, microsecond timing, and an incredibly large simultaneous wavelength sensitivity — potentially 0.1-6 microns from space (though their quantum efficiency decreases in the infrared as the absorbing metal films become more reflective). They will excel in observations of rare, extremely faint sources where every photon matters [50, 51], and for objects showing fast time variability, like pulsars [52, 53, 54, 55], magnetic white dwarfs [56], cataclysmic variables [57], and low-mass X-ray binaries (LMXBs). Figure 1.6 show the kind of combined spectral and timing data that make these devices so interesting. Superconducting detector arrays have already been placed on the 3.5 meter William Herschel Telescope [56] and the Lick Observatory 3-meter telescope [53].

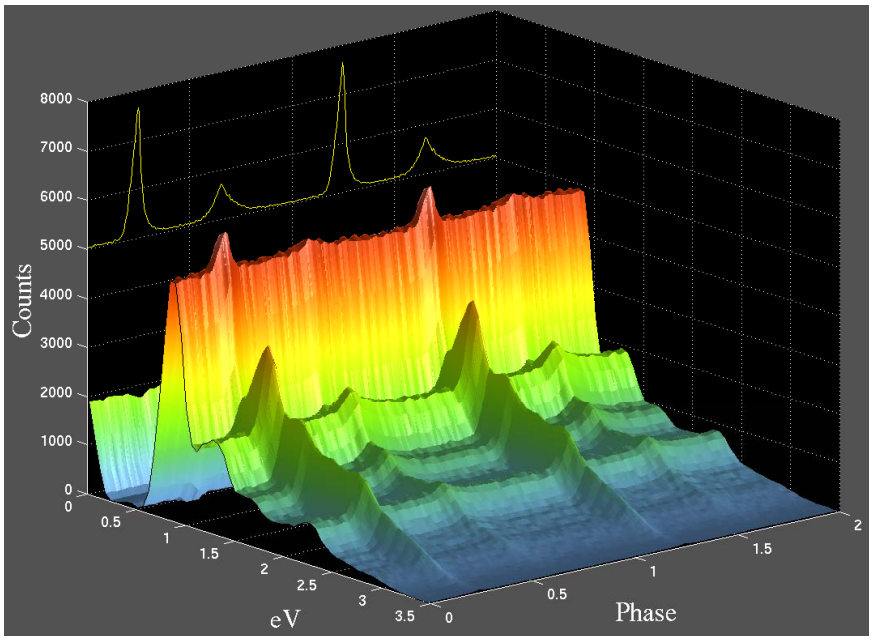

Figure 1.6: Time-resolved spectroscopy of the Crab Pulsar taken with a Stanford TES [52].

Detailed simulations of superconducting detectors for redshift determination of galaxies were performed by the author [50]. In these simulations, template elliptical, spiral, and irregular galaxy spectra were scaled with realistic attenuation and confusion factors, then placed at a redshift of up to 5. Simulated superconducting detector observations of these objects resulted in a simulated data set. A generalized photometric redshift technique was then applied to the simulated data set to generate an estimate of the dispersion in the redshift determined by this technique. Some of the results can be seen in Figure 1.7. The basic result is that a superconducting detector with a resolution of $R = E/\delta E = \lambda/\delta\lambda = 20$ is sufficient for highly accurate redshift determination of galaxies up to a redshift of 5. The high quantum efficiency and lack of read noise means that superconducting detectors can be more efficient than multi-object spectrographs for low resolution observations of very faint sources where the number of objects per spectrograph field is low.

The optical coronagraph version of NASA's Terrestrial Planet Finder [58] (TPF) is an ideal application for superconducting detectors. This proposed mission uses a 3×6 meter primary mirror whose mid-frequency (2-40 cm) spatial imperfections are corrected with an active secondary which has several thousand actuators. This allows a coronagraph to be built that can reject the light from a star by a factor of 10^{10} at angular separations that correspond to the habitable zones of nearby sun-like stars (0.01–1 arcseconds) [59].

Since the diffracted light is only controlled over a small region (a "dark" box), a 64x64 pixel superconducting array would be sufficient and the count rate will be very low. Having an energy-resolving focal plane will allow a relaxation of the mirror tolerances since the diffraction speckles will

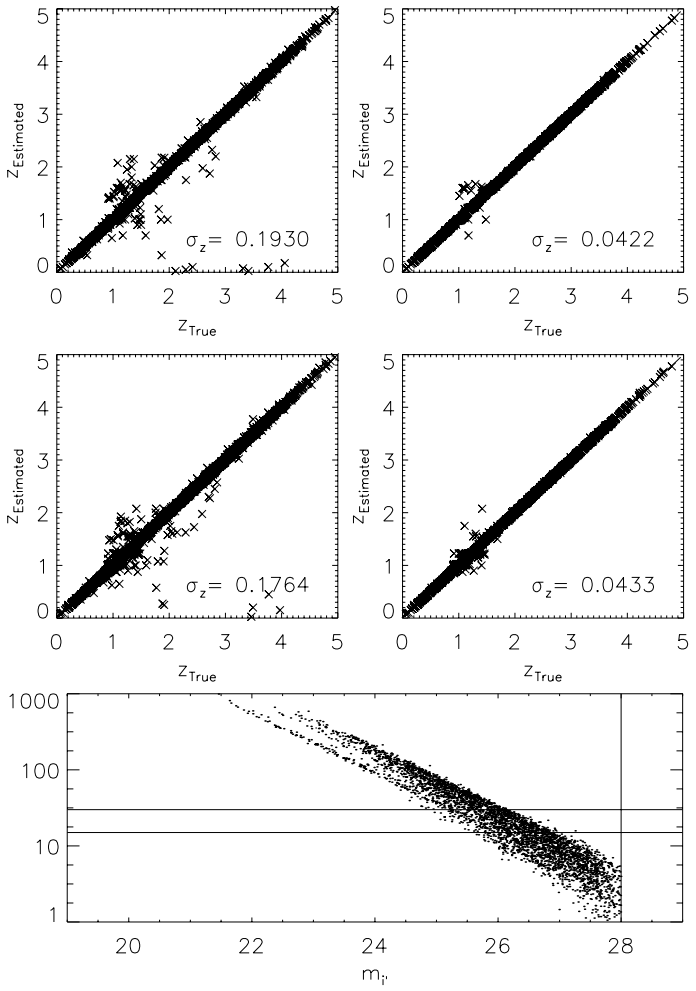

Figure 1.7: Simulations performed to determine how well a superconducting detector can determine the redshift of absorbtion line galaxies. The top four panels show the true versus estimated redshift for simulated spiral galaxies observed with a $R = 55$ MKID detector on the Keck 10m telescope for one hour. The top row contains the simulations without the effects of cosmic variance, a random stellar component added to the simulated spectra in order to simulate the variation of actual galaxies. The second row contains simulations with all of the attenuation and confusion factors, including cosmic variance. In the first column the fitting algorithm fits all galaxies with a broadband S/N ratio greater than 15, while the second column uses a minimum S/N ratio of 30. The bottom panel shows the distribution of broad band S/N ratio versus SDSS i' magnitude with the horizontal lines representing the S/N cuts described previously. The basic result is that a superconducting detector at Keck can accurately determine the redshift of a 26th magnitude galaxy in one hour. For more details see Mazin and Brunner (2000) [50].

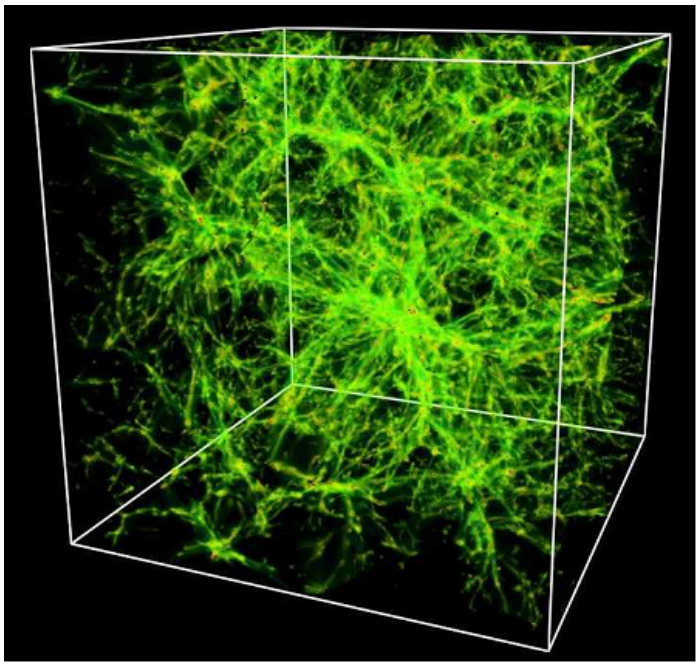

Figure 1.8: Superconducting detectors in the UV will allow us to understand the Intergalactic Medium. This figure shows a simulation of the gas distribution in the universe, the 'Cosmic Web', which future UV missions will explore. Figure courtesy of Davé *et al.* [61].

move with wavelength, while the images due to planets will be stationary. Superconducting detectors will also eliminate the separate low-resolution spectrograph that in a conventional design would be used after the planet is detected to look for spectroscopic signatures of life, such as oxygen and water vapor in the planet's atmosphere. Given a wide enough corrected field of view, a superconducting TPF (S-TPF) could take simultaneous spectra of all the planets around a star.

1.3.1.3 Ultraviolet

Ultraviolet detectors use microchannel plates (MCPs) to achieve high pixel counts, but their quantum efficiencies remain around 20% due to inefficient photocathodes. The quantum efficiency of superconducting detectors should reach above 70% in the UV and their energy resolution should be high ($R > 80$) [60].

Emission lines of many important diagnostic elements are found in the UV, and probing them with superconducting detectors will allow us to understand the ionization, temperature, and pressure of the intergalactic medium [61]. Quasar absorbtion line studies of the Lyman-alpha forest will serve similar purposes. This will allow us to understand the baryon density of the universe and the state of the IGM as a function of time. Figure 1.8 shows a model of the IGM.

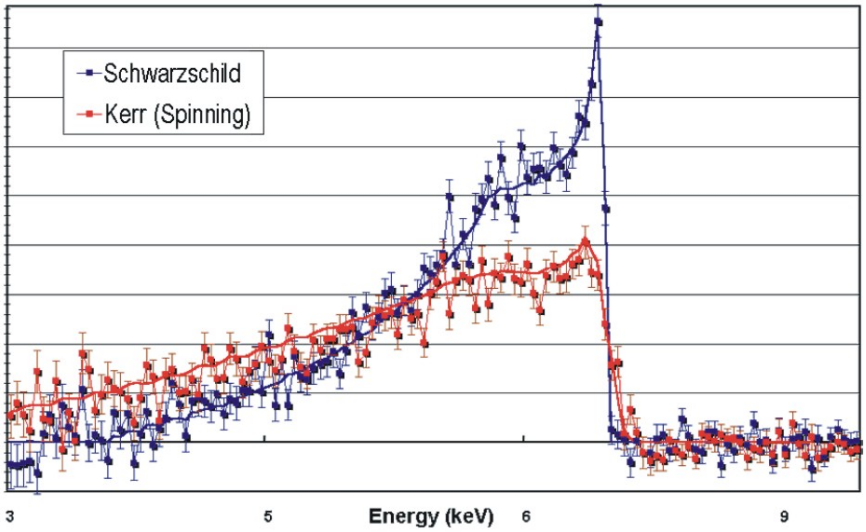

Figure 1.9: Constellation-X will allow detailed measurements of the iron Kα emission line profile in AGN and will measure the gravitationally induced increase in photon wavelength as matter is pulled closer to the event horizon of the black hole. This simulation shows what Constellation-X might see for iron line profiles from accretion disks orbiting Schwarzschild (nonspinning) and Kerr (spinning) black holes. Figure and caption courtesy of the Constellation-X science team [63].

1.3.1.4 X-ray

X-rays are often generated in those parts of the universe that exhibit extreme concentrations of mass and energy, like black holes, active galactic nuclei (AGN), neutron stars, and clusters of galaxies. Their ability to pierce thick veils of dust and gas make them a vital tool in studying these high-energy phenomena. Observations from future X-ray space telescopes will enable tests of Einstein's Theory of General Relativity in the strong-field limit. They will probe the energy generation mechanisms of quasars (Figures 1.9 and 1.10) and stellar-mass black holes. The X-ray emission of distant galaxy clusters will probe the earliest epochs of galaxy formation and large scale structure.

X-ray detectors for next generation missions like NASA's Constellation-X [62] need an energy resolution (FWHM) of several eV at 6 keV, high quantum efficiency, and around 1000 pixels. The Goddard Space Flight Center is pursuing TESs, and groups at Yale and ESA are working on Superconducting Tunnel Junction (STJ) detectors for this application, but have yet to demonstrate systems larger than 25 pixels. MKIDs are exciting additions to this wavelength range because they show a clear path to X-ray arrays of sufficient size for Constellation-X.

1.3.2 X-ray Microanalysis

X-ray microanalysis works by exciting a material using an electron or X-ray beam, then measuring the resulting X-ray fluorescence photons to determine the elemental composition of the material.

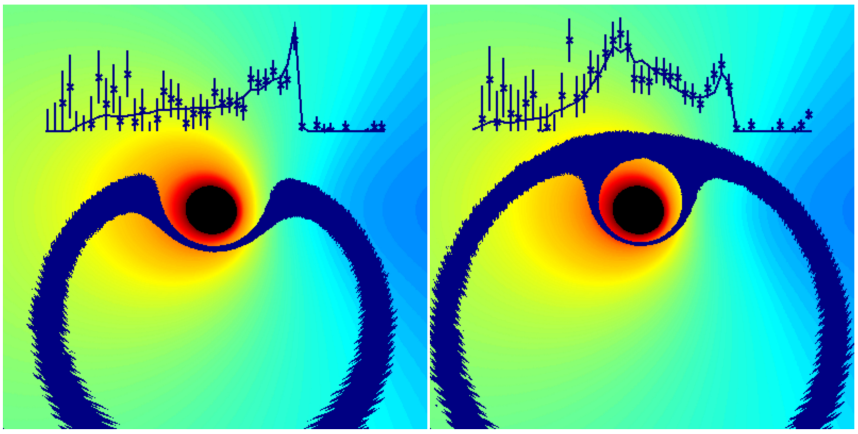

Figure 1.10: This figure illustrates the concept of iron line reverberation mapping, where the time delay between an observed flare and the line response provides information on the mass of the black hole. The figures are snapshots of a simulation of a flare near a supermassive black hole at two different times. It is color coded to show regions of redshift and blueshift. More information is available at the Constellation-X website [63].

Most commercial X-ray microanalysis is done with semiconductor detectors with energy resolutions around 130–175 eV, or wavelength dispersive detectors with a very low collection efficiency but a better energy resolution between 2–20 eV. Superconducting detectors can provide good energy resolution, allowing identification of closely spaced X-ray peaks in complicated spectra. This includes the peak overlaps in important materials (such as TiN and WSi_2) which cannot be resolved using semiconductor X-ray detectors [64]. TES microcalorimeters with better energy resolution ($\sim$ 4 eV FWHM) allow the measurement of chemical shifts which result from different chemical states. As an example, significant chemical shift effects in the Fe L-lines of compounds including Fe, Fe_2O_3, Fe_3O_4, FeS, and FeS_2 have been observed.

The primary driver of this technology is the semiconductor industry and their need for improved particle identification to diagnose wafer processing problems. To demonstrate the usefulness of a TES microcalorimeter for particle identification, the NIST group has performed a proof-of-concept experiment in a scanning electron microscope (SEM) in which they clearly identified 0.1 μm diameter Al_2O_3 particles and 0.3 μm diameter W particles on Si substrates [65].

The benefits of large arrays for X-ray microanalysis include larger collecting areas and higher count rates without the use of X-ray optics. Another possible benefit is the ability to compare spectra from each pixel to learn about local surface roughness [66].

1.3.3 Dark Matter Detectors

One of the most remarkable developments in astronomy in recent years is the consensus that about one third of the energy density of the universe is an unknown form of cold, nonbaryonic dark

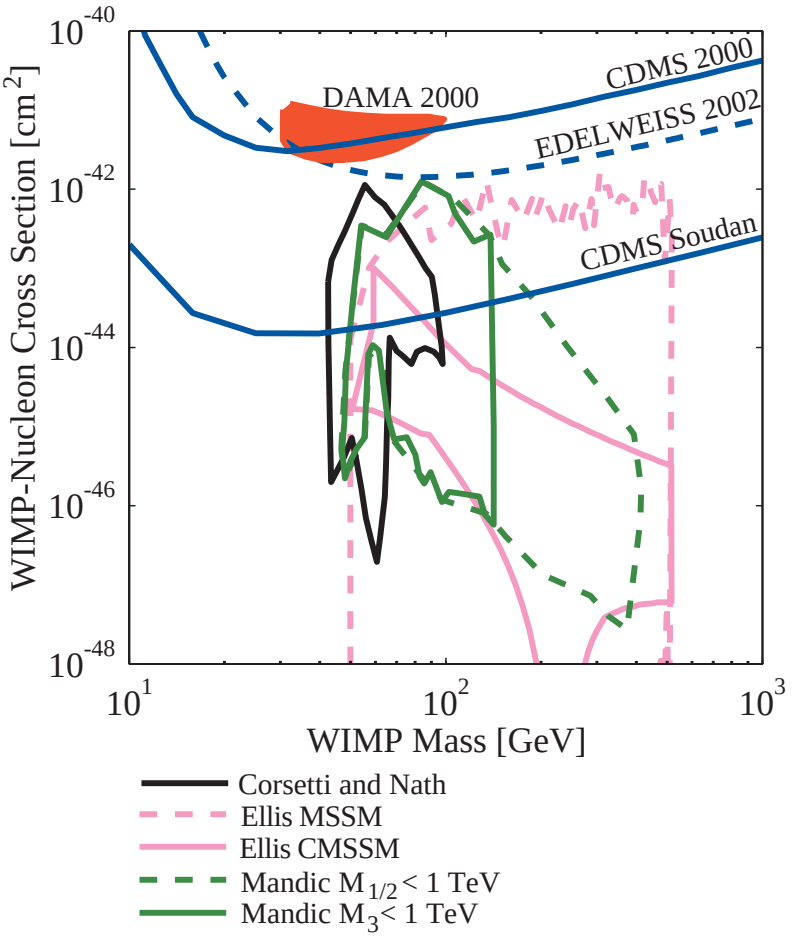

Figure 1.11: Current constraints and allowed parameter space for SUSY WIMPs. Constraints: CDMS 2000 limit [72]; EDELWEISS 2002 limit [73]; DAMA 2000 3σ allowed region [74]. Also shown is the expected CDMS deep-site sensitivity. Allowed parameter space: Corsetti and Nath mSUGRA models [75]; Ellis *et al.* MSSM [76] and constrained MSSM models [77]; Mandic *et al.* mSUGRA models with constraints $M_{1/2} < 1$ TeV or $M_3 < 1$ TeV [78]. Figure from [79].

matter. This dark matter interacts normally with gravity, but is non-luminous and rarely interacts with normal matter [67].

One promising class of candidates for dark matter are known as Weakly-Interacting Massive Particles (WIMPs). They were first proposed by Goodman and Witten 20 years ago based on the interesting coincidence that a stable, neutral particle with mass and interactions characteristic of the electroweak scale would have the properties of nonbaryonic cold dark matter [68, 69].

It is expected that WIMP dark matter can be directly detected via elastic-scattering interactions of WIMPs with nuclei [68, 70]. The WIMP-nucleon cross section is estimated to be around a few interactions per kg of target mass and per day [71]. The average energy imparted to the recoiling nucleus is a few keV to tens of keV.

The current state of WIMP direct detection is summarized in Figure 1.11. Direct-detection experiments are closing in on the bulk of supersymmetry-based WIMP models; some models (not shown) have already been ruled out. Direct accelerator searches have eliminated low-mass WIMP models.

The Cold Dark Matter Search (CDMS) currently uses 4 TES sensors to measure the phonons deposited in the target crystal. The rare interaction of a WIMP scattering off a nucleus creates phonons deep inside a crystal, which then travel to the surface where the phonons are converted to quasiparticles in a thin aluminum film. These quasiparticles then diffuse to one of the four TESs where they are measured.

There are distinct advantages to using an MKID instead of a TES as the phonon sensing detector. With MKIDs it should be possible to instrument the entire surface, rather than just 20% in the CDMS detectors. This should lead to a more precise determination of interaction position and a better determination of the deposited energy.

MKIDs need only one input and one output line, and the possibility of making large room temperature array readouts allow a more straightforward scale-up in the number of detectors than is currently possible. MKIDs are also much simpler to fabricate then the CDMS detectors.

A particle dark matter detector using MKID phonon sensors could provide significant improvements in both low energy electron rejection and in scalability, the two requirements for a next-generation WIMP search experiment.

Chapter 2

Theory of Microwave Kinetic Inductance Detectors

2.1 The Surface Impedance of Superconductors

Before we delve into the particulars of superconducting resonators, it is vital to review the electrodynamics of superconductors [28]. As its name implies, a superconductor below a critical temperature T_c has zero resistance for DC electrical current. This supercurrent is carried by pairs of electrons, known as Cooper pairs. Cooper pairs are bound together by the electron-phonon interaction, with a binding energy

$$2\Delta \approx 3.5 k_B T_c \tag{2.1}$$

where T_c is the superconducting transition temperature. The gap energy of the superconductor Δ stays very close to the zero temperature value, $\Delta(0)$, at temperatures well below T_c.

While superconductors will pass a DC current without resistance, they have a nonzero impedance for AC currents. Consider the case where an electric field is applied near the surface of a superconductor. The field causes the Cooper pairs to accelerate, storing kinetic energy in them. Since there is no dissipation in the superconductor, this energy may be extracted by reversing the electric field. Energy may also be stored in the magnetic field inside the superconductor, though the field only penetrates a short distance $\lambda \sim 50\,\mathrm{nm}$ into the superconductor. The cumulative effect is that a superconductor has a complex surface impedance due to the reactive energy flow between the superconductor and the electromagnetic field. The surface impedance

$$Z_s = R_s + i\omega L_\mathrm{s} \tag{2.2}$$

also includes a surface resistance R_s, which describes losses at angular frequency ω caused by the small fraction of electrons that are not in Cooper pairs, which are called quasiparticles. For temperatures T much lower than T_c, $R_\mathrm{s} \ll \omega L_\mathrm{s}$.

The density of thermally-excited quasiparticles is given by [80]

$$n_{qp}(T) = 2N_0\sqrt{2\pi k_B T\Delta(0)}\exp\left[-\Delta(0)/k_BT\right] \tag{2.3}$$

where N_0 is the single-spin density of electron states at the Fermi energy of the metal. For aluminum, $N_0 = 1.72\times10^{10}\,\mu\mathrm{m}^{-3}\,\mathrm{eV}^{-1}$, including the electron-phonon enhancement factor [81].

According to the Mattis-Bardeen theory [82], the imaginary part of the conductivity is given by the integral

$$\frac{\sigma_2}{\sigma_n} = \frac{1}{\hbar\omega}\int_{\Delta-\hbar\omega}^{\Delta} d\epsilon \frac{\left[1-2f(\epsilon+\hbar\omega)\right]\left(\epsilon^2+\Delta^2+\hbar\omega\epsilon\right)}{\sqrt{\Delta^2-\epsilon^2}\sqrt{(\epsilon+\hbar\omega)^2-\Delta^2}} \tag{2.4}$$

where $f(\epsilon) = 1/[e^{\epsilon/k_BT}+1]$ is the Fermi function and σ_n is the normal state resistance just above T_c. In the limit $k_BT << \Delta(0)$, $\hbar\omega << \Delta(0)$, this integral can be simplified to [83]

$$\frac{\sigma_2}{\sigma_n} \approx \frac{\pi\Delta(T)}{\hbar\omega}\left[1-2\exp(-\Delta(0)/k_BT)\exp(-\hbar\omega/2k_BT)I_0(\hbar\omega/2k_BT)\right] \tag{2.5}$$

where $I_0(x)$ is a modified Bessel function. This expression holds regardless of whether the photon energy $\hbar\omega$ is large or small compared to the thermal energy k_BT; note that at 0.3 K, the crossover $\hbar\omega = k_BT$ occurs at 6 GHz.

The real part of the conductivity is given by a similar integral

$$\frac{\sigma_1}{\sigma_n} = \frac{2}{\hbar\omega}\int_{\Delta}^{\infty} d\epsilon \frac{\left[f(\epsilon)-f(\epsilon+\hbar\omega)\right]\left(\epsilon^2+\Delta^2+\hbar\omega\epsilon\right)}{\sqrt{\epsilon^2-\Delta^2}\sqrt{(\epsilon+\hbar\omega)^2-\Delta^2}}. \tag{2.6}$$

In the limit $k_BT, \hbar\omega << \Delta(0)$, this integral simplifies to

$$\frac{\sigma_1}{\sigma_n} \approx \frac{2\Delta(T)}{\hbar\omega}\exp(-\Delta(0)/k_BT)K_0(\hbar\omega/2k_BT)\left[2\sinh(\hbar\omega/2k_BT)\right] \tag{2.7}$$

where $K_0(x)$ is also a modified Bessel function.

The electrodynamic response of superconductors can sometimes be simplified into one of two limits, the dirty (local) limit or the extreme anomalous limit. In the dirty limit the mean free path of electrons l_{mfp} is much less than the magnetic penetration depth λ and the coherence length $\xi_0 = \hbar v_f/\pi\Delta(0)$, where v_f is the Fermi velocity of the electrons. The extreme anomalous limit occurs when the London penetration depth $\lambda_L = \sqrt{\frac{mc^2}{4\pi ne^2}}$ is much less than the coherence length, where m is the mass on an electron, e is the electron charge, and n is the density of conduction electrons. The thick aluminum films we usually deal with ($\xi_0 \approx 1600$ nm $>> \lambda_L = 16$ nm) are firmly in the extreme anomalous limit. In these limits we can relate the surface impedance Z_s to the complex conductivity $\sigma = \sigma_1 - i\sigma_2$ which can be calculated using the Mattis-Bardeen equations shown above.

In the dirty (local) limit,

$$Z_s = \sqrt{\frac{i\omega\mu_0}{\sigma_1 - i\sigma_2}}. \tag{2.8}$$

For small changes at low temperature, we can approximate this as

$$\delta \ln Z_s = -\frac{1}{2}\delta \ln \sigma \tag{2.9}$$

$$\frac{\delta Z_s}{Z_s} = -\frac{1}{2}\frac{\delta\sigma}{\sigma}. \tag{2.10}$$

We can perform the same procedure in the extreme anomalous limit [84],

$$Z_s = \frac{i\sqrt{3}\omega\mu_0}{2}\left[\frac{3\pi\omega}{4v_f\lambda_L^2}\frac{\sigma_2 + i\sigma_1}{\sigma_n}\right]^{-1/3}. \tag{2.11}$$

For small changes at low temperature we can approximate this as

$$\delta \ln Z_s = -\frac{1}{3}\delta \ln \sigma \tag{2.12}$$

$$\frac{\delta Z_s}{Z_s} = -\frac{1}{3}\frac{\delta\sigma}{\sigma}. \tag{2.13}$$

Figure 2.1 shows σ_1 and σ_2 derived from the Mattis-Bardeen integrals for bulk aluminum as a function of temperature. These formulas are only valid for isotropic, bulk, plane superconductors. A more detailed treatment of surface impedance of superconductors including thin films can be found in Pöpel [84, 85].

2.2 Photon Detection

Now that we understand the equilibrium value of the surface impedance we can try to understand how it changes when energy is absorbed in the superconductor. The process of detecting a photon starts when a photon with energy greater than the gap energy ($h\nu > 2\Delta$) is absorbed in a superconductor. The energy of the photon can break apart one or more Cooper pairs (Fig. 1.1a), creating a cascade of interacting quasiparticles and phonons which quickly cools. The result of the cascade is a population of $N_{\rm qp} \approx \eta h\nu/\Delta$ excess quasiparticles with energies slightly greater than the gap energy and sub-gap phonons in the superconductor. In the previous equation $\eta \approx 0.57$ is the efficiency with which the photon energy is converted to quasiparticles [86]. These quasiparticle excitations will persist until two quasiparticles meet and emit a phonon, recombining into a Cooper pair. The average time this takes is the quasiparticle lifetime, τ_{qp}. During this time, the quasiparticles can diffuse over a distance of $l \approx \sqrt{D\tau_{qp}}$, where D is the diffusion constant of the material. We expect $D \sim 60$ cm^2/s for aluminum and $D > 8$ cm^2/s for tantalum from the measurements of Friedrich *et al.* [87].

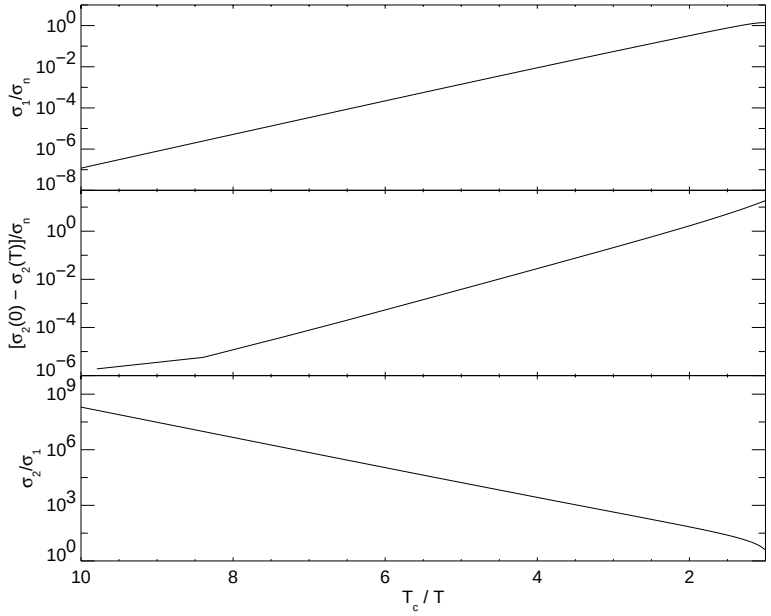

Figure 2.1: Values of σ_1/σ_n, $[\sigma_2(0)-\sigma_2(T)]/\sigma_n$, and σ_2/σ_1 derived from the Mattis-Bardeen integrals for a 320 nm thick aluminum film ($T_c = 1.175$ K) as a function of T_c/T. The key point is that the responsivity of a MKID scales with Q (Section 2.5), which is related to σ_2/σ_1 (Section 2.4), a quantity which increases exponentially as the temperature is lowered.

In an application where the photon energy is too low or the count rate is too high to count individual photons, the absorption of a steady stream of low-energy (mm/sub-mm) photons will raise the steady-state quasiparticle density by an amount $\delta n_{\rm qp} = \eta P \tau_{qp}/\Delta$ where P is the radiant power absorbed by the superconducting resonator.

Having excess quasiparticles in a superconducting film changes the surface impedance in a manner similar to raising its temperature. As we showed in Section 2.1, the surface impedance Z_s of the superconductor changes with temperature, so we should expect Z_s to change when the quasiparticle density is perturbed. The change in the surface impedance is $\delta Z_s = \delta n_{qp} \partial Z_s/\partial n_{qp}$, where the derivative depends on ω, T, and material parameters and can be calculated from Mattis-Bardeen theory. We can roughly approximate this as

$$\delta Z_s/Z_s \approx \delta n_{qp}/2N_0\Delta \tag{2.14}$$

since we expect the fractional change in the surface impedance to be comparable to the fraction of Cooper pairs that are broken. While the changes in δZ_s may be small, we can make a very sensitive measurement of them using a resonant circuit like the one shown in Figure 1.1b. Changes in $L_{\rm s}$ and $R_{\rm s}$ affect the frequency and width of the resonance, respectively, changing the amplitude (shown in Figure 1.1c) and phase (shown in Figure 1.1d) of a microwave signal transmitted through the

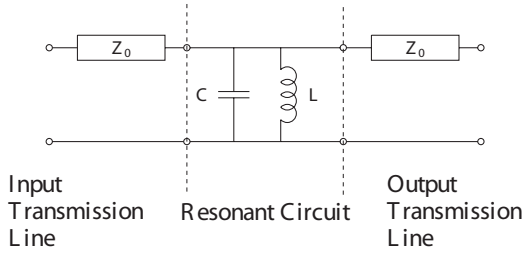

Figure 2.2: A parallel LC resonant circuit.

circuit. Section 2.5 will show how to use the physical properties of the resonant circuit to compute the expected phase change of the microwave probe signal when excess quasiparticles are present. The phase change per injected quasiparticle $d\theta/dn_{qp}$ is the responsivity of the detector. Combining the responsivity with knowledge of how well we can measure phase in a given time period (known as phase noise, which can be intrinsic to the device or be related to the way we generate and read out the signal) will allow us to calculate the noise equivalent power, signal to noise ratio, and dynamic range of a MKID.

2.3 Resonator Theory

The basic equations governing the response of the surface impedance of a superconductor were derived in Section 2.1. Now we must explore several different types of resonant circuits in order to understand how changes in the surface impedance affect the phase of a signal passed though a resonant circuit.

2.3.1 Parallel LC Resonant Circuit

We start by analyzing the simple parallel lumped element LC resonant circuit shown in Figure 2.2 following Zmuidzinas [88]. This LC circuit is connected to two semi-infinite transmission lines which have a characteristic impedance of Z_0. This allows us to calculate the transmission past the resonator and the reflection from the resonator. These quantities are usually expressed in the form of a 2×2 scattering matrix [89] of the circuit. Finding the scattering matrix as a function of resonator parameters will allow us to relate quantities of interest like the resonator quality factor Q to scattering parameters. This is vital for analysis of the real resonator data and for calculating resonator parameters like the responsivity, since the scattering matrix is an easily measured quantity.

Let us first examine the intrinsic quality factor Q of this circuit. If this resonator were somehow excited and allowed to ring, it would oscillate at a frequency $\omega_0 \approx 1/\sqrt{LC}$, and would radiate waves into both transmission lines, thereby losing energy. The oscillation amplitude, the peak voltage

across either L or C, would decay exponentially with time. The quality factor Q is defined in the usual way, $Q = \omega_0 \tau_{1/e}$, where $\tau_{1/e}$ is the time for the *energy* stored in the resonator to decay to $1/e$ of its initial value. Equivalently, $Q = \pi N_{1/e}$, where $N_{1/e}$ is the number of cycles of oscillation before the *amplitude* decays by a factor of $1/e$.

For calculating the quality factor of this circuit, the transmission lines can be replaced by resistors, whose resistances are given by Z_0. The result is a parallel RLC circuit, with $R = Z_0/2$. The quality factor is given by the well-known result, $Q = \omega_0 RC = \omega_0 Z_0 C/2$. This result can be derived quite easily. The energy E stored in the resonant circuit is given by

$$E = 2 \times \frac{1}{2} C \left\langle V^2 \right\rangle \ . \tag{2.15}$$

The averaging is performed over one cycle of the oscillation, and the factor of two accounts for the fact that, on average, half of the energy is stored in the inductor and half in the capacitor. The mean power dissipated is

$$P = \left\langle V^2 \right\rangle / R. \tag{2.16}$$

The time dependence of E is governed by

$$\frac{dE}{dt} = -P = -E/\tau_{1/e}, \tag{2.17}$$

which gives the result that

$$\tau_{1/e} = RC, \tag{2.18}$$

which shows that $Q = \omega_0 RC$.

We can now calculate the scattering matrix. The parallel LC circuit shown in Figure 2.2 is an example of a two-port shunt admittance circuit with $Y = 1/j\omega L + j\omega C$. We scale our units so that the normalizing impedance is 1. Thus, all impedances are divided by Z_0, and all admittances are multiplied by Z_0; we define $\hat{Y} = Z_0 Y$. The input admittance at port 1, with port 2 terminated, or vice-versa, is given by $Y_{in} = \hat{Y} + 1$. The input reflection coefficient is therefore

$$S_{11} = S_{22} = \frac{1 - Y_{in}}{1 + Y_{in}} = \frac{-\hat{Y}}{2 + \hat{Y}}. \tag{2.19}$$

The transmission amplitude can be derived in a similar fashion, and is given by

$$S_{21} = S_{12} = \frac{2}{2 + \hat{Y}}. \tag{2.20}$$

It is easy to check that both of these expressions have the correct limiting values when $\hat{Y} \to 0$ or

$\hat{Y} \to \infty$. Thus, the transmission amplitude for the parallel LC circuit is

$$S_{21} = \frac{2}{2 + (1/j\omega L + j\omega C)\, Z_0}. \tag{2.21}$$

This can be rewritten for ω near ω_0 as

$$S_{21} = \frac{1}{1 + jQ(1 - \omega_0^2/\omega^2)} \tag{2.22}$$

using the standard definitions $\omega_0 = 1/\sqrt{LC}$ and $Q = \omega_0 Z_0 C/2$.

For small perturbations from resonance, $\delta x = \delta\omega/\omega_0 << 1$, we can write

$$S_{21} = \frac{1}{1 + 2jQ\delta x} \tag{2.23}$$

so the power transmission is

$$|S_{21}|^2 = \frac{1}{1 + 4Q^2\delta x^2}. \tag{2.24}$$

At resonance, $\delta x = 0$, and the transmission is unity. The power transmission goes down by a factor of 2 (down by 3 dB) when $\delta x = \pm\frac{1}{2}Q$. Thus, the full width at half maximum (FWHM) of the power transmission curve is given by

$$\Delta\omega(\text{FWHM}) = \omega_0/Q. \tag{2.25}$$

2.3.2 Half Wave Resonator

A half wave transmission line resonator consists of a half wavelength length of transmission line with small coupling capacitors on either end, as shown in Figure 2.3. This circuit will only pass signals near its resonance frequency, leading to a transmission peak on resonance. The half wave transmission line resonator is simple conceptually, easy to build and couple, and its resonance is very easy to find.

It is possible to derive the expression for the quality factor due to loading using energy considerations. This loading (or coupling) calculation yields the coupling Q, Q_c. If all other loss terms are negligible compared to Q_c, then the measured Q of the resonator will be close to Q_c. More generally, the measured Q of a resonator is expected to depend on the total energy loss per cycle of the resonator. We expect energy to leak out through several paths. Some paths, like one through the coupling capacitor, are designed, while others, like the loss of energy to electromagnetic radiation, are governed by geometry and material parameters. These loss terms add like resistors in parallel:

$$\frac{1}{Q(0)} = \frac{1}{Q_{coupling}} + \frac{1}{Q_{dielectric}} + \frac{1}{Q_{radiation}}. \tag{2.26}$$

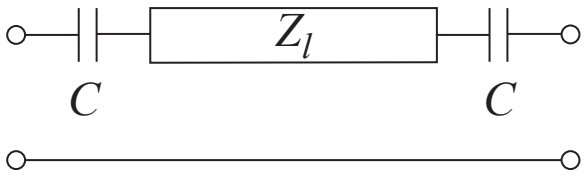

Figure 2.3: A transmission line resonator with series capacitors for input and output coupling. The characteristic impedance of the line is Z_l.

The terms shown here include the energy that leaks out of the resonator at the coupling capacitor, $Q_{coupling}$, dielectric loss, $Q_{dielectric}$, and radiation loss, $Q_{radiation}$. The losses will be discussed extensively in Chapter 3.

The transmission line resonator is initially excited and allowed to freely resonate, just as we assumed for the parallel LC resonator in the previous section. Due to the high impedance coupling, the voltage standing wave on the transmission line has a maximum at the ends, and one or more nodes along the line. Thus, in terms of the voltage V at the end of the line, the energy stored in the capacitance of the transmission line is

$$E_C = \frac{1}{2} \times \frac{1}{2} C_l \left\langle V^2 \right\rangle \tag{2.27}$$

where, as before, the averaging is done over one cycle of the oscillation. The extra factor of $1/2$ is included for the spatial average of the voltage standing wave over the length of the line. Including the energy stored in the transmission line inductance just doubles the energy,

$$E = \frac{1}{2} C_l \left\langle V^2 \right\rangle . \tag{2.28}$$

The power dissipated can be obtained by calculating the current flowing into the transmission line loads

$$P = 2 \left\langle I^2 \right\rangle Z_0 = 2 \left\langle (\omega C V)^2 \right\rangle Z_0. \tag{2.29}$$

In calculating the current, we have assumed that the coupling capacitor C dominates the total impedance. The factor of two accounts for power dissipation at each end. The $1/e$ decay time for the stored energy is therefore

$$\tau_{1/e} = \frac{E}{P} = \frac{C_l}{4 Z_0 (\omega C)^2}. \tag{2.30}$$

The total capacitance of the transmission line can be readily calculated

$$C_l = \mathcal{C} L = \frac{\sqrt{\mathcal{L}\mathcal{C}}}{\sqrt{\mathcal{L}/\mathcal{C}}} L = \frac{L}{\bar{c} Z_l} \tag{2.31}$$

where $\mathcal{C}$ and $\mathcal{L}$ are the capacitance and inductance of the transmission line per unit length, L is the

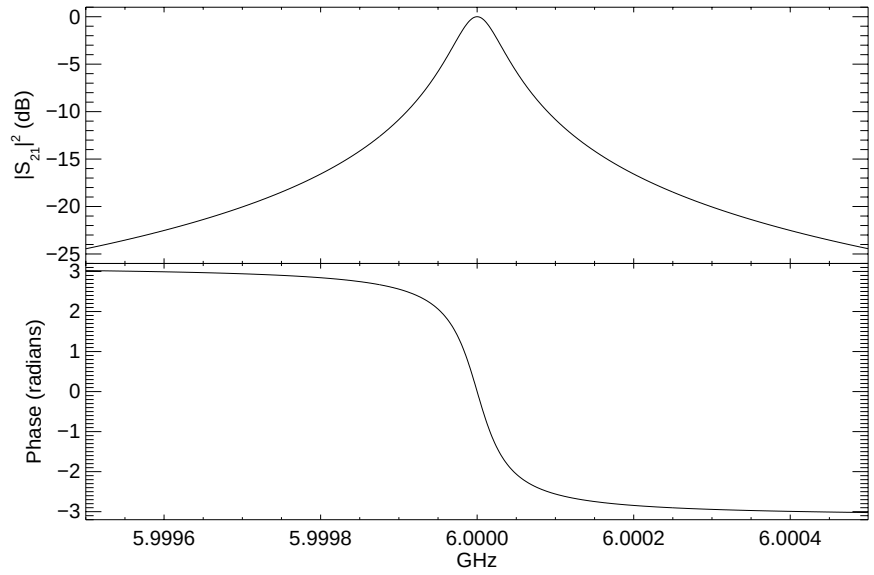

Figure 2.4: The amplitude and phase of a microwave probe signal transmitted though a half wave resonator near resonance. For this simulation, $Q = 1 \times 10^5$ and $f_0 = 6.0$ GHz. The phase is defined as the angle from the center of the resonance feature. This leads to a phase shift of 2π radians instead of the π radians one gets when the phase center is defined as the origin.

length of the transmission line, and $\bar{c}$ is the phase velocity. The admittance of a capacitor C_l at the n^{th} resonance frequency is

$$\omega_n C_l = \frac{\omega_n}{\bar{c}} \frac{L}{Z_l} = \frac{2\pi L}{\lambda_n Z_l} = \frac{n\pi}{Z_l}. \tag{2.32}$$

Putting everything together, we find an expression that determines the amount of power that leaks out through the coupling capacitor

$$Q_c = \omega_n \tau_{1/e} = \frac{n\pi}{4 Z_0 Z_l (\omega_n C)^2}. \tag{2.33}$$

For $\omega \approx \omega_0$ this circuit is functionally identical to the parallel LC resonator, so we can write the transmission through the resonator using Equation 2.22. We can also plot the transmission through the resonator for a simulated resonator with $Q = 1 \times 10^5$ and $f_0 = 6.0$ GHz to get an idea of what actual resonator data will look like. The plotted data is for the case we have analyzed where the energy losses from the resonator are dominated by energy escaping through the coupling capacitor. In regimes where the energy loss is not dominated by Q_c the measured Q will be limited to a value below Q_c and the resonance feature will be smaller. We explore this in more detail in Section 2.3.3.

These resonance curves are commonly expressed in two different ways. We can measure the amplitude and phase of a signal at various frequencies and plot the results, as shown for our simulated resonator in Figure 2.4. This figure shows that a half wave resonator produces a sharp peak in the

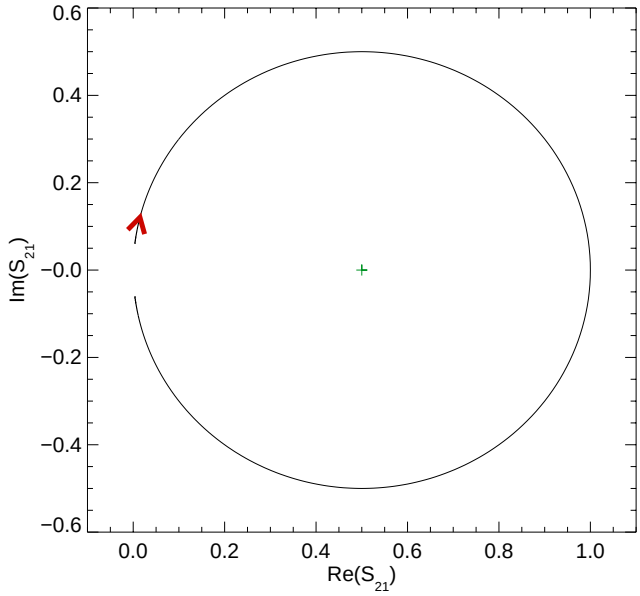

Figure 2.5: The normalized S_{21} trajectory in the complex plane of a half wave resonator near resonance. For this simulation, $Q = 1 \times 10^5$ and $f_0 = 6.0$ GHz. The green cross is the center of the resonance feature. The axis are normalized to give an on resonance transmission magnitude of 1. The frequency ranges from 5.9995 to 6.0005 GHz. The red arrow shows the direction of increasing frequency.

amplitude and a steep slope in the phase of transmission on resonance.

We can also display this data as a trajectory in the complex plane, plotting a point for every frequency that we measure. This traces out a trajectory for the resonator. Figure 2.5 shows this type of plot where the maximum transmission has been normalized to 1. It makes sense to define the phase center as center of the resonance circle instead of the origin (the point where $|S_{21}| = 0$) so that we get 2π of phase shift as we move through resonance regardless of the size (depth) of the resonance feature. We will use this definition of phase unless we specify otherwise.

2.3.3 Quarter Wave Resonator

The quarter wave transmission line resonator, shown in Figure 2.6, consists of a series combination of a coupling capacitor C and quarter wavelength section of transmission line of impedance Z_0, shunting a feed line. Here we follow the analysis of Day [90].

The input impedance, Z_l, of the shorted transmission line is

$$Z_l = Z_0 \tanh\left(i\beta l + \frac{\beta l}{2Q_i}\right), \tag{2.34}$$

where β is the propagation constant, $Q_i = \beta/2\alpha$ is the internal quality factor of the line, and α is

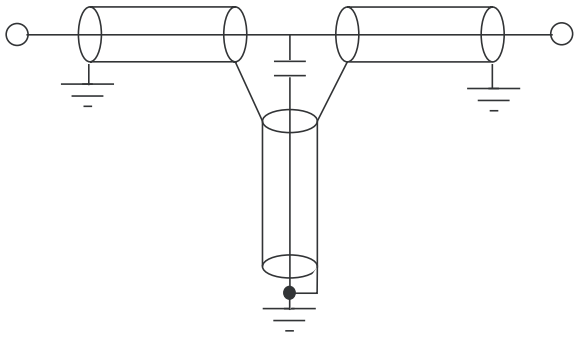

Figure 2.6: A quarter wave transmission line resonator shown represented schematically with coaxial transmission lines.

the attenuation constant. This can be rewritten as

$$Z_l = Z_0 \frac{1 - i \tanh \frac{\beta l}{2Q_i} \cot \beta l}{\tanh \frac{\beta l}{2Q_i} - i \cot \beta l}. \tag{2.35}$$

Near the quarter-wave condition, we can write $\beta l = \frac{\pi}{2}(1 + \frac{\Delta\omega}{\omega_{1/4}})$, where $\Delta\omega = \omega - \omega_{1/4}$, and $\omega_{1/4}$ is the angular frequency when the quarter wave condition is met. For small x, $\cot(\frac{\pi}{2} + x) \approx -x$ and $\tanh x \approx x$. Dropping second order terms, we have

$$Z_l \approx \frac{4Z_0 Q_i/\pi}{1 + 2iQ_i \frac{\Delta\omega}{\omega_{1/4}}}. \tag{2.36}$$

The impedance of the series combination of coupling capacitor and quarter-wave section is

$$Z = \frac{-i}{\omega C} + \frac{4Z_0 Q_i/\pi - \frac{8iZ_0 Q_i^2}{\pi} \frac{\Delta\omega}{\omega_{1/4}}}{1 + 4Q_i^2 \left(\frac{\Delta\omega}{\omega_{1/4}}\right)^2}. \tag{2.37}$$

Resonance occurs at a frequency $\omega_0 < \omega_{1/4}$ where $\mathrm{Im}(Z) = 0$. At that frequency, the transmission line section looks inductive and tunes out the large capacitive reactance of the coupling capacitor.

When $\mathrm{Im}(Z) = 0$ has solutions, it will have a pair of them. The interesting solution is the one at lower frequency, because at the higher solution, which is closer to $\omega_{1/4}$, the real part of the impedance of the transmission line section is very large and does not load the through line.

Solving for ω_0 gives us the 'loaded' resonance frequency that depends on the coupling capacitor

$$\omega_0 - \omega_{1/4} = \frac{-2Z_0 \omega_{1/4} \omega_0 C}{\pi} \approx \frac{-2Z_0 \omega_{1/4}^2 C}{\pi}. \tag{2.38}$$

We can derive a coupling quality factor Q_c in the same manner as for a half wave resonator which

was performed in Equation 2.33. Using this we can rewrite the relative frequency shift as:

$$\frac{\omega_0 - \omega_{1/4}}{\omega_{1/4}} \approx -\sqrt{\frac{2}{\pi Q_c}}. \tag{2.39}$$

We can simplify our expression for Z by looking at frequencies near resonance. We define $\Delta\omega' = \omega - \omega_0$ yielding:

$$Z = \frac{\pi}{4Z_0(\omega_0 C)^2 Q_i}\left(1 + \frac{2iQ_i\Delta\omega'}{\omega_0}\right) \tag{2.40}$$

where we have substituted $\omega_{1/4}$ with ω_0 in places.

The forward scattering matrix element for a shunt impedance is

$$S_{21} = \frac{2}{2 + \frac{Z_0}{Z}}. \tag{2.41}$$

At $\Delta\omega' = 0$, the transmission magnitude past the resonators $|S_{21}|$ is a minimum and

$$S_{21}^{min} = \frac{Q_c}{Q_i + Q_c}. \tag{2.42}$$

The resonance curve can be expressed as:

$$S_{21} = \frac{S_{21}^{min} + 2iQ(0)\delta x}{1 + 2iQ(0)\delta x} \tag{2.43}$$

where $Q(0)$ is the loaded quality factor $Q_iQ_c/(Q_i + Q_c)$ at $T = 0$.

$Q(0)$ can be related to the width of the resonance dip by finding the point at which $Q(0)\Delta\omega'/\omega_0 = \pm 1/2$. At those frequencies,

$$|S_{21}|^2 = \frac{|S_{21}^{min}|^2 + 1}{2}. \tag{2.44}$$

For an over-coupled resonator the -3dB width measured down from the carrier amplitude gives the resonator's quality factor Q.

In the same manner as for the half wave resonator we can examine the amplitude and phase of a microwave signal transmitted past a $Q = 1 \times 10^5$ and $f_0 = 6.0$ GHz resonator. This is shown in Figure 2.7. The complex trajectory of S_{21} is shown in Figure 2.8. As we expect, the quarter wave resonator shows a transmission dip and a steep phase slope on resonance.

2.4 Calculating Resonator Parameters

We can calculate the Q, f_0, and the depth of the resonance feature S_{21}^{min} of a resonator at a given temperature by considering how the surface impedance of the superconductor changes as the temperature is increased.

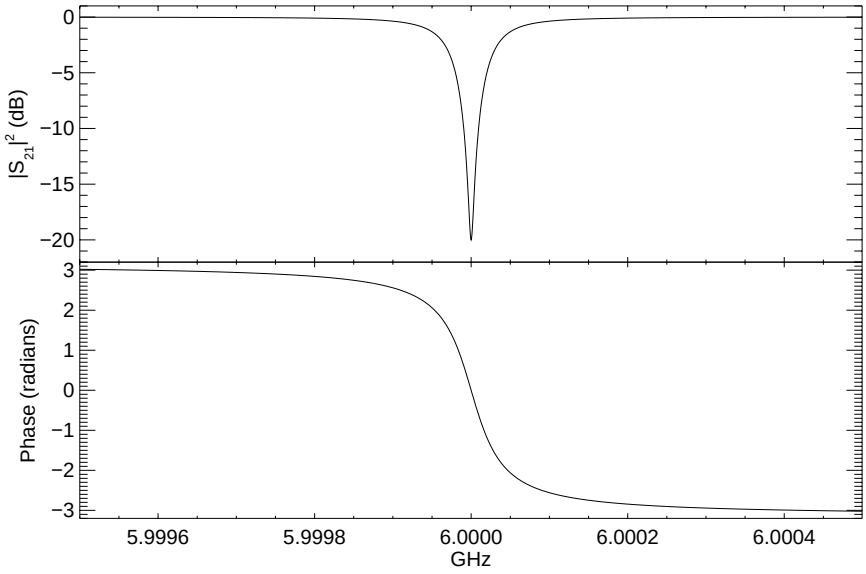

Figure 2.7: The amplitude and phase of a microwave probe signal transmitted past a quarter wave resonator near resonance. For this simulation we assume a coupling limited resonator with $Q_c = 1 \times 10^5$ and $f_0 = 6.0$ GHz. The phase is defined as the angle from the center of the resonance feature.

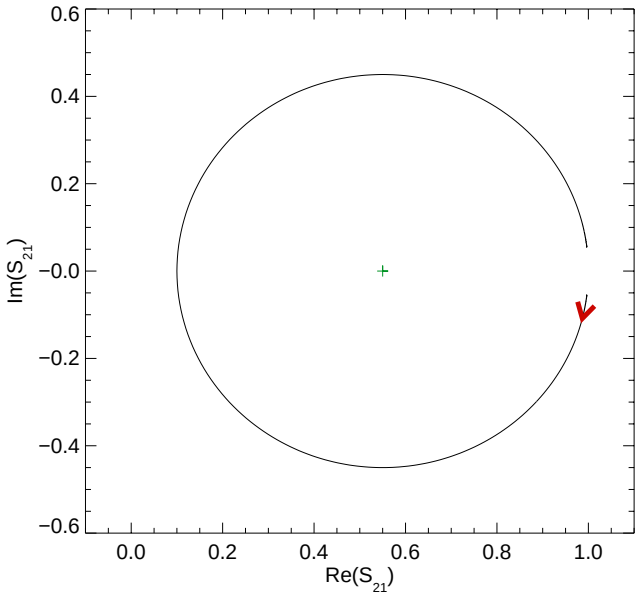

Figure 2.8: The normalized S_{21} trajectory in the complex plane of a quarter wave resonator near resonance. For this simulation, $Q = 1 \times 10^5$ and $f_0 = 6.0$ GHz. The green cross is the center of the resonance feature. The axis are normalized to give an off resonance transmission magnitude of 1. The frequency ranges from 5.9995 to 6.0005 GHz. The red arrow shows the direction of increasing frequency.

Since the resonant frequency of a resonant circuit goes as $f_0 \propto 1/\sqrt{L}$ (Section 2.3.1) a small change in the inductance of a resonant circuit can be approximated as

$$\delta f(T) = -\frac{1}{2}\delta L_s(T). \tag{2.45}$$

This means that the fractional frequency shift of the resonator can be written

$$\frac{\delta f(T)}{f(0)} = \frac{-\alpha \delta L_s(T)}{2L_s(0)}. \tag{2.46}$$

We have included a factor of α that represents the fraction of the total inductance of the transmission line that is contributed by the kinetic inductance

$$\alpha = L_{kin}/L_{total}. \tag{2.47}$$

The Q of a series RLC circuit can be written as $Q = \omega_0 L/R$. Using this allows us to write an equation for $Q(T)$,

$$Q(T) = \frac{\omega_0 L_s(T)}{\alpha R_s(T)}. \tag{2.48}$$

Rewriting this to include a limiting Q as low temperatures gives

$$\frac{1}{Q(T)} = \frac{1}{Q(0)} + \frac{\alpha R_s(T)}{\omega L_s(T)} \tag{2.49}$$

where $Q(0)$ is the Q measured at $T = 0$. This low temperature limit of the resonator quality factor $Q(0)$ is the result of energy leaking out of the resonator as shown in Equation 2.26.

The depth of the resonance dip S_{21} can be calculated in a similar fashion based on Equation 2.42,

$$S_{21}^{min}(T) = \frac{Q(0) + Q(T)(S_{21}^{min}(0) - 1)}{Q(0)}. \tag{2.50}$$

For the extreme anomalous limit we can rewrite Q and f_0 as:

$$\frac{\delta f(T)}{f(0)} = \frac{-\alpha \delta \sigma_2(T)}{6\sigma_2(0)} \tag{2.51}$$

$$\frac{1}{Q(T)} = \frac{1}{Q(0)} + \frac{\alpha \sigma_1(T)}{3\sigma_2(T)}. \tag{2.52}$$

These equations will be very useful to fit the temperature variation of Q, f_0, and S_{21}^{min} in real resonance data.

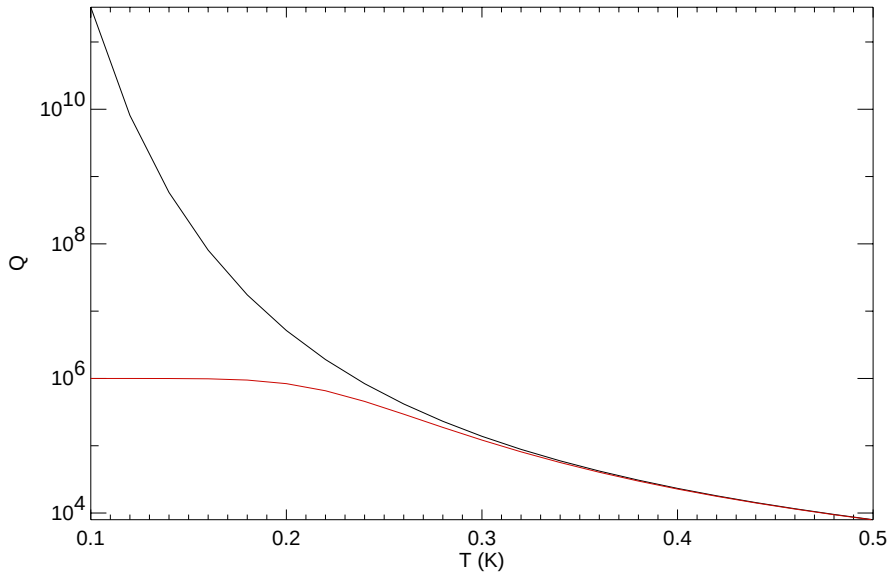

Figure 2.9: We can derive the maximum Q of an aluminum resonator due to metal loss as a function of temperature by using Equation 2.49, shown as the black line. Values of σ_1 and σ_2 are derived from the Mattis-Bardeen integrals for a 320 nm thick aluminum film ($T_c = 1.275$ K). The red line shows the Q we expect from a resonator that is coupling limited to $Q = 1 \times 10^6$.

2.5 Resonator Responsivity

We can calculate the responsivity, the phase change per quasiparticle injected $d\theta/dN_{qp}$, of a resonator using Mattis-Bardeen theory. This derivation assumes that the quasiparticle density in the resonator is raised uniformly. The case where the quasiparticles are injected at a discrete location will be dealt with in Section 2.6.

For a small change in the quasiparticle density around the resonance frequency with the phase center at the center of the resonance feature we can calculate the phase responsivity of the detector as:

$$\frac{d\theta}{dN_{qp}} = \frac{d\phi}{d\omega_0} \cdot \frac{d\omega_0}{dL_{total}} \cdot \frac{dL_{total}}{dN_{qp}} \tag{2.53}$$

$$= \frac{4Q}{\omega_0} \cdot \frac{\omega_0}{2L_{total}} \cdot \frac{dL_{total}}{dN_{qp}} \tag{2.54}$$

$$= \frac{2Q}{L_{total}} \cdot \frac{dL_{total}}{dN_{qp}} \ . \tag{2.55}$$

If we assume the extreme anomalous limit we can use Equation 2.13 and the kinetic inductance fraction α to take into account that only part of the total inductance changes and we get

$$\frac{d\theta}{dN_{qp}} = \frac{2\alpha Q}{\sigma_2(0)} \frac{d\sigma_2(T)}{dN_{qp}} \tag{2.56}$$

where

$$\frac{d\sigma_2(T)}{dN_{qp}} = \frac{d\sigma_2(T)}{dT}\frac{dT}{dN_{qp}}. \tag{2.57}$$

Using Equation 2.5 and 2.3 we can write a messy but analytic expression for the responsivity that proves to be reasonably accurate for the devices we test in this thesis,

$$\frac{d\theta}{dN_{qp}} = \sqrt{\frac{2}{\pi}} \cdot \frac{\hbar\omega I_0(\zeta) - (2\Delta + \hbar\omega)I_1(\zeta)}{\sqrt{\Delta k_B T}(2\Delta + k_B T)} \cdot \frac{\alpha Q}{N_0 V}, \tag{2.58}$$

where $\zeta = \hbar\omega/2k_BT$. For an aluminum resonator at 6 GHz with $\Delta = 170$ meV and at temperatures well below T_c, we can simplify this equation to

$$\frac{d\theta}{dN_{qp}} = 1.63 \times 10^{-7}\frac{\alpha Q}{V}, \tag{2.59}$$

where the units of $d\theta/dN_{qp}$ are radians per quasiparticle and the volume V is in μm^3.

The most important point about this formula is that for a given superconductor and resonant frequency it produces a resonator responsivity scaling law $d\theta/dN_{qp} \propto \alpha Q/V$. This shows that to make more responsive resonators we need to aim for high α and quality factor and low volume.

We can also use what we know about the resonator response to find a more general form for $\theta(T)$. First we calculate the phase response as a function of temperature, then convert this to the phase response per quasiparticle. Taking the derivative of this function at base temperature will give us the phase change per quasiparticle, $d\theta/dN_{qp}$.

First, lets write out the phase as a function of temperature

$$\theta(T) = \tan^{-1}\left(\frac{\text{Im}[S_{21}(T)] - y_c}{\text{Re}[S_{21}(T)] - x_c}\right). \tag{2.60}$$

Here S_{21} is derived from Equation 2.43 and $x_c + iy_c$ is the center of the resonance feature in the complex plane. This leads to

$$\theta(T) = \tan^{-1}\left(\frac{4\frac{\delta\omega}{\omega_0}Q^2 + S_{21min} - y_c}{2\frac{\delta\omega}{\omega_0}Q - 2\frac{\delta\omega}{\omega_0}QS_{21min} - x_c}\right). \tag{2.61}$$

Now we can use the equations for Q, f_0, and S_{21min} as a function of temperature from Section 2.4 to compute $\theta(T)$.

While it is relatively easy to compute numerical values for σ_1 and σ_2 that go into the calculation of Q, f_0, and S_{21min}, the equations quickly become unwieldy in their analytic form. We derive numerical values for these quantities as a function of temperature, then take the numerical derivative at base temperature to determine $d\theta/dN_{qp}$.

2.6 Position-Dependent Response

The transmission line resonators we have discussed have a position dependent response to quasiparticle injection. This is due to the current distribution of the resonator. For a half wave resonator (a transmission line with coupling capacitors at both ends as shown in Figure 2.3), the voltage and current distribution can be written in a modal expansion:

$$V(z,t) = \sum_{n=1}^{\infty} V_n(t)\cos(n\pi z/S) \tag{2.62}$$

$$I(z,t) = \sum_{n=1}^{\infty} I_n(t)\sin(n\pi z/S). \tag{2.63}$$

Where S is the physical length of the resonator. The voltage and current distribution of a quarter wave resonator (one end open, one end shorted as shown in Figure 3.3) can be written in a modal expansion:

$$V(z,t) = \sum_{n=1}^{\infty} V_n(t)\cos[(2n-1)\pi z/2S] \tag{2.64}$$

$$I(z,t) = \sum_{n=1}^{\infty} I_n(t)\sin[(2n-1)\pi z/2S]. \tag{2.65}$$

After a little math it is possible to figure out the change in the surface impedance of the transmission line at resonance n due to a localized injection of quasiparticles in a quarter wave resonator $\delta L_n(T)$,

$$\delta L_n(t) = 2\int_0^S dz \sin^2[(2n-1)\pi z/2]\delta\mathcal{L}(z,t) \tag{2.66}$$

where $\delta\mathcal{L}(z,t)$ is the kinetic inductance as a function of position in the resonator, which in the extreme anomalous limit can be calculated using Equation 2.13 for a given temperature (quasiparticle) distribution in the strip. The overall result is that the response of the resonator to the injection of quasiparticles is position dependent, weighted by the square of the current distribution in the transmission line.

The practical effect of this is that transmission line resonators that are longer than the diffusion length of quasiparticles (Section 3.3.5) cannot resolve the energy of an incoming photon. This occurs because photons absorbed in different locations along the length of the resonators cause different responses for a given photon energy. For example, an event near the shorted end of a quarter wavelength resonator will cause a much greater phase response then an event near the open end. A simple solution is to use a separate photon absorber, and inject the energy from the photon into the sensitive shorted end using quasiparticle trapping from a higher gap absorber for the largest response. Details of this design can be found in Section 3.3.5.

It is also possible to use this position dependence to directly give information on the energy and position of a photon event by laying two resonators next to each other with their couplers at opposite ends. Any events shared between the two resonators will cause a signal in each resonator proportional to the location, and the sum of the signals will give the total energy of the event.

Chapter 3

Designing a Microwave Kinetic Inductance Detector

3.1 Choosing an Architecture

There are various possible layouts that could be used to make a MKID. The simplest are transmission line resonators, such as coplanar waveguide (CPW) (Figure 3.3), microstrip, stripline, and slotline. Cross sections of these transmission line geometries are shown in Figure 3.1. Lumped element devices with distinct capacitors and inductors are another option (Fig. 3.4).

We chose CPW resonators because they are very simple, one layer devices that are easy to understand and do not make use of thin film dielectrics, which may be lossy. A half wave CPW resonator (Figure 2.3) will produce a transmission peak on resonance, and a quarter wave resonator (Figure 3.3) will produce a transmission dip on resonance. These resonators have a position-dependent responsivity — their responsivity peaks where the standing wave current distribution has a maximum, as shown in Section 2.6. For the first resonance, this happens in the center of the strip for the half wave resonator, and at the shorted end for the quarter wave resonator.

This sensitivity peak at the shorted end makes the quarter wave CPW resonator especially useful since the shorted end is a convenient point to inject quasiparticles. This can be achieved by absorbing the radiation in a higher gap superconductor in metal-to-metal contact with the resonator. As quasiparticles diffuse from a higher gap absorber like tantalum into a lower gap resonator like

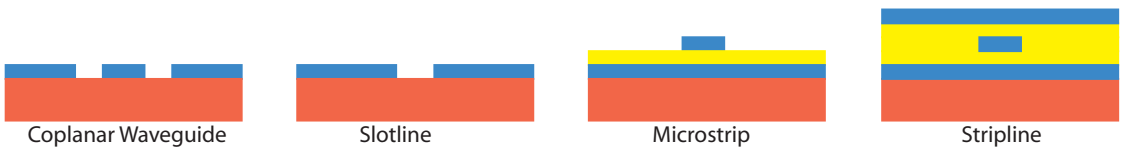

Figure 3.1: Cross sections of various types of thin film transmission lines. Substrates are shown in red, superconductors in blue, and thin film dielectrics in yellow.

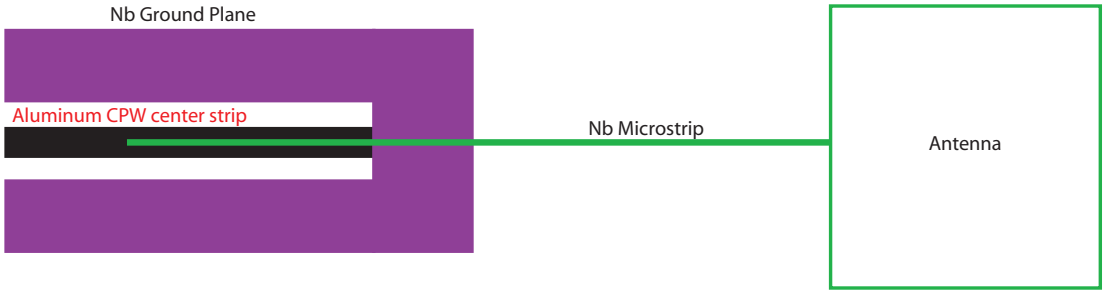

Figure 3.2: Coupling millimeter or submillimeter photons to a quarter wave CPW resonator may be achieved by using an antenna to absorb the incoming radiation and send it down a niobium microstrip. Since the gap frequency of niobium is 750 GHz it will transmit signals of up to this frequency. Running this Nb microstrip over a aluminum ground plane (in this case, the center strip of a quarter wave resonator) will cause the radiation to break Cooper pairs in the ground plane since the radiation is above the gap frequency of aluminum. This will cause a quasiparticle excess that the resonator can detect.

aluminum, they quickly cool by emitting a phonon and cannot return to the higher gap absorber. This is known as quasiparticle trapping. Figure 3.8 shows this process, which is explained in greater detail in Section 3.3.5.

For submillimeter detectors, the energy from an antenna or absorber can be coupled in either by diffusion and quasiparticle trapping or by running a niobium microstrip line over the sensitive end of the resonator. A superconducting transmission line will pass signals below the gap frequency, $\nu_{gap} = \Delta/h$, with very low loss. Radiation above the gap frequency will break Cooper pairs in the superconductor and result in a lossy transmission line. The gap frequency of niobium is over 700 GHz, which is higher than most submillimeter frequencies of interest. The gap frequency of aluminum is 90 GHz, which means this is the lowest frequency that an aluminum MKID can detect. The radiation absorbed by the antenna passes down the microstrip without loss until it transitions from a niobium ground plane to an aluminum ground plane (also the center strip of the CPW resonator). This breaks Cooper pairs, resulting in an excess quasiparticle population in the aluminum ground plane/CPW resonator center strip that will be sensed by the resonator. This is shown in Figure 3.2.

Another major advantage of a quarter wave CPW resonator is that it has nearly perfect transmission away from the resonance frequency, so many resonators can be read out through a single transmission line, as discussed in Section 3.2.

Figure 3.3 shows a microscope photograph of a quarter wave CPW device described in Day*et al.* [27]. The light regions of the photograph are where aluminum is present, and the dark areas are where the bare substrate is exposed. In this photograph and the inset circuit diagram, (A) is the CPW "through" line used for excitation and readout. (B) is the meandered quarter-wavelength

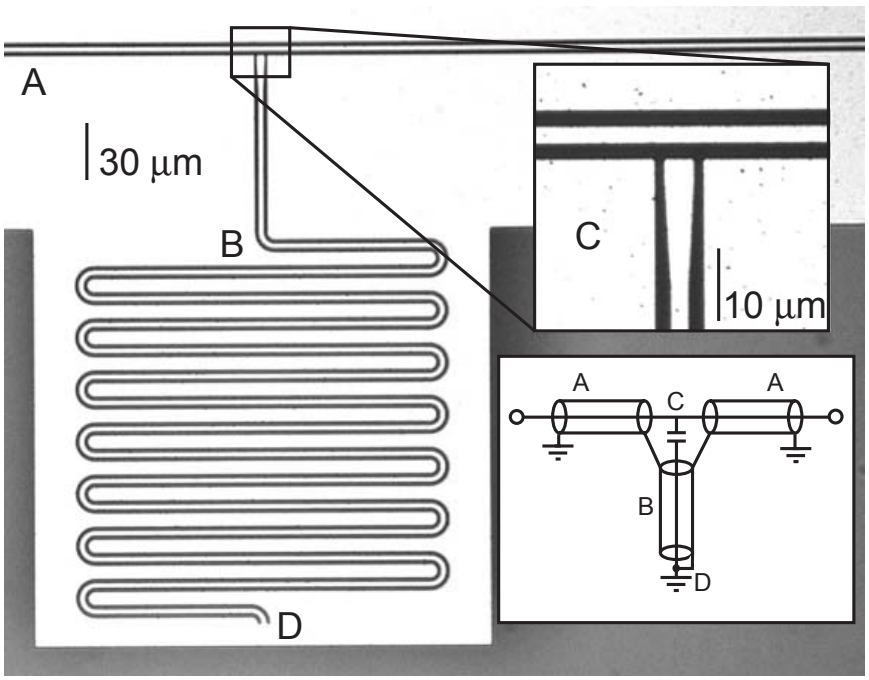

Figure 3.3: A microscope photograph of a quarter wave CPW resonator tested and written up in Day *et al.* [27]. The top inset shows a magnified view of the coupling region, and the bottom inset shows the equivalent circuit.

resonator section, with an overall length of 3 mm and resonance frequency around 10 GHz. (C) is the coupling capacitor and (D) is the short-circuit termination of the resonator. The coupling region is magnified in the top inset. The diagram on the lower right shows the equivalent circuit.

3.2 Frequency Domain Multiplexing

Resonator designs which have good transmission away from resonance lend themselves naturally to frequency domain multiplexing. Each resonator is designed to have a slightly different resonant frequency, and is excited and read out independently. The number of resonators that can be multiplexed through a single transmission line and cryogenic amplifier depends on several factors.

- The frequency separation of resonators must be greater than the width of the typical resonance. From Equation 2.25, this means that the separation must be several times greater than f_0/Q. For a $Q = 1 \times 10^6$ resonator at 6 GHz, the minimum spacing would be around 20 kHz.

- The information content of the kinetic inductance signal that modulates the carrier must not be contaminated by signals from adjacent resonators (crosstalk). For background-limited detection in the millimeter and submillimeter, photon noise will have a spectrum out to a frequency of $(2\pi\tau_{qp})^{-1}$ Hz, where τ_{qp} is the quasiparticle recombination time in the resonator.

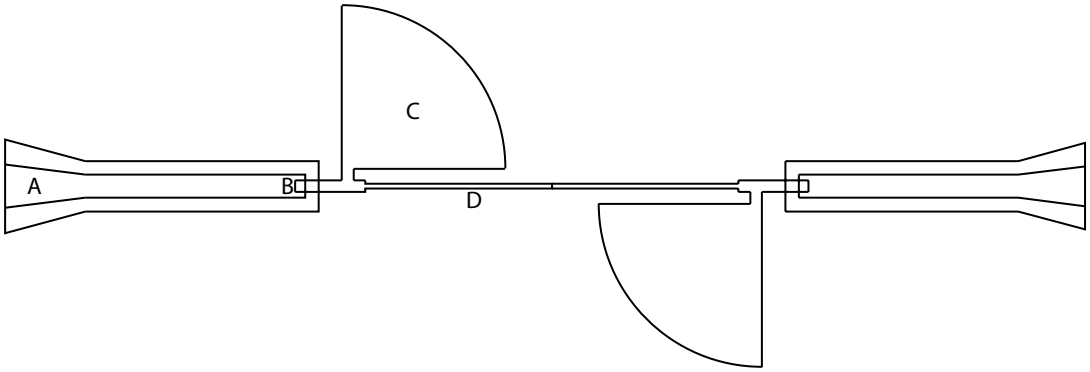

Figure 3.4: A lumped element microstrip resonator fed with a CPW transmission line A. The overlap B serves as the coupling capacitor. The radial stub capacitors C provides the bulk of the capacitance, and the microstrip D provides the inductance.

For optical/UV/X-ray applications it is helpful to sample much faster than the quasiparticle recombination time to reconstruct the pulse shape, which can give interesting information about pulse arrival time, rise time, and saturation effects. For an aluminum resonator this might mean a sample rate of 250,000 samples/second (125 kHz) for an optical/UV/X-ray detector, and only 2000 samples/second (1000 Hz) or less for a submillimeter detector.

- We must provide anti-aliasing filters capable of strongly rejecting signals which are above the frequency domain of interest.

- The coupling Q affects the resonant frequency of a resonator as shown in Equation 2.39. Lithographic variations in the coupler may produce a noticeable frequency shift, though we have not yet simulated the magnitude of this effect.

- The lithographic precision of the resonator length determines how accurately each resonant frequency is set. For a 6 GHz resonator with a length of around $L = 5$ mm and a lithographic precision $\delta L = .2$ μm, we expect to be able to set a resonance to $f_0 \delta L/L = 250$ kHz.

- For high Q resonators in an actual, array misplacing the resonators in the frequency domain might not be an issue since the resonators can be mapped to their appropriate pixel position by mapping the array response. The high Q means that the chances of two resonances overlapping would be small.

- The total power that a cryogenic microwave amplifier can handle may be an issue depending on the number of frequencies sent through the amplifier and the readout power used. This is heavily dependent on the amplifier used and the readout power of the individual resonators, and careful engineering should minimize this issue.

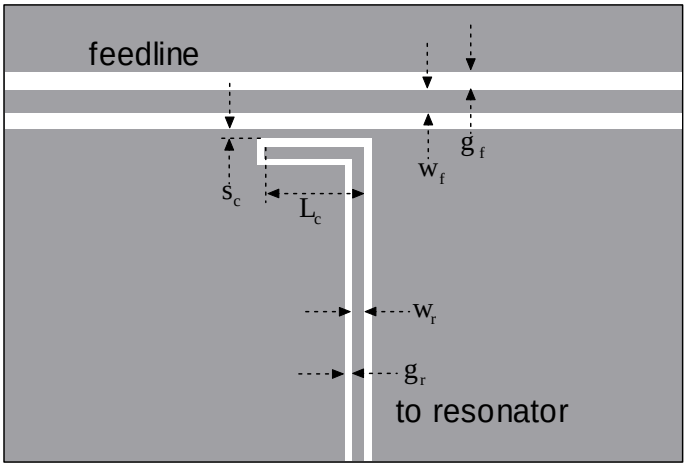

Figure 3.5: The geometry of a CPW resonator and "elbow" coupler. The superconductor is shown in gray, and bare substrate in white. The most common design we use is $w_f = 10$ μm, $g_f = 6$ μm, $w_r = 3$ μm, $g_r = 2$ μm, $s_c = 2\mu$m

- The final constraint is amplifier bandwidth. Amplifiers with multi-octave bandwidths and low noise have been demonstrated [91].

For a pulse counting detector (optical/UV/X-ray), the limiting factor will likely be preserving the information content because of the fast rise times of the pulses. With a 2 MHz resonator spacing and a 4–8 GHz amplifier, 2000 resonators can be accommodated. For the slow response of a submillimeter detector (for example, SHARC2 at CSO samples every 30 milliseconds), the lithographic precision will likely be the dominant error. Assuming a 250 kHz spacing, this will yield 16000 resonators from a 4–8 GHz amplifier.

3.3 Design Parameters

3.3.1 CPW Geometry

There are several variables governing the overall geometry of the resonators we want to design, which is shown in Figure 3.5.

- The transmission line impedance of radio frequency electronics is usually 50 Ω. This, in conjunction with the dielectric constant ϵ of the substrate, sets the ratio of the center strip width to the separation of the ground planes. For $\epsilon \sim 10$, this ratio works out to be about $\frac{3}{7}$. The impedance can be solved for analytically, following Simons [92] for a semi-infinite dielectric:

$$Z_0 = \frac{30\pi}{\sqrt{(1+\epsilon)/2}} \frac{K(k_0')}{K(k_0)} \tag{3.1}$$

$$k_0 = \frac{s}{s+2w} \tag{3.2}$$

$$k_0' = \sqrt{1-k_0^2} \tag{3.3}$$

where s is the width of the center strip, w is the width of the slots in the ground plane, and $K(k_0)$ is the complete elliptic integral with modulus k_0. This is important for the through line that runs past the resonator (the feed line). The CPW line of the actual resonator is decoupled from the feed line by its coupling capacitor so its impedance does not need to be 50 Ω.

- The desired resonant frequency f_0 of the first resonance in conjunction with the dielectric constant ϵ sets the overall length of the resonator if there is no kinetic inductance present. A wave propagating on a lossless transmission line with a vacuum dielectric will move at the speed of light. However, the addition of a dielectric slows down the propagation of the signal to a fraction of the speed in vacuum. This reduced speed, the phase velocity $\bar{c}$, can be calculated as

$$\bar{c} = c\sqrt{\frac{2}{1+\epsilon}} \tag{3.4}$$

from the dielectric constant ϵ of the substrate. In a quarter wave resonator the length of the transmission line l is 1/4 of the wavelength. Putting this all together, the length of a quarter wave resonator works out to be:

$$l = \frac{c}{4f_0}\sqrt{\frac{2}{1+\epsilon}}. \tag{3.5}$$

- The quality factor Q of the resonator from Equation 2.26 is determined by several factors, including coupling, metal loss, radiation loss, and dielectric loss. At $T << T_c$ on a high quality substrate, metal loss and dielectric loss should be small, and radiation loss can be mitigated by going to smaller width CPW lines as shown in Section 3.3.3. The coupling Q, Q_c, is determined by the type of coupler used and will be discussed extensively in Section 3.3.2.

- The volume of the resonator is directly related to the responsivity of the device as the resonance frequency responds to changes in the quasiparticle density. Lowering the volume by going to thinner films or higher resonant frequencies will increase the device responsivity as shown in Section 2.5.

- The thickness of the film not only determines the volume of the film, but also the kinetic inductance fraction α. This means that using thin films (on the order of the penetration depth) can increase the responsivity quite dramatically. See Section 3.3.8.1.

Considering these factors, especially the requirements for high Q and low volume, leads us to choose a CPW line with the minimum feature size easily made with our lithographic process — a

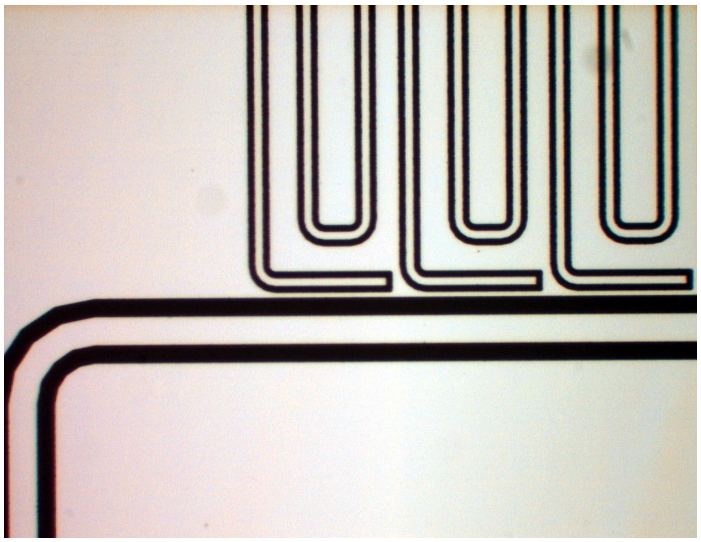

Figure 3.6: A photograph of an array of elbow couplers designed in Section 3.3.2 with dimension specified in Figure 3.5. The light areas are aluminum and the dark areas are bare substrate. The thick CPW line is the feedline, and the thinner sections are the elbow couplers. Each resonator in this picture is meandered three times — sections of three resonators are shown.

3 μm center strip with 2 μm gaps on either side. This yield a $\sim 50\ \Omega$ transmission line when used on a substrate with a dielectric constant $\epsilon \sim 10$, like silicon and sapphire.

3.3.2 Coupling

In order to couple the resonator to a CPW feed line without breaking the ground plane we designed an "elbow coupler", as shown in Figure 3.5 and Figure 3.6. The elbow coupler is designed with a CPW feed line with a 10 μm center strip width and 6 μm gaps. The coupled line is a 3 μm center strip with 2 μm gaps. There is 2 μm of metal between the feedline gap and the coupled line gap.

This design allows us to vary the coupling strength by changing the length of the resonator running parallel to the feed line. Simulations with the electromagnetic microwave simulation package SONNET [93] were run to determine the strength of the coupling as a function of resonant frequency and coupler length. The coupling Q can be computed directly from $|S_{13}|$, the transmission from the feed line through the coupler:

$$Q_c = \frac{\pi}{2\,|S_{13}|^2}. \tag{3.6}$$

This allows us to precisely design couplers with a very wide range in Q without breaking the ground plane. Simulations are under way to estimate the variation in coupling Q we can expect with our lithographic tolerances.

The simulations performed in SONNET allowed us to determine a useful formula for $|S_{13}|$ as a function of frequency f and coupling length L_c. The simulation covers f from 2–20 GHz and L_c

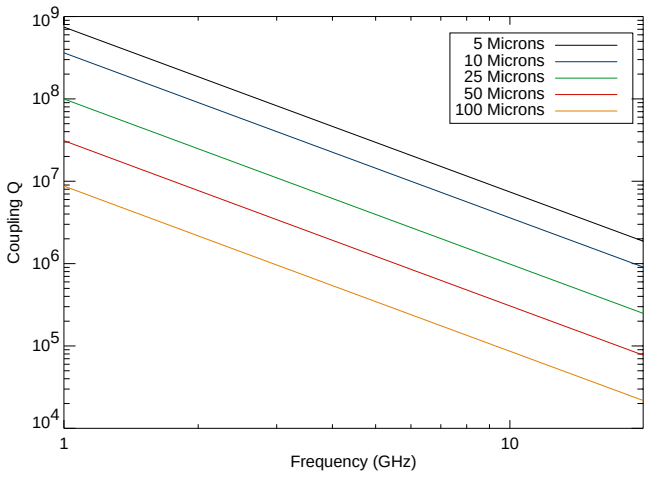

Figure 3.7: Results of SONNET simulations of the elbow coupler showing the theoretical coupling Q resulting from a given coupler length. The legend indicates the length of the CPW line running parallel to the feed line.

from 10–200 μm. The results show a linear dependence that can be fit:

$$|S_{13}| = AfL_c + BL_c + Cf + D. \tag{3.7}$$

From a standard least squares fit, we get:

$$\begin{aligned} A &= 4.01 \times 10^{-6}\ \text{GHz}^{-1} \cdot \mu\text{m}^{-1} \\ B &= -3.35 \times 10^{-8}\ \mu\text{m}^{-1} \\ C &= 2.60 \times 10^{-5}\ \text{GHz}^{-1} \\ D &= 4.55 \times 10^{-8}. \end{aligned}$$

This fit reproduces the results of the SONNET simulation quite well.

With Equations 3.6 and 3.7 we can design a device to have a desired coupling quality factor by appropriately setting the coupling length. As an example, a device working at 6 GHz with Q of 10^6 would have a coupling length around 50 μm. A plot of this coupling Q with frequency for various coupler lengths can be seen in Figure 3.7.

n	1	2	3	4	5
$I'(\epsilon = 10, n)$	1.62	4.92	7.26	9.55	11.9
$Q(s = 5\ \mu\text{m}, L = 1\ \text{cm})$	$2.2 \cdot 10^7$	$2.4 \cdot 10^6$	$1.0 \cdot 10^6$	$5.4 \cdot 10^5$	$3.4 \cdot 10^5$
ν(GHz)	3.2	9.6	16.0	22.4	28.8

Table 3.1: The radiation Q, Q_{rad}, calculated using an analytical model of a straight quarter wave CPW resonator for the first 5 resonant modes. The width of the line s is defined here as the width of the center strip plus the width of one slot, yielding 5 μm for our nominal design.

3.3.3 Radiation Loss

The radiation loss for a straight quarter wave resonator with a semi-infinite dielectric was calculated analytically by Vayonakis [94]:

$$Q_{rad} = \frac{\pi(1+\epsilon)^2}{2\epsilon^{5/2}} \frac{\eta_0}{Z_0} \frac{1}{I'(\epsilon, n)} \frac{1}{n - \frac{1}{2}} \left(\frac{L}{s}\right)^2 \tag{3.8}$$

where $I'(\epsilon, n)$ for a quarter wave resonator is shown in Table 3.1, ϵ is substrate dielectric constant, $\eta_0 = 377\Omega$ is the impedance of free space, Z_0 is the characteristic impedance of the line, n is the mode number, L is the length of the resonator, and s is the width of the center strip plus the width of the gap between the center strip and the ground plane.

For $\epsilon = 10$, we have: $Q_{rad} = 4.53 \frac{1}{I'(\epsilon,n)} \frac{1}{n-\frac{1}{2}} \left(\frac{L}{s}\right)^2$. $I'(\epsilon, n)$ can be computed numerically, and its values as well as Q_{rad} for a 3.2 GHz resonator are given for the first five modes in Table 3.1. These results can be easily scaled to other frequency resonators since $Q_{rad}\ \alpha\ \left(\frac{L}{s}\right)^2$. For a 6 GHz resonator, the $Q_{rad} = 4.53 \frac{1}{1.62} \frac{1}{1-\frac{1}{2}} \left(\frac{5300}{5}\right)^2 = 6.2 \cdot 10^6$.

3.3.4 Quasiparticle Lifetimes

The quasiparticle lifetime τ_{qp} is a measure of the average time a thermal quasiparticle remains above the gap energy before finding a partner and forming a Cooper pair. Since quasiparticles need to find a partner before recombining and the quasiparticle density drops exponentially with temperature, we expect the quasiparticle lifetime to increase exponentially with temperature. Excess quasiparticles injected in a small volume may raise the local quasiparticle density significantly, leading to self-recombination, which can shorten the quasiparticle lifetime [95].

The quasiparticle lifetime is an important factor in determining the sensitivity (NEP, Section 7.1.4.6) of a detector, since the longer quasiparticles linger in the resonator the better chance we have to measure their population accurately. Theoretical quasiparticle lifetimes are given by Kaplan [96]:

$$\frac{1}{\tau_{qp}} = \frac{\pi^{1/2}}{\tau_0} \left(\frac{2\Delta}{k_B T_c}\right)^{5/2} \left(\frac{T}{T_c}\right)^{1/2} \exp\left(-\Delta/k_B T\right) \tag{3.9}$$

where τ_0 is a material dependent time constant related to the electron-phonon coupling strength.

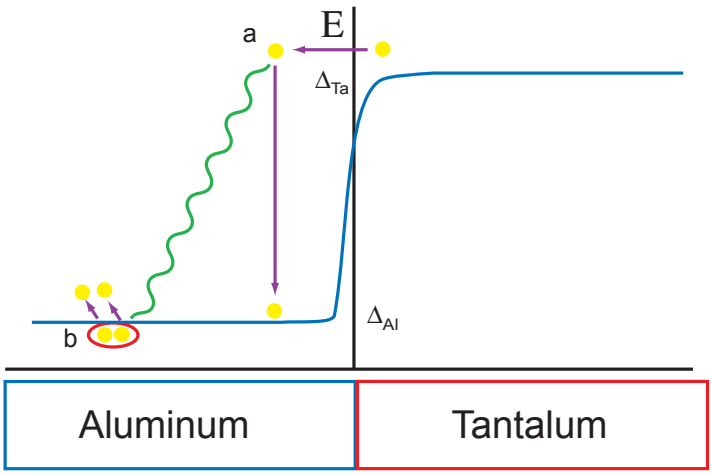

Figure 3.8: An illustration of quasiparticle trapping. As quasiparticles (yellow) diffuse from the higher gap absorber into the lower gap resonator they quickly emit a phonon (a) and drop to an energy just above the resonator gap energy. This phonon may have enough energy to break additional Cooper pairs in the resonator (b). Once the quasiparticle emits the phonon it lacks the energy to diffuse back into the higher gap resonator, trapping it in the resonator.

Kaplan gives $\tau_0 = 4.38 \times 10^{-7}$ for aluminum and $\tau_0 = 1.78 \times 10^{-9}$ for tantalum. Measurements of the lifetimes in aluminum by Gray [97] agree well with this theory for aluminum.

3.3.5 Quasiparticle Diffusion and Trapping

As previously discussed in Section 2.6, a quarter wave resonator's response to quasiparticles peaks near the shorted end. This is where we must inject the quasiparticles created by incoming photons. The easiest way to do this is to take advantage of quasiparticle diffusion and trapping.

A quasiparticle in a superconductor will diffuse a characteristic distance

$$l = \sqrt{D\tau_{qp}} \tag{3.10}$$

where D is the diffusion constant of the superconductor, and τ_{qp} is the quasiparticle recombination time. For common superconductors, l can range from hundreds of microns to several millimeters [87].

When a high gap superconductor with gap Δ_{high} is in metal to metal contact with a lower gap superconductor with gap Δ_{low}, quasiparticles near thermal equilibrium from the high gap superconductor may diffuse into the lower gap superconductor. This can occurs since the average quasiparticle energy $E_{qp} \geq \Delta_{high} > \Delta_{low}$. After entering the low gap superconductor, the quasiparticle quickly cools to a energy near Δ_{low} by emitting a phonon. However, quasiparticles near thermal equilibrium in the low gap superconductor lack the energy to move into the high gap superconductor. This leads to a phenomenon called quasiparticle trapping, as illustrated in Figure 3.8.

The rate of inelastic scattering with phonon emission determines the trapping time τ_{trap}. For an electron with energy E in the limit of zero temperature it is given by Kaplan [96]:

$$\tau_{trap}^{-1} = \tau_0^{-1}(k_B T_c)^{-3} \int_0^{E-\Delta} d\Omega \Omega^2 n(E-\Omega)\left(1 - \frac{\Delta^2}{E(E-\Omega)}\right) \tag{3.11}$$

where τ_0 is a material dependent electron-phonon coupling time constant, Ω is the energy of the phonon being emitted, and n is the density of states. This integral can be solved analytically [95]. For a quasiparticle at Δ_{Ta} injected into aluminum, this timescale should be about 10 ns, much faster than any other timescale in the system.

Fast trapping and the need to trap as many quasiparticles as possible in the center strip for greater response leads to a design such as Figure 3.9. In these devices, the center strip of the resonator climbs on top of the absorber and terminates in a T shape. This bar across the absorber causes most quasiparticles to be trapped in the resonator center strip as they diffuse by, leaving few to be trapped in the ground planes. The width of that bar in the vertical direction can be adjusted to reach an optimal state where most of the quasiparticles are trapped by the smallest possible bar. A small bar is desirable because the bar increases the volume of the resonator, reducing responsivity. If we assume that aluminum has a diffusion constant of 60 cm^2/sec [87] and that $\tau_{trap} = 10$ ns, we can calculate how far a quasiparticle will move in this time with Equation 3.10, to find the trapping length $l_{trap} \approx 8$ μm.

The thickness of the bar (the resonator film thickness) is also important as the proximity effect can modify the gap in the transition region between the absorber and resonator. Calculations by Friedrich [95] for an Al-Ta interface show that aluminum films thicker than ~ 50 nm should work well.

3.3.6 Material Choice

There are a wide variety of superconducting materials suitable for use in a MKID. We chose to use aluminum for the resonator and tantalum for the absorber. Aluminum, with $T_c \approx 1.175$ K, is a very nice material to work with. It performs as expected and is easy to fabricate. Since we need to work far below T_c ($T_{operating} \approx T_c/10$), aluminum is well suited for use in dilution refrigerators. Aluminum's gap frequency of 90 GHz also makes it useful for absorbing submillimeter photons.

Tantalum is a very hard, dense ($\rho \approx 16$ g/cm^3) material with a high atomic number (Z=73) and high transition temperature $T_c \approx 4.5$ K. It has excellent X-ray stopping power (Figure 3.10) [98] and good quantum efficiency in the optical/UV ($\sim 60\%$) [99]. It can be grown in epitaxial form on r-plane sapphire, leading to a high residual resistance ratio (RRR) and a good diffusion constant [100].

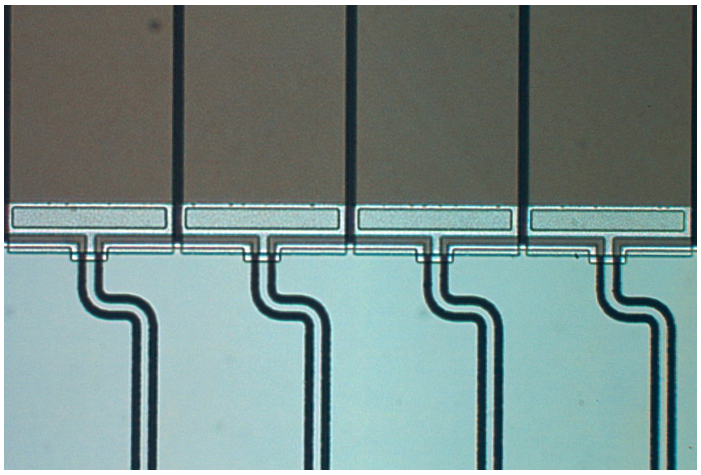

Figure 3.9: Photograph of the Al-Ta interface that serves as the short-circuited end of the resonator. It also acts to trap quasiparticles produced by photon absorbtion in the tantalum into the aluminum resonator. In this photograph, the tantalum is gray and the aluminum is blue. The width of the Ta strips is 50 μm, and the dark gaps are 2 μm.

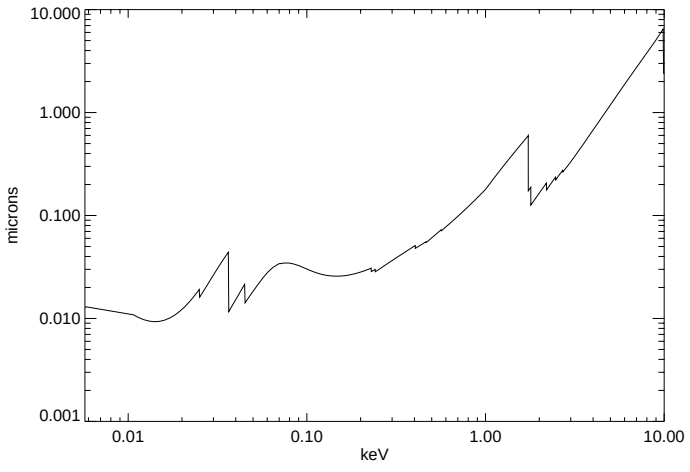

Figure 3.10: The thickness of tantalum needed to stop 63% of incoming X-rays at a given X-ray energy.

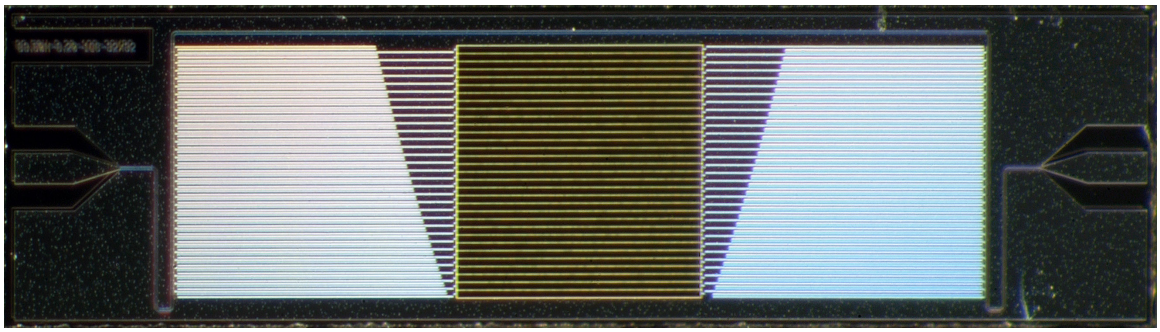

Figure 3.11: Photograph of a 32x32 pixel optical/UV/X-ray MKID array device fabricated at JPL's Microdevices Lab, based on the masks designed in Section 3.7. The black strips with yellow outlines are tantalum absorbers. On each end are the meandered resonators (white) — the length of the resonators decrease towards the top of the device. CPW wire bonding pads are located on the far left and right of the device — these bond pads neck down to become the feedline.

3.3.7 Strip Detectors

The use of quasiparticle diffusion and trapping lets us couple energy from an absorber into a resonator. We can use this to make a single pixel device by attaching a resonator to one side of a square absorber. We can also make a rectangular absorber and attach resonators to both ends. When a photon strikes the strip it will create quasiparticles that will diffuse down the strip until they are trapped at the ends by the lower gap aluminum resonators. The ratio of the signal detected in each end will give the position of the photon absorbtion, and the total will give the photon energy. This strip detector allows us to get a number of virtual pixels from each resonator. The number of virtual pixels possible is related to the energy resolution of the resonators. A microscope photograph of an array of 32 strip detectors is shown in Figure 3.11. A closeup of the absorbing area is shown in Figure 3.12.

Not all the quasiparticles generated in the absorber will make it into the aluminum resonators. Some will be lost to recombination, and some may get past the trapping bar and end up in the aluminum ground planes. The quasiparticles lost to recombination will cause events near the center of the strip to produce less total signal, J, than events at the ends. Following Kraus [13] we can write an expression for the fraction of the total created quasiparticles J_0 that reach the end of the strip

$$J(x_0) = J_0 \frac{\sinh(\beta x_0/L)}{\sinh(\beta)}, \tag{3.12}$$

where x_0 is the distance away from the end of the strip that the photon hit, and L is the length of the strip. The parameter β is related to the diffusion constant D, quasiparticle recombination time τ_{qp}, and the length of the strip L by

$$\beta = L/\sqrt{D\tau_{qp}}. \tag{3.13}$$

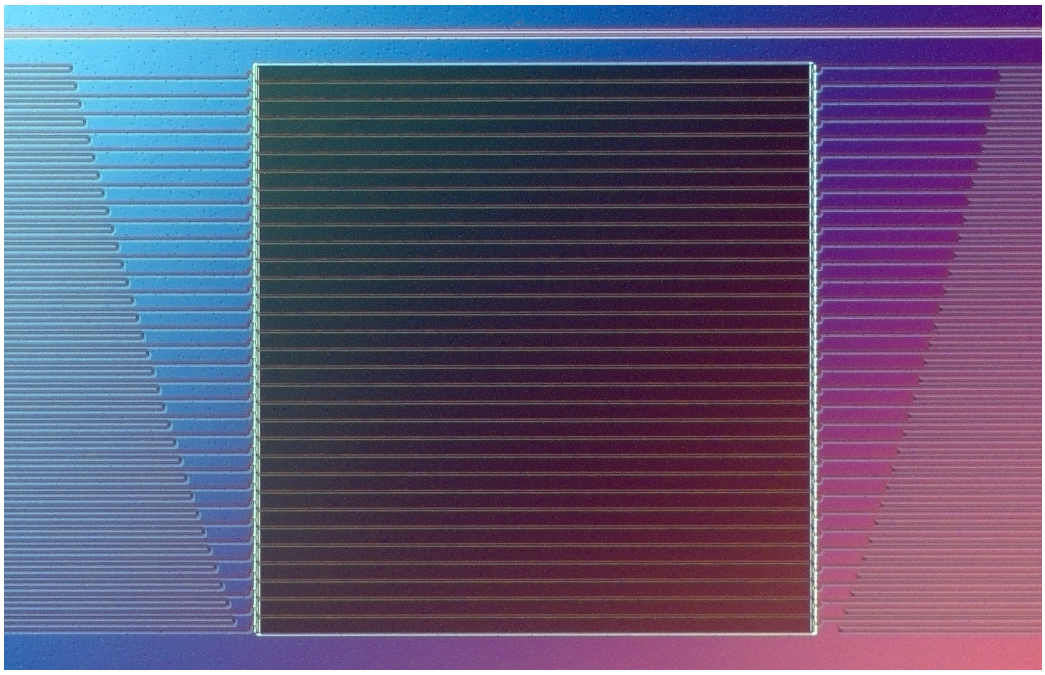

Figure 3.12: A microscope photograph of the absorber strips (1600 × 50 μm) of the optical/UV/X-ray detector shown in Figure 3.11. There are a total of 32 strips (gray) with a MKID resonator attached to each end for a total of 64 resonators.

If we have measured β we can compute the total energy of a photon J_0 and the location x_0 from the signal from the resonators at both ends of the strip, J_1 and J_2

$$J_0 = \sqrt{J_1^2 + J_2^2 + 2J_1 J_2 \cosh(\beta)} \tag{3.14}$$

$$x_0 = \frac{L}{2\alpha} \ln\left[\frac{J_1 \exp(-\beta/2) + J_2 \exp(\beta/2)}{J_1 \exp(\beta/2) + J_2 \exp(-\beta/2)}\right]. \tag{3.15}$$

Figure 3.13 shows the amount of quasiparticles that reach the ends of the strip for various loss factors β.

It is also possible to construct a 2-d imaging detector by using a large square of absorber with a resonator attached to each of the 4 sides. This approach may prove interesting in the X-ray where there are low count rates and a high signal to noise ratio in the pulses.

3.3.8 Other Design Parameters

3.3.8.1 Calculating the Kinetic Inductance Fraction

The fraction of the total inductance that is contributed by the kinetic inductance, $\alpha = L_{kinetic}/L_{total}$, is determined by the film thickness, substrate, penetration depth, and the specific geometry. A closed form has been derived with a conformal mapping technique. This involves mathematically

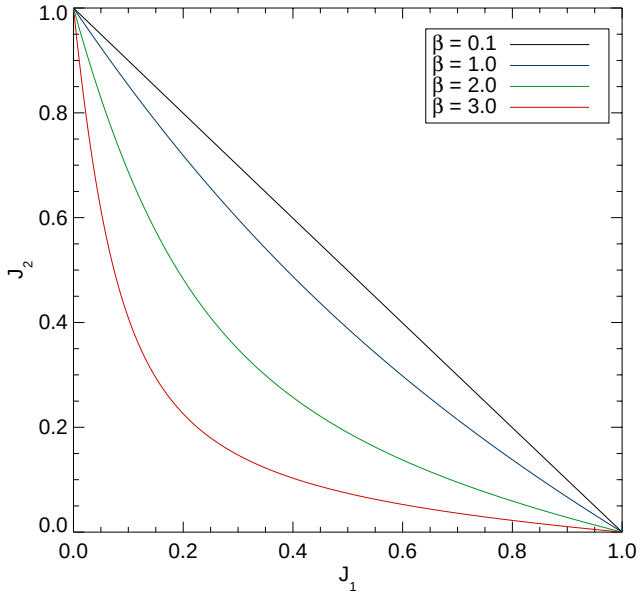

Figure 3.13: The effect of loss in a strip detector. The x-axis and y-axis show the normalized amount of quasiparticles that reach the ends of the strip for a given photon absorbtion position for various loss factors β. For example, an X-ray event in the center of a strip with $\beta = 3$ will deliver 20% of the total quasiparticles to each end of the strip. The remaining 60% will be lost to recombination.

transforming a CPW transmission line geometry into a parallel plate geometry with analytical solutions. In this case, it is only valid for films thinner than twice the magnetic penetration depth λ. Watanabe *et al.* [101] show:

$$\alpha = \frac{4K(k)\lambda^2 g}{K(k')dw + 4K(k)\lambda^2 g} \tag{3.16}$$

$$g = \frac{1}{2k^2K(k)^2}\left[-\ln\frac{d}{4w} - \frac{w}{w+2s}\ln\frac{d}{4(w+2s)} + \frac{2(w+s)}{w+2s}\ln\frac{s}{w+s}\right] \tag{3.17}$$

where K(k) is the complete elliptic integral of the first kind with a modulus $k = w/(w+2s)$, $k' = \sqrt{1-k^2}$, d is the film thickness, w is the width of the center strip, and s is the width of the gap between the center strip and ground plane. A plot of the results from the conformal mapping technique is shown in Figure 3.14. Numerical simulations for thicker films can also be performed [102].

The responsivity of the resonator depends linearly on the volume of the resonator and the kinetic inductance fraction, as shown in Section 2.5. Based on Figure 3.14, reducing the film thickness from 220 nm to 50 nm will increase the responsivity by a factor of $220/50 = 4.4$ from reducing the volume, and a factor of ~ 6 from an increasing α for an overall responsivity gain of ~ 25. This is good way to tune the responsivity of a device without making new mask designs. We expect films as thin as 20 nm to be practical.

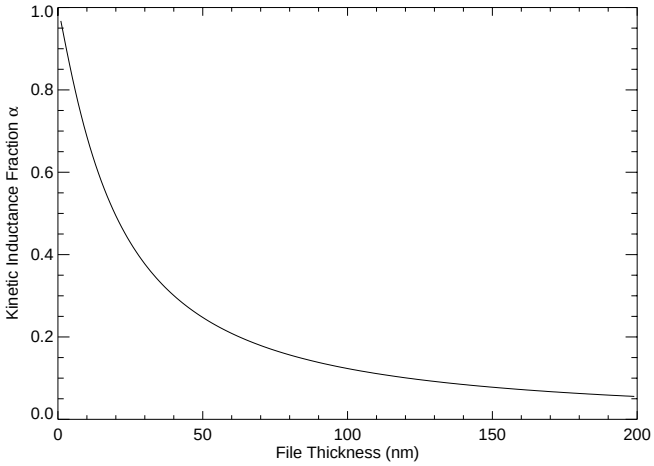

Figure 3.14: The fraction of the total inductance contributed by the kinetic inductance as a function of film thickness for a CPW line with a 3 μm center strip and 2 μm gaps. The line is based on an analytical solution [101] and is expected to be valid only for film thicknesses less that twice the magnetic penetration depth ($\sim$ 100 nm).

3.3.8.2 Resonator Bandwidth

The resonator bandwidth f_{res} is the roll-off frequency which determines how fast a resonator can respond to changes in the driving signal

$$f_{res} = \frac{f_0}{2Q}. \tag{3.18}$$

This leads directly to a timescale for the system to relax back to its equilibrium state after being perturbed

$$\tau_{res} = \frac{1}{2\pi f_{res}} = \frac{Q}{\pi f_0}. \tag{3.19}$$

For our devices the resonator response is faster than the quasiparticle recombination time ($\tau_{res} < \tau_{qp}$). This means that the pulse rise time will be the resonator response time since this is as fast as the resonator can react. In an absorber coupled detector where the quasiparticles are slowly injected into the resonator by diffusion the rise time may be dominated by the diffusion timescales. The pulse decay time will be τ_{qp} since this is the slowest timescale in the system.

The slow rise time of high-Q resonators is not a real problem for optical/UV/X-ray photon detectors, and is irrelevant for submillimeter detectors. However, WIMP detectors based on MKIDs need to use rise time information to discriminate surface events from events deep in the crystal for background rejection. More work is needed to determine whether a MKID design can provide suitable rejection of surface events.

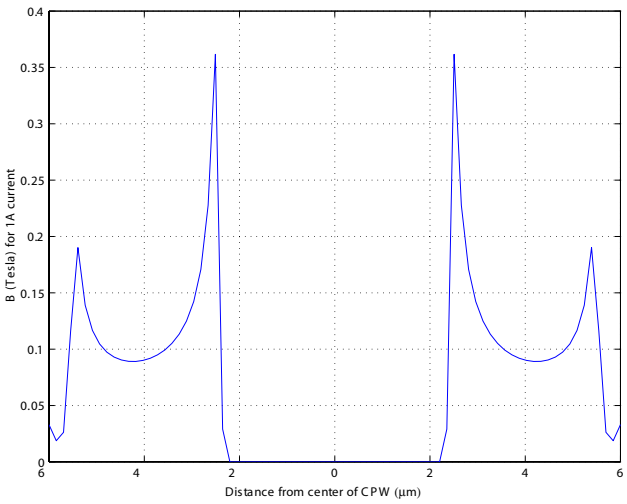

Figure 3.15: A simulation of the magnetic fields from a 1 Amp current flowing in a CPW line with a 5 μm center strip and 3 μm gaps.

3.3.8.3 Readout Power

The maximum microwave power that can be used to read out a resonator is an important parameter as it sets the ultimate signal to noise that is achievable if the dominant noise source is amplifier white noise, as shown in Section 5.4.2. It is possible to calculate the stored energy in a resonator since $Q = \omega_0 E_{stored}/P_{out}$ is a measure of the energy stored divided by the energy lost per cycle. In a coupling limited resonator the energy lost per cycle is related to $|S_{13}|$ from Equation 3.6

$$P_{out} = \omega_0 S_{13} = \omega_0 \sqrt{\frac{\pi}{2Q_c}}. \tag{3.20}$$

The total energy stored is $L\left\langle I^2 \right\rangle$, so we can derive the current in the resonator

$$\left\langle I^2 \right\rangle = \frac{1}{L}\sqrt{\frac{\pi Q_c}{2}}, \tag{3.21}$$

where L is the total inductance of the line and Q_c, the coupling quality factor, is approximately equal to the measured quality factor since we have assumed a coupling-limited resonator. From this equation and a simulation of the magnetic fields in our CPW geometry (Figure 3.15) we can derive the total current in the line, and hence the magnetic field. We expect our resonators to saturate when the magnetic field becomes an appreciable fraction of the critical magnetic field of the superconductor film of the resonator.

From actual data we see the onset of nonlinear behavior at magnetic fields of about 1% of the critical field. This may be due to the finite element simulation breaking down in the sharply peaked area near the slots.

3.4 Theoretical Noise Sources

We expect the noise sources in MKIDs to come from two sources: noise sources that are intrinsic to the resonator, like fluctuations in the number of quasiparticles present at a given time, and noise that is inherent in our readout system. The noise sources that we expect to come from the resonator will be discussed in this section. Noise issues associated with our readout technique will be discussed in Chapter 5.

3.4.1 Generation-Recombination Noise

The most fundamental noise source of a kinetic inductance detector is due to fluctuation in the kinetic inductance due to the random generation and recombination of thermal quasiparticles in the superconductor. Since the number of thermal quasiparticles in a superconductor falls exponentially with temperature this noise source is improved by colder operation. The NEP from generation-recombination (g-r) noise can be written [36]

$$NEP_{gr} = 2\Delta\sqrt{N_{eq}/\tau_{qp}} \tag{3.22}$$

where N_{eq} is the equilibrium number of quasiparticles in the resonator and τ_{qp} is the quasiparticle lifetime. The g-r noise will be a white noise with this level, rolled off by the quasiparticle lifetime τ_{qp} and the resonator response time τ_{res} of Section 3.3.8.2. Figure 3.16 shows the expected g-r noise from a 3 μm center strip, 6 GHz aluminum on sapphire, 220 nm thick resonator with $\tau_{qp} = 200$ μs as a function of temperature. At 100 mK the NEP from g-r noise is around 10^{-20} W/Hz$^{-1/2}$, which is good enough for any currently envisioned application.

3.4.2 Fano Noise

For an optical/UV/X-ray pulse counting detector there is a fundamental limit on the energy resolution of the device based on the intrinsic quasiparticle creation statistics called the Fano Limit. This limit arises because the number of quasiparticles created by absorbing a photon is a noisy process

$$\sigma_N = \sqrt{F\eta h\nu/\Delta}, \tag{3.23}$$

where $\eta = 0.57$ is the efficiency of creating quasiparticles [86], $h\nu$ is the energy of the incident photon, Δ is the gap energy of the superconducting absorber, and $F \approx .2$ is the Fano factor [103]. The Fano factor accounts for the fact that the variance in the number of quasiparticles created is not N_{qp}, but is in fact smaller, FN_{qp}. This occurs because the energy cascade that takes the original photon's energy and converts it into quasiparticles and phonons is highly correlated because of the ability of

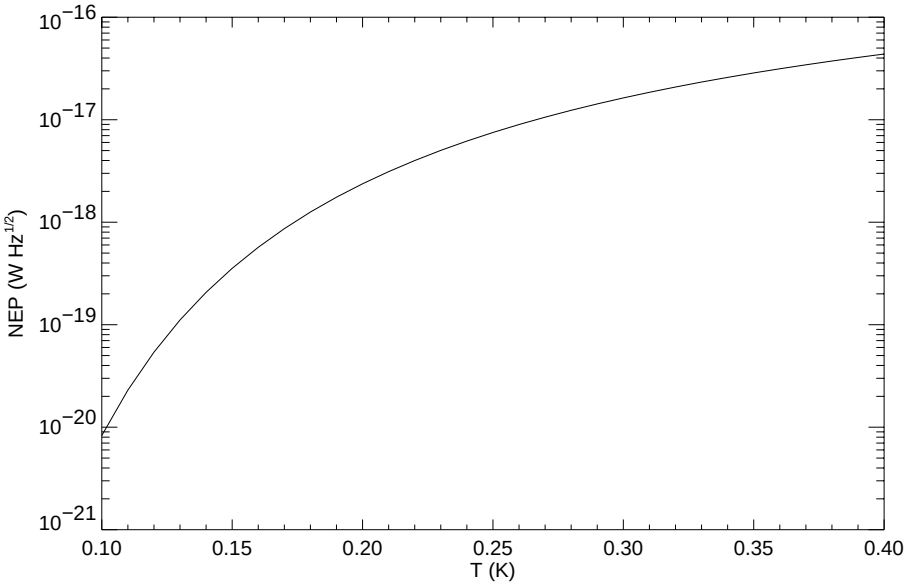

Figure 3.16: Expected generation-recombination noise from a 3 μm center strip, 6 GHz aluminum on sapphire, 220 nm thick resonator with $\tau_{qp} = 200$ μs as a function of temperature.

	Niobium $T_c = 9.25$ K $\Delta = 1.4$ meV	Tantalum $T_c = 4.47$ K $\Delta = .68$ meV	Aluminum $T_c = 1.175$ K $\Delta = .18$ meV	Titanium $T_c = 0.4$ K $\Delta = .06$ meV	Hafnium $T_c = 0.128$ K $\Delta = .02$ meV
IR (0.62 eV)	15	22	42	73	126
Optical (3.1 eV)	34	48	94	163	282
UV (10.3 eV)	61	88	171	297	514
X-ray (6 keV)	1500	2140	4000	7200	12500

Table 3.2: Energy resolution $R = E/\Delta E$ limits for different superconducting absorbers for photon counting detectors. These calculations were done with an IR wavelength of 2 μm, optical wavelength of .4 μm, UV wavelength of .12 μm, and X-ray energy of 6 keV.

the quasiparticles and phonons to interact with each other. The maximum energy resolution of the detector $R = E/\delta E$ is then:

$$R = \frac{1}{2.355}\sqrt{\frac{\eta h\nu}{F\Delta}}. \tag{3.24}$$

From this formula we can calculate the maximum energy resolution for a given photon energy and absorber gap. Table 3.2 shows energy resolution calculations for IR, optical, UV, and X-ray photons for several common superconductors.

3.5 Calculating Responsivity

We now know enough of the geometry to calculate the responsivity of our baseline device: a coupling limited $Q = 1 \times 10^6$, 6 GHz Al on sapphire resonator, with a 3 μm center strip, 2 μm gaps, $\alpha = 0.061$, and a film thickness of 220 nm. From Equation 3.5 we can calculate that the resonator will be about 5300 μm long. This gives us a volume of 5300 $\mu m \times 3\ \mu m \times .2\ \mu m = 3180\ \mu m^3$.

Using Equation 2.58 of Section 2.5, we calculate the phase change per quasiparticle for this resonator to be 1.8×10^{-4} degrees per quasiparticle. The value scales linearly with Q as long as the film thickness and resonator geometry remain the same, and can easily be applied to other Q resonators using the scaling relation of Equation 2.59. This value is too responsive for X-ray detectors — the maximum phase response of an MKID is around 150 degrees, and putting in too much energy will saturate the detector. It is not quite responsive enough for an optical detector because the phase change of an optical photon will be very small.

For X-ray detectors, a slightly thicker film with a $Q = 5 \times 10^4$ will work well. For optical detectors, a thinner film (40 nm) with $Q = 1 \times 10^5$ will work well.

A submillimeter detector from the ground will work in a slightly different regime as the continuous loading from the atmosphere will quickly establish a new quasiparticle equilibrium in the detector. Using the resonant frequency of this new equilibrium as the microwave probe frequency will allow us to track the variation of the sky and astronomical sources with sufficient dynamic range and noise performance. This is a real advantage of MKIDs — they can be tuned in real time to get the best noise performance for the current atmospheric conditions. This works since the quasiparticle recombination rate goes down as the loading goes up — it may be instructive to think of the equivalent statement for a TES. It is like having a TES where the thermal conductance G increases in a predictable fashion when the loading is increased, making it useful over a much greater range of input powers.

3.6 Test Wafer Layout

To learn more about the performance of quarter-wave resonators, a special one layer mask was designed containing frequency multiplexed resonators of many different geometries. The purpose of this mask is to test different superconductors and substrates to learn about their performance in our application. This mask should allow characterization of the Q and noise performance of resonators in a single cooldown. Data from this mask are presented in Chapters 7 and 8. The devices on this wafer are labelled by letters corresponding to the following list:

A. Straight resonators with increasing coupling Q

B. Meandered resonators with increasing coupling Q to test the effect of different meandering patterns

C. Many closely spaced straight resonators to test frequency accuracy and large array effects

D. Various coupling Q and center strip widths to test noise and loss as a function of volume

G. Single resonators

I. Resonators with the same coupling Q but varying frequency

J. An interesting subset of the devices from A and D

K. An interesting subset of the devices from A, D, and I

W. 4 GHz resonators meandered into a large square pattern

3.7 Optical/UV/X-ray Array Wafer Layout

We also designed a photon counting detector array based on a quarter wave geometry using the strip detectors principles discussed in Section 3.3.7. We started by choosing a 50 μm square pixel size in order to allow strong (low Q) coupling (a $\sim$ 50 μm coupler gives $Q_c \sim 1 \times 10^6$) if needed and a good match to the plate scale of optical telescopes. In order to pack the resonators close together we meandered them three times on this 50 micron pitch. This allowed us to change the resonant frequency by varying the resonator length without setting the CPW feed line at an angle. Strips with aspect ratios of 12, 20, and 32 correspond to lengths of 0.6 mm, 1.0 mm, and 1.6 mm. These will roughly translate into the number of spatial pixels along the strip if the signal to noise is adequate. We would like to use the 32 pixel (1.6 mm) long strips, but the diffusion constant and recombination time of the tantalum will ultimately determine how long a strip is practical.

3.8 Array Fabrication

Masks were laid out at Caltech for resonators designed to these specifications. After fabrication of the masks by an external mask vendor, devices were fabricated at JPL's Microdevices Laboratory. Aluminum films were deposited by DC magnetron sputtering in a UHV deposition system on high resistivity silicon. The CPW transmission lines were patterned using contact lithography and etched in a parallel plate reactive ion etcher (RIE) using a mixture of boron trichloride and chlorine gas.

Chapter 4

Dilution Refrigerator for MKID Measurements

4.1 Kelvinox Description

Testing MKIDs requires cooling devices to temperatures around 10% of their superconducting transition temperature, T_c. For our aluminum resonators, this works out to around 120 mK. The most common technology for reaching this temperature range is a commercially available dilution refrigerator. We use an Oxford Kelvinox 25 shown in Figures 4.1 and 4.2.

The internal cabling of the Oxford Kelvinox dilution refrigerator used for kinetic inductance device measurements is shown in Figure 4.3. Four stainless steel 0.085" coaxial cables about one meter long bring signals from room temperature at the top of the dewar to the 4 Kelvin heatsink. The input signal goes through a cold 40 dB attenuator and a DC block (inner and outer conductors are blocked). After the DC block, niobium coax (shown in blue) is used to bring the signal to the cold stages because of its low thermal conductivity. The niobium coax is heat sunk with thermal clamps shown as yellow boxes at the 1 Kelvin pot and the still. Immediately before and after the resonator are 50 GHz low pass filters, described in Section 4.3.2. The resonator itself resides in a sample box inside a cryoperm magnetic shield described in Section 4.3.1 that should reduce the ambient field by a factor of ∼1000. Only non-magnetic components and coatings are used inside the magnetic shield. The output signal of the resonator passes through a low 50 GHz low pass filter, then through niobium coax and a DC block, before reaching a directional coupler. The directional coupler is optional, but allows us to input a carrier suppression signal (Section 5.2.3) before the amplifier, if desired. The microwave amplifier is a low noise 4–8 GHz HEMT from Chalmers [91] (Section 5.4.2).

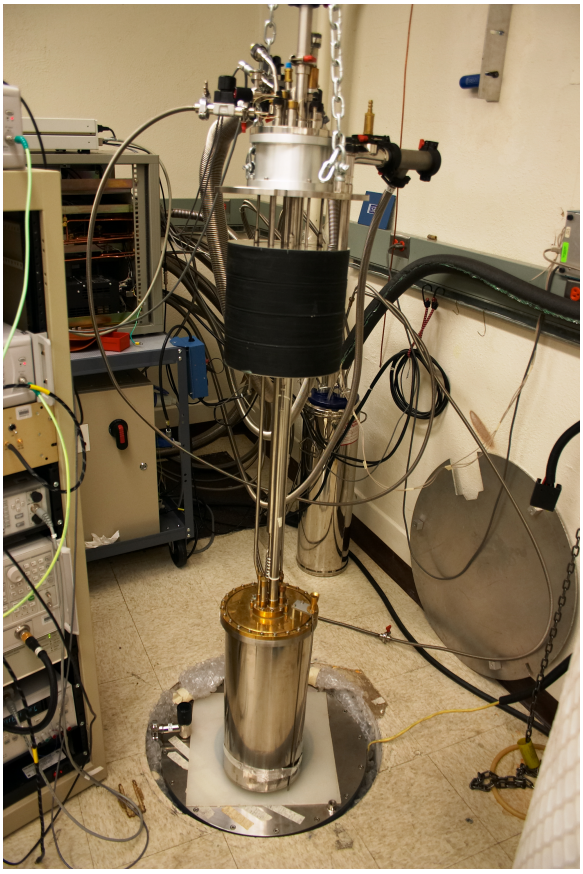

Figure 4.1: The dilution fridge insert of the Oxford Kelvinox 25.

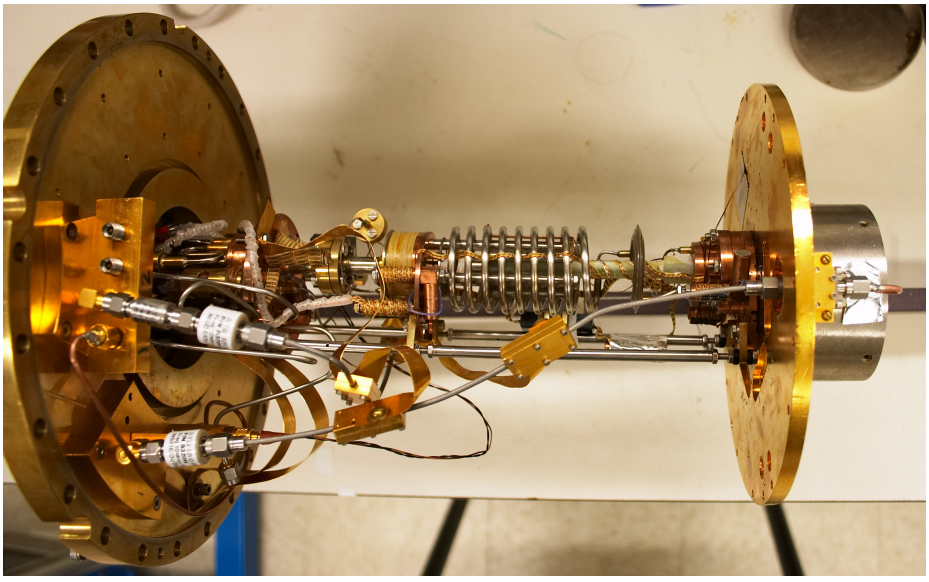

Figure 4.2: The internals of the dilution fridge insert of the Oxford Kelvinox 25.

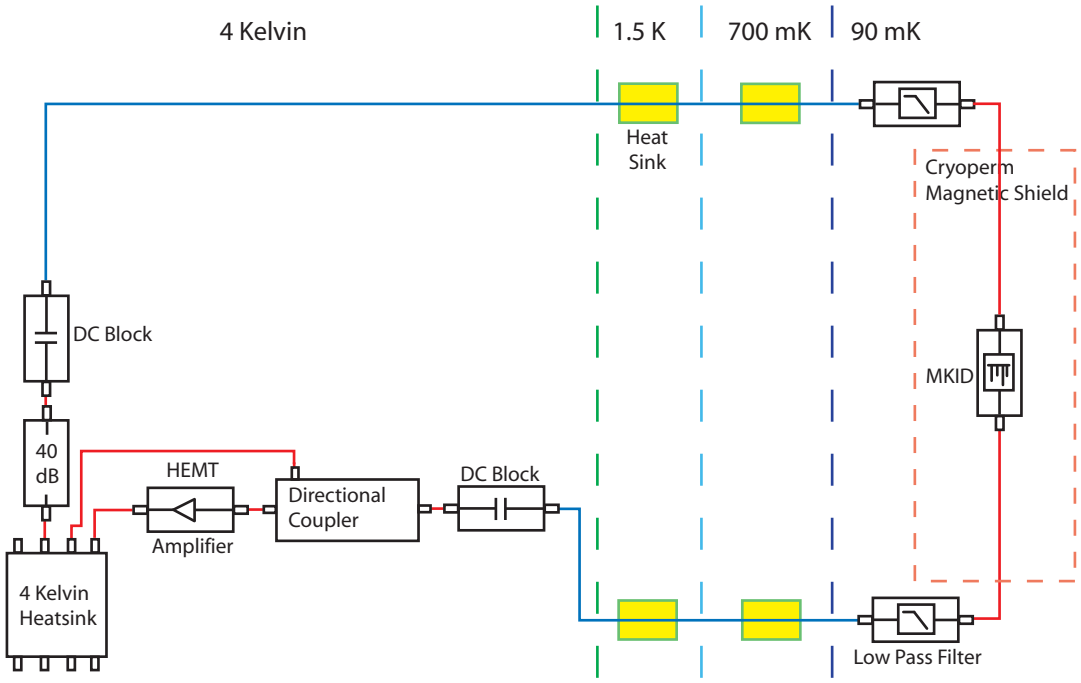

Figure 4.3: Internal cabling of the Kelvinox dilution refrigerator.

4.2 Device Mounting

After the devices have been made at JPL's MDL, the wafer is diced to yield rectangular chips. The exact dimensions of rectangular chips and the thickness of the wafers vary, depending on the substrate and mask design. These chips are then glued with GE varnish into a sample box made of oxygen-free high purity copper that has been plated with a non-magnetic gold layer. The box has microwave coaxial K-connectors, rated to 40 GHz, on each end. The center pin of the coaxial K-connector is soldered to a microstrip line on a duroid circuit board. This circuit board is a microstrip to CPW transition structure tested by John Ward [104] that has good performance up to 26 GHz. The duroid CPW line is then wire bonded to the resonator chip, and wire bonds are placed along the sides of the chip to ensure a good ground connection. Figure 4.4 shows a chip mounted in a sample box. Figure 4.5 shows the sample box mounted in the dilution fridge. The top of the magnetic shield has been removed for clarity.

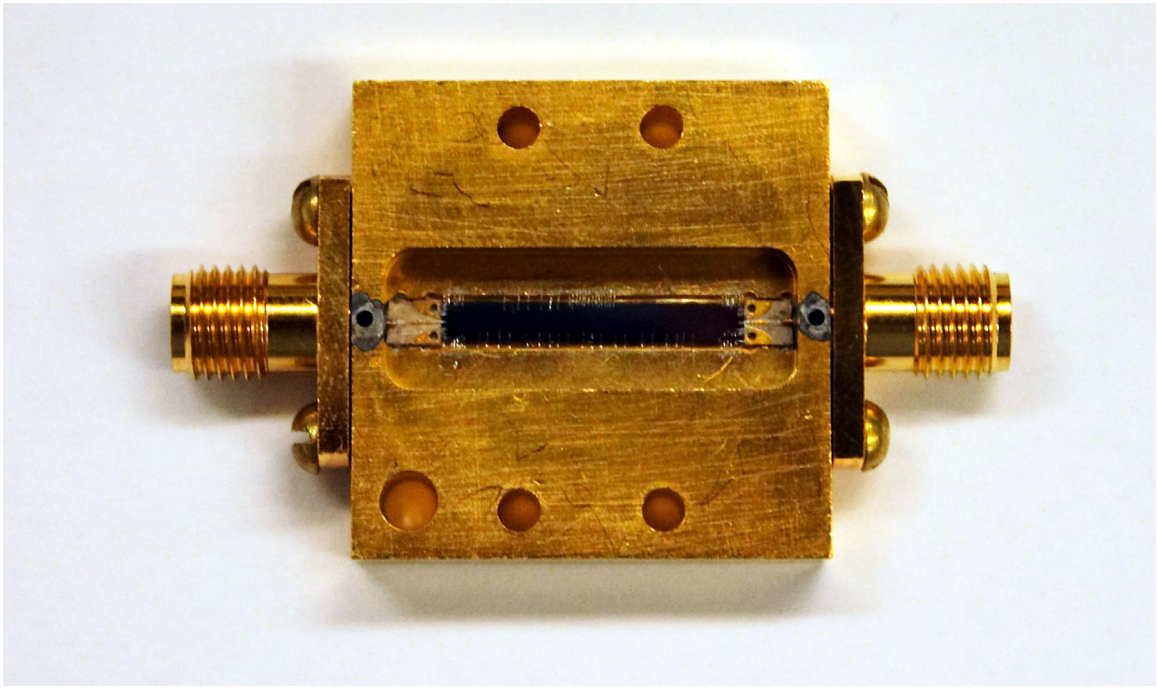

Figure 4.4: A aluminum on silicon device from the test mask mounted in a sample box. The box is 1" by 1" by 0.225". The wire bonds from the side of the channel to the ground plane on the chip are designed to suppress undesired waveguide transmission modes that could cause excess microwave leakage through the box.

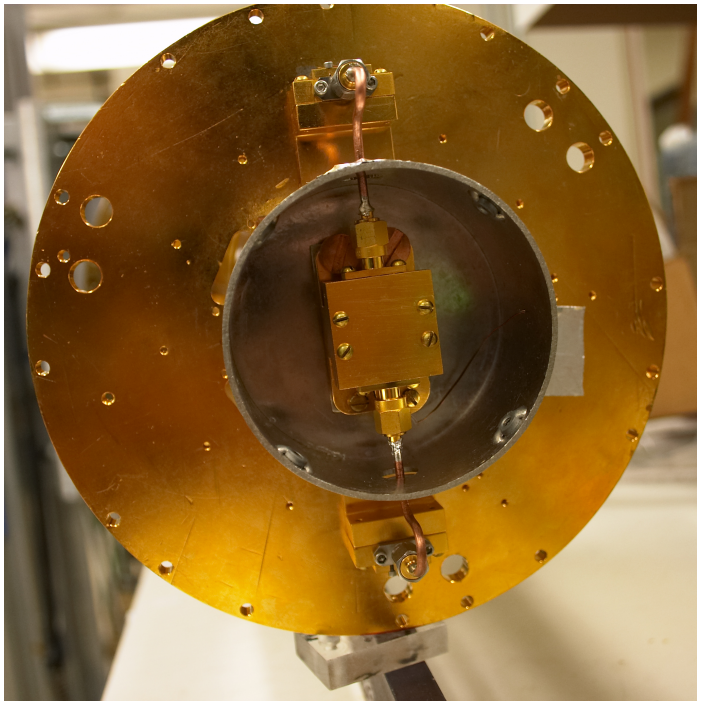

Figure 4.5: Picture of the sample box mounted on the mixing chamber. The top of the magnetic shield has been removed for clarity.

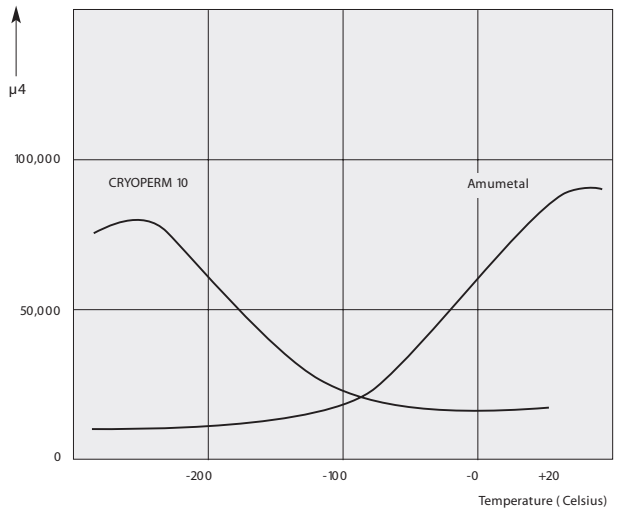

Figure 4.6: Magnetic permeability of Cryoperm and Amumetal shielding as a function of temperature. The left axis is the magnetic permeability μ/μ_0 at 4 mA/cm and the temperature is Celsius.

4.3 Device Isolation

A superconducting detector is an extremely sensitive device, and must be carefully isolated to ensure that it is not affected by unwanted signals. Possible sources of excess noise include amplifier bias line pickup, static or dynamic magnetic fields, and pair breaking radiation (> 90 GHz) reaching the resonator.

4.3.1 Magnetic Shield

Shielding a device against magnetic fields is accomplished by surrounding it with a material with a high magnetic permeability. For a room temperature device, μ-metal is often used, but its performance degrades considerable as it is cooled. For cryogenic applications, there are two possibilities — a superconducting shield, like Niobium, or a non-superconducting alloy like Amuneal's cryoperm (Figure 4.6), which performs well at these temperatures.

For the best possible shielding a two stage system is often used, with an outer Niobium shield and an inner cryoperm shield. The inner cryoperm shield is needed because the Niobium can trap magnetic flux. A system like this may be needed in an adiabatic demagnetization refrigerator (ADR) due to the strong magnetic fields present during operation.

For our case, we can calculate the amount of attenuation we expect from a spherical shield of high permeability material. Using Equation 5.122 from Jackson [105] we can calculate the reduction

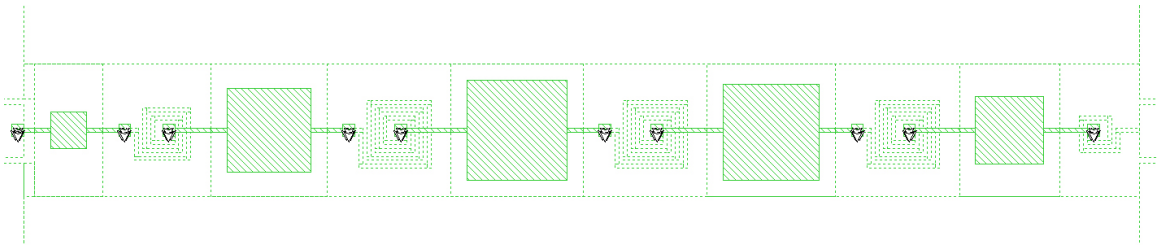

Figure 4.7: The design of the 50 GHz low pass filter.

of the external field

$$R = \frac{9\mu_0}{2\mu\left(1 - \frac{a^3}{b^3}\right)} \tag{4.1}$$

where μ is the magnetic permeability of the shielding material, a is the inner radius of the shield, and b is the outer radius of the shield. For a cryoperm shield with $\mu/\mu_0 = 70,000$ (Figure 4.6), an outer radius of 1.5", and a wall thickness of .058", we calculate R=0.00057, reducing the ambient field by a factor of 1750. This should be considered an upper limit as our actual shield is not spherical, is penetrated in several places for cabling and thermal links, and could suffer from magnetic saturation effects depending on the magnitude and frequency of the applied magnetic field.

Another step taken to minimize magnetic fields was to remove all magnetic materials from inside the magnetic shield. This included changing the gold plating to remove the nickel diffusion barrier (silver was used instead) and replacing the stainless steel coaxial connectors and screws with beryllium copper or brass.

While these steps are important to rule out magnetic effects as a major contributor to noise, we do not expect trapped flux to be a major issue for our detectors. Work by Stan *et al.* [106] has imaged trapped flux in superconductors and shown that below a critical magnetic field no flux will be trapped in a strip. For our 3 μm strips this critical field works out to be around 3 Gauss. This means that even without a magnetic shield the Earth's field of 0.5 Gauss should not cause trapped flux in the center strips of our resonators. It also appears that regions near the edges of strips tend to expel flux. Since the electromagnetic fields of our transmission lines are confined to the areas near the gaps in the CPW transmission lines we don't expect to trap flux in the active region.

4.3.2 50 GHz Low Pass Filters

The gap frequency of Aluminum is around 90 GHz. This means that radiation from the 4 Kelvin stage can break Cooper pairs, causing an excess quasiparticle population that will produce excess noise and loss in the resonator. In order to filter out pair breaking radiation that could come down the Niobium coaxial lines we developed 50 GHz low-pass filters that sit on the mixing chamber that are designed to block frequencies from 50 GHz up to several hundred GHz.

Anastasios Vayonakis designed the filter. It is a 5-pole low pass filter using superconducting spiral inductors and thin-film capacitors, fabricated out of niobium on a silicon substrate with a SiO_2 dielectric. The filter itself is quite small, 0.42 × 0.05 mm, and fits in a small 0.87 × 0.17 mm channel designed to suppress spurious resonances up to 350 GHz. The filter layout is shown in Figure 4.7. Measurements show that the filter has good transmission at low frequencies, but the high frequency of the cutoff (50 GHz) makes the stop band attenuation hard to measure with our current instrumentation.

4.3.3 HEMT Amplifier Biasing

The 4–8 GHz HEMT amplifier [91] we are using has two bias lines feeding it, the gate voltage V_g and the drain voltage V_d. The amplifier is grounded to the case. Ground loops can cause fluctuations in V_g which can cause the amplifier gain to fluctuate.

In order to provide a constant bias voltage an active feedback system is employed. This system attempts to maintain a constant drain current by using a feedback loop to modulate the gate voltage. Even with this system in place we experience excess 60 Hz pickup from the HEMT amplifier. We believe this is due to problems with the fabrication of the bias circuit board in our HEMT amplifier, and we will be replacing the amplifier as soon as a new unit becomes available.

4.4 Temperature Measurement and Control

Temperature is measured by a calibrated Lake Shore RX-202A-CD RuO_2 thermometer with a room temperature resistance of 2 kΩ located inside the magnetic shield on the same gold-plated copper block that the sample is attached to. Lakeshore quotes the temperature accuracy of this sensor at ±5 mK. The sensor is read out with a Lakeshore 370 AC resistance bridge, which allows a very accurate measurement of the resistance with low excitation power so that self heating of the sensor is not a concern. The 370 bridge also contains a PID temperature controller that we have attached to the heater on the mixing chamber, allowing for accurate temperature control.

Chapter 5

Two-Channel Test Setup for MKID Measurements

In order to learn more about the performance and noise issues of our kinetic inductance detectors a fully automated readout system capable of measuring two resonators simultaneously was constructed. This system was designed to have low intrinsic noise and the capability to be upgraded into a readout for a moderately sized array. This chapter will explain the details of the readout system and the characterization performed on it.

5.1 Readout System Overview

Several data sets are needed to characterize each resonator. First, we need to identify the resonance feature. This means that we need to measure the microwave transmission amplitude and phase as a function of frequency. Second, we measure the noise of the resonator at a given microwave frequency. This involves measuring the amplitude and phase fluctuation of the microwave signal transmitted past the resonator over a period of time, then taking the Fourier transform to find the power spectra of the amplitude and phase noise. Finally, we need a system that can register the changes in the transmitted signal when a transient event, like an X-ray, perturbs the resonator. For all these data sets we need to be able to vary the power of the microwave probe signal in order to explore power dependent effects and resonator saturation.

The basic circuit we use to get this data is shown in Figure 5.1. A microwave frequency synthesizer creates a signal which is split in two by a microwave signal splitter (each copy of the signal has an amplitude 3 dB less than the input). One copy goes into the LO port of an IQ mixer. The other copy goes through the cryostat, resonator, and amplifiers and into the RF port of the IQ mixer. The IQ mixer is really two mixers, one which includes a 90 degree phase shift before its LO as, shown in Figure 5.2. Ideally, this detection scheme, called homodyne mixing because the same signal is used for the LO and RF, produces as an output value the real part of the transmission signal in the I

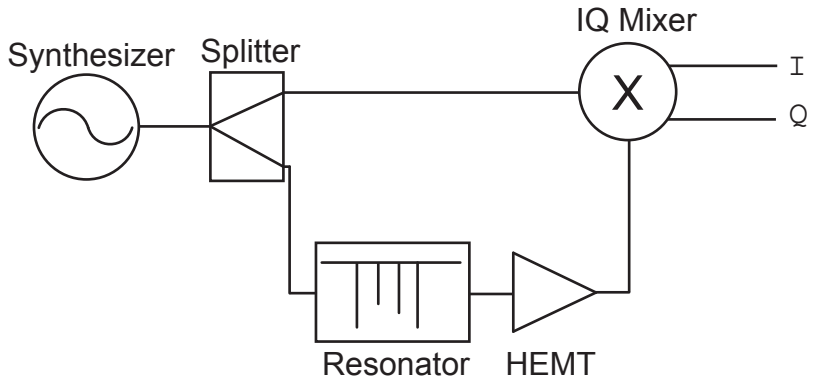

Figure 5.1: The circuit diagram of a homodyne detection scheme.

channel and the imaginary part in the Q channel. In reality, the I and Q values we get from a real IQ mixer need to be scaled individually to account for the different conversion losses of the I and Q channels and to account for other imperfections (like phase balance and leakage) in order to give the actual real and imaginary parts of the transmission. We can calibrate this imperfection by Taylor expanding the IQ mixer output signal I for small changes of the wave amplitude of the signal at the RF port of the IQ mixer a_{RF}. This expansion yields:

$$\mathrm{I} = \mathrm{I}_0|a_{LO}|^2 + c_1|a_{RF}|^2 + c_2\mathrm{Re}(a_{RF}a_{LO}^*) + c_3\mathrm{Im}(a_{RF}a_{LO}^*) + O(3) \tag{5.1}$$

$$\mathrm{Q} = \mathrm{Q}_0|a_{LO}|^2 + d_1|a_{RF}|^2 + d_2\mathrm{Re}(a_{RF}a_{LO}^*) + d_3\mathrm{Im}(a_{RF}a_{LO}^*) + O(3) \tag{5.2}$$

where a_{LO} is the wave amplitude at the LO port of the IQ mixer and can be considered a constant, I_0 and Q_0 are DC offset voltages, and the constants c_1, c_2, c_3, d_1, d_2, and d_3 parameterize the response of the I or Q channels to the input signals. For our data analysis in later chapters we assume $c_1 = c_3 = 0$ and $d_1 = d_2 = 0$. The total amplitude of the signal is $\sqrt{\mathrm{I}^2 + \mathrm{Q}^2}$, and the phase of the signal is $\tan^{-1}(\mathrm{Q/I})$. The I and Q channels are amplified, filtered, and digitized for further analysis.

This chapter will describe the readout system we designed. We will start by exploring the microwave system, which includes all the components before the output of the IQ mixers. We will then proceed to the low frequency system which follows the signal path from the output of the IQ mixers to the analog to digital converter.

5.2 Microwave System Description

The basic microwave signal path is shown in Figure 5.3 and Figure 5.5. The signals coming from two Anritsu MG3692A 2–20 GHz synthesizers at a power level of 16 dBm are sent into separate four

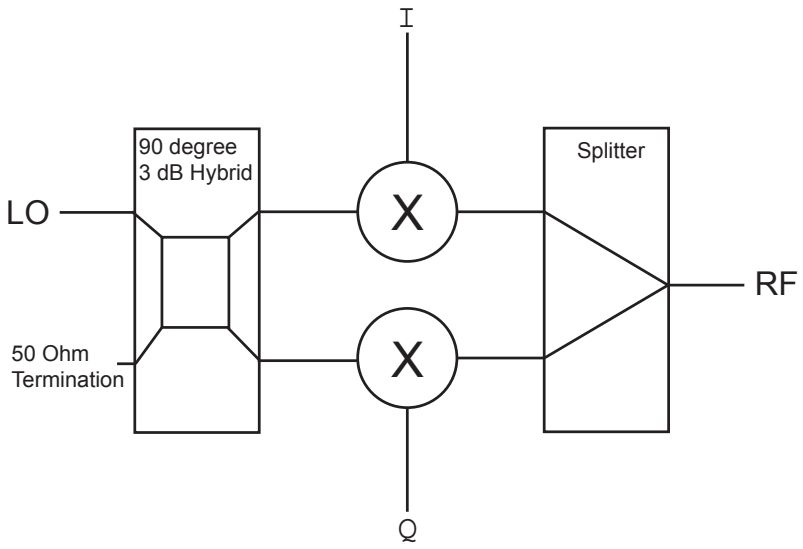

Figure 5.2: The circuit diagram of an IQ mixer.

way splitters. There are two synthesizers because this system in designed to read out two resonators simultaneously. One branch is then sent into the LO port of the corresponding IQ mixer, arriving with a power of around 8 dBm. Another copy of the signal is sent to a MCE Weinschel 8310-204-2-F 2 channel microwave attenuator. The output of the attenuators are combined and sent into the cryostat. After emerging from the cryostat, the signal is boosted by two room temperature Miteq 2–8 GHz amplifiers with a total gain of 71 dB.

After the amplifiers, the signal is sent into a directional coupler — the coupled port provides a copy of the signal at -20 dB which is available as a diagnostic. Connecting a power meter or a microwave spectrum analyzer allows important diagnosis of any system problems. After the directional coupler the signal is split with a 2-way splitter. Each copy is passed through a microwave switch, then into the RF port of an IQ mixer. The switches allow us to turn off the input signals in order to get the DC voltage offsets.

This homodyne detection scheme gives the real and quadrature components of the microwave signal, which after suitable scaling allows us to measure amplitude and phase of the signal transmitted past the resonator. Figure 1.2 shows how this scheme can be extended into a large array readout.

Figure 5.3 shows the microwave connections of the large components. The microwaves are carried to and from the cryostat by flexible microwave cabling. All static microwave connections are made with semi-rigid 0.085" copper coaxial cable. Not shown are the low frequency connections, including power to the RF box (+15,-15, GND), the signal cable from the RF box to the ICS-145 digitizer in the VME crate, the 10 MHz reference signals from the rubidium frequency standard, a cable from the Agilent 34970A digital signal generator to the RF box, and the ethernet connections.

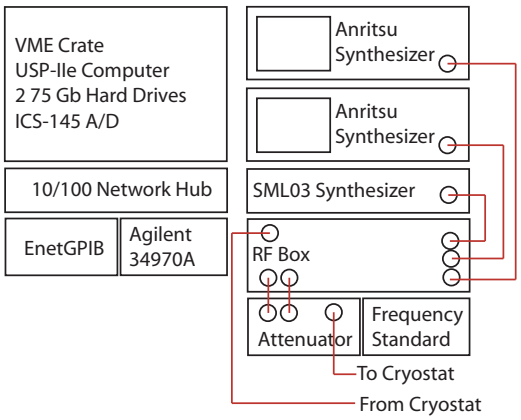

Figure 5.3: Rack layout and wiring of the microwave side of the readout.

Figure 5.5 is a wiring diagram of the radio frequency ('RF') box — this is where all the action happens. Listed below are the inputs and outputs, with the numbers corresponding to the labels in Figure 5.5.

1. Carrier Suppression Output, see Section 5.2.3
2. Voltage Controlled Attenuator Input, 0–5 Volts, see Section 5.2.3
3. Voltage Controlled Phase Shifter Input, 0–28 Volts, see Section 5.2.3
4. Difference frequency from SML03 synthesizer for phase noise monitoring, see Section 5.2.2
5. Anritsu Synthesizer 1 Input, +16 dBm
6. Output to Weinschel Attenuator 1
7. Anritsu Synthesizer 2 Input, +16 dBm
8. Output to Weinschel Attenuator 2
9. Input from Cryostat and Room Temperature Amplifiers
10. Diagnostic Copy of Signal (at -20 dB)
11. Positronics ODD44 connector to ICS-145 Analog to Digital Converter, see Section 5.3

Not shown are the connections to the 4 switches, a, b, c, and d. These switches are turned on with a 5 Volt TTL signal on pins 1, 2, 3, and 4 respectively on the DB-9 connector on the back of the box. This signal is supplied by the Agilent 34970A.

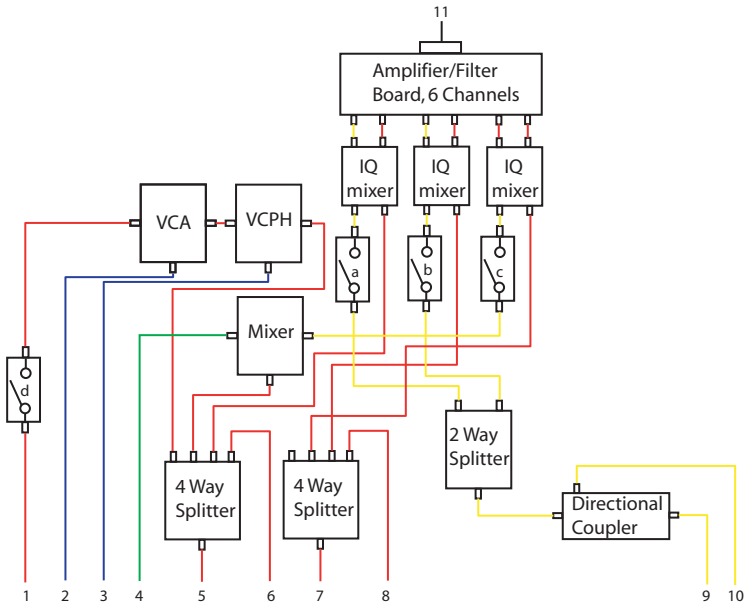

Figure 5.4: The wiring of the RF Box.

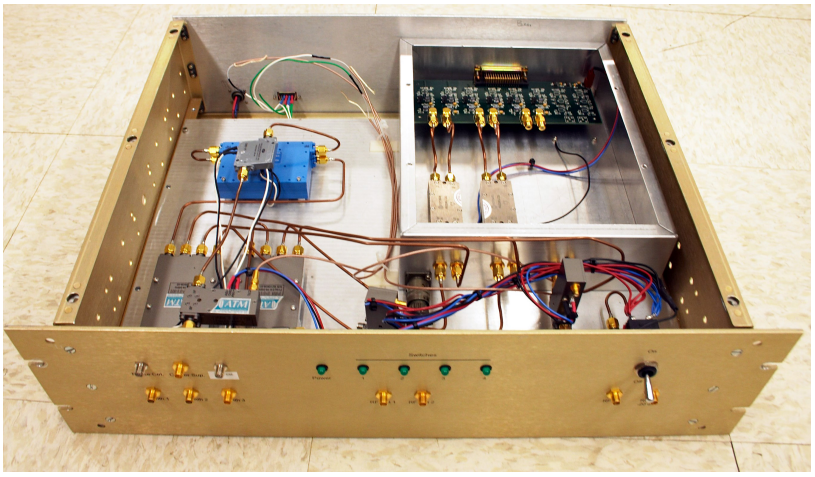

Figure 5.5: Top view of the RF box with the top off.

Figure 5.6: Front view of the RF Box.

5.2.1 Variable Attenuators

The Weinshel 8310-204-2-F [107] variable attenuator is a two channel unit that provides 0–62 dB of attenuation in steps of 2 dB. Copies of the Anritsu signals are passed through channels 1 and 2, then combined with a power combiner and sent into the cryostat. The unit is controlled over GPIB.

5.2.2 Phase Noise Monitoring

The system is also designed to take a third frequency, generated by a Rhode&Schwartz SML03 synthesizer [108], that is the difference frequency between the two mixers. This allows us to mix the SML03 output with one of the Anritsu outputs to generate a signal at the same frequency as the second Anritsu. Using one Anritsu signal as the RF, and the other as the LO on an IQ mixer, allows us to measure the phase noise of the synthesizers.

5.2.3 Carrier Suppression

Carrier suppression involves using a signal with the same amplitude but a 180 degree phase difference to cancel the carrier before the first amplifier. This can reduce the effect of $1/f$ phase and gain noise of the HEMT amplifier. It is of most use when the power at the HEMT input is >-80 dBm [109].

Since our noise excess is vastly greater than the $1/f$ noise of the HEMT (Section 7.1.4), this feature of the readout has not yet been used. However, if we succeed in lowering the excess noise it might be an important way to get better performance at the low offset frequencies required for submillimeter detectors.

The RF box shown in Figure 5.5 includes two components, VCA and VCPH, which are used for carrier suppression. VCA is a voltage controller attenuator, and VCPH is a voltage controlled phase shifter. If a directional coupler is inserted into the cryostat before the HEMT amplifier, then the signal that passes through these components can be made to efficiently cancel the carrier.

5.2.4 Rubidium Frequency Standard

The frequency of standard quartz oscillators can drift by as much 1 part in 10^6 on rather short timescales [110]. Since we are looking at very high Q resonators we need much better frequency stability over both short and long timescales in order to have consistent data from one measurement to the next and between runs. Our Stanford Research Systems FS725 Benchtop Rubidium Frequency Standard provides multiple 10 MHz signals that discipline our frequency synthesizers. This unit has an Allan variance of $< 2 \times 10^{-11}$ on time scales of less than 100 seconds and a phase noise of -130 dBc/Hz at 10 kHz.

5.3 Low Frequency System Description

After the IQ mixers, the I and Q signals are sent into a custom amplifier board. This board contains two stages. First, the signal is amplified by a voltage gain of 7 by an Analog Devices AD797 operational amplifier. The signal is then passed into a Linear Technologies LTC1565-31 650 kHz Continuous Time Low Pass Filter. This 7-pole filter in a SO-8 chip provides excellent rejection of nearby carriers that can be aliased into our A/D converters and anti-aliasing for high frequency noise. This filter has a voltage gain of 1/2 since it is being used in non-differential mode. This results in an overall voltage gain of 3.5 from the output of the IQ mixer to the digitizer.

5.3.1 A/D Conversion

After amplification and filtering the signals are sent into an ICS-145 A/D card residing in a VME crate and controlled by a Themis USP-IIe single board computer. This board has 32 channels, and each channel can be sampled up to 2.5 Ms/sec at 16 bits.

5.3.2 GPIB Control

A National Instruments ENET-GPIB100 module is used for instrument control. This box acts as an Ethernet to GPIB gateway, allowing simple instrument control from Solaris C code. This box is used to control the RF attenuators, Agilent 34970A, RF synthesizers, and Lakeshore 370 Resistance Bridge. GPIB addresses are assigned as follows:

GPIB Address	Item
5	Anritsu Synth 1
6	Anritsu Synth 2
9	Agilent 34970A
10	MCE Attenuator
12	Lakeshore 370 Resistance Bridge

5.3.3 Computer

The ICS-145 card transfers data over the VME backplane to a Themis USP-IIe single board SPARC computer. This system runs Solaris 8 and has 150 Gb of hard disk space. It acts as the primary interface between users and the test stand.

5.3.3.1 Instrument Control Software

A set of Solaris C instrument control functions has been written to allow easy access to commonly needed data acquisition functions. These functions, detailed below, require the files gpibdev.h and gpibdev.c.

- void GpibInitDev(void) This function initializes the GPIB routines and must be called first.
- void DioDout(int *channel*, char *bitmask*) This function activates switches 1–4 in the RF box using the Agilent 34970A. *Channel* should be set to 1. *Bitmask* is an eight bit number, and sets the switches on where there is a binary 1. For example, 1 turns on switch 1, and 3 turns on switch 1 and 2.
- void AtnSetAtten(int *channel*, int *atten*) This function sets the attenuation level for the MCE attenuator. *Channel*=1 sets the attenuation for Anritsu Synth 1, and *Channel*=2 sets the attenuation for Anritsu Synth 2. *Atten* can range from 0 to 62 dB in steps on 2 dB.
- void SynSetLevel(int *channel*, double *level*) This function sets Anritsu Synth *channel* to a power level in dBm. *Level* can be from -20 to +18 dBm.
- void SynSetFreq(int *channel*, double f) This function sets Anritsu Synth *channel* to a frequency f in GHz.
- double RdgGetTemp(void) This function returns the current mixing chamber temperature in Kelvin.

5.4 Microwave System Characterization

5.4.1 Microwave Synthesizers

The microwave synthesizers consist of two Anritsu MG3692As with the ultra low phase noise option. These synthesizers have the lowest phase noise available in the 2–20 GHz region. Figure 5.7 shows the phase noise specifications from Anritsu. Measurements made by beating the two synthesizers against each other show that our synthesizer's output matches the specifications fairly well.

Since the IQ mixer is mixing copies of the signal from the same synthesizer it is immune to phase fluctuations from the synthesizer unless a process in one of the arms can change the signal. The effect of this is that synthesizer phase noise is heavily suppressed at frequencies below the resonator bandwidth (see Section 3.3.8.2) and is small compared to other noise sources.

5.4.2 Microwave Amplifiers

The progress in low noise high electron mobility transistor (HEMT) amplifiers over the last decade has been impressive. Cryogenic HEMTs now achieve noise temperatures of order 0.5 K/GHz to 100 GHz, and have been demonstrated at frequencies up to 200 GHz [37]. These advances are what make frequency multiplexed MKID detectors feasible.

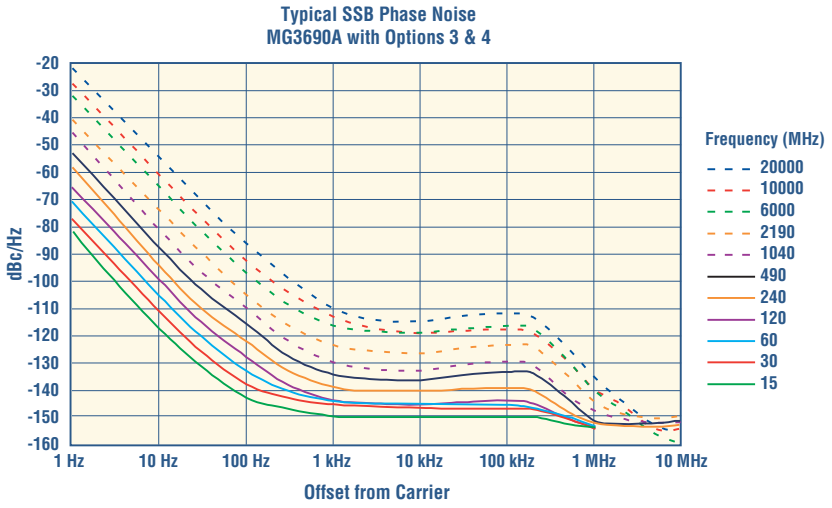

Figure 5.7: Phase noise specification of the Anritsu synthesizers.

We are currently using a HEMT amplifier from Chalmers [91], with a 4–8 GHz bandwidth, 14 dB of gain, and a noise temperature of 4 Kelvin. The amplifier bias is set to $V_d = .35$ and $V_g = .05$. From this noise temperature we can compute the expected white voltage noise from the amplifier in V $\mathrm{Hz}^{-1/2}$ from

$$V_n = \sqrt{4k_b T_n R} \tag{5.3}$$

where R is impedance of the amplifier (50 Ohms).

The phase uncertainty contributed by an amplifier with a noise temperature T_n after an integration time τ is given by

$$\sigma_\phi = \sqrt{\frac{k_B T_n}{2P_s \tau}}. \tag{5.4}$$

Here P_s is the power of the microwave signal at the input of the readout amplifier. Apart from a numerical factor this expression replicated the standard quantum limit when an amplifier operating at the quantum limit is assumed ($k_B T_n = \hbar\omega$).

The phase uncertainty can be reduced simply by increasing the readout power P_s, but is limited by the maximum power the resonator can handle before heating, increased dissipation, and nonlinear effects become important, as discussed in Section 3.3.8.3.

After the HEMT, we use two Miteq 2–8 GHz amplifiers with a noise temperature of 120 Kelvin and a combined gain of 71 dB. Attenuators may be added before or after the second amplifier to tune the output power into the desired range for optimal operation of the IQ mixer.

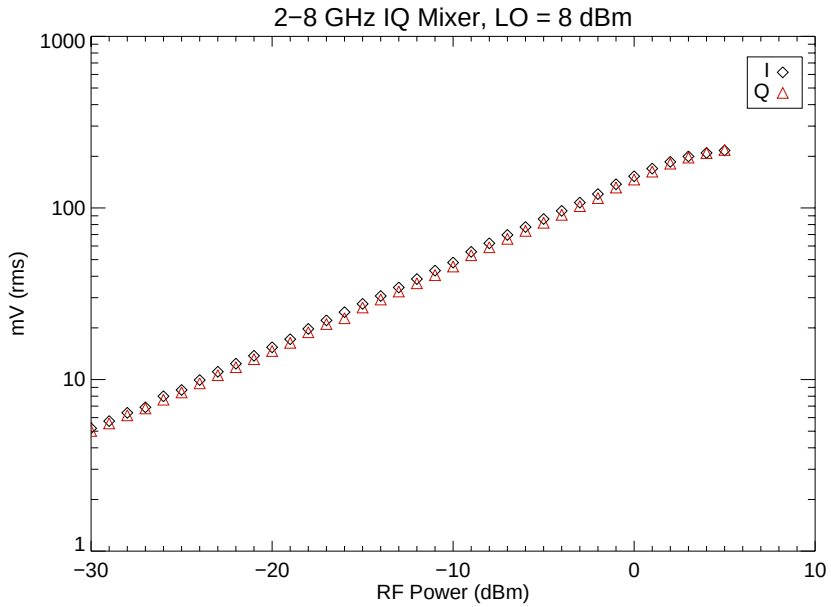

Figure 5.8: The output voltage of the I and Q channels of the Miteq 2–8 GHz mixer at 6 GHz when driven with a +8 dBm LO. The offset voltages of this mixer is $I_{offset} = -23.2$ mV, $Q_{offset} = 1.48$ mV.

5.4.3 IQ Mixers

To characterize the IQ mixers, RF signals from the Anritsu synthesizers were sent into an IQ mixer at slightly different frequencies. The output sine waves in the I and Q channels were measured with an oscilloscope at different RF powers. This allows determination of the saturation power of the mixer and the I and Q single side band (SSB) conversion losses at a given LO power. Figure 5.8 shows the output voltage for the IQ mixer as a function of the RF input power level, and shows a saturation RF power of around 2 dBm. Combining the data from Figure 5.8 with the measured output impedance of the IQ mixer (140 Ohms) allows us to calculate the conversion loss of the mixer. The spec sheet for the mixer indicates we should expect around -8.3 dB of conversion loss, and we measure -7.8 dB for the I channel, and -8.2 dB for the Q channel assuming a 50 Ohm load.

In this homodyne scheme the IQ mixer converts a microwave signal to zero frequency. The power spectra of the fluctuations at the output of the IQ mixer, S_{IQ}, can be written as

$$S_{IQ} = \frac{1}{2} G_{cl}^2 S_{RF} \tag{5.5}$$

where G_{cl} is the conversion loss of the mixer, and S_{RF} is the noise spectrum of the carrier.

Taking noise spectrum of the IQ mixer with the LO on at 8 dBm and the RF input either terminated or powered with a -20 dBm copy of the LO shows the intrinsic noise of the IQ mixer. The black spectrum in Figure 5.11, the IQ mixer noise times the amplifier board gain, shows that

this noise is fairly low at high offsets, but contains a large $1/f$ component. Measuring a different type of IQ mixer shows significantly lower total and $1/f$ noise, so there is some hope we can reduce this noise through selection of better components.

5.5 The Low Frequency System Characterization

5.5.1 Amplifier and Filter Board

The amplifier and filter board uses an AD797 op-amp front end with a input noise of 1.2 nV $\mathrm{Hz}^{-1/2}$. This is lower than the noise of the IQ mixer with no signal input, so this amplifier will add negligible noise to the overall measurement.

The Linear Technologies filter that follows the AD797 does have a significant $1/f$ noise component, as shown in the green curve on Figure 5.11. The filter will start to dominate the HEMT noise and the IQ mixer $1/f$ noise below 10 Hz. While this $1/f$ noise is not a problem for pulse detection due to the short timescales associated with the pulse, it can be a problem for a submillimeter detector that works at low offset frequencies. In this case, techniques such as phase modulation can be used to mitigate the $1/f$ noise, or lower $1/f$ noise filtering techniques and IQ mixers may be employed.

5.5.2 Noise Analysis Routines

Analysis of our data requires the generation of power spectra with the correct normalization. In order to get the best signal to noise out of our data our routine breaks 10 seconds worth of data taken at .25 MS/sec into different sized chunks and performs FFTs and averages. We use a Hann window [111],

$$W(x) = \frac{1}{2}\left[1 - \cos\left(\frac{2\pi x}{N}\right)\right] \tag{5.6}$$

where each discretely sampled point in a data set of N points with $x = 0 \ldots N-1$ is weighted by $W(x)$. The Hann window is simple to compute and is a good tradeoff between losing signal to noise and the amount of power contributed by adjacent frequency bins. This window function changes the normalization of the power spectrum — in order to get the correct values in nV^2 Hz^{-1} we need to compute

$$S_V(\nu) = \frac{3N}{\sum W(x)}\left|\frac{1}{N}\sum_{x=0}^{N-1} f(x)e^{i2\pi\nu x/N}\right|^2 . \tag{5.7}$$

5.5.3 Characterization of Readout Noise

All the machinery necessary to test the low frequency part of the system with the ICS-145 A/D converters and with a Stanford Research SR760 Spectrum Analyzer as a sanity check is now in place.

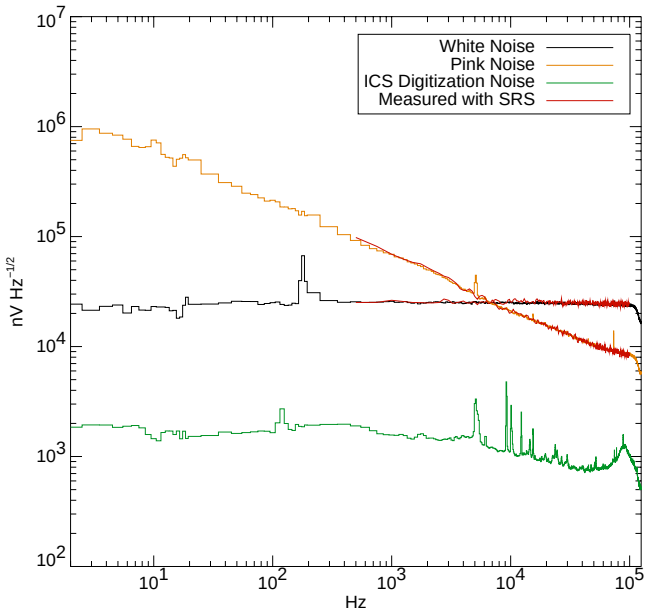

Figure 5.9: In order to check that we are correctly calculating the power spectrum, analog signals from a Stanford Research DS360 Low Distortion Function Generator was sent into both the ICS-145 board and a Stanford Research Low Frequency Spectrum Analyzer. This figure shows the power spectrum of several signals using both methods, and the overlap between the two is excellent. The lowest curve is what the ICS-145 sees with its input grounded (although a 3' cable is attached, so there is likely some pickup around 10 kHz).

This will give us confidence that we can predict the amount of noise in our resonator measurements that is due to the readout system.

First, we test our power spectrum routine by sending known white noise and pink noise signals generated with a Stanford DS360 Low Distortion Function Generator directly into the ICS-145. Power spectra of these noise signals are shown in Figure 5.9, and the excellent match between the signals we compute with the routines of Section 5.5.2 and the SRS760 shows we are making the conversion to the frequency domain correctly.

Having verified that we are generating our power spectra correctly, we can find the baseline noise of the ICS-145 by using a 50 Ω terminator on channels 1–4 and plotting the power spectra as the lowest curve on Figure 5.9. The ICS-145 digitization noise at 10 kHz is around ∼1000 nV $\mathrm{Hz}^{-1/2}$.

We test the signal to noise ratio of the ICS-145 by using the DS360 to generate a 1.8 V_{pp} 10 kHz sine wave and send it into channel 1 of the ICS. The ratio of the power in the peak of Figure 5.10 to the baseline is the signal to noise ratio. The signal to noise ratio measured is -90 dB, just beating the specified -89 dB at 8x oversampling. Attaching the signal source appears to raise the background noise of the ICS by a factor of three.

We can now hook the entire system up, turning components on sequentially from the amp board

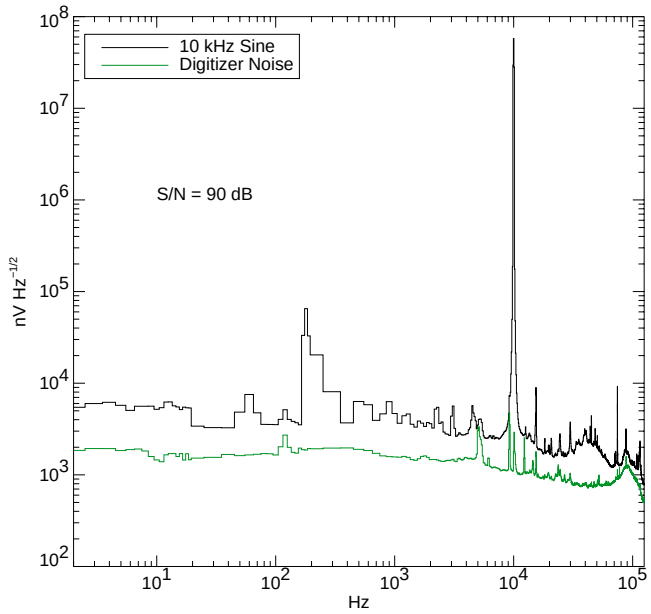

Figure 5.10: Power spectrum of a 10 kHz sine wave digitized with the ICS-145. The large 10 kHz peak is the input signal, while the much smaller peaks at 120 Hz and above 10 kHz are due to pickup.

towards the cryostat, and check the end to end noise with and without an input signal.

- The lowest curve of Figure 5.11, shown in black, is the noise of the IQ mixer times the gain of the amplifier board.
- The next curve, shown in green, is the noise of the entire system with the room temperature microwave amplifiers turned off. It is higher than the green curve because of the noise contribution of the Linear Technologies low-pass filter.
- The blue curve is the digitization noise of the ICS-145.
- The noise of the signal with the room temperature microwave amplifiers turned on is shown in red.
- The orange curve shows the off resonance voltage noise in the phase direction measured with all the components running. See Section 6.3 for a description of how the noise is translated into phase and amplitude noise. The noise of the cryogenic HEMT dominates the system noise.
- The dashed black curve shows the on resonance voltage noise in the phase direction of resonator 1 from Section 7.1 measured at a power of -90 dBm. This gives you a preview of the excess noise we detect, and shows just how high it is compared with our readout system noise.

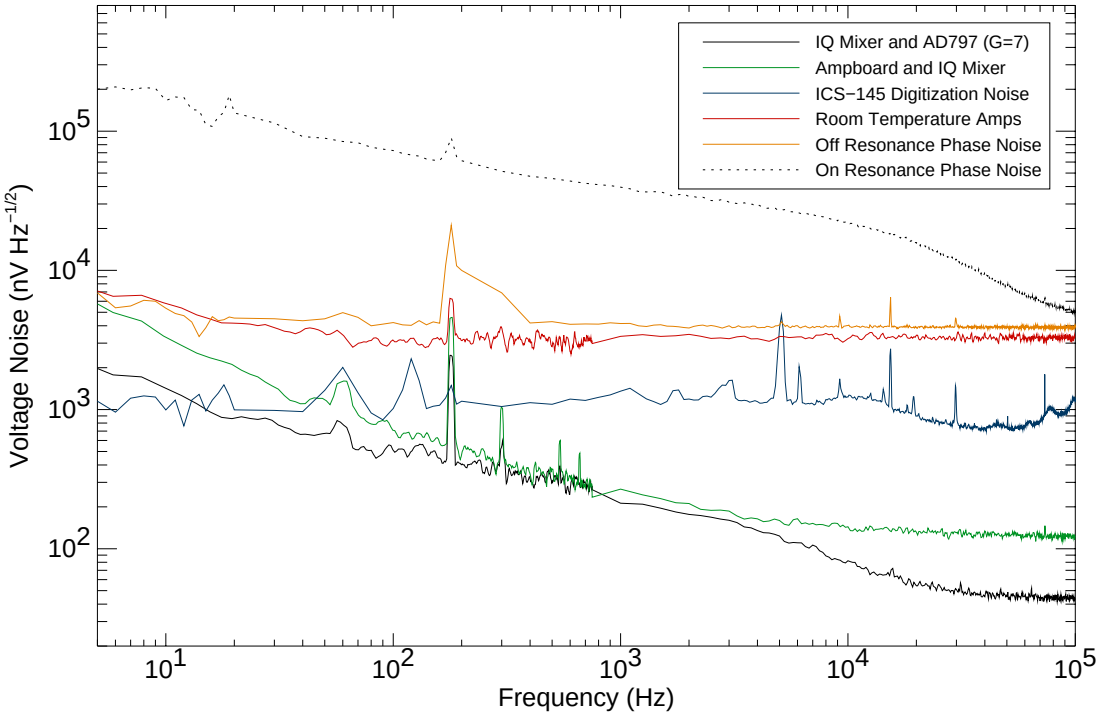

Figure 5.11: Power spectra of the entire readout system as various components are turned on.

Figure 5.12: Picture of the entire readout system during a cooldown.

5.5.4 Noise Summary

The overall effect is that the HEMT noise and room temperature amplifier noise are fairly similar as desired and dominate all other noise sources for high offset frequencies. Below 10 Hz, the $1/f$ noise from the IQ mixers and active low pass filters begins to dominate. We can tune the system by changing the RF gain and the amplifier board gain to produce the best dynamic range for a given input power level.

Another way to improve the dynamic range at high readout powers where the digitization noise becomes important would be to AC couple the signals — this would allow much higher gain at the first low frequency stage. This is practical only if a provision is provided to measure the DC values at the IQ outputs by a different method.

5.6 Future Readout Schemes

The readout described in this section is impractical for large arrays due to the size and expense of the components. Simpler systems with less features but equivalent performance can be constructed.

5.6.1 Single Board RF Signal Generation and Recovery

The simplest way to increase the number of resonators we can read out is to replace the synthesizer and IQ mixers with a custom solution. A custom 2 channel RF board using microwave integrated circuits was designed to do just this. This board contains 2 frequency synthesizers based on the Phillips SA8028 PLL chip, 2 0–31 dB digital attenuators, and IQ mixers based on the Analog Devices AD8347 IQ demodulator. This board generates two frequencies in the 0.5 to 2.5 GHz range. For an actual readout system we would generate the readout frequencies in this frequency range and then block up-convert the signals with a mixer and one of the Anritsu signal generators to excite the resonators, and then block down-convert for signal recovery. The board is shown in Figure 5.13.

The components of this board are programmed by a SPI bus. All the components work, but the built-in amplifier in the IQ mixer is AC coupled, meaning it is only valuable for pulse detection work. A plot of the phase noise of the frequency synthesizers is shown in Figure 5.14. This phase noise we measure is not as good as the manufacturer's specifications for the PLL and VCO, so further work should be able to significantly improve the synthesize phase noise from this type of circuit.

5.6.2 Integrated Digitization and Analysis

A further step would be to integrate a custom analog to digital converter and digital signal processor after the IQ mixer. A system like this is vital for real time pulse processing in order to reduce the data rate bottlenecks that can occur when using fast analog to digital conversion on many channels.

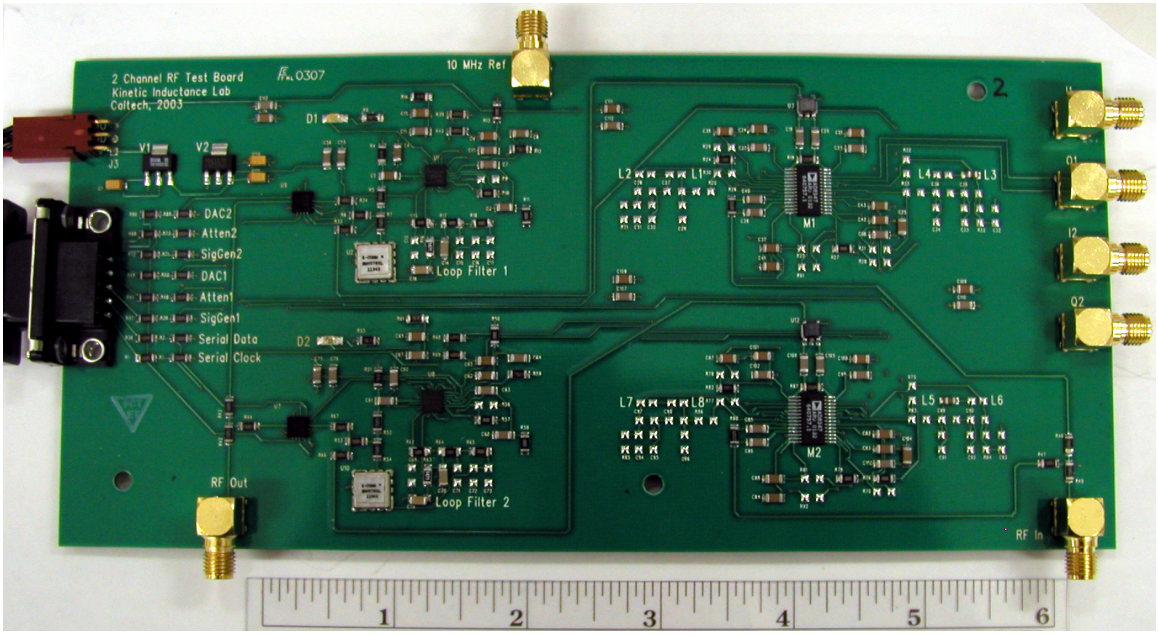

Figure 5.13: A custom two channel single RF board readout using microwave integrated circuits developed for the wireless industry. The board was designed to be much larger than necessary to make it easy to modify.

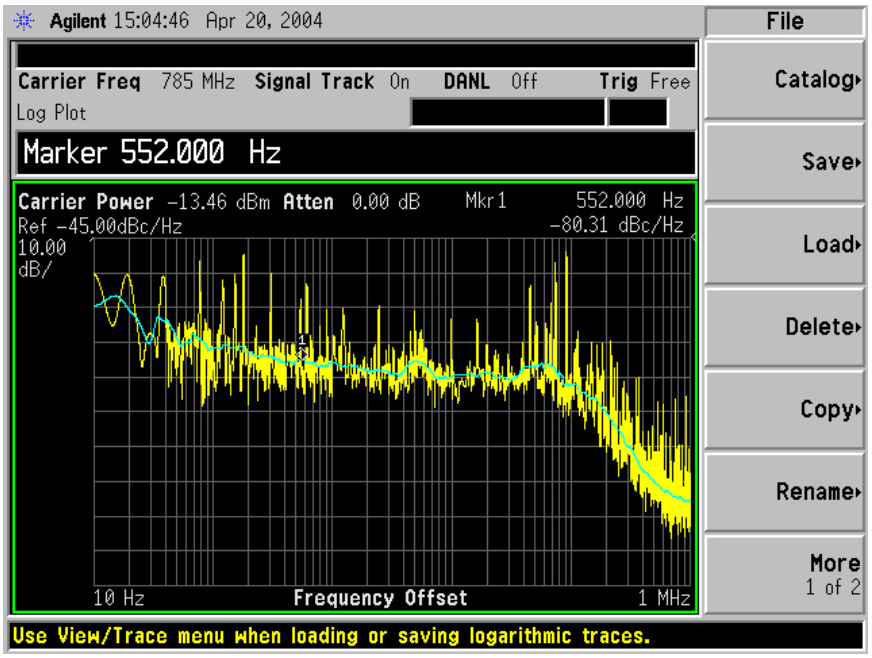

Figure 5.14: The phase noise of the custom two channel single RF board readout using microwave integrated circuits developed for the wireless industry at 785 MHz taken with an Agilent PSA spectrum analyzer. The spectrum is fairly flat with a level of -80 dBc/Hz until the noise rolloff at around 100 kHz. The specifications of the PLL and VCO used in this circuit indicate that substantially better phase noise performance is possible from these components.

5.6.3 Fully Digital Solutions

Very fast 16 bit digital to analog converters have recently become available. These converters enable the generation of arbitrary signals with frequency components of up to 50 MHz through a process known as direct digital synthesis (DDS). Combining this technology to create the readout frequencies with fast A/D converters (like the Analog Devices AD6645 105 Ms/s 14 bit A/D) and digital radio technology (like the Analog Devices AD6654 Receiver) will allow extremely compact, high channel count readouts.

Chapter 6

Resonator Data Analysis

A significant amount of data reduction must be performed before the raw IQ data from the readout system can be interpreted. The initial data reduction breaks down into three main areas — fitting the IQ resonance sweeps to obtain resonator parameters, fitting the resonator parameters to get fundamental material parameters, and computing noise spectra.

6.1 Fitting Resonator Parameters

A resonance transmission curve in the complex plane (the resonator trajectory vs. frequency) can be fit with a robust nine parameter model that accounts for all the behavior observed in our resonance data. The parameters of the model are shown in Table 6.1. This model has a lot of parameters and a rather complex phase space — care must be taken in choosing starting values. After a careful automated look at the data to determine the starting parameters, a Monte Carlo method is employed to help insure that the fitting routine finds a global minimum.

Using the process described in Section 5.1 we can equate the transmission in the complex plane to the actual IQ data. Treating the I-axis as the real part of the transmission and the Q-axis as the

Parameter	Symbol	Description
Q	Q	Resonator quality factor
f_0	f_0	Resonance frequency
Amplitude	a	Off resonance amplitude
IQ Velocity	v	Off resonance IQ velocity
Carrier Offset	c	Linear offset of the beginning and end of the resonance curve
Rotation Angle	θ	Rotation angle of the data with respect to the origin
I Gain	g_I	Gain of the I channel
Q Gain	g_Q	Gain of the Q channel
I Center	I_c	Center of the resonance circle in the I direction
Q Center	Q_c	Center of the resonance circle in the Q direction

Table 6.1: Parameters used to fit the resonance curve.

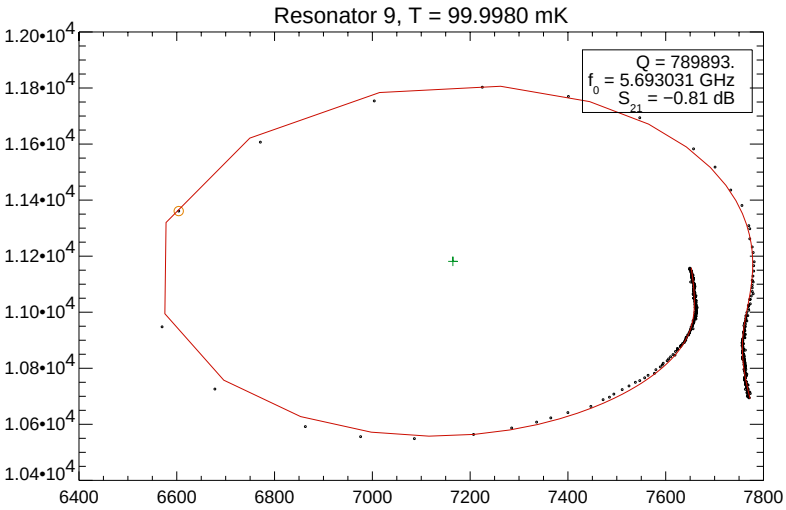

Figure 6.1: An example of the resonance fitting function's ability to match difficult resonator data. The black points are actual measured IQ data, and the red line is the result of a fit to the data. The green cross is the calculated center of the resonance, and the orange circle is where the derivative of the distance between IQ points reaches a maximum — this should correspond with the resonant frequency of the device. The parameter values for this fit are Q = 789892.56, $f_0 = 5.6930312$, $a = 3.6921007$, $v = 1738.3526$, $c = 4849.9218$, $\theta = 0.43856595$, $g_I = 1202.1240$, $g_Q = 1280.4136$, $I_c = 7164.7115$, and $Q_c = 11181.436$. The axis values are the raw digitized values from the ICS-145.

imaginary part of the transmission simplifies the algebra of the fitting function. The fitting function is evaluated in several steps for clarity.

$$dx = \frac{x - f_0}{f_0} \tag{6.1}$$

$$f = \frac{2iQdx}{1 + 2iQdx} - \frac{1}{2} + cdx + a[1 - \exp(ivdx)] \tag{6.2}$$

This function describes a resonance feature centered at (0.5,0) in the complex plane, with the resonant frequency at (0,0) and the cross over of the resonance loop at (1,0) with an added leakage term. The first term is derived from Equation 2.43, the second term is an offset to move the resonance feature in the complex plane, and the last two terms are leakage terms. This function must now be scaled, rotated by an angle θ, and offset to match the resonance data.

$$f_1 = g_I \,\text{real}(f) + ig_Q \,\text{imaginary}(f) \tag{6.3}$$

$$f_2 = f_1 \exp(i\theta) \tag{6.4}$$

$$f_3 = f_2 + (I_c + iQ_c) \tag{6.5}$$

Equation 6.5 represents the final fitting function.

6.2 Deriving Material Parameters

Once the resonator quality factor and resonant frequency have been extracted as a function of temperature, they can be fit by the approximation to Mattis-Bardeen theory in the extreme anomalous limit using the equations of Section 2.4.

Previous experiments have shown a fairly wide dispersion in the gap Δ of aluminum from one measurement to the next. For example, Biondi and Garfunkel [112] measure a value of $\Delta = 1.60 k_B T_c$ and Wells [113] measures $\Delta = 1.72 k_B T_c$.

These equations show that α and Δ are highly degenerate. Since we can estimate the kinetic inductance fraction α reasonably well from numerical electromagnetic field simulations using Ansoft's Maxwell program, we can fix this value of α and derive the gap parameter Δ. This is not an ideal approach, and we are currently developing a special test device that will allow us to directly measure α instead of relying on theoretical predictions.

To obtain Δ we fit for Q and f_0 simultaneously. The fits we use for Q and f_0 produce error bars, but the errors of f_0 seem quite low. We multiply the f_0 error bars by a constant in order to get roughly equal χ^2 values from each equation in the joint fit we perform on Equations 2.46 and 2.49.

6.3 Noise Analysis

Noise in the complex transmission plane forms a two dimensional blob. If this blob is round then the noise can be simply described by one noise spectrum. However, the noise blob is usually elliptical. This happens because different effects can cause the resonator transmission to change in different ways. Fluctuations in the gain of the transmitted signal moves the transmitted signal radially towards and away from the center of the resonance loop (amplitude noise), while fluctuations in the phase or frequency of the transmitted signal move the transmitted signal tangentially with respect to the center of the resonance loop (phase noise). This is an important way of identifying noise sources — sources of white noise like amplifier noise should have equal phase and amplitude components, while noise sources that affect the resonator's inductance or capacitance should move the transmission in the phase direction.

The raw IQ noise data we take consists of 10 seconds of data sampled at a 250 kHz/second sample rate with our 16 bit ICS-145 A/D converter. The data then has the value of the center of the resonance loop (I_c,Q_c) subtracted off. The angle of the point on the resonance loop corresponding to the frequency the data was taken at is measured, and the IQ data is rotated by this angle so that phase fluctuations are in the Q' direction, and amplitude fluctuations are in the I' direction.

The data is then Fourier transformed using the formalism of Section 5.5.2. The resulting power spectrum is then divided by the mean voltage difference r between the data and the center of the

resonance feature. Since the fluctuations are small dividing by the mean distance r gives the power spectrum of the noise in the phase direction $\tan^{-1}(\sqrt{S_{Q'}}/r) \approx S_{Q'}/r^2 = S_\theta$ in radians^2/Hz. The same operation performed on $S_{I'}$ gives the power spectrum of the amplitude noise. The noise power spectrum S_θ in radians^2/Hz can be translated directly into the industry standard for phase noise, dBc/Hz using the following equation:

$$S_\theta^* = 10 \log_{10} S_\theta. \tag{6.6}$$

The same procedure is performed on the off resonance data except instead of using the center of the resonance loop as our zero point we use the measured value on the IQ plane when there is no signal input into the cryostat.

Chapter 7

Aluminum on Silicon Resonator Measurements

This chapter deals with results from the Material Test Mask described in Section 3.6, designed to test various resonator parameters using a simple single layer mask. This mask contains frequency multiplexed devices with various geometries, couplings, and resonant frequencies to allow us to derive resonator parameters for a given superconductor and substrate combination with the fewest possible cooldowns.

The primary goal of this mask is to determine the source of the excess phase noise we see on resonance by seeing how this noise changes as we vary the resonator parameters. Secondary goals are to see how well we can set a resonator's Q and resonant frequency, to study the effects of meandered versus straight resonators, and to understand the various loss mechanisms that limit the quality factor of the resonators.

In Section 7.1 we discuss the results of a 320 nm aluminum on silicon B0 device. The B signifies the type of device as described in Section 3.6, and the 0 helps identify the device if there are several subtypes (for example, with different resonant frequencies). This thick device has resonators with 3 μm center strips with various Qs and different meandering patterns.

In Section 7.2 we discuss the results of a 40 nm thick aluminum on silicon B0 device. This thin device has resonators with 3 μm center strips with various Qs and different meandering patterns. Comparison of thick and thin film data sets in Sections 7.2 and 7.3 will allow us to explore how the excess noise is affected by changes in film thickness.

In Section 7.4 we discuss the results of a 320 nm K0 aluminum on silicon device. This thick device has straight resonators with center strips ranging from 3 to 20 microns with various Qs. This allows us to probe the relation between noise and center strip width.

7.1 Thick Aluminum Resonator Device Results

A B0 device made out of 320 nm aluminum on 5 kΩ cm undoped silicon, fabricated by Rick LeDuc at JPL, was cooled down in our fridge on March 5, 2004.

The test mask layout B0 was originally designed to test the effects of meandering on resonator Q. We will briefly look at the effects of meandering, but this device is also a good noise test device because it contains multiple resonators of similar Q, so even if one resonator is damaged another with similar Q should be available. It contains 12 devices with 3 different meanders of 4 different quality factors. The device contains straight resonators, long resonators folded back several times in a rectangular arrangement, and tightly meandered resonators in a square pattern. Table 7.1 shows the design parameters (designed for 220 nm thick Al on Sapphire) vs. the measured values. The highest Q straight resonator was seen to have obvious damage under the microscope and is expected to be absent.

Several data sets were taken on this resonator, including:

- IQ data during the transition from the normal to superconducting state to determine T_c.
- Resonance curves and noise data at 120 mK for various input power levels for all resonators. Note that all powers mentioned in this text are estimated at the input of the sample box.
- Resonance curves and noise data from 100–320 mK, every 5 mK, for a low, medium, and high power level for all resonators.
- Power sweeps at 120 mK for several resonators.
- Quasiparticle lifetime data using the microwave pulse saturation method described in Section 7.1.4.4.

Fitting the data with the routines described in Section 6.1 gives us the resonator Q, f_0, and the depth of the resonance dip S_{21}^{min}. This procedure is described in Section 6.2. The Q and f_0 vs. temperature data can then be fit with Mattis-Bardeen theory to derive the superconducting energy gap, Δ, given the thickness dependent kinetic inductance fraction α. Results for this device are presented in Section 7.1.3.

The resonance curve data can be used to convert the noise data into phase and amplitude noise. This data can then be fit by various noise models in order to try and understand the source of the on resonance noise as described in Section 6.3. This analysis for the thick film B0 device is performed in Section 7.1.4.

Finally, we can use the resonance sweeps vs. temperature, the resonator geometry, and Δ to derive the phase response per quasiparticle, $d\phi/dN_{qp}$. Once this is understood we can convert the

Resonator	Design Q	Length (μm)	Meanders	Q	f_0 (GHz)	S_{21} (dB)
1	1×10^5	5439.04	0	91159	5.47813	-16.9
2	1×10^5	5420.98	4	43359	5.68844	-23.5
3	1×10^5	5403.02	15	52037	5.76883	-24.5
4	5×10^5	5385.19	0	167418	5.52744	-8.0
5	5×10^5	5367.48	4	-	-	-
6	5×10^5	5349.88	15	172437	5.84202	-10.1
7	1×10^6	5332.40	0	421992	5.75668	-0.6
8	1×10^6	5315.03	4	536632	5.89772	-7.4
9	1×10^6	5297.77	15	438622	5.98780	-12.9
10	5×10^6	5280.63	0	-	-	-
11	5×10^6	5263.59	4	1135722	5.95595	-3.3
12	5×10^6	5246.67	15	972613	6.04810	-5.1

Table 7.1: Measured Q and f_0 of a 320 nm thick aluminum on high purity silicon B0 device from the test mask. All resonators have a 3 μm center strip and 2 μm gaps. The meanders column indicates how many times the resonator was folded back on itself. The readout power used was approximately -96 dBm at the input to the sample box.

measured phase noise into the resonator's noise equivalent power (NEP) and energy resolution for a given quasiparticle lifetime. This procedure is carried out in Section 7.1.4.6.

While the Q and the size of the resonance feature were fairly consistent between devices of similar coupling geometry (for example, resonators 1,2, and 3) on this device, the meandered devices had slightly different resonant frequencies than expected, most likely due to the meandering reducing the phase velocity of the lines and not taking into account the effect of coupler strength on the resonant frequency during the design process.

Figure 7.1 shows the resonant frequency of the devices with the x-axis corresponding to the resonator numbers in Table 7.1.

7.1.1 Transition Temperature

The superconducting transition temperature of the device is measured by observing the microwave transmission of the feedline as the device is cooling through the superconducting transition temperature. Since these films have a high normal state resistivity the transmission is low until they become superconducting. The place where the transmission starts to increase for this film is $T_c = 1.275$ K. Using the results of Wells [113] as a basis, we can guess that $\Delta = 1.72 k_B T_c = 0.189$ meV. This is an upper limit, as our data seems to agree more with a lower ratio like the Biondi and Garfunkel [112] value for aluminum of $\Delta = 1.60 k_B T_c = 0.175$ meV.

7.1.2 Quality Factors

The quality factors of the resonators on this device ranged from around 45,000 to over 1 million. We can derive the internal loss Q, Q_i, and the coupling Q, Q_c, using Equation 2.42 and $Q(0) =$

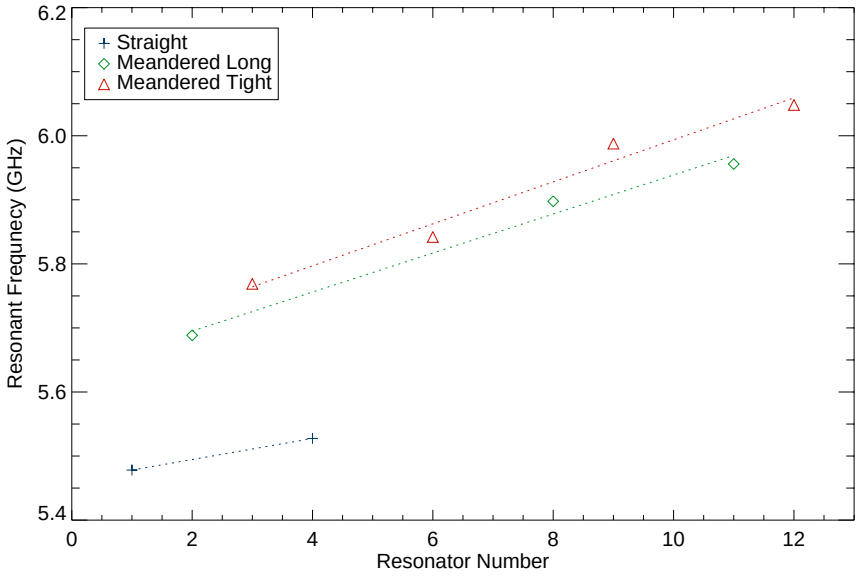

Figure 7.1: The resonant frequencies of the devices on the 320 nm thick B0 device. The meandered resonators have slightly shifted resonance frequencies.

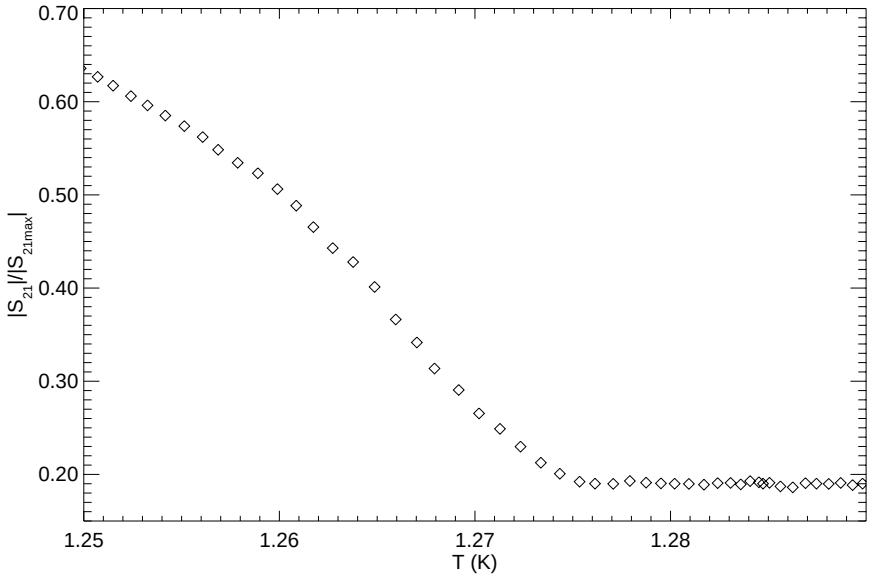

Figure 7.2: The transmission magnitude of the system relative to the transmission magnitude at base temperature for the 320 nm Al on Si B0 device. Since this device has a low normal state resistivity it is harder to measure its superconducting transition temperature from IQ data than for thinner films. The T_c for this device is around 1.275 K.

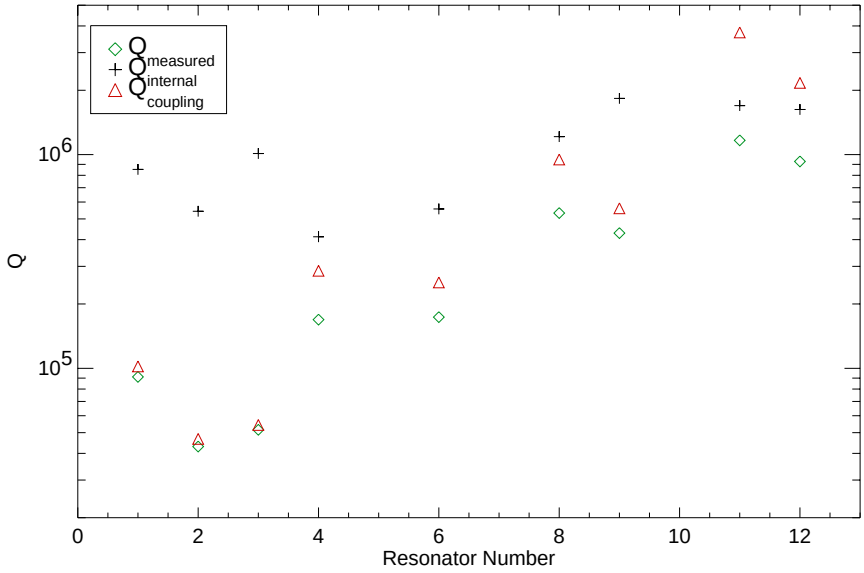

Figure 7.3: The internal quality factors of the devices on the 320 nm thick B0 device. The IQ sweep data for this plot was taken at a power of -96 dBm.

$Q_iQ_c/(Q_i + Q_c)$. Applying this to the data set shown in Table 7.1 yields Figure 7.3. This figure shows that the internal Q varies by a factor of 5. The coupling Q is much more predictable except for the lowest Q (longest) couplers, where more variation is seen. The mean value of $Q_i = 1.08 \times 10^6 \pm 5.4 \times 10^5$. The variation in internal Q could be related to a positional dependent radiation coupling to resonant modes of the cavity that the device is mounted in. This idea is pure speculation and more experiments are needed to quantify variations in Q_i and Q_c.

7.1.3 Derived Material Parameters

Using the fitting equations in Section 6.2 we can fit the resonator Q and f_0 data to determine the kinetic inductance fraction α given a known gap Δ, or for Δ if we know α. We can derive a reasonable value of α from field simulations of our CPW line, while our only handle on the value of Δ is from published values on the ratio Δ/k_bT_c. Given the lower uncertainties on α we choose to fix this value and fit for Δ.

Figure 7.4 shows the fits for resonator 1. Simulations of the kinetic inductance fraction performed with Ansoft's Maxwell 2D EM field simulator yield $\alpha = 0.0553$ for a 320 nm thick aluminum on silicon CPW line with this geometry. Fitting for the gap give a best fit value of $\Delta = 0.169$ meV. This value seems a very low, yielding $\Delta/k_bT_c = 1.54$, but is not very different from the Biondi and Garfunkel [112] value.

To get an idea of the degeneracy between α and Δ we can make a contour plot of χ^2 with varying

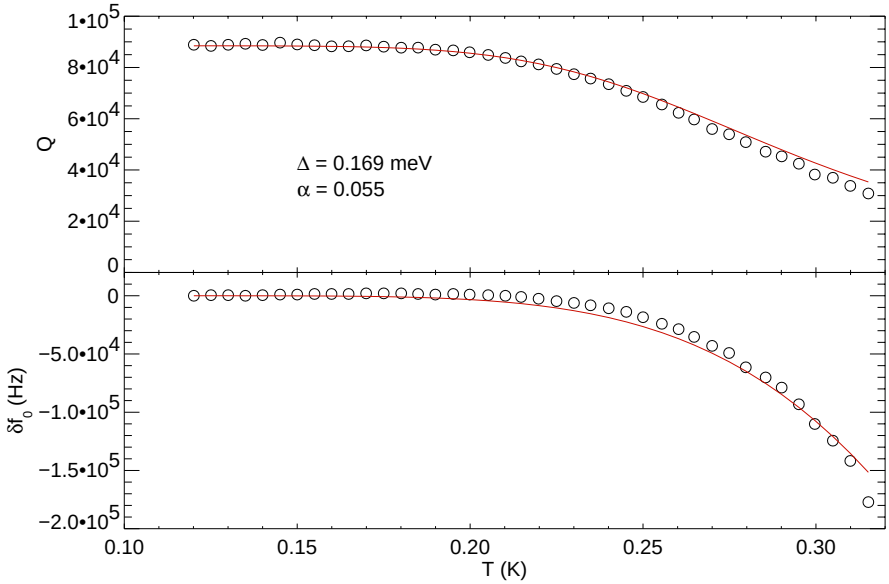

Figure 7.4: Fits to the Q and f_0 data from resonator 1 from the 320 nm Al on Si B0 device using Mattis-Bardeen theory in the extreme anomalous limit.

α and Δ in Figure 7.5. This plot shows that α and Δ are highly degenerate.

7.1.4 Noise

To take noise data we tune to the resonance frequency of the device then record 10 seconds of IQ data, as described in Section 6.3. We then tune off resonance and repeat this procedure. Since a quarter wave resonator has nearly perfect transmission off resonance the off resonance noise represents the readout noise of the system uninfluenced by any resonator effects. We are forced to neglect the highest Q data in this section due to inadequate frequency sampling of the IQ curve. This occurs because we used a frequency sampling optimized for the low Q resonators, which caused the high Q resonators to have insufficient frequency resolution.

When this procedure is performed on resonance, we notice a significant excess phase noise component that is not present in the off resonance data. Figure 7.6 shows the on and off resonance noise of resonator 1. Both the on resonance amplitude noise and the off resonance phase and amplitude noise for these resonators have a fairly flat spectrum with a value far below the observed on resonance phase noise. The value of the on resonance amplitude noise is higher than the off resonance value because it is calculated with respect to the phase center of the resonance, not origin as is the case for the off resonance data. Figure 7.7 shows the phase noise we measure at 120 mK for all the resonators.

A quick glance at this data shows that the phase noise increases as the device Q is increased,

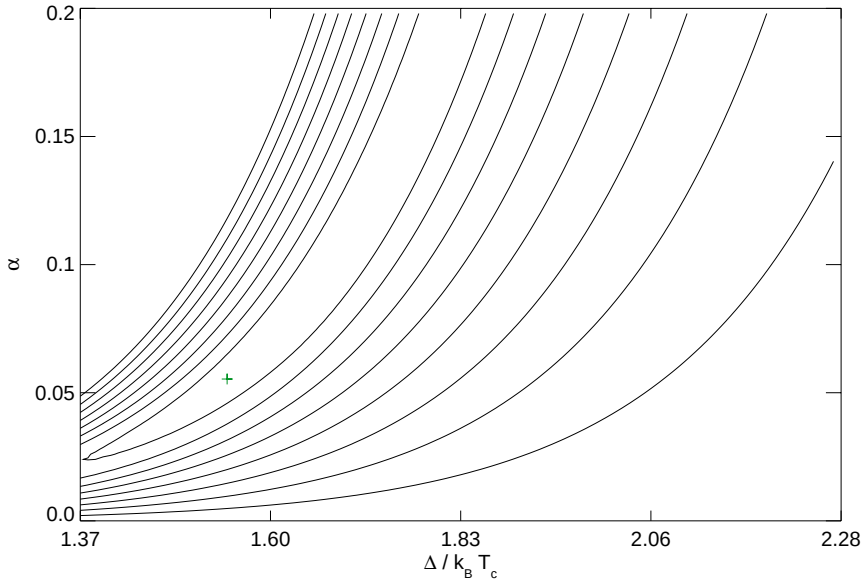

Figure 7.5: The χ^2 of resonator 2 from the 320 nm Al on Si B0 device using Mattis-Bardeen theory in the extreme anomalous limit as α and Δ are varied. The green cross represents the best fit value of $\Delta = 0.169$ meV for our estimated $\alpha = 0.0553$. The lines are increasing contours of χ^2 spaced by multiples of the minimum χ^2, so the first contour is twice the minimum value of χ^2, the second is three times the minimum value of χ^2, etc.

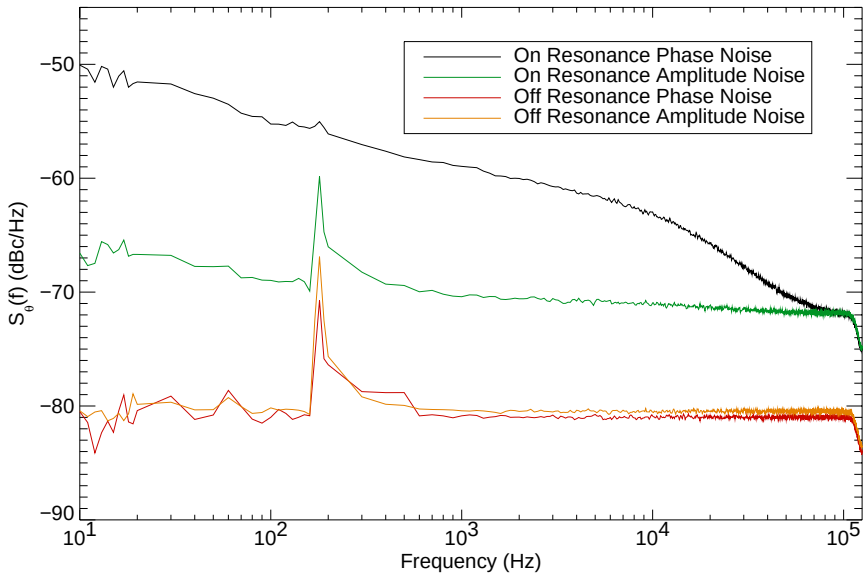

Figure 7.6: The on and off resonance phase and amplitude noise of resonator 4 ($Q = 167418$) from the 320 nm thick Al on Si B0 device measured at a constant readout power of -96 dBm.

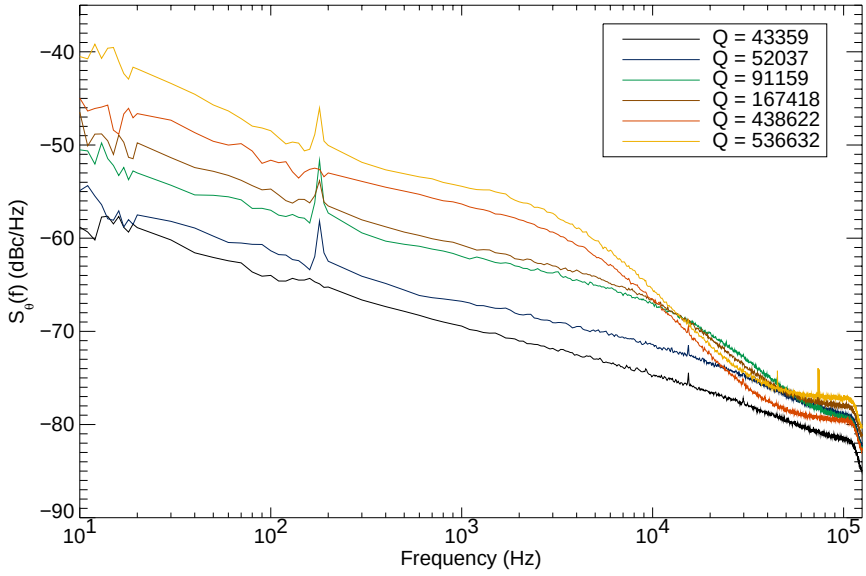

Figure 7.7: The phase noise of 3 μm center strip resonators from the 320 nm thick Al on Si B0 device measured at a constant readout power of -96 dBm. The phase noise increases and the noise roll-off frequency decreases with increasing resonator Q. The flattening of the noise spectra above ∼50 kHz (more obvious is the higher Q resonators) shows the readout noise floor for this particular resonator at this readout power.

Q	Resonator Bandwidth (Hz)	Noise Roll-off (Hz)
43359.8	65595	33721
52037.6	55429	29526
91160.0	30046	18125
167419.	16507	11287
438622.	6825	5899
536632.	5495	3909

Table 7.2: Measured noise roll-off frequency of 320 nm thick Al on Si B0 resonators.

and that the roll-off frequency of the noise decreases as Q is increased. We can perform fits to the phase noise spectrum to help understand the noise. Fitting a power law spectrum with a single pole roll-off and an amplifier white noise floor results in the fits shown in Figures 7.8. There is a mid-frequency ($\sim 10^3$ Hz) flattening of the noise spectra that this fit function does not account for, but the roll-off frequency does match the resonator bandwidth (Equation 3.18) fairly well as shown in Table 7.2, except in the case of the lowest Q resonators. Figure 7.9 shows the correlation between the resonator bandwidth calculated from the fit value of Q and the fit noise roll-off frequency. The excess noise and the roll-off frequency tracking the resonator bandwidth is our first evidence that we are measuring excess substrate noise.

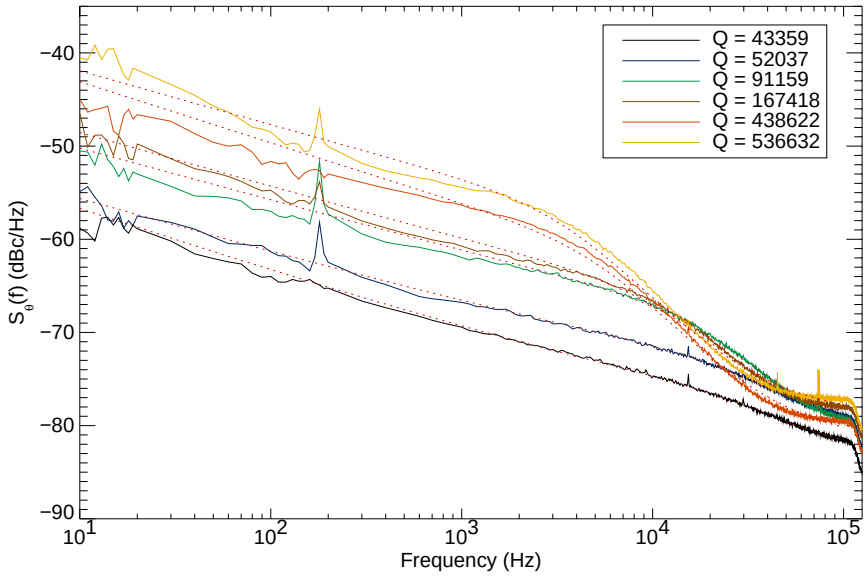

Figure 7.8: The phase noise fits of 3 μm center strip resonators from the 320 nm thick Al on Si wafer measured at a readout power of -96 dBm. Quality factors of these resonators are listed on the right side of the plot.

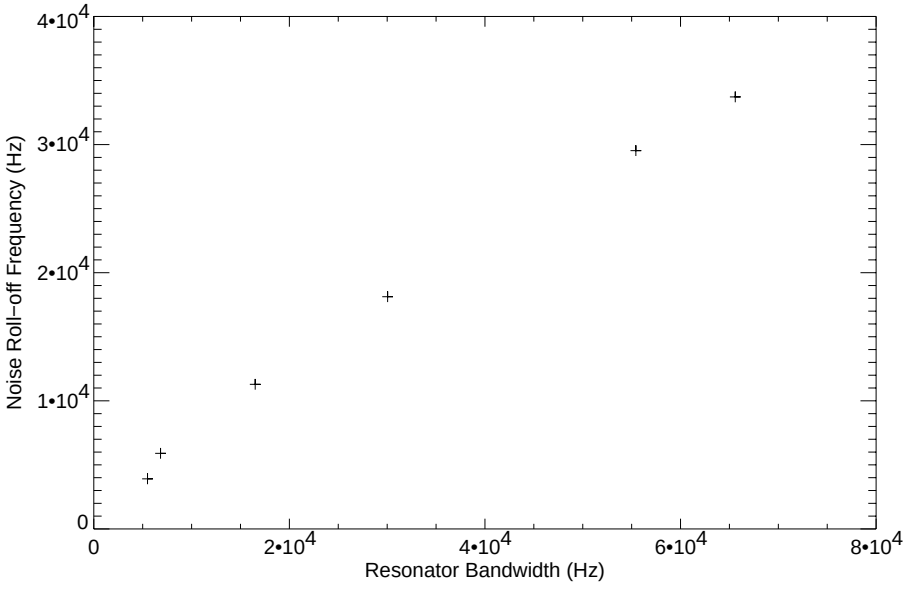

Figure 7.9: The resonator bandwidth and noise roll-off frequencies from Table 7.2. The noise roll-off is clearly related to the resonator bandwidth.

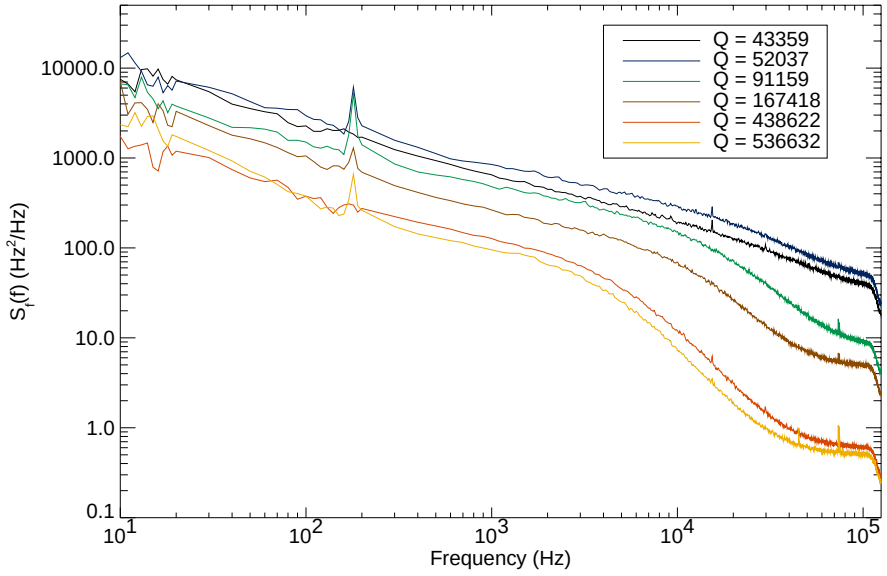

Figure 7.10: The frequency noise of 3 μm center strip resonators from the 320 nm thick Al on Si B0 device at a readout power of -96 dBm. The Q indicated in the legend is the Q derived from a fit at this power level.

7.1.4.1 Frequency Noise

It is possible to transform the phase noise into an equivalent frequency noise by dividing the spectrum by the slope of the phase change (radians/Hz) near resonance

$$S_F(\omega) = S_\theta(\omega)\left(\frac{f_0}{4Q}\right)^2 \tag{7.1}$$

where $S_F(\omega)$ is the frequency noise in Hz^2/Hz, $S_\theta(\omega)$ is the phase noise in radians^2/Hz, Q is the resonator quality factor, and f_0 is the resonant frequency. The phase angle θ is defined from the center of the resonance circle, with a range of 0 to 2π.

This phase slope can also be determined numerically by finding the slope of the phase vs. frequency plot for a given resonator. This method has the advantage that it automatically corrects for the fact that our data may not be taken exactly at the true resonance frequency of the resonator due to the way the resonance frequency is calculated during data taking. We will use this empirical method to calculate frequency noise.

Frequency noise can be thought of as the frequency perturbation necessary to cause the observed phase noise. It is a good way to compare the noise of resonators with different measured quality factors. As one can see in Figure 7.10, for a fixed readout power the frequency noise goes down as Q increases. This is seen clearly in the $1/f$ region where the resonator bandwidth is not rolling off the noise.

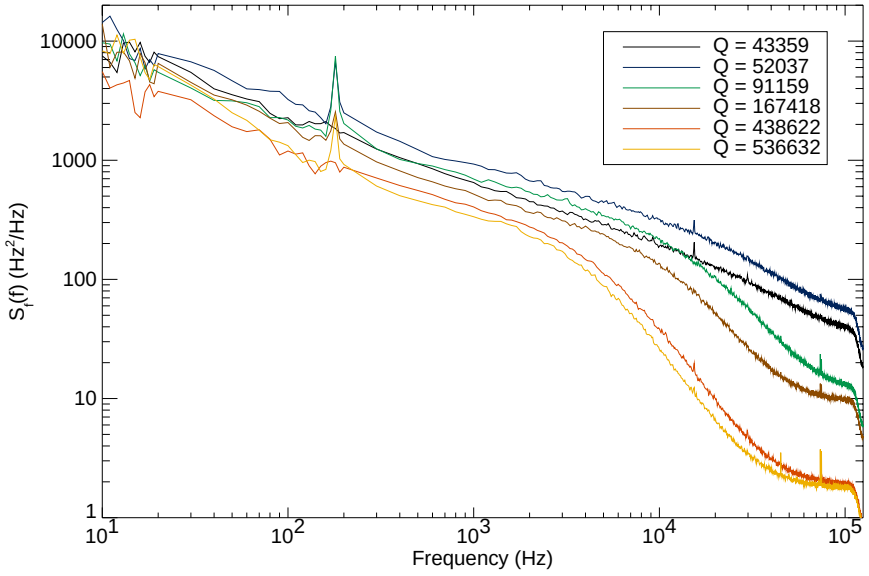

Figure 7.11: The frequency noise of 3 μm center strip resonators from the 320 nm thick Al on Si B0 device at a readout power of -96 dBm scaled by the $\sqrt{Q}$, and divided by the $\sqrt{Q}$ of the lowest Q resonator. The Q indicated in the legend is the Q derived from a fit at this power level.

One possible explanation for this behavior is that the excess noise is caused by substrate fluctuations and is sensitive to the electromagnetic field in the substrate. This would mean that resonators with higher stored energy should have lower frequency noise since they have higher electromagnetic fields in the substrate. There are two ways to test this hypothesis. The first is by scaling the frequency noise taken at a constant readout power by the $\sqrt{Q}$ (and normalizing by the $\sqrt{Q}$ of the lowest Q resonator) since the stored energy in the resonator goes as $\sqrt{Q}$ for a strongly coupled resonator, which applies to all the resonators considered in this section. This approach is shown in Figure 7.11. This approach will only work if the noise has a power dependance that scales as the square root of the readout power. This will be discussed further in the next section.

The second method is to determine the saturation energy of each resonator and determine the phase noise for a power just below saturation. This method is effective because we believe the saturation readout power occurs because the magnetic field in the resonator is becoming an appreciable fraction of the critical magnetic field. All resonators with the same lateral geometry just below saturation power on the same device should have similar electromagnetic fields in the substrate since they are all the same superconducting film. This approach is shown in Figure 7.12.

While these corrections do not make the frequency noise plots identical, their distribution is narrowed significantly by both methods. This is a clear indication that our excess noise depends on the amount of stored energy in the resonator.

It is instructive to plot the frequency noise of a single resonator as a function of temperature as

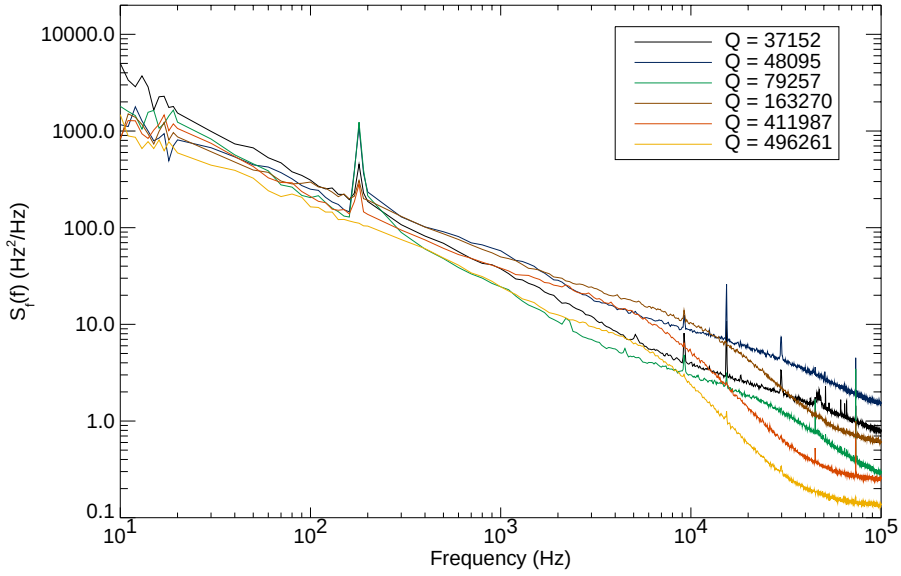

Figure 7.12: The frequency noise of 3 μm center strip resonators from the 320 nm thick Al on Si B0 device at a readout power just below the saturation readout power of each individual resonator. The Q indicated in the legend is the Q derived from a fit at the power level the noise data was taken at.

shown in Figure 7.13. Resonator 2 was selected because it has a low coupling Q so that the measured Q does not change much over temperature. This plot shows that there is a noticeable flattening of the noise spectrum as temperature increases. The effect is too large to be accounted for by the small change in measured Q. We believe that this might be due to the actual physics of the noise — if some unknown fluctuators are present in the substrate their population may vary with temperature, causing the observed change in the spectral index of the noise.

7.1.4.2 Noise Power Dependance

If the effects of readout noise are negligible, the resonator should have the same phase noise, regardless of the power level driving the resonator, until a certain point when the driving power exceeds the power handling capacity of the superconducting transmission line. At this point non-linear effects set in and the resonance shape is distorted. The readout noise is negligible for all the resonators we discuss except the lowest Q resonators at offset frequencies above 10 kHz, where HEMT noise can start to dominate (see Section 5.5.3).

Both the phase and frequency noise of our resonators clearly depend on the readout power used to measure them. To show this is not a readout effect, we can plot the actual voltage noise as a function of readout power. Since the resonance circle in the IQ plane gets bigger with higher readout power, the voltage noise should scale linearly as the readout power is increased. However, we actually

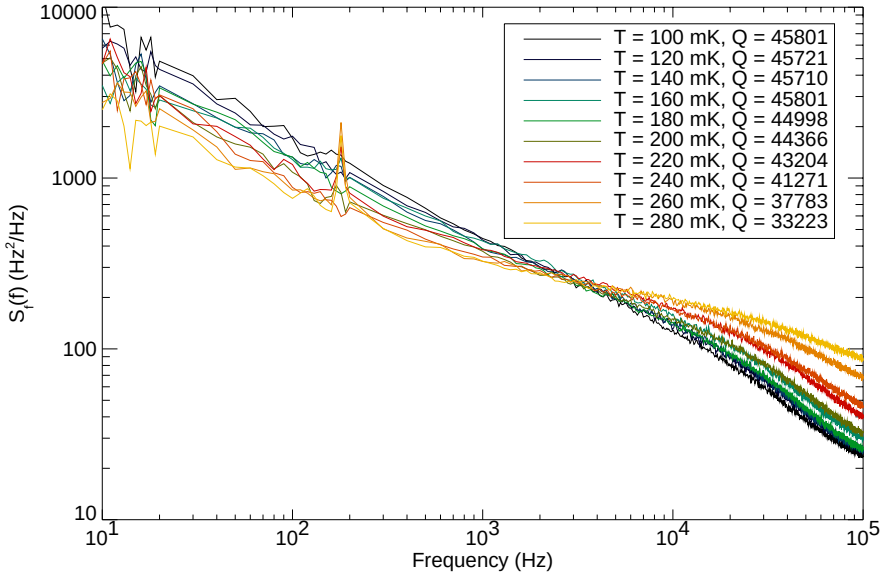

Figure 7.13: The frequency noise of resonator 2 from the 320 nm thick Al on Si B0 device at a readout power of -96 dBm at various temperatures. The Q indicated in the legend is the Q derived from a fit at this power level and temperature.

observe the voltage noise remaining constant or even going down as readout power increases, showing unequivocally that the phase noise is going down as the readout power is increased. Figures 7.14 and Figures 7.15 show the phase and frequency noise of resonator 1 as a function of readout power. The highest readout powers (shown in the darkest colors) are well beyond the saturation power of the resonator. This accounts for the drastic $1/f$ noise excess seen in these spectra.

Another way to look at this is shown in Figure 7.16. In this plot, we have integrated the total phase jitter in different bands (10-100 Hz, 100-1000 Hz, etc.) and plotted the results as a function of power. This plot makes it clear that the higher frequency noise keeps improving as the power is increased, while the lower frequency components stop improving around about 10 dB before the saturation readout power. The power law index of improvement in the noise at high frequencies, shown as the blue line in the plot, is -0.43.

Even eliminating the saturated resonators, the noise improves much more at high frequencies than at low frequencies. It appears that the low frequency noise stops improving at rather low readout powers, while the higher frequency component keeps improving until saturation.

More work needs to be done to understand this effect, but the practical effect is that the devices should be run near their saturation power for the best performance.

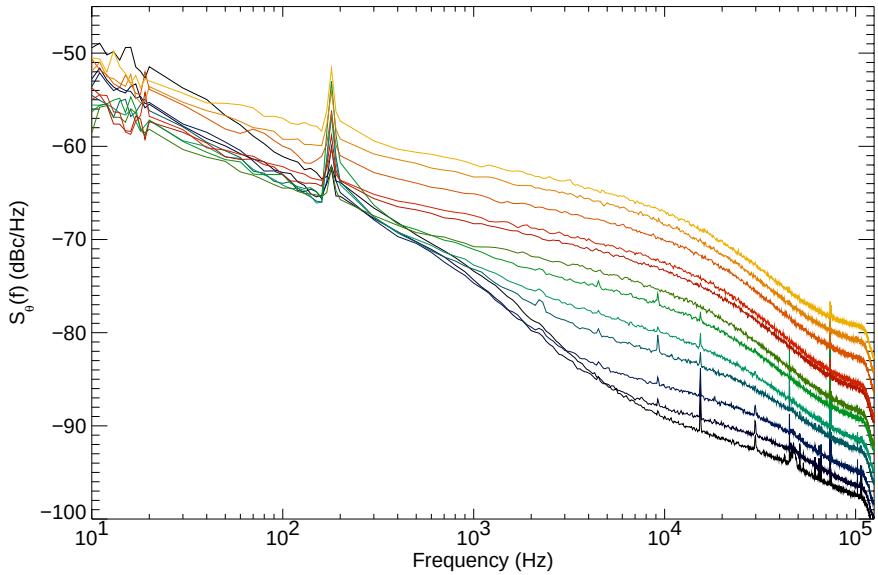

Figure 7.14: The phase noise of resonator 1 from the 320 nm thick Al on Si B0. The readout power ranges from -74 dBm (shown in black) to -96 dBm (shown in orange) in steps of 2 dBm.

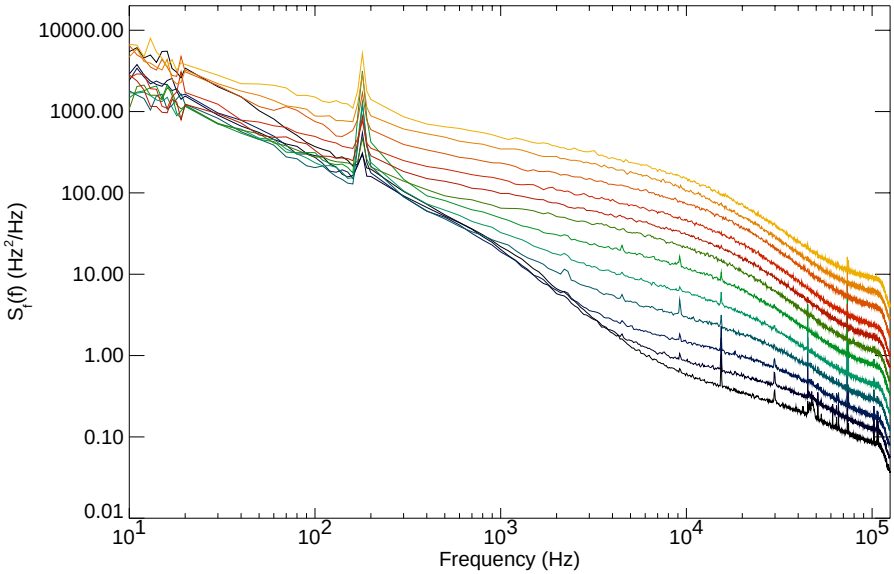

Figure 7.15: The frequency noise of resonator 1 from the 320 nm thick Al on Si B0. The readout power ranges from -74 dBm (shown in black) to -96 dBm (shown in orange) in steps of 2 dBm.

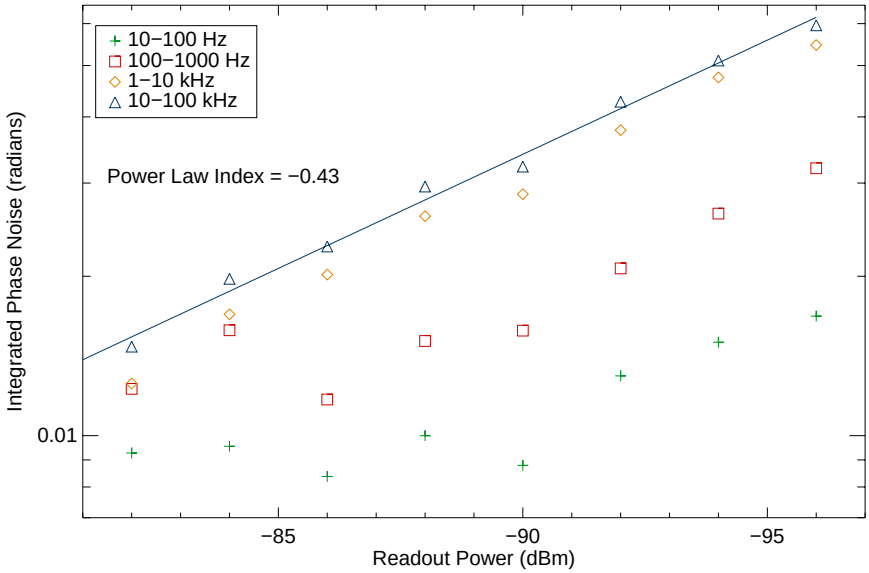

Figure 7.16: The integrated phase noise of resonator 1 from the 320 nm thick Al on Si B0 in several different frequency ranges plotted against readout power.

7.1.4.3 Phase Change per Quasiparticle

The phase change per quasiparticle, $d\theta/dN_{qp}$, can be derived by plotting resonance curves made at various temperatures on top of each other as in Figure 7.17. Using the resonance center of the lowest temperature data point, we can calculate the phase angle of a given frequency (usually the resonant frequency of the lowest temperature resonator) as a function of temperature as shown in Figures 7.18.

There is a large phase variance that increases with Q for the low temperature data points that is not predicted by superconductivity theory. We believe this is a result of two-level behavior of glassy materials in the substrate at low temperature causing a small change in the dielectric constant [114, 115]. This strange behavior should not pose a problem for a detector since when energy is injected into the resonator it will be injected as quasiparticles. Since these quasiparticles will not significantly heat the substrate, the zero phase point should be quite stable. Other substrates, like sapphire, show much less pronounced low temperature effects. Low Q resonators show less pronounced low temperature effects then high Q resonators. It is possible that the excess noise we observe is associated with two-level states in the substrate.

By using the material parameters, known geometry, and Equation 2.3 we can convert the temperature axis of this plot to the number of quasiparticles in the center strip as shown in Figure 7.19. There is some ambiguity in this conversion since heating the film causes quasiparticles in both the center strip and the ground plane. Considering only the quasiparticles in the center strip will cause

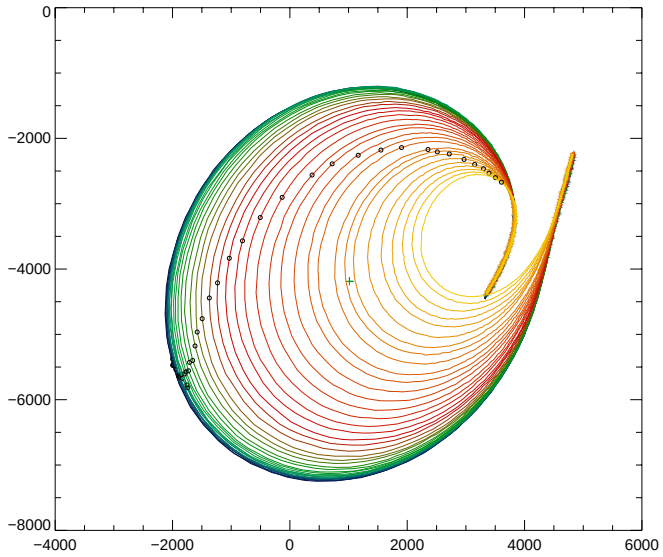

Figure 7.17: The IQ curves of a resonator 1 from the 320 nm thick Al on Si B0 device. The quality factors of this resonator at 120 mK is 90,000. The resonance shrinks and shifts frequency as the device is warmed from 120 mK to 320 mK. The green cross is the resonance center from the fits to the lowest temperature resonance curve. The black circles are points of constant frequency (the resonant frequency of the lowest temperature resonance curve).

us to slightly underestimate the number of quasiparticles needed to cause a given phase change, resulting in a small overestimate of the responsivity to quasiparticles injected in the center strip.

After this conversion we can fit a straight line to the data points in the linear range to get $d\theta/dN_{qp}$. The actual values can be found in Table 7.3.

We can also compute $d\theta/dN_{qp}$ using the parameters we fit for in Section 7.1.3. This is accomplished by calculating the phase at a given temperature using Equation 2.61. This gives us an equation for phase as a function of temperature, $\theta(Q(T), \delta\omega/\omega_0(T), S_{21}^{min}(T))$. These functions can be computed in the extreme anomalous limit using the equations of Section 6.2. The green curve on Figure 7.19 shows this calculation. This is not a fit, but a theoretical prediction using only $Q(T=0), \omega_0(T=0), \Delta(T=0), \alpha$, and $S_{21}^{min}(T=0)$ which were previously fit for.

7.1.4.4 Quasiparticle Lifetimes

During this run a method was employed to allow us to determine the quasiparticle lifetime in the film. The first and second synthesizers were set to the resonant frequency of the chosen resonator. The first synthesizer was set to a nominal readout power of -82 dBm and the second to a higher power of around -66 dBm, which is enough to easily saturate the resonator. A fast diode switch was put in front of the second synthesizer and driven with a 100 Hz TTL square wave.

The result of this setup is that 100 times a second the resonator is hit with a very strong

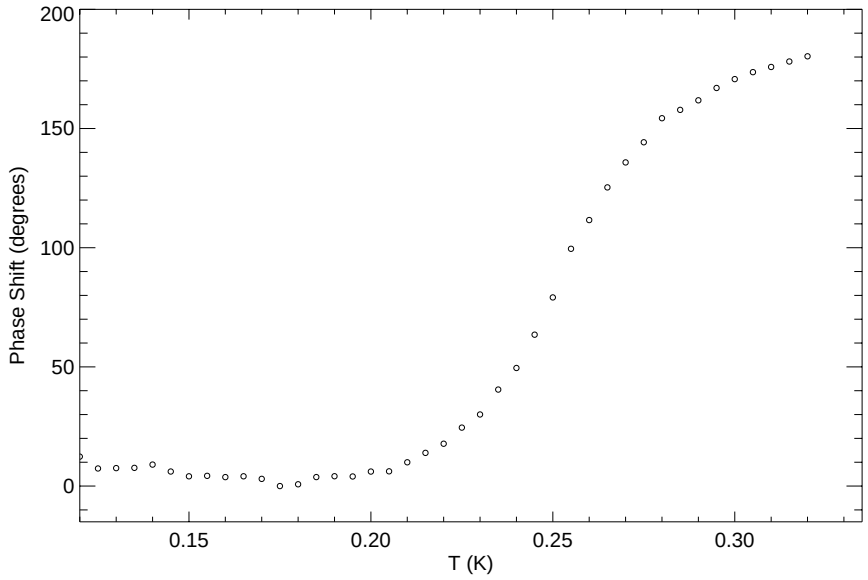

Figure 7.18: The phase shift vs. temperature at constant frequency of resonator 1 from the 320 nm thick Al on Si B0 device. The quality factor of this resonator is 90,000.

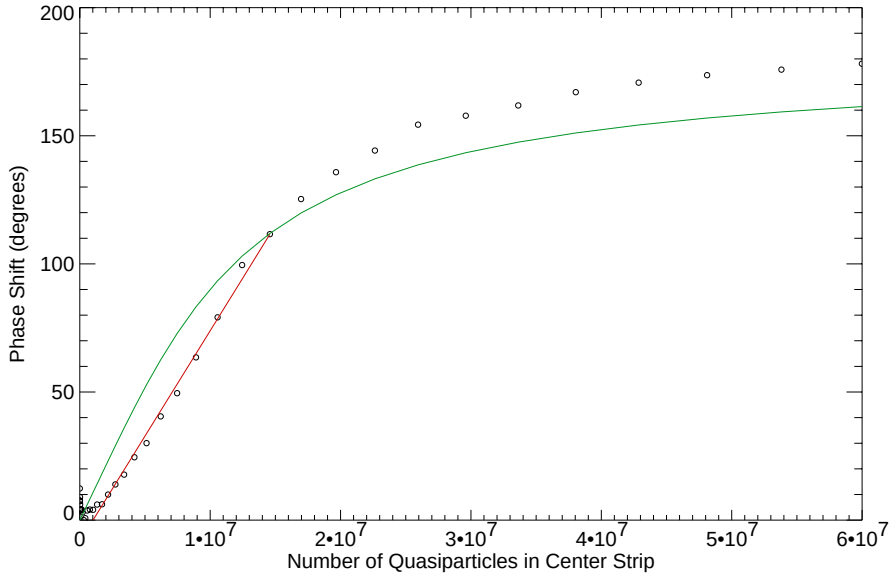

Figure 7.19: The phase shift vs. quasiparticle number at constant frequency of resonator 1 from the 320 nm thick Al on Si wafer. Quality factors of this resonator is $Q = 90,000$. The red line is the fit to the data used to derive $d\theta/dN_{qp}$. The green line is a theoretical prediction based on the fits of Section 7.1.3 and Equation 2.60

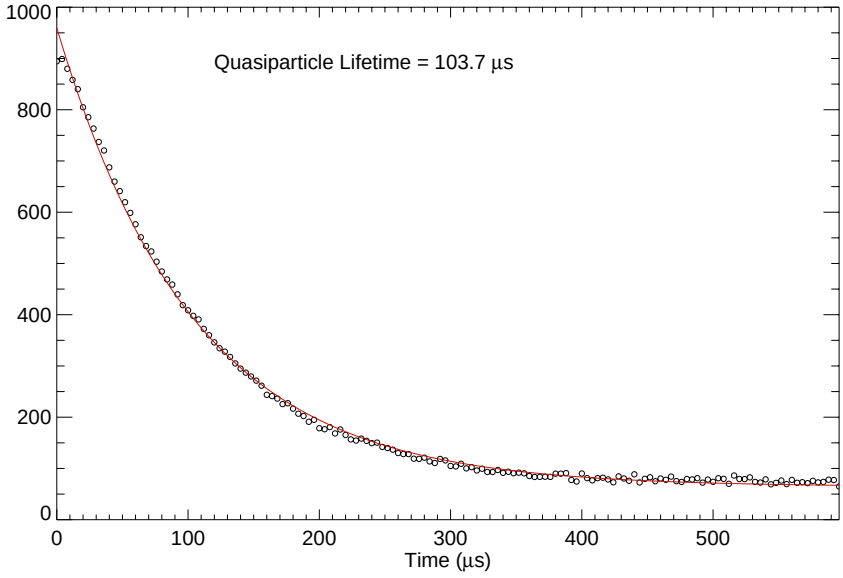

Figure 7.20: The recovery of resonator 1, a $Q = 90,000$ 320 nm thick Al on Si device, at 120 mK after it has been excited by a strong microwave pulse. Since the resonator decay time of this device is only several microseconds, the long decay time must be caused by quasiparticles recombining in the resonator.

microwave pulse, which drives it off resonance and creates quasiparticles in the resonator. When the pulse turns off these quasiparticles decay back to the ground state. This decay can be observed with the first synthesizer as seen in Figure 7.20. Performing this procedure at different temperatures yields Figure 7.35, which shows that the lifetime saturates around 180–200 mK at a value of around 100 microseconds. This is similar to the value measured in Day *et al.* [27].

This device, however, has a shorted end where the quasiparticles in the center strip can diffuse into the ground plane. Since aluminum has a fast diffusion constant we expect that the lifetime we see is limited by out-diffusion of quasiparticles, and should be considered a lower limit of the quasiparticle lifetime. Measurements taken by Peter Day using a LED to illuminate a resonator with a tantalum plug at the end show lifetimes of 500–600 microseconds for a similar aluminum film.

7.1.4.5 Saturation Energy

A simple calculation can be performed using the calculated responsivity $d\theta/dN_{qp}$ to determine the maximum photon energy that a resonator can accommodate, as shown in Section 3.5:

$$E_{max} = \frac{\theta_{max}\Delta}{d\theta/dN_{qp}} \tag{7.2}$$

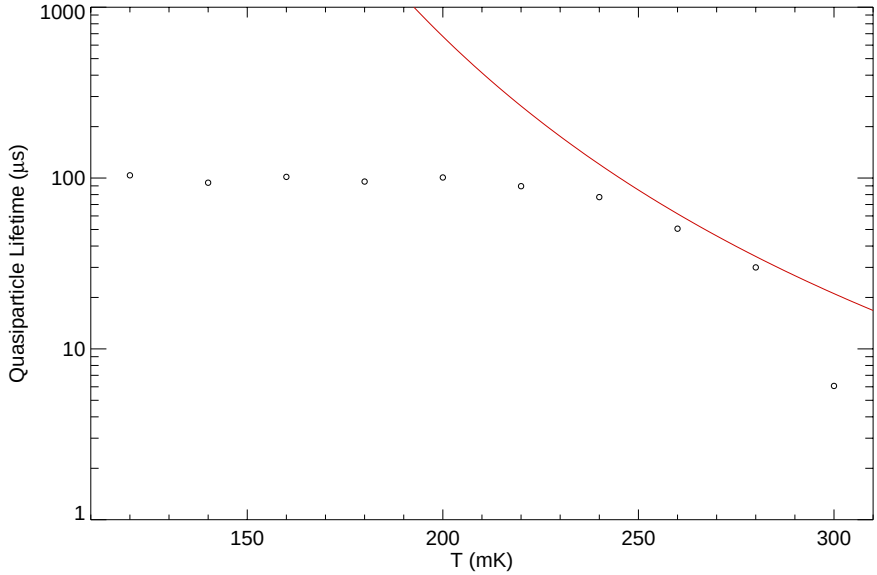

Figure 7.21: The measured quasiparticle lifetimes in the 320 nm thick Al on Si B0 device as a function of temperature. The red line is the theoretical lifetime from Equation 3.9.

where θ_{max} is the phase angle at which the responsivity begins to deviate from linearity. A reasonable value of θ_{max} is 90 degrees.

This is approximately the saturation energy of a single photon event. For a steady state input of energy like in a submillimeter detector, we need to calculate the radiant energy required to create this many quasiparticles.

$$P = \frac{N_{qp}\Delta}{\eta\tau_{qp}} \tag{7.3}$$

In this case η is an efficiency factor that depends on the difference between the gap frequency of the superconductor and the frequency of the incoming photons, and is expected to be between 0.5 and 1. Saturation powers calculated using $\tau_{qp} = 200$ μs are shown in Table 7.3.

7.1.4.6 NEP

Now that we have calculated $d\theta/dN_{qp}$ we can convert our resonator phase noise $S_\theta(\omega)$ into a noise equivalent power (NEP). NEP is defined as the amount of radiant power needed to achieve a signal to noise ratio of 1 per square root bandwidth in a detector at a given modulation frequency,

$$\mathrm{NEP}^2(\omega) = S_\theta(\omega)\left(\frac{\eta\tau_{qp}}{\Delta}\frac{\partial\theta}{\partial N_{\mathrm{qp}}}\right)^{-2}(1+\omega^2\tau_{qp}^2)(1+\omega^2\tau_{res}^2). \tag{7.4}$$

To do this computation we assume $\tau_{qp} = 200$ μs, $\eta = 0.57$, calculate the resonator timescale τ_{res} from Equation 3.19, and use the previously discussed values of $d\theta/dN_{qp}$ and Δ.

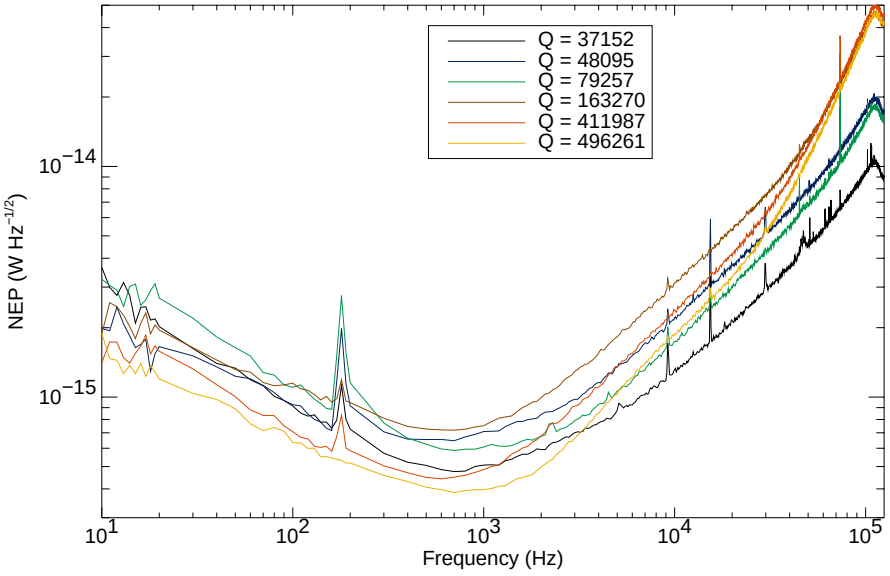

Figure 7.22: The noise equivalent power (NEP) of resonators from the 320 nm thick Al on Si B0 device. The NEPs are calculated for a microwave readout power just below the saturation value.

Q	Readout Power (dBm)	$d\theta/dN_{qp}$ (radians/qp)	Saturation Energy (eV)	Saturation Power (W)	minimum NEP (W Hz$^{-1/2}$)	ΔE (eV)
37152	-77	6.8×10^{-8}	3800	3.0×10^{-12}	4.8×10^{-16}	19.7
48095	-81	7.4×10^{-8}	3600	2.9×10^{-12}	6.5×10^{-16}	30.0
79257	-81	1.4×10^{-7}	1900	1.5×10^{-12}	5.9×10^{-16}	25.1
163270	-87	2.1×10^{-7}	1250	9.9×10^{-13}	7.1×10^{-16}	38.4
411987	-93	7.6×10^{-7}	350	2.8×10^{-13}	4.4×10^{-16}	26.7
496261	-91	9.2×10^{-7}	290	2.3×10^{-13}	3.8×10^{-16}	21.2

Table 7.3: Calculated saturation energies, minimum values of the NEP, and energy resolution for the resonators discussed in this section.

Using this NEP it is possible to calculate the expected energy resolution of the detector [1].

$$\Delta E = \left(\int_0^\infty \frac{4df}{\mathrm{NEP}^2(f)} \right)^{-1/2} \tag{7.5}$$

Calculated energy resolutions are shown in Table 7.3.

Figure 7.22 shows that the NEPs of the resonators are quite independent of Q when read out with a power just below the resonators's saturation power.

Resonator	Design Q	Length (μm)	Meanders	Q	f_0 (GHz)	S_{21} (dB)
1	1×10^5	5439.04	0	61506	4.626282	-20.4
2	1×10^5	5420.98	4	48333	4.812422	-18.9
3	1×10^5	5403.02	15	41027	4.888949	-19.1
4	5×10^5	5385.19	0	151607	4.667417	-7.26
5	5×10^5	5367.48	4	153548	4.863028	-7.23
6	5×10^5	5349.88	15	214991	4.933397	-7.03
7	1×10^6	5332.40	0	181245	4.749466	-1.13
8	1×10^6	5315.03	4	204028	4.949294	-2.08
9	1×10^6	5297.77	15	192654	5.027983	-3.49
10	5×10^6	5280.63	0	260150	4.784568	-0.34
11	5×10^6	5263.59	4	343452	4.988847	-0.85
12	5×10^6	5246.67	15	262125	5.067240	-0.81

Table 7.4: Measured Q and f_0 of a 40 nm thick aluminum on silicon B0 device from the test mask. This data was taken at a readout power of -104 dBm.

7.2 Thin Aluminum on Silicon Resonator Results

A B0 device made out of 40 nm thick aluminum on 5 kΩ cm silicon, fabricated by Rick LeDuc at JPL, was cooled down in our fridge on February 25, 2004. Several data sets were taken, including:

- IQ data away from resonance during the transition from normal to superconducting to determine T_c.
- Resonance curves and noise data at 120 mK for various input power levels for all resonators.
- Resonance curves and noise data from 120–320 mK, every 5 mK, for a low, medium, and high power level for all resonators.
- Power sweeps at 120 mK for several resonators.
- Quasiparticle lifetime data using the microwave pulse saturation method described in Section 7.1.4.4.

While the Q and the size of the resonance feature were fairly predictable on this device, the meandered devices had slightly different resonant frequencies than expected in a manner similar to the thicker resonators. Figure 7.23 shows the resonant frequency of the devices with the x-axis corresponding to the resonator numbers in Table 7.4.

This device has 1/8 the thickness of the 320 nm thick device discussed in Section 7.1, and since it is thin we expect the kinetic inductance fraction α to increase by a factor of 5–10 as shown in Figure 3.14. The end result is that this device should provide a phase response per quasiparticle $d\theta/dN_{qp} \sim 100\times$ higher than the thick B0 device.

One important note about the thin film devices is that their readout power handling capacity was significantly worse than the thicker films devices. Readout saturation powers were about 20

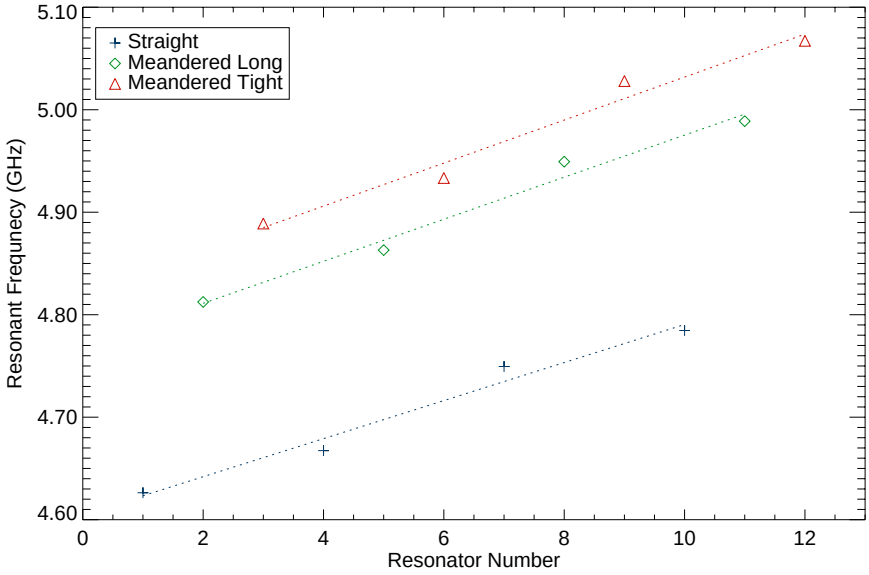

Figure 7.23: The resonant frequencies of the resonators on the 40 nm thick Al on Si B0 device. The meandered resonators have slightly shifted resonance frequencies.

dB lower than devices with identical lateral geometry but thicker films. Since the excess noise we measure improves with readout power we do not expect the NEP of the thin film devices to improve linearly with $d\theta/dN_{qp}$.

7.2.1 Transition Temperature

The superconducting transition temperature of the device is measured by observing the transmission of the feedline as the device is cooling through the superconducting transition temperature. Since these thin films have a high normal state resistivity, the transmission is essentially zero until they become superconducting. The place where the transmission starts to increase is $T_c = 1.41$ Kelvin for this device as shown in Figure 7.24. The increase in T_c as the film gets thinner is consistent with expectations for aluminum [116, 117].

7.2.2 Quality Factors

The quality factors of the resonators on this device ranged from around 40,000 to 300,000. We can analyze this data in the manner of Section 7.1.2 which yields Figure 7.25. This figure shows that the internal Q varies by less that it did on the thicker films, and is limited to a lower value($3.53 \times 10^5 \pm 1.35 \times 10^5$ instead of $1.08 \times 10^6 \pm 5.4 \times 10^5$). The cause of the variation of the internal Q is not understood, but our current speculation is that it is related to the fabrication process.

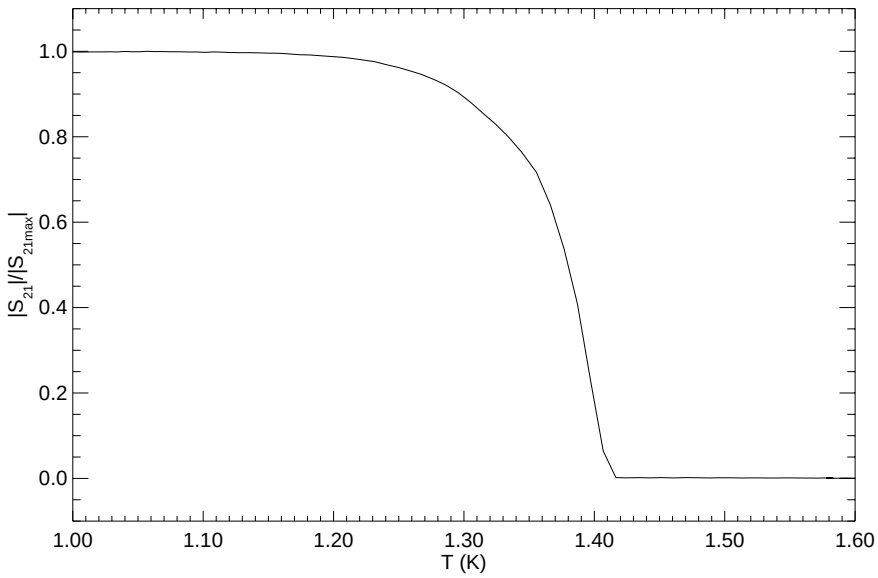

Figure 7.24: The transmission magnitude of the system relative to the transmission magnitude at base temperature for the 40 nm Al on Si B0 device. Since this device has a high normal state resistivity it is easy to measure its superconducting transition temperature from IQ data. The T_c for this device is around 1.41 K.

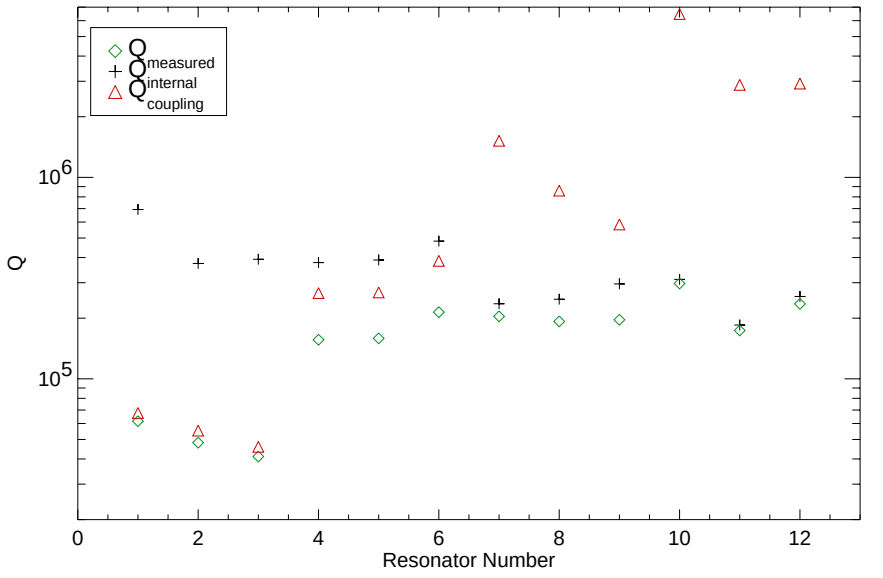

Figure 7.25: The internal quality factors of the devices on the 40 nm thick Al on Si B0 device. The IQ sweep data for this plot was taken at a power of -104 dBm.

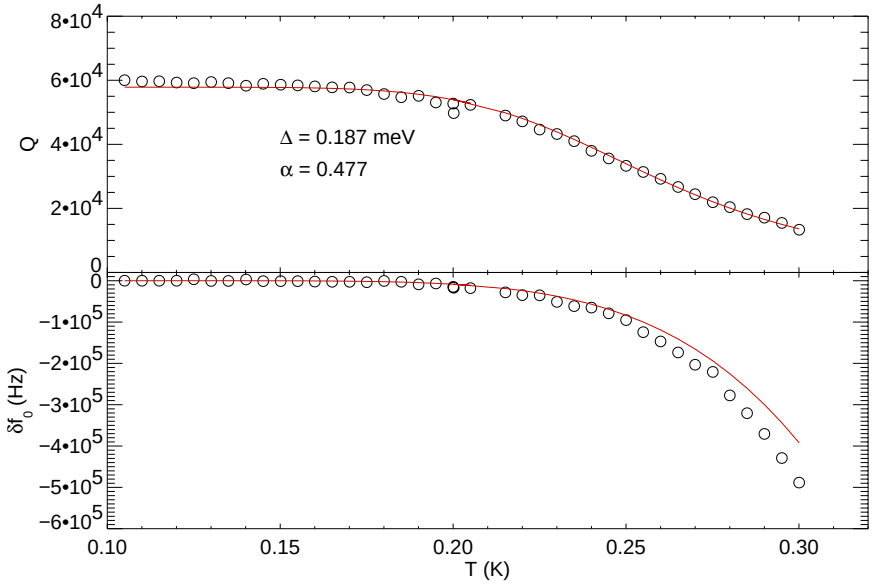

Figure 7.26: Fits to the Q and f_0 data from resonator 1 from the 40 nm Al on Si B0 device using Mattis-Bardeen theory in the extreme anomalous limit with Δ fixed at a value of 0.187 meV. Despite the fact that these equations aren't valid at this film thickness they still provide a reasonable fit.

7.2.3 Derived Material Parameters

The films used in these resonators are thinner than twice the penetration depth in aluminum, $2\lambda \sim 100$ nm. In this regime the electron mean free path is limited to the film thickness. This means that we may no longer be in the extreme anomalous limit, and we must use different equations to predict the behavior of the resonators. This work is ongoing by Jiansong Gao, and we expect some results soon. One simple way to estimate the change in the kinetic inductance is to compare the resonant frequencies of two different thicknesses as is shown in Section 7.3.

Despite the fact that we don't expect the equations in Section 6.2 to work for these resonators, they give reasonable agreement with the data using a value of $\alpha = 0.47$ derived from EM simulations performed by Jiansong Gao. The reasons for this match are not understood, but the fit to resonator 1 can be seen in Figure 7.26.

Using $\alpha = 0.47$ we derive a best fit value of $\Delta = 0.183$ meV. This value seems a little low, yielding $\Delta/k_bT_c = 1.51$, but is not very different from the Biondi and Garfunkel [112] value and the value we derived for the thicker films. Since the equations we used are know to be wrong we do not believe this ratio, and we will use the 320 nm thick derived value of $\Delta/k_bT_c = 1.54$ ($\Delta = 0.187$ meV) when we analyze the NEP of this device.

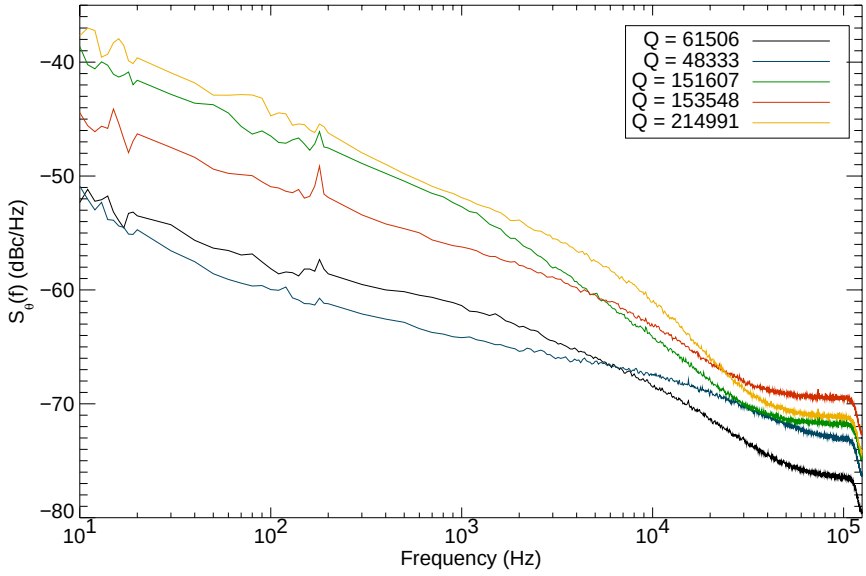

Figure 7.27: The phase noise of resonators 1,2,4,5, and 6 from the 40 nm thick Al on Si B0 device measured at a constant readout power of -104 dBm. The phase noise increases and the noise roll-off frequency decreases with increasing resonator Q.

Q	Resonator Bandwidth (Hz)	Noise Roll-off (Hz)
61506	37608	11089
48333	49783	31543
151608	15393	5730
153548	15835	8650
214992	11473	6370

Table 7.5: Measured noise roll-off frequency of 40 nm thick aluminum on silicon resonators.

7.2.4 Noise

Following the procedure outlined in Section 7.1.4 we can analyze the noise of these thin resonators. We will limit ourselves to the resonators with lower coupling Qs, and omit resonator 3 due to problems in the data collection. This leaves resonators 1,2,4,5, and 6 from Table 7.4.

We can perform fits to the phase noise spectrum to help understand the noise, as shown in Figure 7.28 and Table 7.5. The noise roll-off frequency does not fit as well as for the thick data, but this can be understood by looking at the fits. The thin data tends to have a flatter mid-frequency region than the thick data, leading to poor fits.

7.2.4.1 Frequency Noise

We can perform the same transformation as in Section 7.1.4.1 to derive the frequency noise for these resonators. We plot the frequency noise at -104 dBm in Figure 7.29, the same data set scaled by

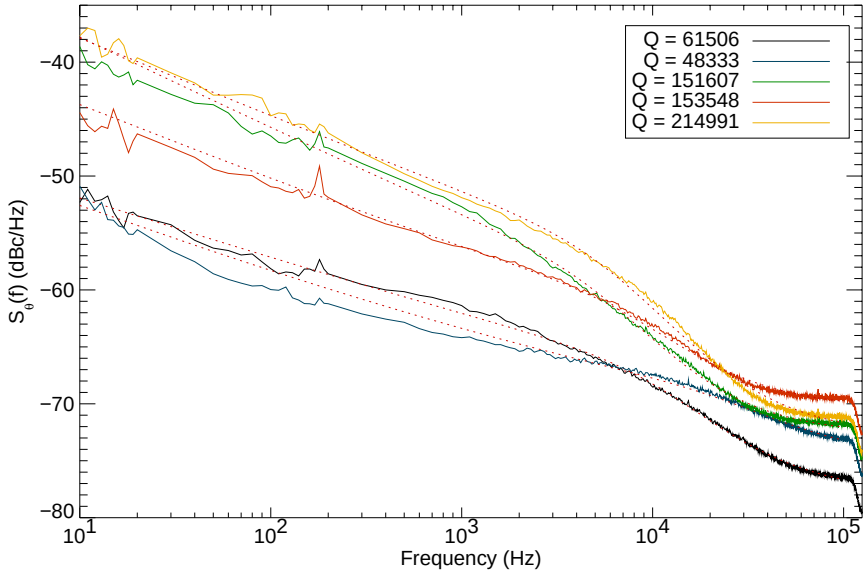

Figure 7.28: The phase noise fits of resonators from the 40 nm thick Al on Si B0 wafer measured at a readout power of -104 dBm. Quality factors of these resonators are listed on the right side of the plot.

$\sqrt{Q}$ in Figure 7.30, and at a readout power just below the individual resonator's saturation power in Figure 7.31.

The results of this procedure is a nearly identical result to those seen for the thick film devices, showing that the frequency noise of resonators depends on stored energy in the resonator, and not on Q. Section 7.3 will compare the noise of resonators from the thick and thin film devices.

7.2.4.2 Noise Power Dependance

The phase noise versus readout power for resonator 1 from the 40 nm B0 device is plotted in Figure 7.32. It shows a very similar trend to the thick data, where the phase noise drops as the readout power and the stored energy in the resonator increases.

7.2.4.3 Phase Change per Quasiparticle

One of the most interesting results from the thin film resonators is a direct comparison of the phase change per quasiparticle in the center strip to a resonator of identical geometry from the thick film device. From Figure 7.34 and Tables 7.3 and 7.6 we can look up $d\theta/dN_{qp}$ for the thick and thin resonator 2. Resonator 2 from the 320 nm thick devices has $Q = 48095$ and $d\theta/dN_{qp} = 7.4 \times 10^{-8}$. Resonator 2 from the 40 nm thick devices has $Q = 49333$ and $d\theta/dN_{qp} = 6.7 \times 10^{-6}$.

Dividing the values of $d\theta/dN_{qp}$ gives a responsivity 91 times greater for the thin film for a given Q. Taking out the change in volume by a factor of $320/40 = 8$ and the change in the kinetic

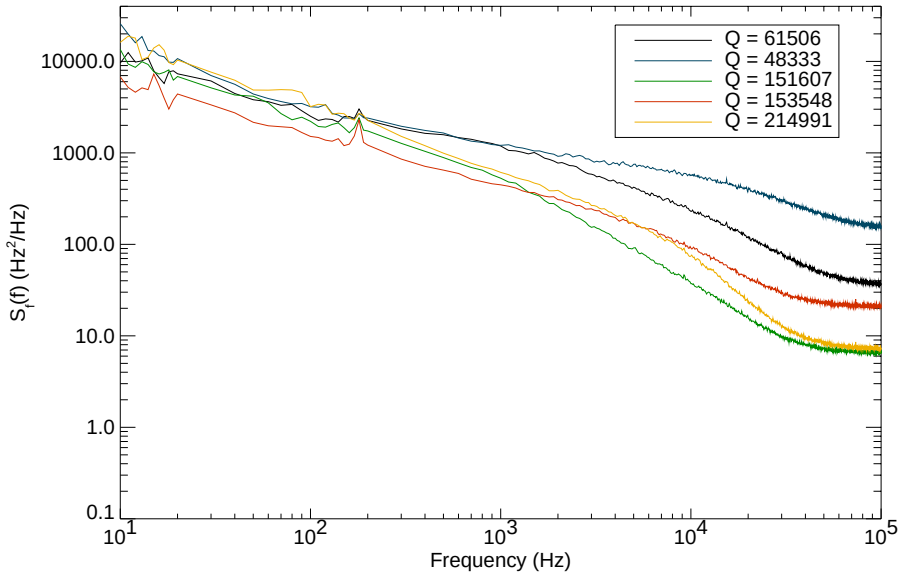

Figure 7.29: The frequency noise of resonators from the 40 nm thick Al on Si B0 device at a readout power of -104 dBm. The Q indicated in the legend is the Q derived from a fit at this power level.

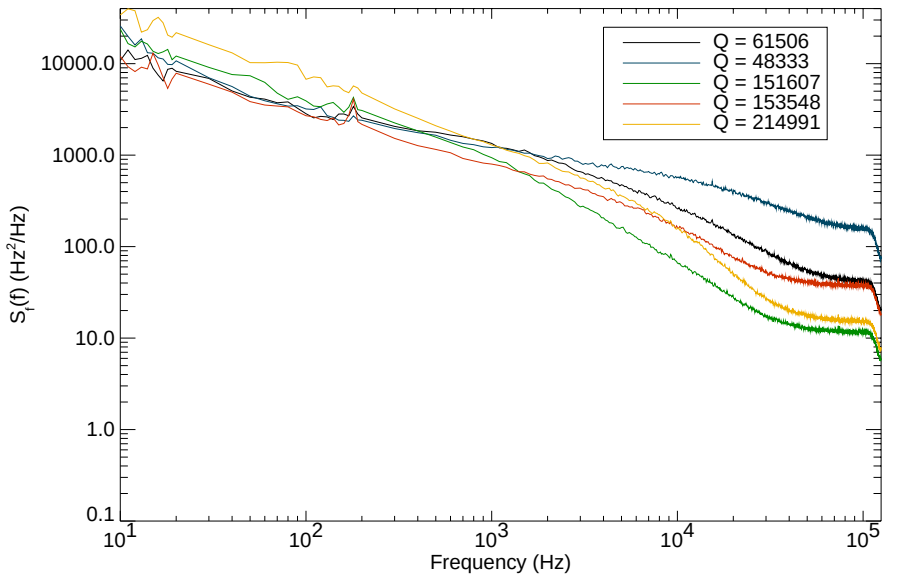

Figure 7.30: The frequency noise of resonators from the 40 nm thick Al on Si B0 device at a readout power of -104 dBm scaled by the $\sqrt{Q}$ divided by the $\sqrt{Q}$ of the lowest Q resonator. The Q indicated in the legend is the Q derived from a fit at this power level.

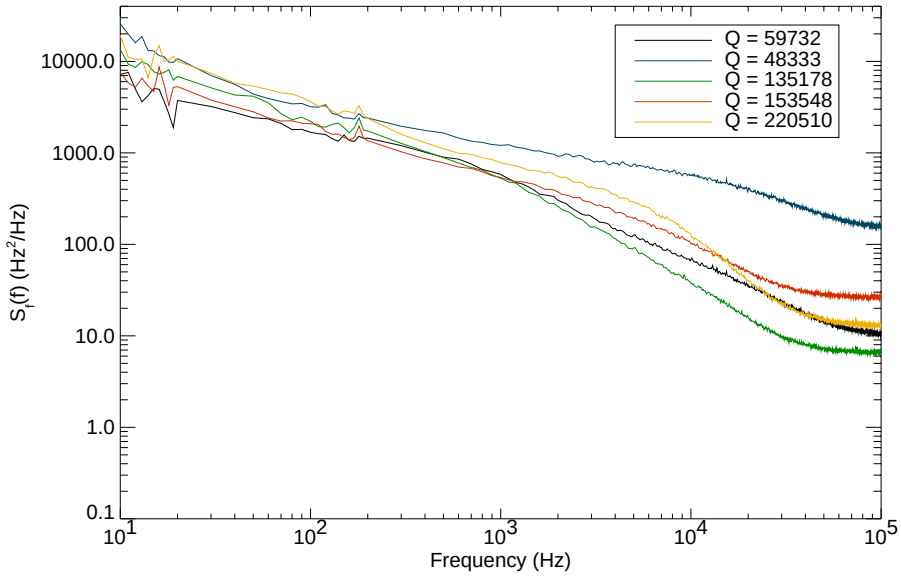

Figure 7.31: The frequency noise of resonators from the 40 nm thick Al on Si B0 device at a readout power just below the saturation readout power of each individual resonator. The Q indicated in the legend is the Q derived from a fit at the power level the noise data was taken at.

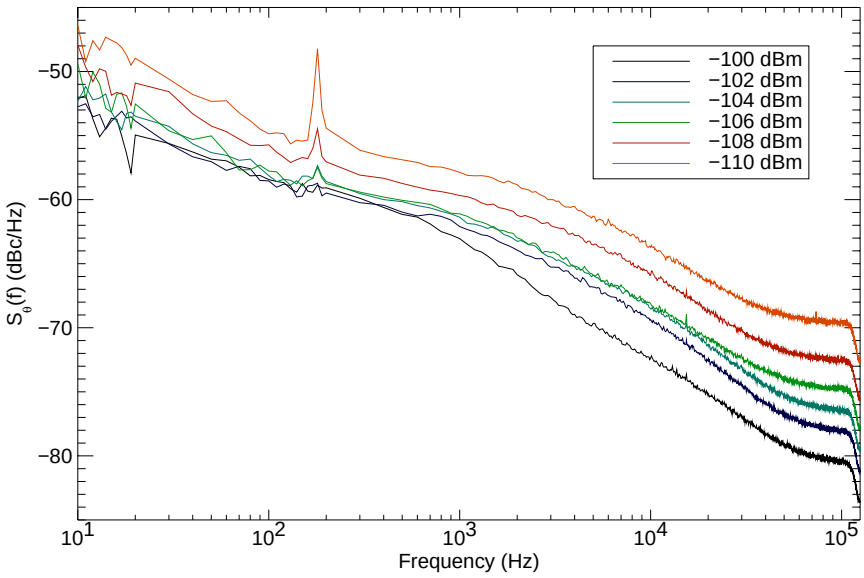

Figure 7.32: The phase noise of resonator 1 from the 40 nm thick Al on Si B0. The readout power ranges from -100 dBm to -110 dBm in steps of 2 dBm.

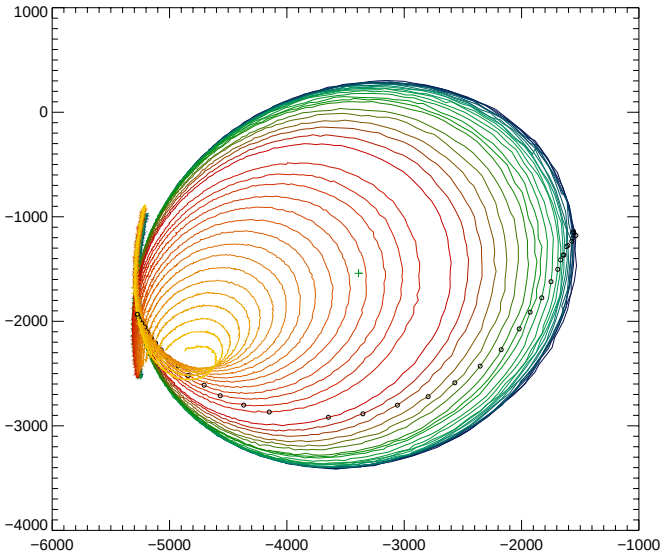

Figure 7.33: The IQ curves of a resonator 2 from the 40 nm thick Al on Si B0 device. The quality factor of this resonator is $Q = 48,333$. The resonance shrinks and shifts frequency as the device is warmed from 120 mK to 320 mK. The green cross is the resonance center from the fits to the lowest temperature resonance curve. The black circles are points of constant frequency (the resonant frequency of the lowest temperature resonance curve).

inductance fraction of $\alpha = .47/.055 = 8.5$ leaves a factor of 1.3 that is probably due to the increase of the gap as the film becomes thinner. This effect can be estimated using Equation 2.58.

Figure 7.34 shows the responsivity of resonator 2. The estimated responsivity of the device is shown in green, and is an excellent match to the actual data despite the problems we expected applying bulk aluminum calculations to this thin film data.

7.2.4.4 Quasiparticle Lifetimes

We can take data on the quasiparticle lifetimes using the method of Section 7.1.4.4. For this film thickness we get a quasiparticle lifetime of approximately 65 microseconds, as seen in Figure 7.35.

7.2.4.5 Saturation Energy

We can calculate the saturation energies using the methods of Section 7.1.4.5. Results range from 10–47 eV as shown in Table 7.6. These thin film devices saturate at very low powers suitable for optical/UV detectors.

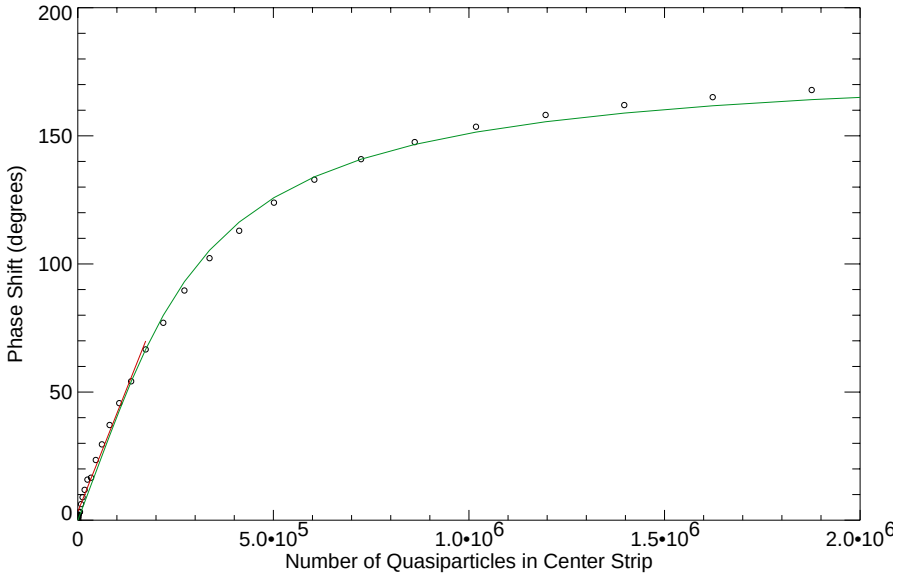

Figure 7.34: The phase shift vs. quasiparticle number at constant frequency of resonator 2 from the 40 nm thick Al on Si B0 device. Quality factors of this resonator is $Q = 48,333$. The red line is the fit to the data used to derive $d\theta/dN_{qp}$.

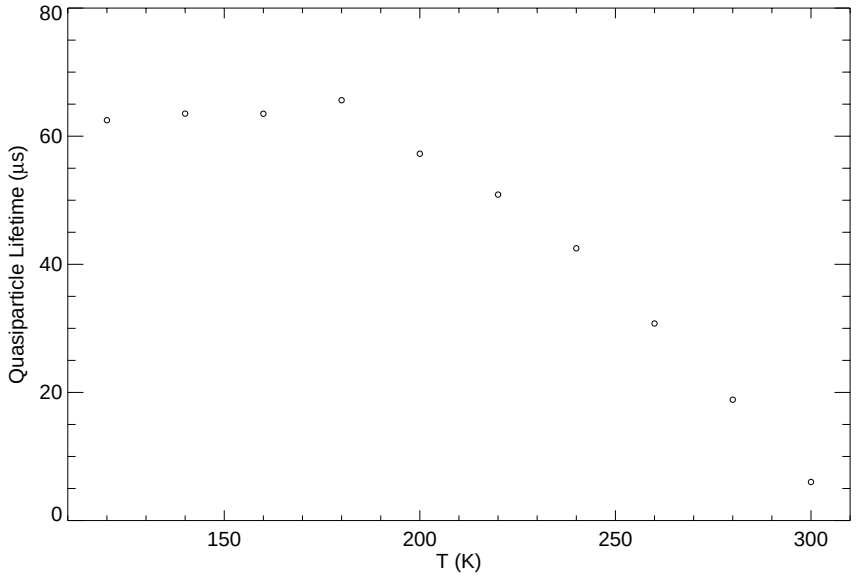

Figure 7.35: The measured quasiparticle lifetimes in the 40 nm thick B0 device as a function of temperature.

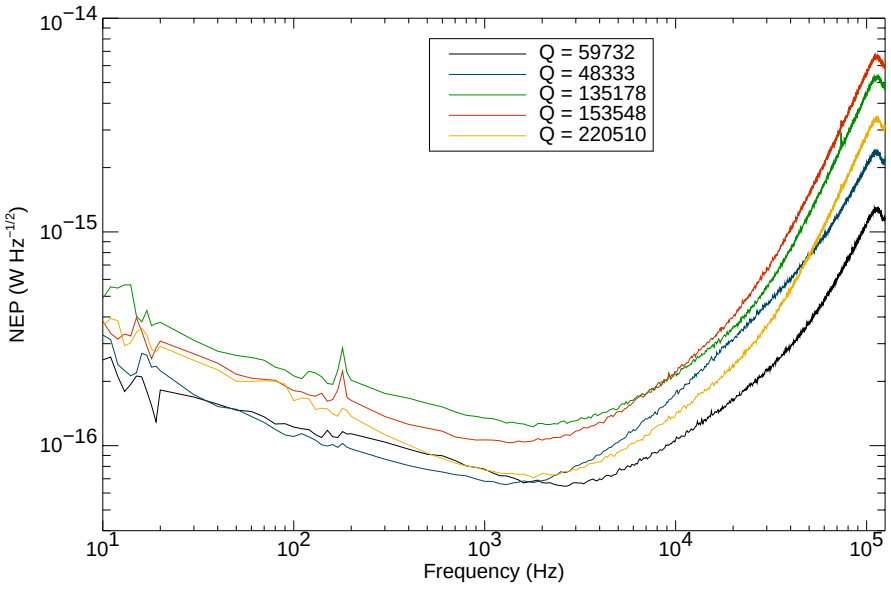

Figure 7.36: The noise equivalent power (NEP) of resonators from the 40 nm thick Al on Si B0 device. The NEPs are calculated for a readout power just below the saturation value.

7.2.4.6 NEP

We can calculate the NEP and energy resolution using the procedure of Section 7.1.4.6 at readout powers just below the saturation power of the individual resonators results in Figure 7.36 using $\tau_{qp} = 65$ μs derived in Section 7.2.4.4.

The NEPs for the thin film resonators are lower than the thick film resonators by a factor of ~ 10. The improvement in NEP was not as great as the improvement in $d\theta/dN_{qp}$ because the much lower saturation power of these resonators resulted in higher frequency noise as shown in Section 7.2.4.2.

Since the responsivities are up by a factor of ~ 90 the dynamic range has been reduced by about $90/10 = 9$. This is acceptable for an optical/UV device because the quasiparticle creation (Fano) statistics limit the energy resolution as discussed in Section 3.4.2. The signal to noise ratios that we see in the low Q resonators is close to state-of-the-art for superconducting optical detectors.

These resonators needed very low readout powers to avoid saturation. As we will see in Chapter 8, resonators on sapphire appear to be able to deal with much higher readout powers than resonators on silicon. Since the phase noise goes down as the readout power goes up on both silicon and sapphire (Section 9.4.2), we expect thin films on sapphire to have significantly better performance.

Q	Readout Power (dBm)	$d\theta/dN_{qp}$ (radians/qp)	Saturation Energy (eV)	Saturation Power (W)	minimum NEP (W Hz$^{-1/2}$)	ΔE (eV)
59732	-101	8.0×10^{-6}	47	9.1×10^{-14}	6.4×10^{-17}	1.8
49333	-105	6.7×10^{-6}	44	1.1×10^{-13}	6.6×10^{-17}	2.6
135178	-103	1.4×10^{-5}	22	5.3×10^{-14}	1.2×10^{-16}	3.9
153548	-105	1.3×10^{-5}	23	5.7×10^{-14}	1.0×10^{-16}	3.7
229510	-107	2.9×10^{-5}	10	2.5×10^{-14}	7.1×10^{-17}	2.4

Table 7.6: Calculated saturation energies, minimum values of the NEP, and energy resolution for the resonators discussed in this section taken at a readout power just below the saturation power.

7.3 Comparison of 320 and 40 nm Data

It is very interesting to compare the results from identical resonators from the thick and thin B0 cooldowns. The geometries and substrate are identical except for thickness, and the strongly coupled devices have similar measured Q. The resonant frequencies of the thin devices are about 850 MHz lower than the thick devices because the kinetic inductance increases as the film gets thinner. We can use this to estimate the kinetic inductance fraction, since the increase in the total inductance can be written:

$$r = \left(\frac{\omega_{0thick}}{\omega_{0thin}}\right)^2 = 1.4 \tag{7.6}$$

$$r = \frac{L + \alpha_{thin}L}{L + \alpha_{thick}L} = \frac{1 + \alpha_{thin}}{1 + \alpha_{thick}} \tag{7.7}$$

$$\alpha_{thin} = r(1 + \alpha_{thick}) - 1 \tag{7.8}$$

Using the value of α for the numerical simulations of $\alpha_{thick} = 0.055$ allows us to use Equation 7.8 to derive $\alpha_{thin} = 0.477$. This is in poor agreement with the analytic formula of Watanabe[101], which predicts $\alpha \approx 0.25$ for $\lambda = 50$ nm (a more exact calculation would calculate λ as a function of thickness), but in good agreement with numerical EM field simulations performed by Jiansong Gao which yield $\alpha_{thin} = 0.47$.

The thin devices saturate at much lower readout powers than the thick devices. For example, the thick resonator 1 can be read out at -80 dBm, while the maximum power that the thin version of resonator 1 can be read out at is -100 dBm. In order to compare noise at similar stored energy, we need to use resonators with similar Q read out a power below the saturation power of the thin resonators. For this section we will consider resonators 1, so a power of -104 dBm, 4 dB below saturation of the thin resonator, will be used.

Figure 7.37 and Figure 7.38 show the phase and frequency noise of this pair of resonators. There is excellent agreement of the noise spectra, even though the responsivity of the thin resonator is more that 100 times greater than the thick resonator. *This effectively rules out any source of noise which includes quasiparticles.* These sources include generation-recombination noise and excess pair

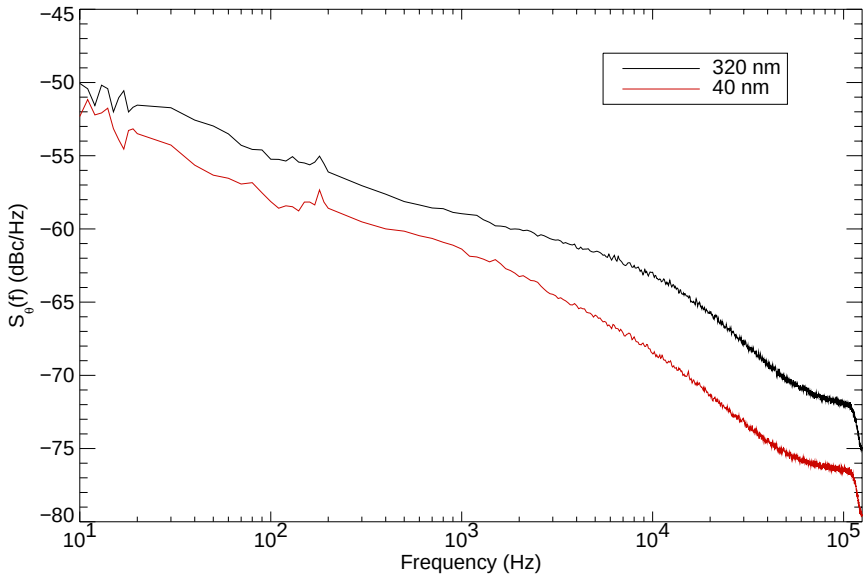

Figure 7.37: The phase noise of resonator 1 from the 40 and 320 nm thick Al on Si B0 device at a readout power of -104 dBm.

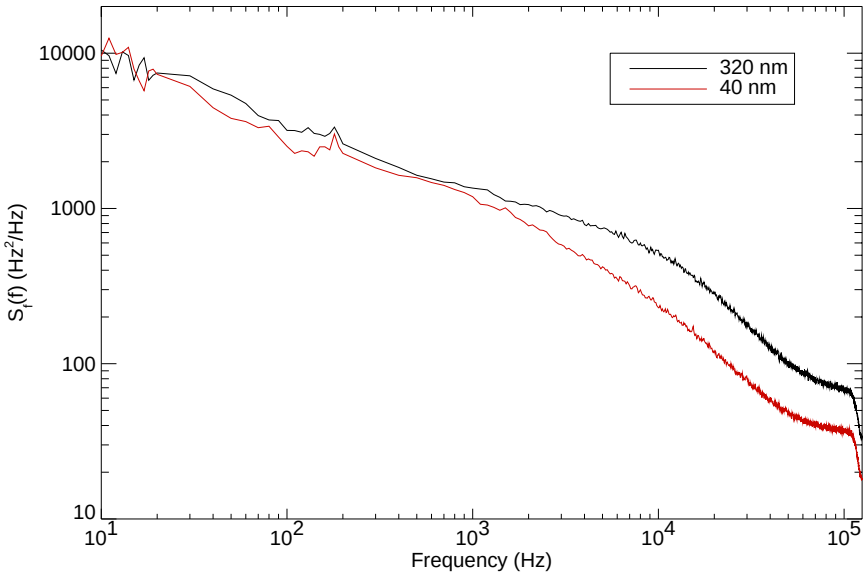

Figure 7.38: The frequency noise of resonator 1 from the 40 and 320 nm thick Al on Si B0 device at a readout power of -104 dBm.

breaking radiation coming down the coaxial lines.

The excellent agreement of the frequency noise spectra over such a wide range in responsivity is very strong evidence that the excess noise we see is caused by the substrate and not anything related to the superconductor.

7.4 The Variation of Resonator Parameters with Width

Since we have already investigated the performance of 3 μm center strip resonators with the B0 devices we will focus in this section on what is distinctive about the K0 device — the resonators with varying center strip widths. This K0 device is from the same wafer as the 320 nm thick Al on Si B0 device discussed previously.

These resonators contain the same coupling structure as the B0 devices, but after the coupler they neck out to a wider center strip. The center strips and the gaps scale simultaneously to preserve the characteristic impedance of the transmission line.

In this device the first 16 resonators are a series whose purpose was to study the relationship between line width, Q, and noise. We expect the wider lines to have more radiation loss than the thinner lines, but the other parameters that should affect the Q, dielectric loss and coupling, should remain constant. The wider lines should have lower Qs and smaller resonance features. The lengths of these devices were designed with the phase velocity of the 3 μm line as a starting point. The thicker lines will have a slightly different phase velocity, making their actual resonant frequencies lower than designed. This effect can be enough to make the 10 and 20 μm center strip resonators swap positions in frequency space. Table 7.7 contains the resonator data.

7.4.1 Frequency Accuracy

Resonators 17 – 22 offer a good test of how accurately we can place resonators in the frequency domain. This is a key factor in determining how many resonators we can multiplex. Figure 7.39 shows a standard deviation from the best fit line of 310 kHz, which matches well the estimate of 250 kHz in Section 3.2. The affect of coupler strength on the expected resonant frequency is not included in this fit.

7.4.2 Quality Factors

We can analyze the quality factor and S21 data in the manner of Section 7.1.2 which yields Figure 7.40. This figure shows that the coupling Q remains the same, while the loss (though to be radiation loss) increases as we go to wider center strips.

Resonator	Design Q	Length (μm)	Strip Width (μm)	Measured Q	Measured f_0 (GHz)
1	5×10^5	5439.04	3	172063	5.539126
2	5×10^5	5420.98	5	163485	5.559916
3	5×10^5	5403.02	10	116501	5.566732
4	5×10^5	5385.19	20	52893	5.564437
5	1×10^6	5367.48	3	325922	5.593139
6	1×10^6	5349.88	5	382592	5.620091
7	1×10^6	5332.40	10	297658	5.634985
8	1×10^6	5315.03	20	212752	5.640208
9	5×10^6	5297.77	3	786800	5.693031
10	5×10^6	5280.63	5	89564	5.713115
11	5×10^6	5263.59	10	-	-
12	5×10^6	5246.67	20	-	-
13	1×10^7	5229.85	3	859439	5.767844
14	1×10^7	5213.14	5	444272	5.781438
15	1×10^7	5196.54	10	428559	5.788201
16	1×10^7	5180.04	20	110648	5.785309
17	5×10^4	5162.65	3	19321	5.900421
18	1×10^5	5147.36	3	40578	5.918658
19	5×10^5	5131.17	3	129098	5.936260
20	1×10^6	5115.09	3	238292	5.955446
21	5×10^6	5099.10	3	367274	5.973263
22	1×10^7	5093.21	3	327008	5.991648

Table 7.7: Measured Q and f_0 of a 320 nm thick aluminum on silicon K0 device from the test mask.

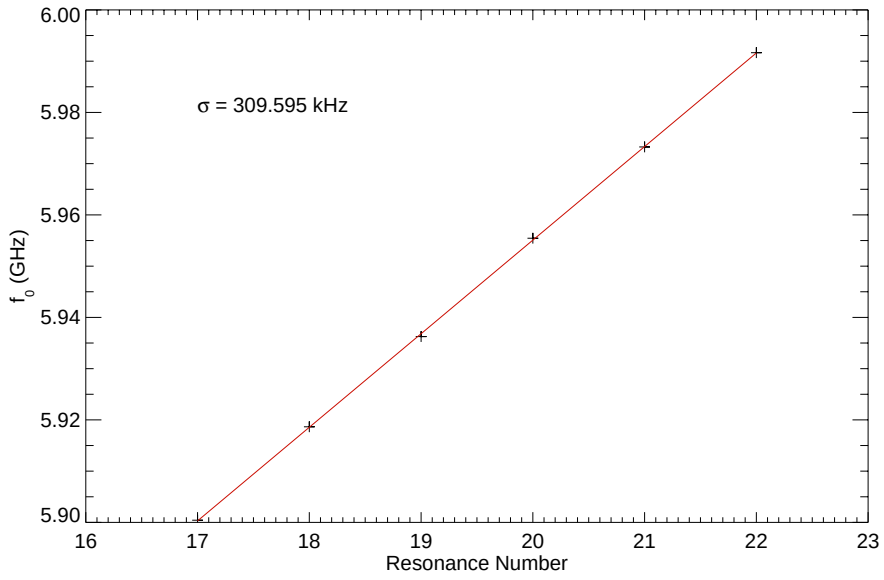

Figure 7.39: A linear fit shows that the mean error in placing a resonator is about 310 kHz.

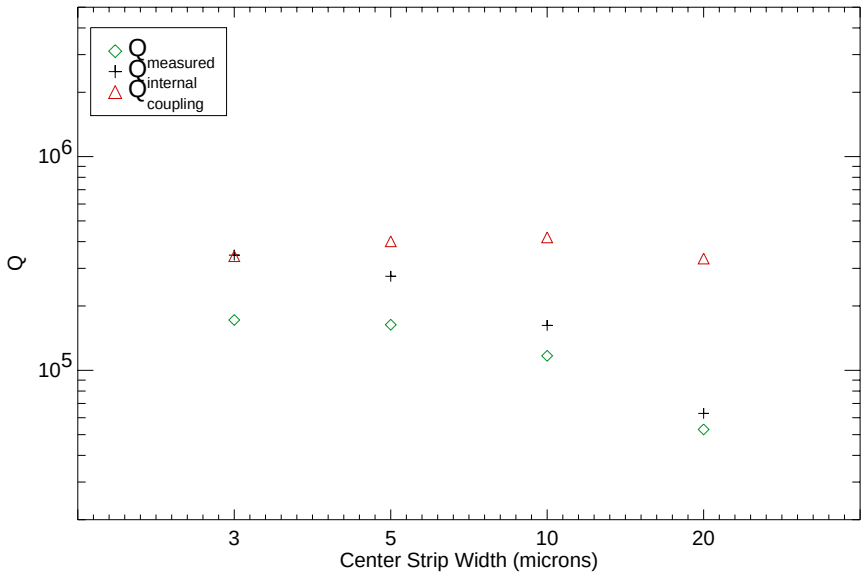

Figure 7.40: The internal quality factors of the first four resonators on the 320 nm thick K0 device. The IQ sweep data for this plot was taken at a power of -86 dBm. The zero point for resonator 4 was corrupted, so the resonance dip was estimated based on the other three data points.

7.4.3 Noise

Following the procedure outlined in Section 7.1.4 we can analyze the noise of the K0 resonators. We will limit ourselves to the resonators with the lowest coupling Qs. This leaves resonators 1,2,3, and 4 from Table 7.7.

7.4.3.1 Frequency Noise

We can perform the same transformation as in Section 7.1.4.1 to derive the frequency noise for these resonators. We plot the frequency noise at -86 dBm in Figure 7.42. This is not a particularly good way to compare the resonators since their different geometries and quality factors result in quite different electromagnetic fields in the substrate, which we have previously shown is a dominant effect in the noise of the 3 μm center strip resonators. We lack power sweep data for this device that might allow us to compare resonators with different strip widths at equivalent fields in the substrate. Future work will attempt to remedy this oversight. At a constant readout power we observe no systematic effects of frequency noise based on the resonator center strip width.

7.4.3.2 NEP

We can analyze the NEP of these resonators to look for any trends as a function of width. The results are shown in Figure 7.43 and Table 7.8. The most interesting thing we find by looking at

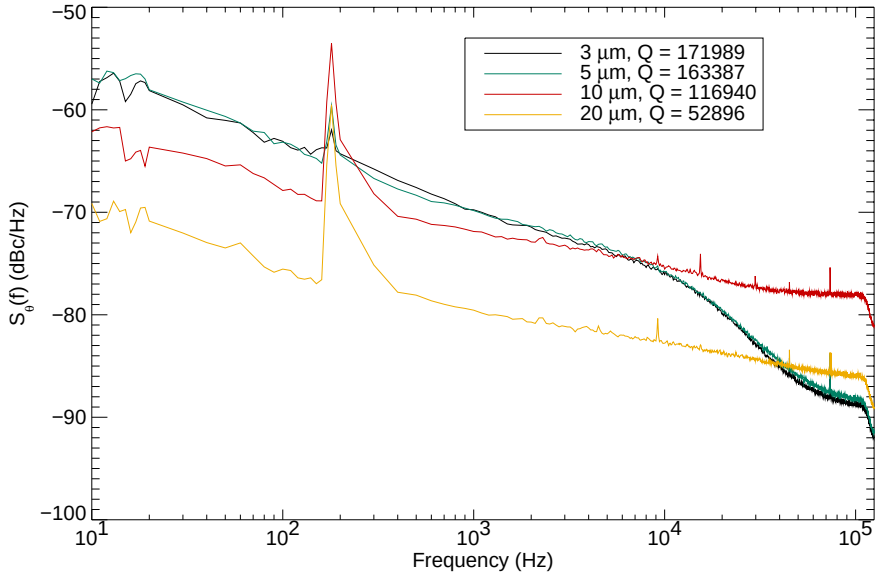

Figure 7.41: The phase noise of resonators 1,2,3, and 4 from the 320 nm thick Al on Si K0 device measured at a constant readout power of -86 dBm.

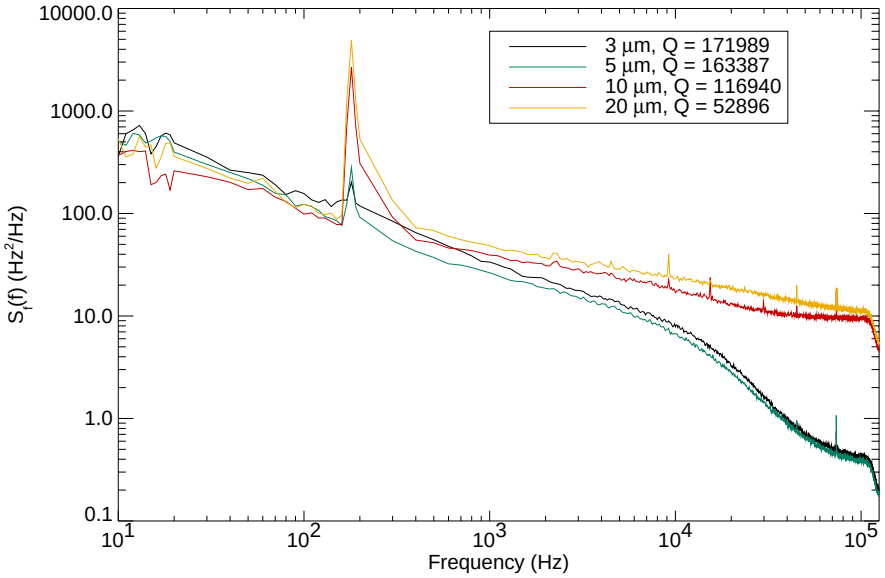

Figure 7.42: The frequency noise of resonators from the 320 nm thick Al on Si K0 device at a readout power of -86 dBm. The frequency noise appears to be independent of the center strip width.

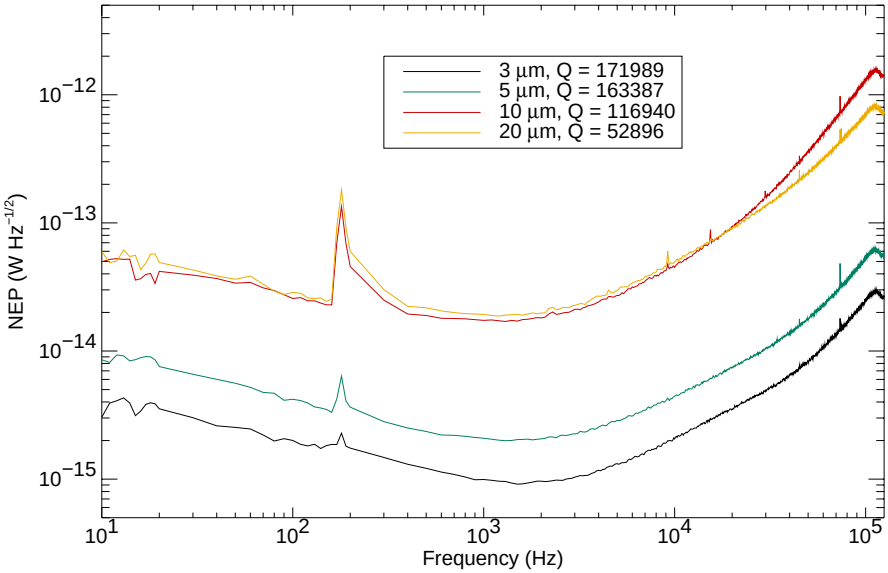

Figure 7.43: The noise equivalent power (NEP) of resonators from the 320 nm thick Al on Si K0 device read out at -86 dBm.

Q	Readout Power (dBm)	$d\theta/dN_{qp}$ (radians/qp)	Saturation Energy (eV)	Saturation Power (W)	minimum NEP (W Hz$^{-1/2}$)	ΔE (eV)
171989	-86	1.7×10^{-7}	1600	1.3×10^{-12}	9.1×10^{-16}	33
163387	-86	7.3×10^{-8}	3600	2.9×10^{-12}	2.0×10^{-15}	71
116940	-86	8.9×10^{-9}	30600	2.5×10^{-11}	1.7×10^{-14}	711
52896	-86	3.4×10^{-9}	78000	6.3×10^{-11}	1.9×10^{-14}	756

Table 7.8: Calculated saturation energies, minimum values of the NEP, and energy resolution for the resonators discussed in this section taken at a readout power of -86 dBm.

this data is that resonators 3 and 4 have nearly identical NEPs despite having volumes that differ by a factor of two. This seems to be happening due to responsivity issues — resonator 3 has twice the Q and 1/2 the volume of resonator 4, so it should have 4 times the responsivity, but from fits to the data the responsivity is only a little more than twice as large as that of resonator 4. More work needs to be done to understand this issue, but for practical purposes it is likely not important as the large center strip devices are of limited usefulness due to their low responsivity and high radiation loss.

Chapter 8

Aluminum on High Purity Sapphire Resonator Measurements

A W0 device made using 205 nm aluminum on sapphire, fabricated by Rick LeDuc at JPL, was cooled down in our fridge on April 15, 2004. The dicing process damaged many of the devices, and the W0 device was the most interesting of the remaining devices.

We have previously tested resonators made of Union Carbide sapphire that is at least 10 years old. This is the first device we have tested made on sapphire left over from the Herschel project. As we will see in this chapter, it yields some very interesting surprises.

The test mask layout W0 was designed with 7 resonators, each with a 3 μm center strip, meandered into a rectangular pattern with ~ 200 μm spacing between meanders. The resonators have a frequency spacing of 20 MHz. The design parameters compared with the measured values can be seen in Table 8.1.

Several data sets were taken on this resonator, including:

- IQ data during the transition from the normal to superconducting state to determine T_c.
- Resonance curves and noise data at 120 mK for various input power levels for all resonators.
- Resonance curves and noise data from 100–320 mK, every 5 mK, for a low and medium power level for all resonators.
- Power sweeps at 120 mK for all resonators.

We will follow the procedures laid out in Section 7.1 for the data analysis.

8.1 Frequency Accuracy

These resonators show good frequency accuracy as shown in Figure 8.1, with a mean spacing of 18.5 MHz and a standard deviation from a straight line of 1.25 MHz.

Resonator	Design Q	Length (μm)	Width (μm)	Q	f_0 (GHz)	S_{21} (dB)
1	5×10^4	8158.58	3	36765	3.866248	-14.1
2	1×10^5	8117.98	3	44452	3.885510	-5.1
3	5×10^5	8077.79	3	72303	3.905354	-1.4
4	1×10^6	8038.00	3	51329	3.924317	-0.6
5	5×10^6	7998.60	3	-	-	-
6	1×10^7	7959.58	3	87420	3.958528	-1.9
7	4.1×10^7	7920.94	3	-	-	-

Table 8.1: Measured Q and f_0 of a 205 nm thick aluminum on sapphire W0 device from the test mask. The readout power used was -90 dBm.

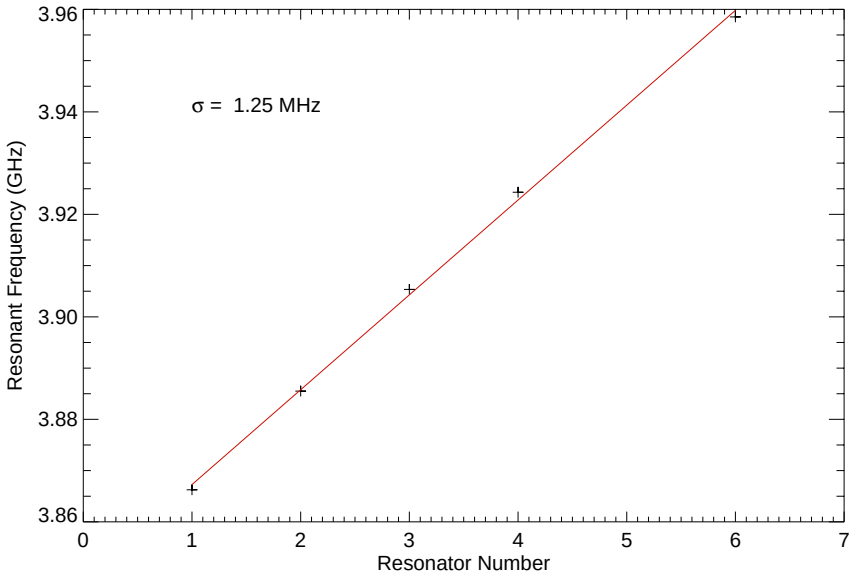

Figure 8.1: The resonant frequencies of the devices from the 205 nm aluminum on sapphire W0 device. The standard deviation of the resonant frequencies from a straight line is 1.25 MHz.

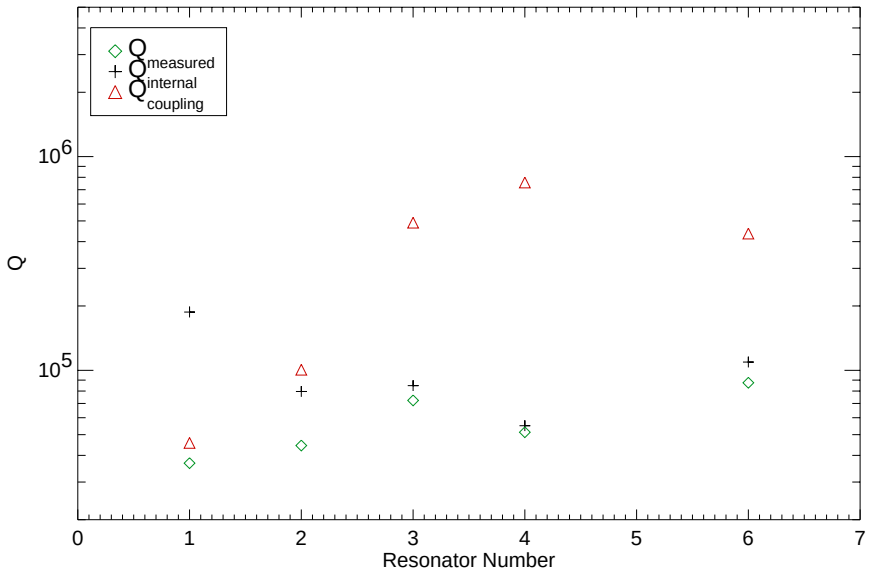

Figure 8.2: The quality factors of the resonators from the 205 nm aluminum on sapphire W0 device.

8.2 Quality Factor

The quality factors of the resonators are shown in Figure 8.2. This plot shows that the internal quality factor of these resonators is much lower than for the thick aluminum on silicon devices ($\sim 1\times10^5$ vs $\sim 1\times10^6$). Since these resonators are 3 μm center strip and are lower frequency than the thick aluminum on silicon devices, their radiation loss should be lower, and the thickness difference is not great enough to make metal loss a dominant term. This leaves several obvious possibilities. The first is that the dielectric is lossy, the second is that the aluminum film is contaminated in some way that increases the loss, and the third is that there are some surface and/or processing problems in the fabrication. The first option seems unlikely since the dielectric has such good noise performance. The second option seems unlikely since the residual resistivity ratio (RRR $\sim$ 10) of the film is good and because the transition temperature of 1.23 K (Section 8.3) seems reasonable. Surface contamination or fabrication issues seems to be the most likely candidate, since the most recent data we have taken of a new device fabricated on the same sapphire substrate shows high internal Q with the same good noise performance.

8.3 Transition Temperature

The superconducting transition temperature of the device is measured by observing the transmission of the feedline as the device is cooled through the superconducting transition temperature. Since these films have a high normal state resistivity, the transmission is low until they become

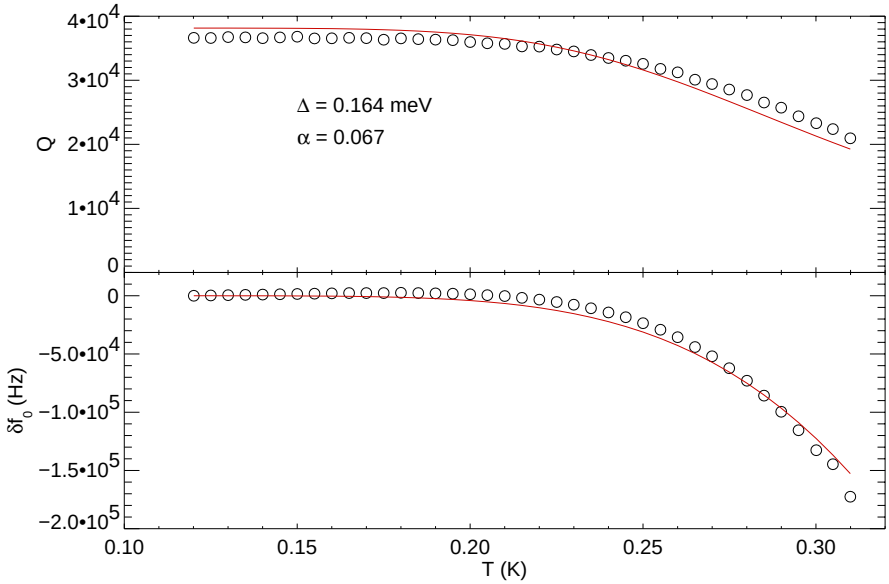

Figure 8.3: Fits to the Q and f_0 data from resonator 2 from the 205 nm Al on Sapphire W0 device using Mattis-Bardeen theory in the extreme anomalous limit.

superconducting. The place where the transmission starts to increase for this film is $T_c = 1.23$ K.

8.4 Derived Material Parameters

Using the fitting equations in Section 6.2 we can fit the resonator Q and f_0 data to determine the superconducting gap Δ. Figure 8.3 shows the fits for resonator 2. We use a value of $\alpha = 0.067$ derived from the numerical simulation. This fit yields $\Delta = 0.164$ meV, and a ratio $\Delta/k_bT_c = 1.55$, which is in good agreement with the values we derive for the thick aluminum on silicon films.

While the value of α is in agreement the fits are not as good as for the 320 nm aluminum on silicon resonators.

8.5 Noise

To take noise data we tune to the resonance frequency of the device then record 10 seconds of IQ data as described in Section 6.3. We then tune off resonance and repeat this procedure. The off resonance noise allows us to understand the readout noise of our system.

In this section we will compare the results of resonator 1 from the W0 mask with resonator 2 from the 320 nm aluminum on silicon devices tested in Section 7.1 since these two resonators have nearly identical quality factors. We only analyze resonator 1 because the low internal Q means the higher Q resonators on this sample do not have deep resonance features.

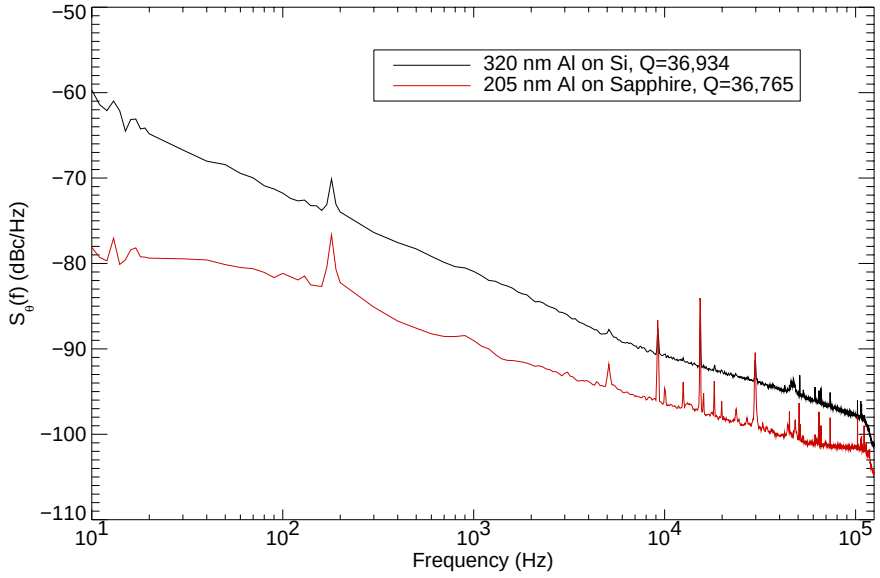

Figure 8.4: A comparison of the phase noise of resonator 2 from the 320 nm Al on Si B0 device and resonator 1 from the 205 nm Al on Sapphire W0 device. Despite having nearly identical quality factors the sapphire device shows significantly lower phase noise. The devices were read out at a power level 4 dB lower than their saturation power.

Figure 8.4 shows that despite having nearly identical quality factors the sapphire device shows significantly lower phase noise and a more shallow slope leading to much better phase noise performance at low frequencies.

8.5.1 Frequency Noise

Figure 8.5 shows that despite having nearly identical quality factors the sapphire device shows significantly lower frequency noise and a more shallow slope leading to much better frequency noise performance at low frequencies. The devices were read out at a power level 4 dB lower than their saturation power. Since we are comparing the frequency noise of two resonators with nearly identical geometries and quality factors on different substrates this is *direct proof of substrate noise*. No other explanation we have considered could produce these results:

1. Since both these devices were tested in the same fridge, at the same temperature, and have nearly identical responsivities any noise source involving quasiparticles should produce the same results regardless of substrate.

2. Trapped magnetic flux should produce similar effects in both devices since they have nearly identical lateral geometries and were both tested inside a magnetic shield, so both should have similar amounts of trapped magnetic flux.

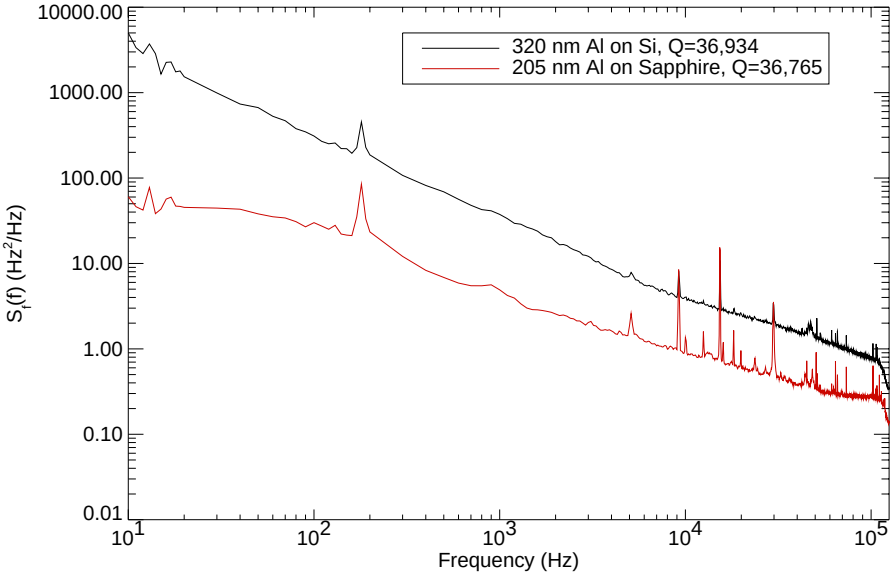

Figure 8.5: A comparison of the frequency noise of resonator 2 from the 320 nm Al on Si B0 device and resonator 1 from the 205 nm Al on Sapphire W0 device. Despite having nearly identical quality factors the sapphire device shows significantly lower frequency noise. The devices were read out at a power level 4 dB lower than their saturation power. *This is direct proof of substrate noise.*

3. Both these resonances were over-coupled with deep resonance features, so the readout noise, especially below 10 kHz, is well below the measured noise.

8.5.2 Noise Power Dependance

Plotting the measured frequency noise as a function of readout power results in Figure 8.6. There are several interesting things about this plot. First, the resonator doesn't saturate until a readout power 12 dB higher than the equivalent Q Al on Si device. This is despite the fact that we have a thinner film, and the size of the effect means that an explanation of the saturation power having to do with the critical magnetic fields in the superconductor is likely wrong. Other possible sources for the reduced saturation power include surface roughness and fabrication effects, or possibly different Kapitza resistances of the aluminum-substrate interfaces.

The second interesting effect is that we observe a very similar response of the shape of the spectrum to higher readout power as we see in the Al on Si devices. As the power is increased, the high frequency noise keeps falling, but the lower frequency noise stops improving at powers well below the saturation readout power.

Another way to look at this is shown in Figure 8.7. In this plot, we have integrated the total phase jitter in different bands (10-100 Hz, 100-1000 Hz, etc.) and plotted the results as a function of power. This plot makes it clear that the higher frequency noise keeps improving as the power is

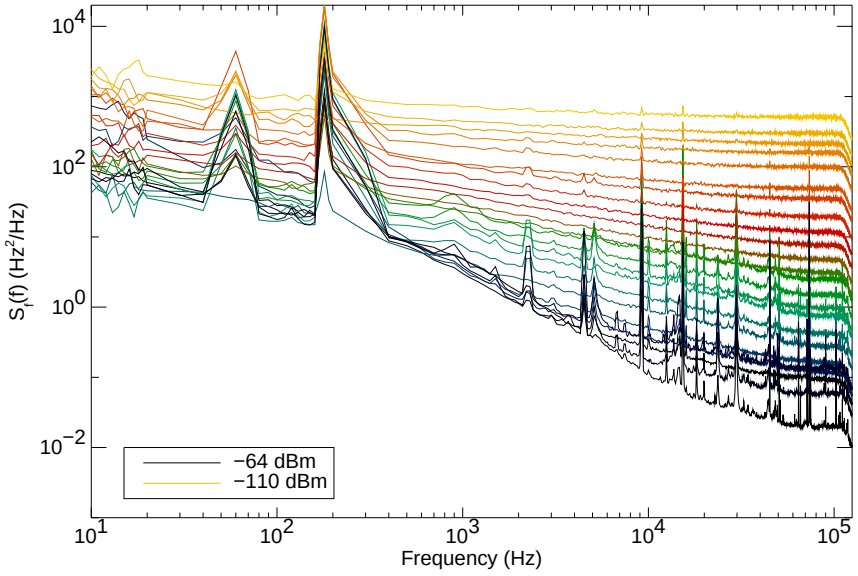

Figure 8.6: The frequency noise of resonator 1 from the 205 nm thick Al on Sapphire W0 device. The readout power ranges from -64 dBm (shown in black) to -110 dBm (shown in yellow) in steps of 2 dBm.

increased, while the lower frequency components stop improving around about 10-20 dB before the saturation readout power. The power law index of improvement in the noise at high frequencies, shown as the blue line in the plot, is -0.44. This is in excellent agreement with the power dependence of the noise in silicon (-0.43, from Section 7.1.4.2), and means that the mechanism that generates the noise in the different substrates is probably related.

8.5.3 Phase Change per Quasiparticle

The phase change per quasiparticle, $d\theta/dN_{qp}$, can be derived by plotting resonance curves made at various temperatures on top of each other as in Figure 8.8. Using the resonance center of the lowest temperature data point, we can calculate the phase angle of a given frequency (usually the resonant frequency of the lowest temperature resonator) as a function of temperature.

By using the material parameters and known geometry we can convert the temperature axis of this plot to the number of quasiparticles in the center strip as shown in Figure 8.9. We derive a value of $d\theta/dN_{qp} = 7.35 \times 10^{-8}$ radians/quasiparticle for this resonator.

8.5.4 Saturation Energy

A simple calculation can be performed using the calculated value of $d\theta/dN_{qp}$ to determine the maximum radiant photon energy that a resonator can accommodate as shown in Equation 7.2. For

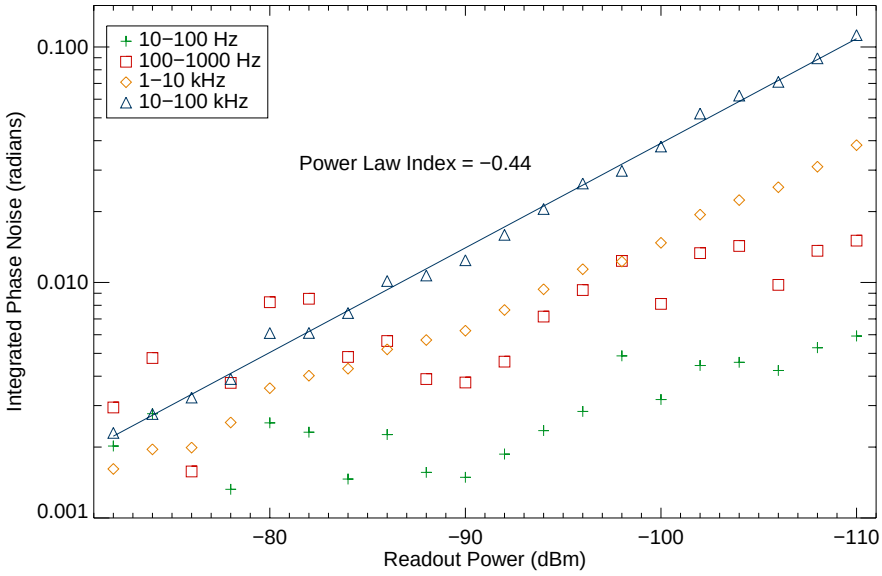

Figure 8.7: The integrated phase noise of resonator 1 from the 205 nm thick Al on Sapphire w0 in several different frequency ranges plotted against readout power. Notice the slope of the power dependance (blue line) is nearly identical to the slope of the silicon data in Section 7.1.4.2.

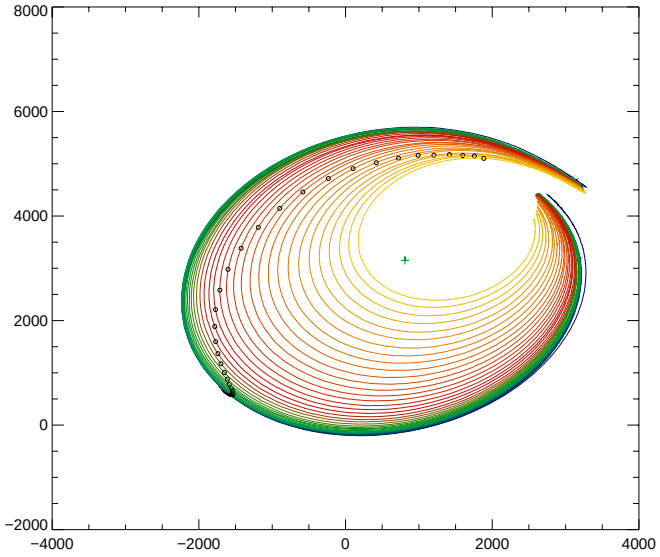

Figure 8.8: The IQ curves of a resonator 1 from the 205 nm thick Al on Sapphire W0 device. Quality factor of this resonator is $Q = 36,000$. The resonance shrinks and shifts frequency as the device is warmed from 120 mK to 320 mK. The green cross is from the fits to the lowest temperature resonance curve. The black circles are points of constant frequency (the resonant frequency of the lowest temperature resonance curve).

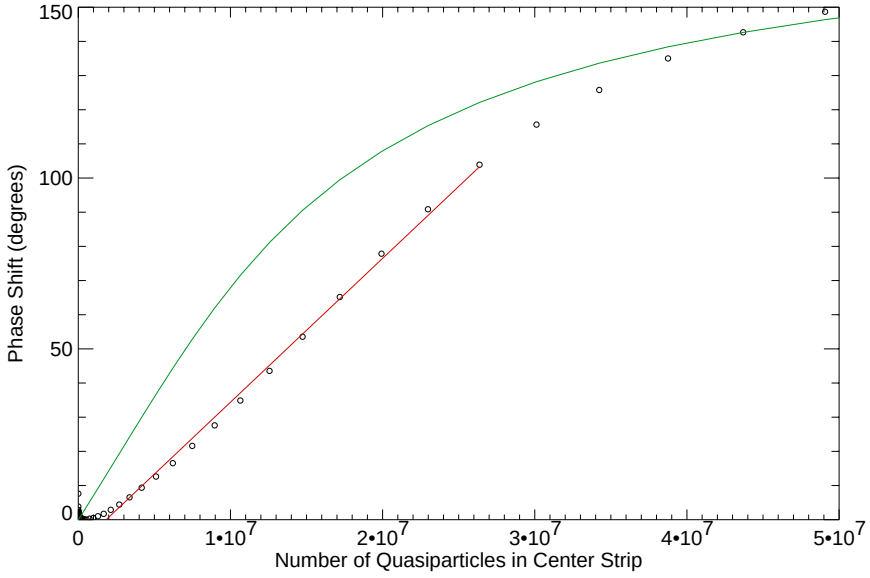

Figure 8.9: The phase shift vs. quasiparticle number at constant frequency of resonator 1 from the 205 nm thick Al on Sapphire wafer. Quality factors of this resonator is $Q = 36,000$. The red line is the fit to the data used to derive $d\theta/dN_{qp}$. The green line is the estimated responsivity from equation 2.60.

resonator 1 the saturation power is 3500 eV.

This is approximately the saturation energy of a single photon event. For a steady state input of energy like in a sub-mm detector, we need to calculate the radiant energy required to create this many quasiparticles using Equation 7.3. The steady state saturation power for resonator 1 with $\tau_{qp} = 200$ μs is 2.8 pW.

8.5.5 NEP

Now that we have calculated $d\theta/dN_{qp}$ we can convert our resonator phase noise $S_\theta(\omega)$ into a noise equivalent power (NEP) and energy resolution following the method of Section 7.1.4.6. The results are shown in Figure 8.10.

The NEP is around 10 times better at 10 Hz and almost three times as good as the aluminum on silicon device at higher frequencies. The calculated energy resolution is 8.0 eV. This is a good comparison, as the longer lengths of the W0 resonators just about cancels out the extra thickness of the B0 resonators, leaving us with almost identical responsivities. This is yet more evidence that the source of the excess noise is the substrate.

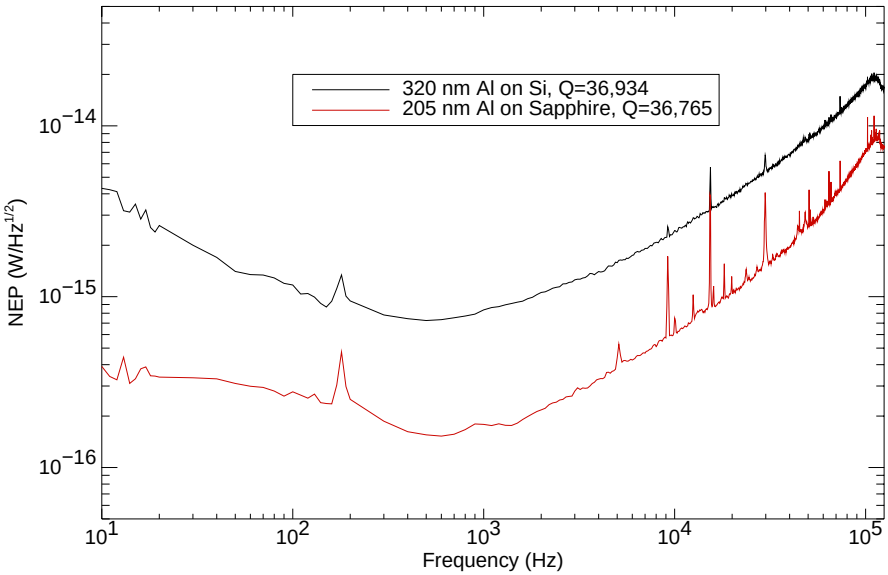

Figure 8.10: The noise equivalent power (NEP) of resonators 1 from the 205 nm thick Al on sapphire W0 device compared with resonator 3 from the 320 nm Al on Si B0 device. The NEPs are calculated for a readout power 4 dB below the saturation value.

Chapter 9

Etched Aluminum on Silicon Resonator Measurements

The previous chapters have clearly shown that the leading candidate for the excess noise is substrate noise. In order to provide a conclusive test and to develop a resonator with better sensitivity we designed a new mask. In this mask a quarter wave transmission line similar to the ones previously tested is etched with a selective etch that removes silicon in areas that are not covered by aluminum or a lithographic stencil. This was accomplished by etching the silicon wafer in a parallel plate etcher using sulphur hexaflouride gas. The etch conditions are tailored to etch silicon with a significant isotropic component such that the silicon substrate is removed both vertically and laterally in exposed regions. This digs trenches in the slots between the CPW lines, causing most of the field lines to be in vacuum instead of dielectric. A cross section of this geometry is shown in Figure 9.1.

The device we test in this chapter, labelled C1, has resonators with a 7 μm center strip and 2 μm gaps. The aluminum is 220 nm thick. It was fabricated on 15 kΩ cm Topsil silicon. The silicon is etched away to leave an overhang of aluminum that extends 2–3 μm into the silicon. The resonators use an elbow coupler as in the previous chapters. In this specific device the coupler was

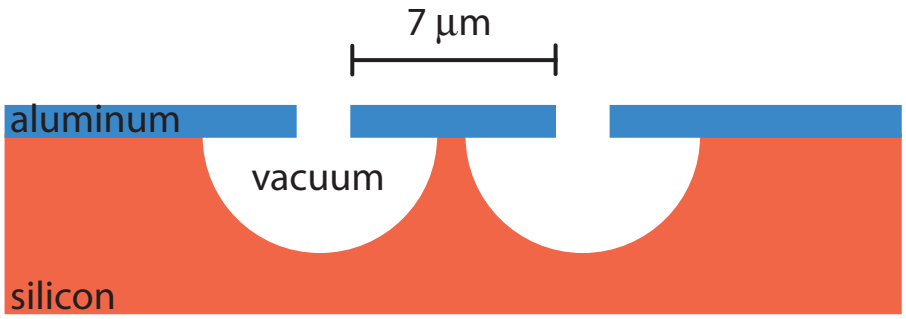

Figure 9.1: A cross section of an etched CPW line made to reduce the fraction of the electromagnetic field in the substrate.

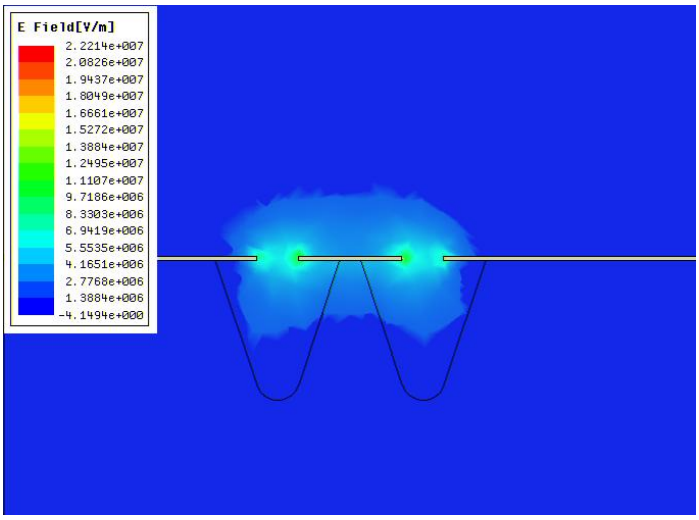

Figure 9.2: Results of a HFSS simulation of an etched CPW resonator with a 5 μm center strip, 2 μm gaps, and an undercut of 2 μm. The field is mainly in vacuum, which reduces the effective dielectric constant and increases the phase velocity of the line.

Resonator	Design Q	Length (μm)	Width (μm)	Q	f_0 (GHz)	S_{21} (dB)
1	2×10^4	9775.5	7	21266	6.937827	-3.3
2	5×10^4	9692.7	7	54193	7.066365	-5.4
3	1×10^5	9611.3	7	126077	7.173029	-1.9
4	2×10^5	9452.4	7	241253	7.249912	-2.1
5	4×10^5	9374.9	7	180154	7.330586	-1.5

Table 9.1: Measured Q and f_0 of a 220 nm thick aluminum on sapphire C1 device from the etch test mask. The readout power used was -74 dBm.

protected during the etch — other versions in the mask set have etched couplers. Simulations were performed with Ansoft's HFSS package to determine the phase velocity of lines etched with these parameters and to determine the required length for a given resonant frequency and the coupler length required for a given Q in a manner similar to Section 3.3.2. A simulations of the fields in an etched CPW device is shown in Figure 9.2.

This device was designed to have a 2 micron undercut, but was slightly over-etched to about a $\sim$ 3 μm undercut, so we expect resonance frequencies slightly higher than predicted. The device was accidently abraded with a silicon slurry during the wafer dicing process. This left the aluminum film looking quite poor visually, but the device displayed the appropriate feedline resistance when warm and resonances when cold so it is likely the damage was cosmetic. Table 9.1 gives a summary of the device parameters and actual measured values.

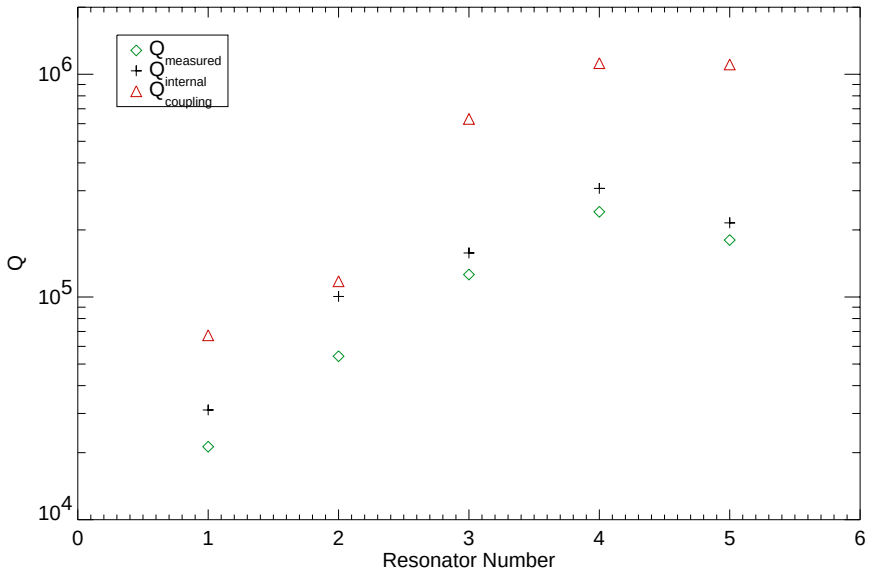

Figure 9.3: The quality factors of the resonators from the etched aluminum on silicon C1 device.

9.1 Effective Dielectric Constant

We expect the improvement in the noise performance of the device to scale with the amount of the electromagnetic field in the substrate. One way to characterize this is by calculating the effective dielectric constant of the transmission line ϵ_{eff}. Our simulations indicate this geometry should have $\epsilon_{eff} \approx 2.3$. Since we know the design length of the resonators l and the resonant frequencies we can solve Equation 3.5 for ϵ_{eff},

$$\epsilon_{eff} = \frac{c^2}{8 f_0^2 l^2} - 1. \tag{9.1}$$

For this device $\epsilon_{eff} = 2.3$. This can be compared to the dielectric constant of an unetched CPW line on silicon, $(1 + \epsilon)/2 \approx 6$.

9.2 Quality Factor

The quality factors of the resonators are shown in Figure 9.3. This plot shows that the internal quality factor of these resonators is much lower than for the thick aluminum on silicon devices ($\sim 1 \times 10^5$ vs $\sim 1 \times 10^6$) and varies quite a bit from resonator to resonator. It is possible the low internal quality factor is due to the damage to the aluminum film from the silicon etch or the dicing process. More tests of etched resonators will be required to tell if this is a real issue.

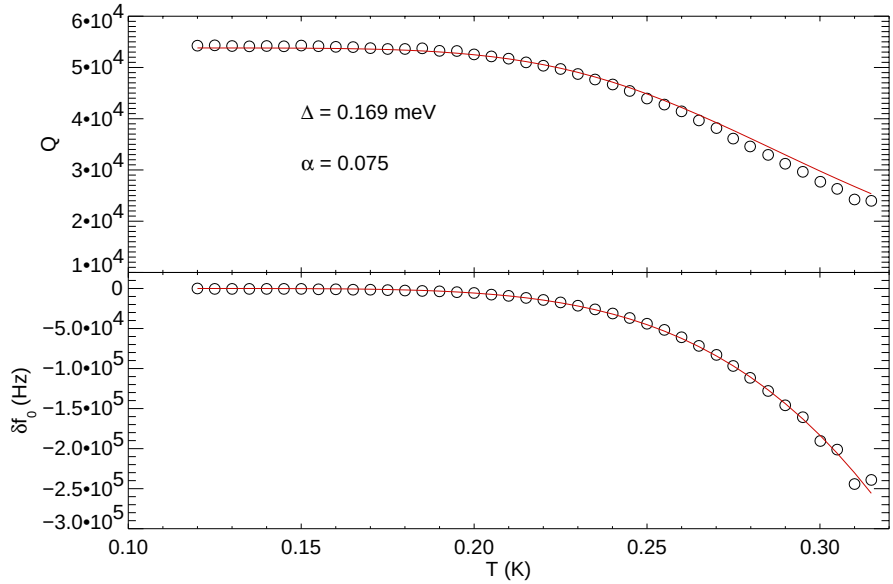

Figure 9.4: Fits to the Q and f_0 data from resonator 2 from the etched C1 device using Mattis-Bardeen theory in the extreme anomalous limit.

9.3 Derived Material Parameters

Using the fitting equations in Section 6.2 we can fit the resonator Q and f_0 data to determine the kinetic inductance fraction α or the gap Δ. Figure 9.4 shows the fits for resonator 2. Since we don't have a good estimate of the α of this device we choose to fix $\Delta = 0.169$ meV, the value we derived for our thick film resonators. This results in a value of $\alpha = 0.075$.

9.4 Noise

To take noise data we tune to the resonance frequency of the device then record 10 seconds of IQ data, as described in Section 6.3. We then tune off resonance and repeat this procedure. The off resonance noise allows us to understand the readout noise of our system. We will not show the data from the lowest Q resonator because the low Q means that its measured spectrum is almost entirely readout noise.

The phase noise performance of the etched resonators are much better than the aluminum on silicon resonators tested in Chapter 7. Figure 9.5 shows the phase noise of the five resonators. There is still an excess phase noise, and we observe that higher Q resonators have more phase noise as we have previously seen.

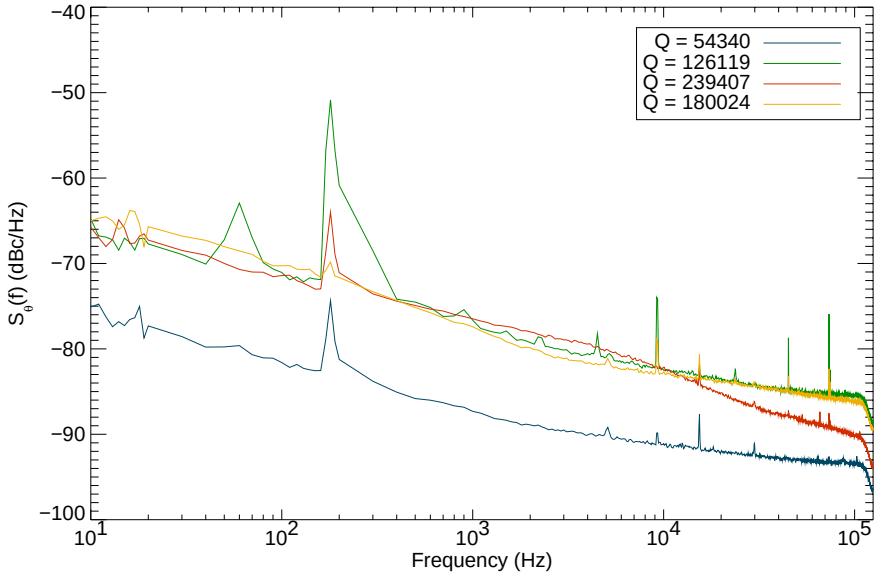

Figure 9.5: A comparison of the phase noise of the resonators from the etched C1 device. The devices were read out at a power level of -74 dBm.

9.4.1 Frequency Noise

We can perform the same transformation as in Section 7.1.4.1 to derive the frequency noise for these resonators. We plot the frequency noise at -74 dBm in Figure 9.6, the same data set scaled by $\sqrt{Q}$ in Figure 9.7, and at a readout power just below the individual resonator's saturation power in Figure 9.8. The lower Q device's noise at high offset frequencies is so low that they become dominated by readout noise.

9.4.2 Noise Power Dependance

Plotting the measured frequency noise as a function of readout power results in Figure 9.9. There are several interesting things about this plot. First, the resonator doesn't saturate until a readout power 6–8 dB higher than the equivalent Q unetched Al on Si device.

The second interesting effect is that we observe a very similar response of the shape of the spectrum to higher readout power as we see in the unetched Al on Si devices. As the power is increased, the high frequency noise keeps falling, but the lower frequency noise stops improving at powers well below the saturation readout power.

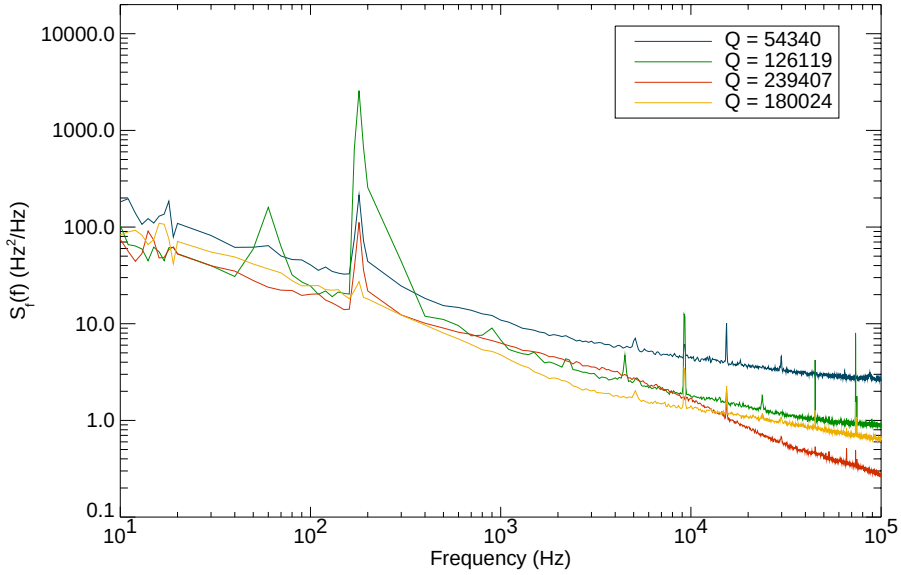

Figure 9.6: A comparison of the frequency noise of resonators from the etched C1 device. The devices were read out at a power level of -74 dBm.

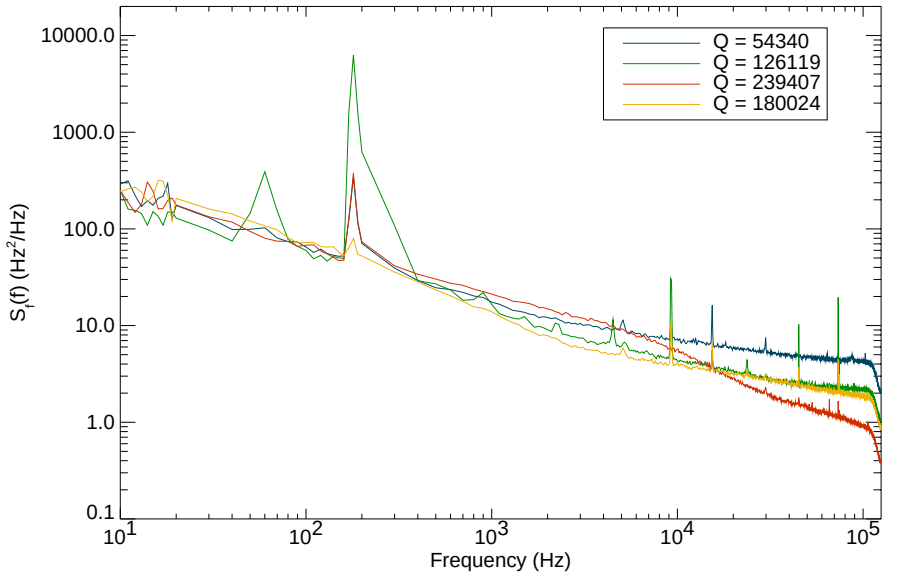

Figure 9.7: A comparison of the frequency noise of resonators from the etched C1 device scaled by the $\sqrt{Q}$, and divided by the $\sqrt{Q}$ of the lowest Q resonator. The devices were read out at a power level of -74 dBm.

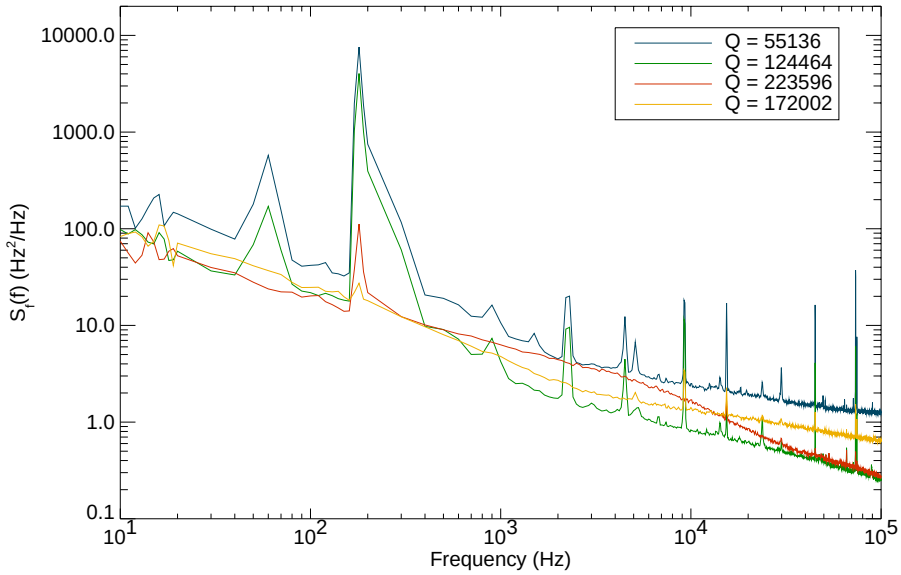

Figure 9.8: A comparison of the frequency noise of resonators from the etched C1 device. The devices were read out at a power level just below their saturation readout power, except for the lowest Q resonators where data collection problems corrupted the highest power data. The power level used for the $Q = 20,004$ resonator is far below its saturation value, which helps explain why it doesn't match the other data.

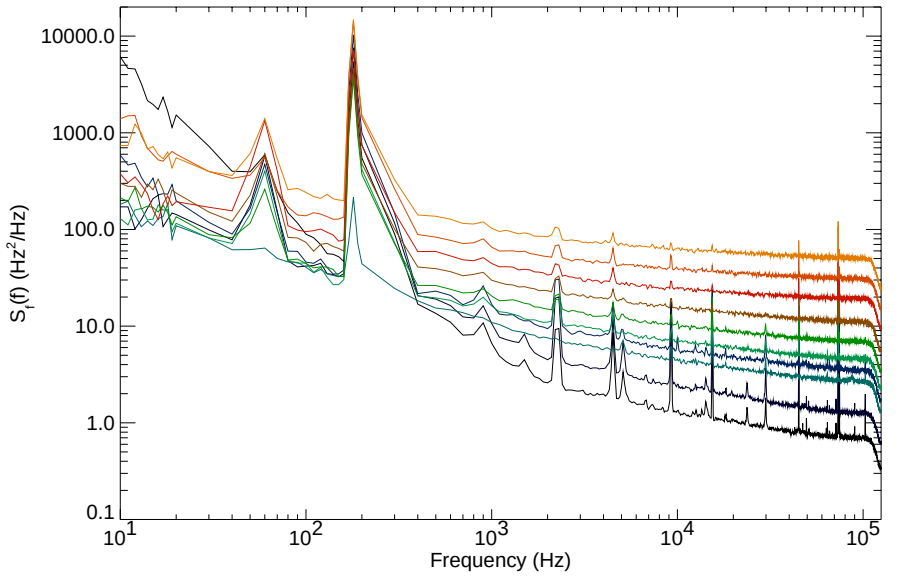

Figure 9.9: The frequency noise of resonator 2 from the etched C1 device. The readout power ranges from -68 dBm (shown in black) to -86 dBm (shown in yellow) in steps of 2 dBm.

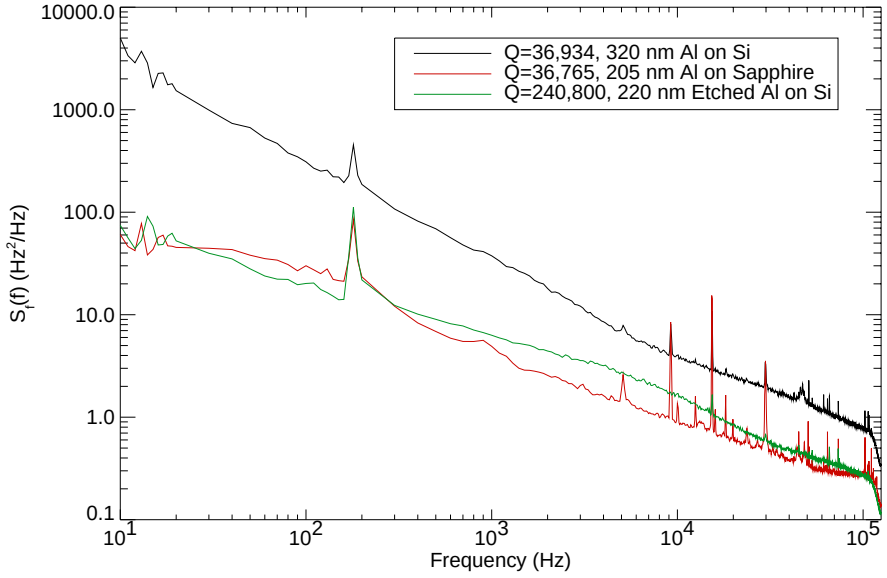

Figure 9.10: The frequency noise of resonator 4 from the etched C1 device compared with unetched Al on Si and Al on sapphire resonators. The devices were read out at a power level slightly lower than their saturation power.

9.4.3 Frequency Noise Comparison

It is very interesting to compare the results of the etched resonators to the previous results from the unetched aluminum on silicon (15 kΩ cm silicon was used for the etched devices vs. 5 kΩ cm silicon for the unetched) and aluminum on sapphire results. Figure 9.10 shows the frequency noise of the etched devices is very similar to the noise of the aluminum on sapphire devices despite the silicon substrate and lower powers the data was taken with. This clearly shows that the excess noise is due to substrate noise, and that we should be able to eliminate this effect by completely removing dielectrics from regions where there are electromagnetic fields.

Since the etched data and the sapphire data were taken at significantly different resonant frequencies it is interesting to divide the frequency noise spectrum by f_0^2 to get the fractional frequency fluctuations. Figure 9.11 shows the fractional frequency fluctuations for various resonators.

9.4.4 Phase Change per Quasiparticle

The phase change per quasiparticle, $d\theta/dN_{qp}$, can be derived by plotting resonance curves made at various temperatures on top of each other as in Figure 9.12. Using the resonance center of the lowest temperature data point, we can calculate the phase angle of a given frequency (usually the resonant frequency of the lowest temperature resonator) as a function of temperature.

By using the material parameters and known geometry we can convert the temperature axis of

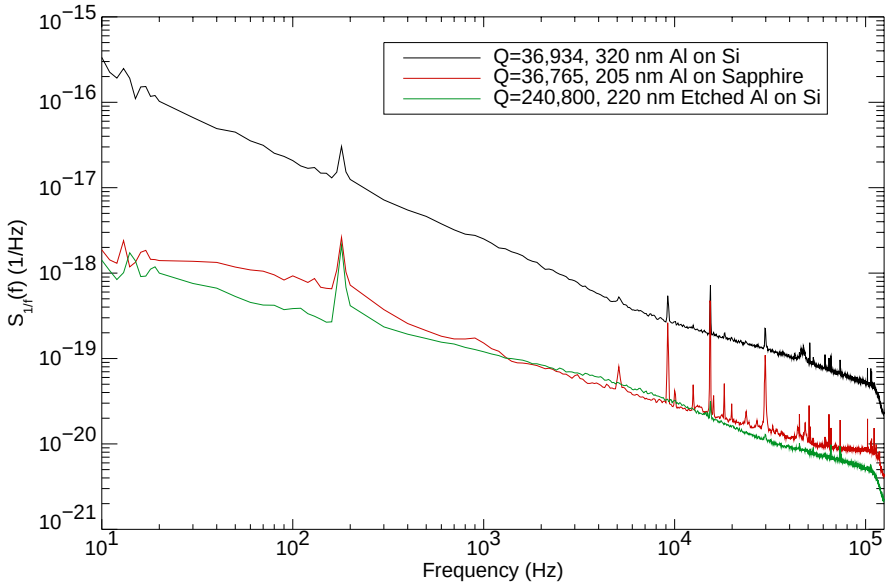

Figure 9.11: The fractional frequency noise of resonator 4 from the etched C1 device compared with unetched Al on Si and Al on sapphire resonators. The devices were read out at a power level slightly lower than their saturation power.

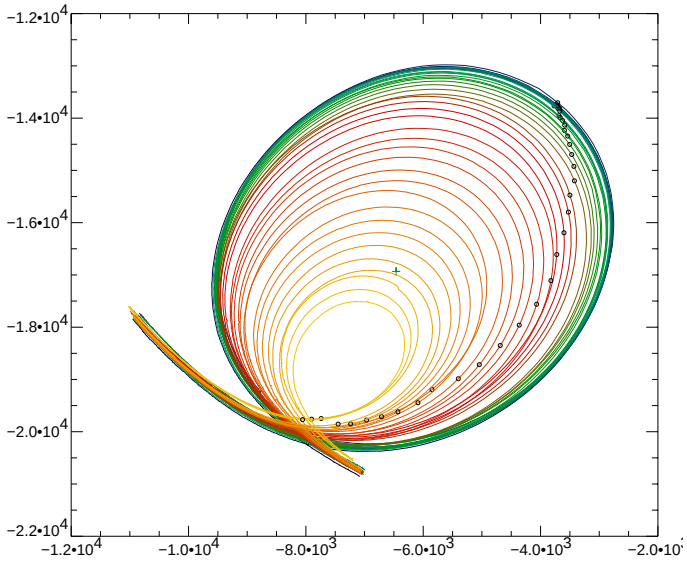

Figure 9.12: The IQ curves of a resonator 2 from the etched C1 device. Quality factors of this resonator is $Q = 54,200$. The resonance shrinks and shifts frequency as the device is warmed from 120 mK to 320 mK. The green cross is from the fits to the lowest temperature resonance curve. The black circles are points of constant frequency (the resonant frequency of the lowest temperature resonance curve).

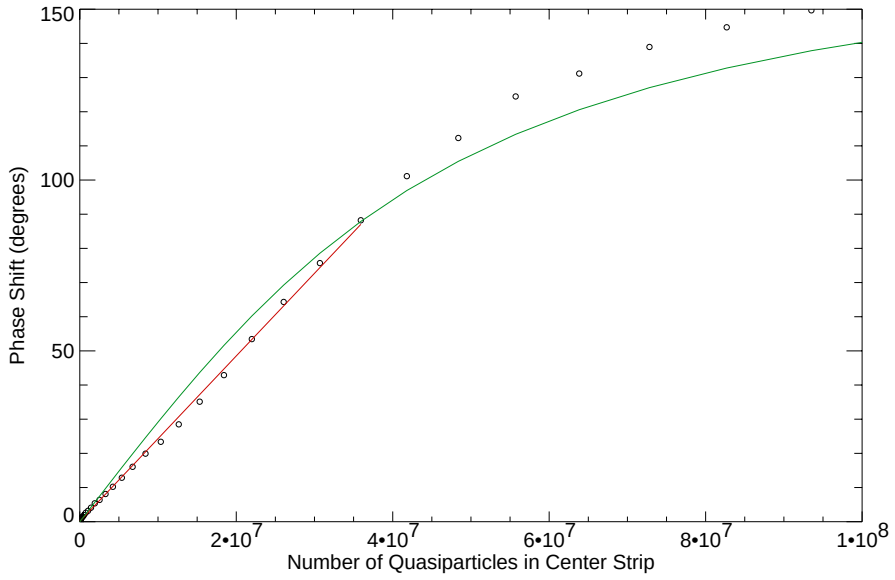

Figure 9.13: The phase shift vs. quasiparticle number at constant frequency of resonator 2 from the etched C1 device. Quality factors of this resonator is $Q = 54,200$. The red line is the fit to the data used to derive $d\theta/dN_{qp}$. The green line is the estimated responsivity from Equation 2.60.

this plot to the number of quasiparticles in the center strip as shown in Figure 9.13. We derive a value of $d\theta/dN_{qp} = 4.2 \times 10^{-8}$ radians/quasiparticle for resonator 2 and $d\theta/dN_{qp} = 1.8 \times 10^{-7}$ for resonator 4.

9.4.5 Saturation Energy

A simple calculation can be performed using the calculated value of $d\theta/dN_{qp}$ to determine the maximum radiant photon energy that a resonator can accommodate using Equation 7.2. For resonator 2 the saturation power is 6300 eV.

This is approximately the saturation energy of a single photon event. For a steady state input of energy like in a sub-mm detector, we need to calculate the radiant energy required to create this many quasiparticles using Equation 7.3. The steady state saturation power for resonator 1 with $\tau_{qp} = 200$ μs is approximately 5.0 pW.

9.4.6 NEP

Now that we have calculated $d\theta/dN_{qp}$ we can convert our resonator phase noise $S_\theta(\omega)$ into a noise equivalent power (NEP) and energy resolution following the method of Section 7.1.4.6. The results are shown in Figure 9.14. The NEP of the etched devices is about four times better than the thick aluminum on silicon devices at low offset frequencies, despite a volume that is around three times

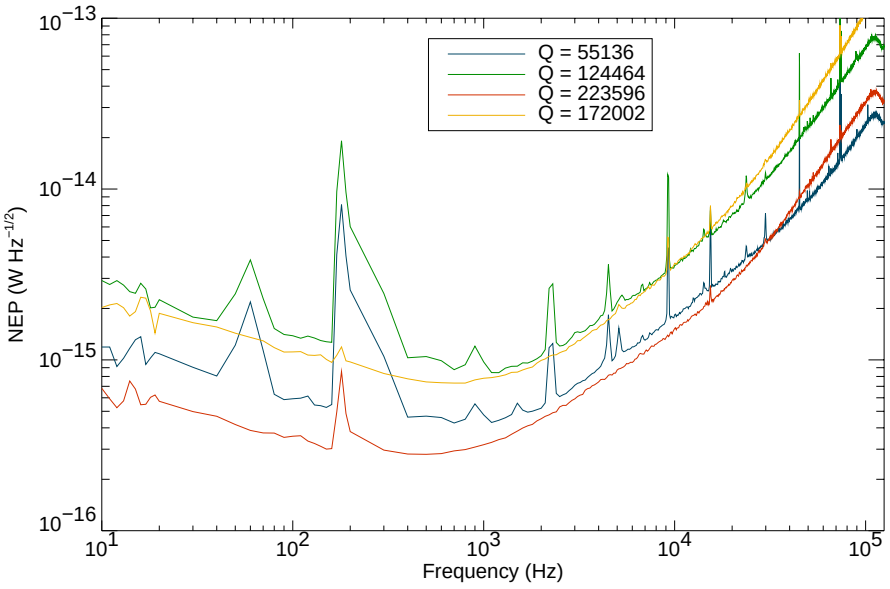

Figure 9.14: The noise equivalent power (NEP) of resonators from the etched C1 device. The NEPs are calculated for a readout power 2 dB below the saturation value.

larger. The calculated energy resolution for resonator 1 is 23 eV and 17 eV for resonator 4. It should be possible to make a very nice ground-based submillimeter detector with this performance, and simulations of other devices from this mask lead us to expect further reductions in the substrate noise using different etched CPW geometries.

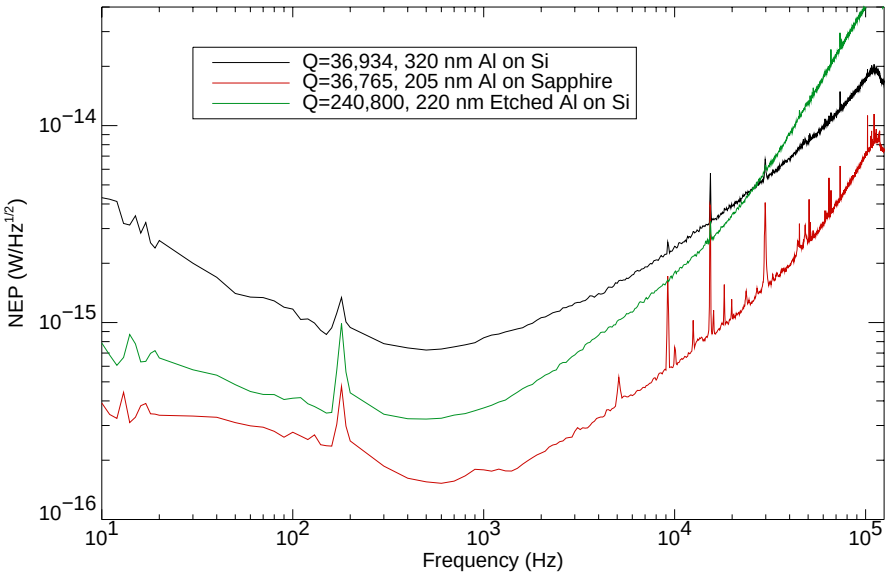

Figure 9.15: The noise equivalent power (NEP) of resonator 4 from the etched C1 device compared with unetched Al on Si and Al on sapphire resonators. The NEPs are calculated for a readout power 2 dB below the saturation value.

Chapter 10

Optical/UV/X-ray Prototype Arrays using Aluminum on Sapphire

A device from the optical/UV/X-ray array mask described in Section 3.7 was tested. The naming scheme used for these devices is:

S(center strip width in μm).(pixel size in μm)(T,H,B)-(Resonator 0 f_0 in GHz).(Resonator spacing in MHz)-(Design Q)-(Strip length in pixels)x(Number of strips).

In this scheme, T designates devices with no protect layer over the tantalum to protect it from the aluminum etch, H designated devices with a thin trapping bar and a SiO protect layer, and B designates devices with a large trapping bar and a SiO protect layer (Section 3.3.5).

This device, designated S3.50T-6.20-1Q6-32x32, has 3 μm center strips, 50 μm wide absorbers, a start frequency of 6 GHz, 20 MHz resonator spacing, a design Q of 1×10^6, and 32 1.6 mm long strips for a total of 64 resonators and 1024 virtual pixels if the energy resolution proves sufficient.

This wafer was fabricated with 220 nm thick Aluminum resonators and 200 nm thick epitaxial Tantalum absorbers on Union Carbide sapphire substrate. There are known issues with the aluminum resonator climbing up on to the tantalum absorber that can cause step coverage problems at the shorted end of the resonator. Despite this problem, this device has at least 52 of the 64 resonators working properly.

10.1 Resonator Parameters

The 52 resonators we detect can be identified by carefully considering their resonance frequency and the order in which they were detected. Figure 10.1 shows that we can identify the resonators well, but that there is some discrepancy between the left and right sides of the array — the right side has a slightly higher (by about 10 MHz) resonant frequency than expected. This does not cause any problems in actual use, but we must understand it before we go to smaller frequency spacing

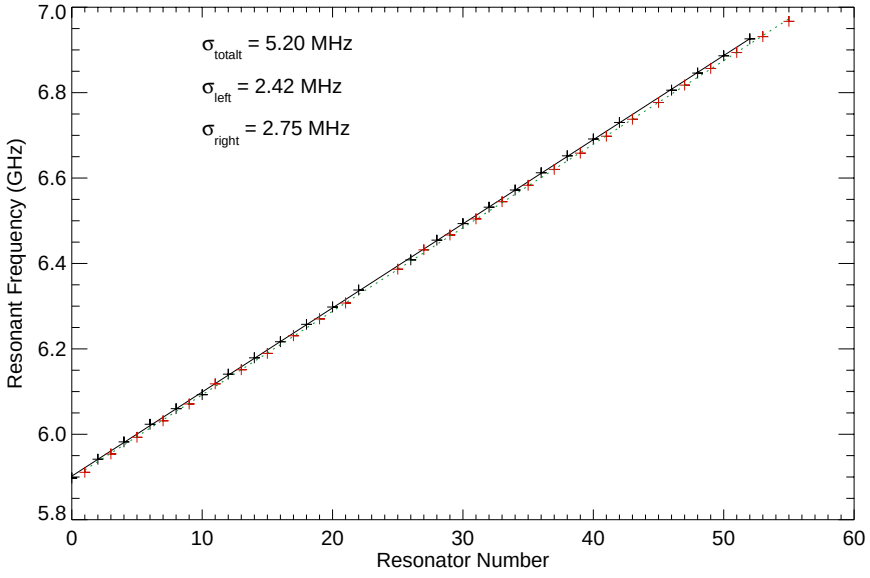

Figure 10.1: The measured resonance frequency of the S3.50T-6.20-1Q6-32x32 device. The devices on the left side of the device are in black, and the devices on the right side are in red. The total standard deviation of all the points from the best fit line is 5.2 MHz, but if you consider the left and right side of the device independently the agreement with the expected values is much better.

between resonators.

We can now assemble a map of the resonator to determine which strips can function as strip detectors. On this particular device 24 strips have functional resonators on both ends (Figure 10.2).

10.2 Noise

As in Section 7.1.4 we can analyze the phase and frequency noise performance of the resonators on the test mask. In this section we will compare the resonator at 6.4934 GHz with Q=148,774 from the optical array mask to resonator 2 from the 320 nm Al on the Silicon B0 device (Q=167,797) and resonator 1 from the 205 nm Al on Sapphire W0 device.

The noise shown in Figure 10.3 and 10.4 indicates that the Union Carbide sapphire used in this mask shows a noise level intermediate between the silicon and the high purity sapphire masks.

10.2.1 Phase Change per Quasiparticle

The phase change per quasiparticle, $d\theta/dN_{qp}$, can be derived by plotting resonance curves made at various temperatures on top of each other as shown in Figure 10.5. Using the resonance center of the lowest temperature data point, we can calculate the phase angle of a given frequency (usually the resonant frequency of the lowest temperature resonator) as a function of temperature.

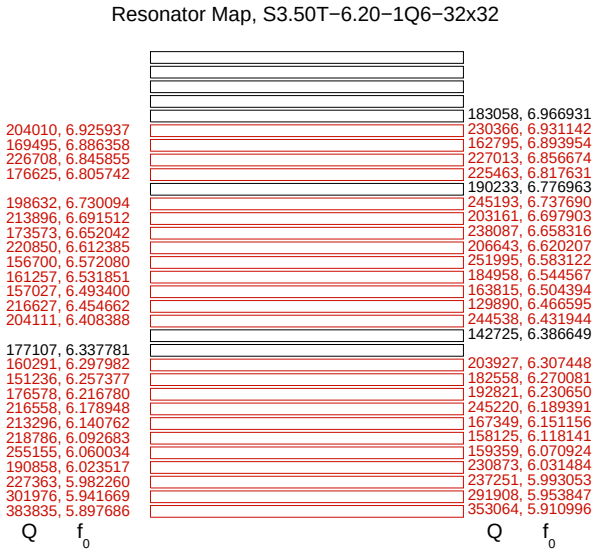

Figure 10.2: The measured Q and resonance frequency of the S3.50T-6.20-1Q6-32x32 device. Strips shown in red have active resonators on both sides.

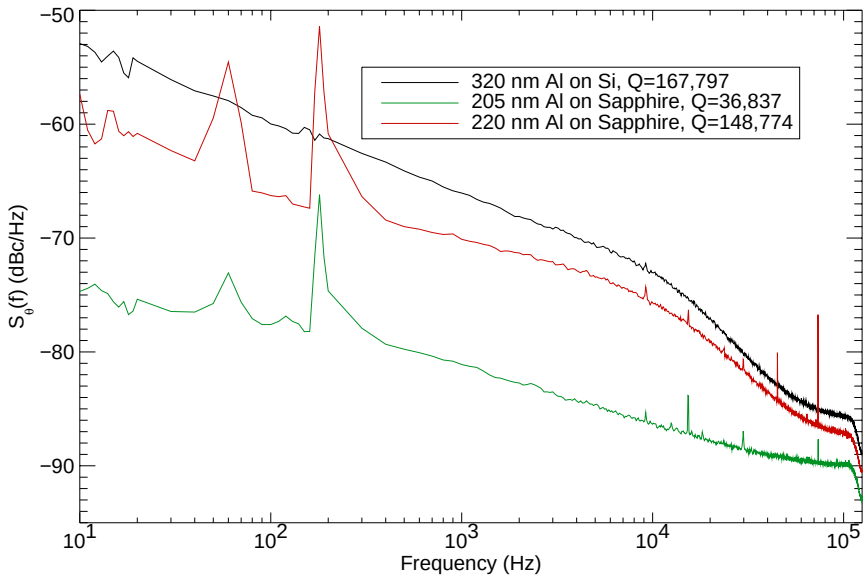

Figure 10.3: A comparison of the phase noise of the resonator at 6.4934 GHz with Q=148,774 from the optical array mask to resonator 2 from the 320 nm Al on the Silicon B0 device (Q=167,797) and resonator 1 from the 205 nm Al on Sapphire W0 device at a constant readout power of -88 dBm.

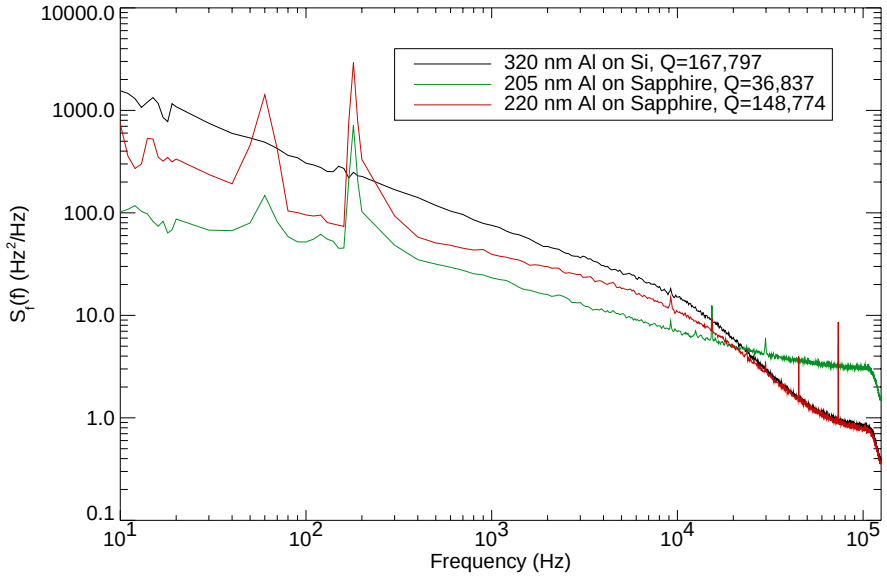

Figure 10.4: A comparison of the frequency noise of the resonator at 6.4934 GHz with Q=148,774 from the optical array mask to resonator 1 from the 320 nm Al on the Silicon B0 device (Q=167,797) and resonator 1 from the 205 nm Al on Sapphire W0 device at a constant readout power of -88 dBm.

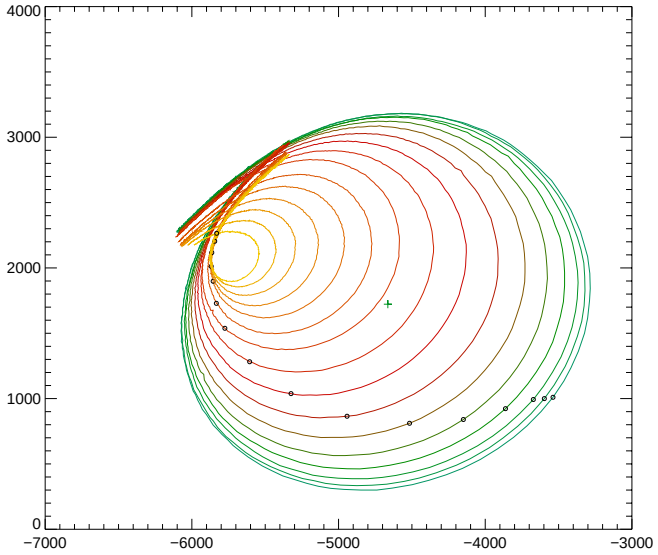

Figure 10.5: The IQ curves of the resonator at 6.4934 GHz from the 220 nm thick Al on Sapphire optical array device. The quality factor of this resonator is Q=148,774. The resonance shrinks and shifts frequency as the device is warmed from 160 mK to 320 mK. The green cross is from the fits to the lowest temperature resonance curve. The black circles are points of constant frequency (the resonant frequency of the lowest temperature resonance curve).

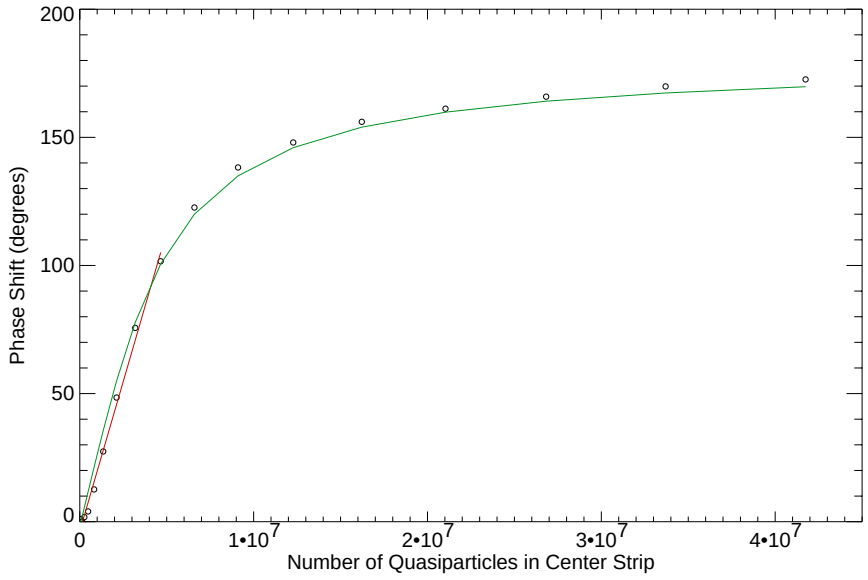

Figure 10.6: The phase shift vs. quasiparticle number at constant frequency of the resonator at 6.4934 GHz from the 220 nm thick Al on Sapphire optical mask device. Quality factors of this resonator is Q=148,774. The red line is the fit to the data used to derive $d\theta/dN_{qp}$. The green line is the estimated responsivity from equation 2.60.

We do not have a transition temperature for this device, but using the calculated $\alpha = 0.062$ we can adjust Δ to get a good match to the responsivity shown in Figure 10.6. We find that $\Delta = 0.170$ matches the data well. We derive a value of $d\theta/dN_{qp} = 4.1 \times 10^{-7}$ radians/quasiparticle for this resonator.

A simple calculation can be performed using the calculated value of $d\theta/dN_{qp}$ to determine the maximum radiant photon energy, which gives 650 eV. This is approximately the saturation energy of a single photon event. This corresponds to a steady state saturation power with $\tau_{qp} = 200$ μs of 0.52 pW.

10.2.2 Noise Equivalent Power

The noise equivalent power of the optical array resonator device is a little lower than the equivalent device from the test mask. For this analysis $\Delta = 0.170$ meV and $\tau_{qp} = 200$ μs. The minimum value of the NEP is 2.2×10^{-16} W Hz$^{-1/2}$ and the expected energy resolution is 13 eV.

10.3 X-ray Detection

The device was illuminated by a specially designed X-ray florescence source. This consists of a 50 mCurie iron-55 source that illuminates a piece of NIST K3760 glass [64] at a 45 degree angle. This

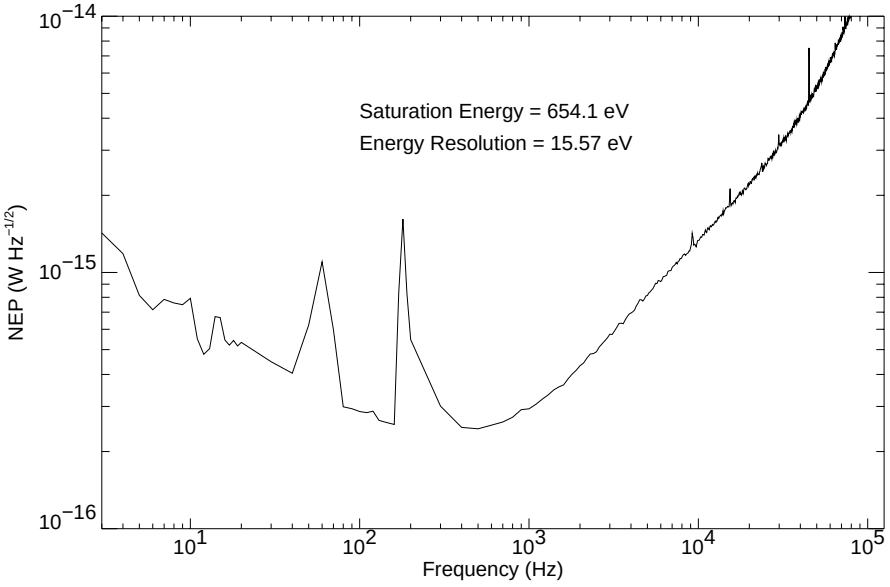

Figure 10.7: The NEP of the resonator at 6.4934 GHz at a readout power of -88 dBm.

produces X-ray fluorescence lines between 500 and 2000 eV. The X-rays are sent through a small hole which acts as a collimator before they illuminate the surface of the device.

Unfortunately, there is a problem with the connection of the aluminum and tantalum films. This is likely the result of either the step coverage problems described previously, or the lack of a clean interface between the metals. This means that we do not see coincident pulses on the resonators on either end of a strip, but we do see coincident pulses from adjacent resonators when X-rays are absorbed in the aluminum ground planes between the adjacent resonators.

Figure 10.8 shows a single X-ray pulse recorded from a $Q = 168470$ resonator. It is not possible to convert this into the energy of the photon since events in the aluminum suffer from the position dependent response described in Section 2.6. The quasiparticle recombination time $\tau_{qp} = 264.5$ μs is measured by fitting an exponential to the tail of the pulse, and should be considered a lower limit since diffusion away from the resonator may limit the lifetime.

Since the noise excess we see is purely in the phase direction it is possible to just measure the change in amplitude to determine the deposited energy. This could potentially be a powerful technique since the amplitude noise is expected to be dominated by HEMT noise, and there can be a significant change in the transmitted magnitude during a photon event. For this data set we find that the amplitude pulses have a significantly lower signal to noise than the phase pulses, but it is possible a better HEMT could change this situation. Eventually a pulse extraction technique that uses all the available IQ data and noise covariance matrix will be needed to extract the maximum amount of information from a pulse.

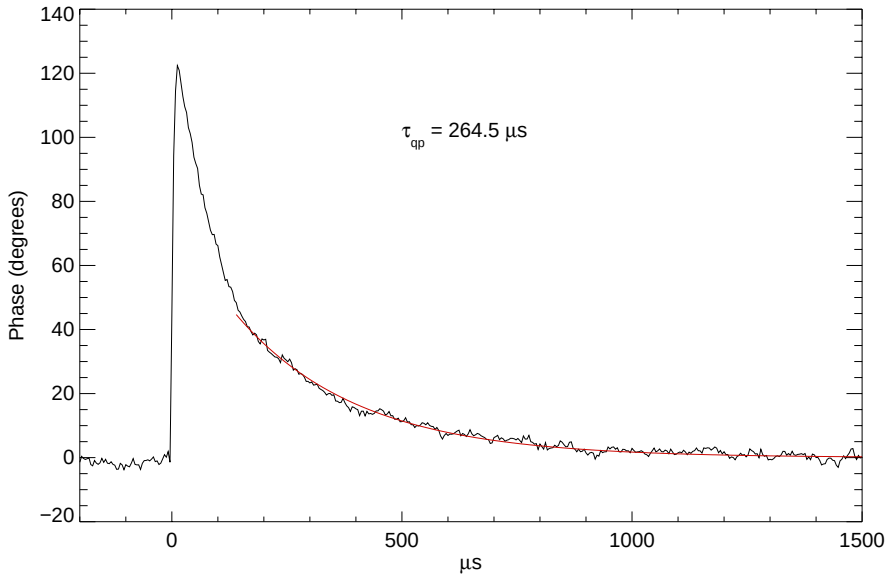

Figure 10.8: A X-ray from our fluorescence source causes a phase change in the resonator. The red line is a fit to the exponential tail of the pulse, which gives a lower limit on the quasiparticle lifetime, $\tau_{qp} = 264.5$ μs.

Chapter 11

Conclusions

In order to understand the noise performance of a MKID we must observe how the noise changes as we vary resonator parameters. The possible parameters that can be varied on a CPW resonator are:

- **Resonator Material**. The superconductor used to make the resonator. All resonators discussed in this thesis are made of aluminum.
- **Resonator Thickness**. The thickness of the superconducting resonator. Thinner devices have lower volume and higher kinetic inductance fractions leading to higher responsivities.
- **Substrate**. The substrate material affects the dielectric loss, noise, and phase velocity of the resonator. Substrates with lower concentrations of impurities or different types of impurities may reduce the excess noise. This is an important area for further research.
- **CPW Geometry**. The width of the center strip of the resonator controls the volume and the radiation loss of the resonator.
- **Meandering**. More compact resonator layouts have slightly higher internal Q.
- **Coupling Q**. Device quality factors and the size of the resonance can be changed by changing the strength of the coupling.
- **Resonant Frequency**. The resonant frequency of the device is determined by its length and the substrate dielectric constant. Higher frequency resonators have smaller volumes.
- **Readout Power**. The maximum readout power is a function of Q and thickness of the superconducting film used in the resonator. We observe lower phase noise as we go to higher powers.
- **Fields in the Substrate**. The strength of the fields of the quasi-TEM mode that propagates down the transmission line in the substrate can affect the noise of the resonator.

We have changed many of these parameters, and the basic result we see is that there is a phase noise excess that scales with Q, so that the frequency noise of devices on the same substrate with different Q is nearly identical for the same stored energy, regardless of film thickness and responsivity. While the magnitude of the noise changes with substrate, the power dependence of the noise seems to behave the same on different substrates.

We have considered many different possible noise sources, including trapped magnetic flux, pair breaking radiation from the 4K stage coming down the coax, and synthesizer frequency or power fluctuations. We believe we have eliminated all of these through careful shielding and testing to ensure that the effects we see are due to the resonators and not the outside world.

The evidence conclusively points to the substrate as the source of the noise. The noise is consistent with a substrate noise rolled off by the resonator bandwidth. Measurements of resonators with different thicknesses, with responsivities that are different by a factor of 100, that show similar frequency noise at the same readout power, leaves substrate noise as the most likely source of the excess noise. The observation that changing substrates improves the frequency noise is more proof that the substrate is the source of the excess noise. The final piece of evidence is that etching the substrate away causes the noise excess to drop dramatically.

Substrate noise is a fundamental problem but should be amenable to reduction through careful engineering. We expect further improvements using etched CPW geometries that remove more of the substrate from areas near electromagnetic field concentrations. We can also experiment with other geometries, like suspended microstrips and CPW lines, that should completely replace the noisy dielectrics with vacuum near the transmission lines. Experiments with high purity substrates like sapphire and germanium may also lead to more sensitive detectors. Using these techniques we expect to be able to drastically reduce the remaining substrate noise.

MKIDs should now be considered one of the leading technologies to reach the ambitious goals laid out by the scientific community for future ground and space missions. This thesis, in combination with our previous work, demonstrates that every important aspect of a kinetic inductance detector works: photon response, sensitive detection, and frequency domain multiplexing. We have developed array devices with many resonators, and read out sections of these arrays successfully. Our devices scale to large arrays very well, and we expect to soon surpass the pixel count of conventional superconducting technologies. We hope to begin work soon on the electronics required to read out these large arrays. The sensitivity of MKIDs is already good enough to be useful in ground based submillimeter astronomy, and we expect further improvements as our program to reduce the substrate noise matures. An optical camera for Palomar and a submillimeter camera for CSO are a logical next step. This technology will enable many thousand pixel arrays in the astronomical wavelengths of interest on timescales of years, not decades.

There are several areas where we still do not understand MKIDs.

1. We do not understand the physical mechanism of the noise. While the noise seems to originate in the substrate, we do not understand the actual mechanism that generates the noise.

2. The internal Q of the resonators varies between fabrications runs on the same substrate, and we do not understand the parameters that control the internal quality factor.

3. The saturation power of the 205 nm thick aluminum on sapphire resonators was about 12 dB higher than the saturation power of the 320 nm thick aluminum on silicon resonators, despite nearly identical CPW geometries. A model based on the critical magnetic field of the CPW line cannot explain this behavior.

These outstanding issues do not present substantial obstacles to using MKIDs as detectors. Understanding them may give us more insight into the basic physics of MKIDs and give us leverage in designing better detectors. We are currently working to understand all of these issues.

MKIDs are a joy to work with, and do not exhibit the kinds of annoying behavior common with other superconducting technologies, like trapped flux, or non-uniform magnetic biasing in junctions, or the complexity of SQUID based multiplexers for TESs. MKIDs are stable, predictable, and simple devices. They will be a vital part of our efforts to understand the universe in the years to come.

Bibliography

[1] S. Moseley, J. Mather, and D. McCammon, "Thermal detectors as X–ray spectrometers," *J. Appl. Phys.*, vol. 56, no. 5, pp. 1257–1262, 1984.

[2] W. S. Holland, C. R. Cunningham, W. K. Gear, T. Jeness, K. Laidlaw, J. F. Lightfoot, and E. I. Robson, "SCUBA: a submillimeter camera operating on the James Clerk Maxwell Telescope," in *Advanced Technology MMW, Radio, and Terahertz Telescopes* (T. G. Phillips, ed.), vol. 3357, pp. 305–318, 1998.

[3] J. Glenn, J. Bock, G. Chattopadhyay, S. F. Edgington, A. E. Lange, J. Zmuidzinas, P. D. Mauskopf, B. Rownd, and L. Yuen, "BOLOCAM: a millimeter–wave bolometric camera," *Proc. SPIE*, vol. 3357, pp. 326–334, 1998.

[4] J. Cottam, K. Boyce, G. Brown, E. Figueroa-Feliciano, R. Kelley, V. Ponce, F. Porter, C. Stahle, and W. Tillotson, "Characterization of the Astro–E2 X-ray spectrometer," *Proceedings of LTD-10*, vol. 520, pp. 368–371, 2004.

[5] C. Enss, "Magnetic sensors for X-ray and gamma-ray detection," in *Low Temperature Detectors* (F. Porter, D. McCammon, M. Galeazzi, and C. Stahle, eds.), vol. 605 of *AIP Conference Proceedings*, pp. 5–10, 2002.

[6] K. Irwin, G. Hilton, D. Wollman, and J. Martinis, "X–ray detection using a superconducting transition–edge sensor microcalorimeter with electrothermal feedback," *Appl. Phys. Lett.*, vol. 69, no. 13, pp. 1945–1947, 1996.

[7] M.D. Audley *et al.*, "SCUBA-2: A large-format TES array for submillimetre astronomy," *Proceedings of LTD-10*, vol. 520, pp. 479–482, 2004.

[8] B. Cabrera, R. Clarke, P. Colling, A. Miller, S. Nam, and R. Romani, "Detection of single infrared, optical, and ultraviolet photons using superconducting transition edge sensors," *Appl. Phys. Lett.*, vol. 73, no. 6, pp. 735–737, 1998.

[9] K. Irwin, G. Hilton, J. Martinis, S. Deiker, N. Bergren, S. Nam, D. Rudman, and D. Wollman, "A Mo-Cu superconducting transition-edge microcalorimeter with 4.5 eV energy resolution at 6 keV," *Nucl. Instrum. Meth.*, vol. A444, no. 1-2, pp. 184–187, 2000.

[10] J. Chervenak, K. Irwin, E. Grossman, J. Martinis, C. Reintsema, and M. Huber, "Superconducting multiplexer for arrays of transition edge sensors," *Appl. Phys. Lett.*, vol. 74, no. 26, pp. 4043–4045, 1999.

[11] J. Yoon, J. Clarke, J. Gildemeister, A. Lee, M. Myers, P. Richards, and J. Skidmore, "Single superconducting quantum interference device multiplexer for arrays of low-temperature sensors," *Appl. Phys. Lett.*, vol. 78, no. 3, pp. 371–373, 2001.

[12] D. Twerenbold, "Giaever–type superconducting tunneling junctions as high-resolution X–ray–detectors," *Europhys. Lett.*, vol. 1, no. 5, pp. 209–214, 1986.

[13] H. Kraus, F. Vonfeilitzsch, J. Jochum, R. Mossbauer, T. Peterreins, and F. Robst, "Quasiparticle trapping in a superconductive detector system exhibiting high-energy and position resolution," *Physics Letters B*, vol. 231, pp. 195–202, 1989.

[14] R. Schoelkopf, S. Moseley, C. Stahle, P. Wahlgren, and P. Delsing, "A concept for a submillimeter-wave single-photon counter," *IEEE Trans. Applied Superconductivity*, vol. 9, no. 2, pp. 2935–2939, 1999.

[15] A. Peacock, P. Verhoeve, N. Rando, A. vanDordrecht, B. Taylor, C. Erd, M. Perryman, R. Venn, J. Howlett, D. Goldie, J. Lumley, and M. Wallis, "Single optical photon detection with a superconducting tunnel junction," *Nature*, vol. 381, no. 6578, pp. 135–137, 1996.

[16] K. Segall, C. Wilson, L. Li, A. Davies, R. Lathrop, M. Gaidis, D. Prober, A. Szymkowiak, and S. Moseley, "Single photon imaging X–ray spectrometers," *IEEE Trans. Applied Superconductivity*, vol. 9, no. 2, pp. 3326–3329, 1999.

[17] K. Segall and D. Prober, "Quantum partition noise in a superconducting tunnel junction," *Phys. Rev. B*, vol. 64, no. 18, pp. art. no.–180508, 2001.

[18] C. Wilson, L. Frunzio, and D. Prober, "Time-resolved measurements of thermodynamic fluctuations of the particle number in a nondegenerate fermi gas," *Phys. Rev. Lett.*, vol. 87, no. 6, pp. art. no.–067004, 2001.

[19] R. Schoelkopf, P. Wahlgren, A. Kozhevnikov, P. Delsing, and D. Prober, "The radio-frequency single-electron transistor (RF- SET): A fast and ultrasensitive electrometer," *Science*, vol. 280, no. 5367, pp. 1238–1242, 1998.

[20] T. Stevenson, F. Pellerano, C. Stahle, K. Aidala, and R. Schoelkopf, "Multiplexing of radio-frequency single-electron transistors," *Appl. Phys. Lett.*, vol. 80, no. 16, pp. 3012–3014, 2002.

[21] S. Lee, J. Gildemeister, W. Holmes, A. Lee, and P. Richards, "Voltage-biased superconducting transition-edge bolometer with strong electrothermal feedback operated at 370 mK," *Appl. Opt.*, vol. 37, no. 16, pp. 3391–3397, 1998.

[22] N. Rando, J. Verveer, S. Andersson, P. Verhoeve, A. Peacock, A. Reynolds, M. Perryman, and F. Favata, "S-Cam: A spectrophotometer for optical astronomy: Performance and latest results," *Rev. of Sci. Instrum.*, vol. 71, no. 12, pp. 4582–4591, 2000.

[23] G. Angloher, P. Hettl, M. Huber, J. Jochum, F. von Feilitzsch, and R. Mossbauer, "Energy resolution of 12 eV at 5.9 keV from Al- superconducting tunnel junction detectors," *J. Appl. Phys.*, vol. 89, no. 2, pp. 1425–1429, 2001.

[24] L. Li, L. Frunzio, C. Wilson, D. Prober, A. Szymkowiak, and S. Moseley, "Improved energy resolution of X–ray single photon imaging spectrometers using superconducting tunnel junctions," *J. Appl. Phys.*, vol. 90, no. 7, pp. 3645–3647, 2001.

[25] B. Mazin, P. Day, J. Zmuidzinas, and H. LeDuc, "Multiplexable kinetic inductance detectors," in *Ninth International Workshop on Low Temperature Detectors* (F. S. Porter, D. McCammon, M. Galeazzi, and C. K. Stahle, eds.), vol. 605 of *AIP Conf. Proc.*, pp. 309–312, AIP: New York, 2002.

[26] B. A. Mazin, P. K. Day, H. G. Leduc, A. Vayonakis, and J. Zmuidzinas, "Superconducting kinetic inductance photon detectors," *Proc. SPIE*, vol. 4849, pp. 283–289, December 2002.

[27] P. Day, H. Leduc, B. Mazin, A. Vayonakis, and J. Zmuidzinas, "A superconducting detector suitable for use in large arrays," *Nature*, vol. 425, pp. 817–821, 2003.

[28] M. Tinkham, *Introduction to Superconductivity.* McGraw–Hill: New York, second ed., 1996.

[29] D. McDonald, "Novel superconducting thermometer for bolometric applications," *Appl. Phys. Lett.*, vol. 50, no. 12, pp. 775–777, 1987.

[30] J. Sauvageau and D. McDonald, "Superconducting kinetic inductance bolometer," *IEEE Trans. Magnetics*, vol. 25, no. 2, pp. 1331–1334, 1989.

[31] J. Sauvageau, D. Mcdonald, and E. Grossman, "Superconducting kinetic inductance radiometer," *IEEE Trans. Magnetics*, vol. 27, no. 2, pp. 2757–2760, 1991.

[32] E. Grossman, D. Mcdonald, and J. Sauvageau, "Far-infrared kinetic-inductance detectors," *IEEE Trans. Magnetics*, vol. 27, no. 2, pp. 2677–2680, 1991.

[33] D. Osterman, R. Patt, D. Audley, and R. Kelley, "An X-ray microcalorimeter with kinetic inductance thermometer and dc SQUID read-out," *J. Low Temp. Phys.*, vol. 93, no. 3-4, pp. 251–256, 1993.

[34] N. Bluzer, "Analysis of quantum superconducting kinetic inductance photodetectors," *J. Appl. Phys.*, vol. 78, no. 12, pp. 7340–7351, 1995.

[35] A. Sergeev and M. Reizer, "Photoresponse mechanisms of thin superconducting films and superconducting detectors," *Intl. J. Mod. Phys. B*, vol. 10, no. 6, pp. 635–667, 1996.

[36] A. Sergeev, V. Mitin, and B. Karasik, "Ultrasensitive hot-electron kinetic-inductance detectors operating well below the superconducting transition," *Appl. Phys. Lett.*, vol. 80, no. 5, pp. 817–819, 2002.

[37] S. Weinreb, T. Gaier, R. Lai, M. Barsky, Y. Leong, and L. Samoska, "High-gain 150-215-GHz MMIC amplifier with integral waveguide transitions," *IEEE Microwave Guided Wave Lett.*, vol. 9, no. 7, pp. 282–284, 1999.

[38] P. deBernardis *et al.*, "A flat universe from high-resolution maps of the cosmic microwave background radiation," *Nature*, vol. 404, p. 955, 2000.

[39] D. Spergel *et al.*, "First year Wilkinson Microwave Anisotropy Probe (WMAP) observations: Determination of cosmological parameters," *Ap. J. (Suppl.)*, vol. 148, p. 175, 2003.

[40] J. Kovac, E. Leitch, C. Pryke, J. Carlstrom, N. Halverson, and W. Holzapfel, "Detection of polarization in the cosmic microwave background using DASI," *Nature*, vol. 420, pp. 772–787, 2002.

[41] J. Tauber, "The Planck Mission," *IAU Symposium no. 201*, 2000.

[42] Infrared, Submillimeter, and Millimeter Working Group, "Detector needs for long wavelength astrophysics," June 2002.

[43] M. Kamionkowski and A. H. Jaffe, "Detection of gravitational waves from inflation," *Int. J. Mod. Phys.*, vol. 16, pp. 116–128, October 2001.

[44] W. Hu and S. Dodelson, "Cosmic microwave background anisotropies," *Annual Reviews*, vol. 40, pp. 171–216, 2002.

[45] G. Hinshaw *et al.*, "First year Wilkinson Microwave Anisotropy Probe (WMAP) observations: The angular power spectrum," *Ap. J. (Suppl.)*, vol. 148, p. 119, 2003.

[46] A. Sajina, "Submillimetre and near-infrared observations of galaxies selected at 170 microns," *Mon. Not. Roy. Astron. Soc.*, vol. 343, no. 4, pp. 1365–1365, 2003.

[47] "http://safir.jpl.nasa.gov/technologies/index.asp."

[48] W. Duncan *et al.*, "SCUBA-2: Application of LTD technology," in *Low Temperature Detectors* (F. Porter, D. McCammon, M. Galeazzi, and C. Stahle, eds.), vol. 605 of *AIP Conference Proceedings*, pp. 577–584, 2002.

[49] J.E. Gunn *et al.*, "The Sloan digital sky survey photometric camera," *The Astronomical Journal*, vol. 116, pp. 3040–3081, 1998.

[50] B. Mazin and R. Brunner, "Simulated extragalactic observations with a cryogenic imaging spectrophotometer," *Astron. J.*, vol. 120, no. 5, pp. 2721–2729, 2000.

[51] J. de Bruijne, A. Reynolds, M. Perryman, A. Peacock, F. Favata, N. Rando, D. Martin, P. Verhoeve, and N. Christlieb, "Direct determination of quasar redshifts," *Astron. & Ap.*, vol. 381, no. 3, pp. L57–L60, 2002.

[52] R. Romani, A. Miller, B. Cabrera, E. Figueroa-Feliciano, and S. Nam, "First astronomical application of a cryogenic transition edge sensor spectrophotometer," *Ap. J.*, vol. 521, no. 2, pp. L153–L156, 1999.

[53] R. Romani, A. Miller, B. Cabrera, S. Nam, and J. Martinis, "Phase-resolved crab studies with a cryogenic transition-edge sensor spectrophotometer," *Ap. J.*, vol. 563, pp. 221–228, Dec. 2001.

[54] B. Kern and C. Martin, "Optical pulsations from the anomalous X-ray pulsar 4U0142+61," *Nature*, vol. 417, p. 527, 2002.

[55] B. Kern, C. Martin, B. Mazin, and J. Halpern, "Optical pulse-phased photopolarimetry of PSR B0656+14," *Ap. J.*, vol. 572, p. ?, 2003.

[56] C. Bridge, M. Cropper, G. Ramsay, M. Perryman, J. de Bruijne, F. Favata, A. Peacock, N. Rando, and A. Reynolds, "STJ observations of the eclipsing polar HU Aqr," *Mon. Not. Roy. Astron. Soc.*, vol. 336, pp. 1129–1138, 2002.

[57] A. Reynolds, J. de Bruijne, M. Perryman, A. Peacock, and C. Bridge, "Temperature determination via STJ optical spectroscopy," *Astron. & Ap.*, vol. 400, p. 1209, 2003.

[58] M. Kuchner and D. Spergel, "Terrestrial planet finding with a visible light coronograph," in *Scientific Frontiers in Research on Extrasolar Planets* (D. Deming and S. Seager, eds.), vol. 294, 2003.

[59] C. Beichman, N. Woolf, and C. Lindensmith, eds., *The Terrestrial Planet Finder*. NASA Jet Propulsion Laboratory, 1999.

[60] T. Peacock, P. Verhoeve, N. Rando, M. Perryman, B. Taylor, and P. Jakobsen, "Superconducting tunnel junctions as detectors for ultraviolet, optical, and near infrared astronomy," *Astron. & Ap. (Suppl.)*, vol. 123, no. 3, pp. 581–587, 1997.

[61] R. Davé, R. Cen, J. P. Ostriker, G. L. Bryan, L. Hernquist, N. Katz, D. H. Weinberg, M. L. Norman, and B. O'Shea, "Baryons in the Warm-Hot Intergalactic Medium," *Ap. J.*, vol. 552, pp. 473–483, May 2001.

[62] P. de Korte, "Cryogenic imaging spectrometers for X–ray astronomy," *Nucl. Inst. Meth. A*, vol. 444, no. 1-2, pp. 163–169, 2000.

[63] "http://constellation.gsfc.nasa.gov/docs/science/blackholes.html."

[64] D. Wollman, S. Nam, D. Newbury, G. Hilton, K. Irwin, N. Bergren, S. Deiker, D. Rudman, and J. Martinis, "Superconducting transition-edge-microcalorimeter X- ray spectrometer with 2 eV energy resolution at 1.5 keV," *Nucl. Instrum. Meth.*, vol. A444, no. 1-2, pp. 145–150, 2000.

[65] D. Newbury, D. Wollman, G. Hilton, K. Irwin, N. Bergren, D. Rudman, and J. Martinis, "The approaching revolution in X-ray microanalysis: The microcalorimeter energy dispersive spectrometer," *J. Radioanalytical and Nucl. Chem.*, vol. 244, pp. 627–635, 2000.

[66] D. Wollman. Private communication.

[67] P. J. E. Peebles, *Principles of Physical Cosmology.* Princeton, NJ: Princeton University Press, 1993.

[68] M. W. Goodman and E. Witten, "Detectability of certain dark–matter candidates," *Phys. Rev. D* , vol. 31, pp. 3059–3063, 1985.

[69] B. W. Lee and S. W. Weinberg, "Cosmological lower bound on heavy–neutrino masses," *Phys. Rev. Lett.*, vol. 39, pp. 165–168, 1977.

[70] J. R. Primack, D. Seckel, and B. Sadoulet, "Detection of cosmic dark matter," vol. 38, pp. 751–807, 1988.

[71] G. Jungman, M. Kamionkowski, and K. Griest, "Supersymmetric dark matter," *Phys. Rep.* , vol. 267, pp. 195–373, 1996.

[72] D. Abrams *et al.*, "Exclusion limits on the WIMP-nucleon cross section from the Cryogenic Dark Matter Search," *Phys. Rev. D* , vol. 66, pp. 122003–1–35, Dec. 2002.

[73] A. Benoit *et al.*, "Improved exclusion limits from the EDELWEISS WIMP search," *Physics Letters B*, vol. 545, pp. 43–49, Oct. 2002.

[74] R. Bernabei, P. Belli, R. Cerulli, F. Montecchia, M. Amato, G. Ignesti, A. Incicchitti, D. Prosperi, C. J. Dai, H. L. He, H. H. Kuang, and J. M. Ma, "Search for WIMP annual modulation signature: Results from DAMA/NaI-3 and DAMA/NaI-4 and the global combined analysis," *Phys. Lett. B* , vol. 480, pp. 23–31, 2000.

[75] A. Corsetti and P. Nath, "Gaugino mass nonuniversality and dark matter in supergravity, strings, and D-brane models," *Phys. Rev. D* , vol. 64, pp. 125010–1–11, Dec. 2001.

[76] J. Ellis, A. Ferstl, and K. A. Olive, "Exploration of elastic scattering rates for supersymmetric dark matter," *Phys. Rev. D* , vol. 63, pp. 065016–1–13, Mar. 2001.

[77] J. Ellis, A. Ferstl, and K. A. Olive, "Re-evaluation of the elastic scattering of supersymmetric dark matter," *Phys. Lett. B* , vol. 481, pp. 304–314, May 2000.

[78] V. Mandic, A. Pierce, P. Gondolo, and H. Murayama, "The Lower Bound on the Neutralino-Nucleon Cross Section," pp. hep–ph/0008022, 2000.

[79] R. J. Gaitskell and V. Mandic. Dark Matter Tools Working Group limit plotter, http://dmtools.berkeley.edu/limitplots.

[80] W. Eisenmenger, *Nonequilibrium Superconductivity, Phonons, and Kapitza Boundaries, Chapter 3*. New York: Plenum Press, 1981.

[81] W. McMillan, "Transition temperature of strong-coupled superconductors," *Phys. Rev.*, vol. 167, no. 2, pp. 331–344, 1968.

[82] D. C. Mattis and J. Bardeen, "Theory of the anomalous skin effect in normal and superconducting metals," *Phys. Rev.*, vol. 111, pp. 412–417, 1958.

[83] B. Geilikman and V. Kresin, *Kinetic and Nonsteady-state Effects in Superconductors*. John Wiley and Sons, 1974.

[84] R. Pöpel, *Superconducting Quantum Electronics*. Springer-Verlag, 1989.

[85] R. Pöpel, "Surface impedance and reflectivity of superconductors," *J. Appl. Phys.*, vol. 66, pp. 5950–5957, 1989.

[86] A. G. Kozorezov, A. F. Volkov, J. K. Wigmore, A. Peacock, A. Poelaert, and R. den Hartog, "Quasiparticle–phonon downconversion in nonequilibrium superconductors," *Phys. Rev. B*, vol. 61, pp. 11807–11819, May 2000.

[87] S. Friedrich, K. Segall, M. Gaidis, C. Wilson, D. Prober, A. Szymkowiak, and S. Moseley, "Experimental quasiparticle dynamics in a superconducting, imaging X–ray spectrometer," *Appl. Phys. Lett.*, vol. 71, no. 26, pp. 3901–3903, 1997.

[88] J. Zmuidzinas, "Transmission line resonators, unpublished." 2001.

[89] D. Pozar, *Microwave Engineering.* John Wiley & Sons, 2 ed., 1998.

[90] P. Day, "Quarterwave transmission line resonators, unpublished." 2002.

[91] N. Wadefalk, A. Mellberg, I. Angelov, M. Barsky, S. Bui, E. Choumas, R. Grundbacher, E. Kollberg, R. Lai, N. Rorsman, P. Starski, D. Stenarson, J.and Streit, and H. Zirath, "Cryogenic wide-band ultra-low-noise IF amplifiers operating at ultra-low DC power," *IEEE Trans. Microwave Theory Tech.*, vol. 51, pp. 1705–1711, 2003.

[92] R. Simons, *Coplanar Waveguide Circuits, Components, and Systems.* Wiley-Interscience, 2001.

[93] *Sonnet User's Manual Release 6.0.* Liverpool, NY: Sonnet Software, Inc., 1999.

[94] A. Vayonakis, "Radiative losses from 2-d apertures." 2001.

[95] S. Friedrich, *Superconducting Single Photon Imaging X-ray Spectrometers.* PhD thesis, Yale University, 1997.

[96] S. Kaplan, C. Chi, D. Langenberg, J. Chang, S. Jafarey, and D. Scalapino, "Quasiparticle and phonon lifetimes in superconductors," *Phys. Rev. B*, vol. 14, no. 11, pp. 4854–4873, 1976.

[97] K. E. Gray, "Steady state measurements of the quasiparticle lifetime in superconducting aluminum," *J. Phys. F: Metal Phys.*, vol. 1, pp. 290–308, 1971.

[98] C. Chantler, K. Olsen, R. Dragoset, A. Kishore, S. Kotochigova, and D. Zucker, "X-ray form factor, attenuation and scattering tables (version 2.0)," *J. Phys. Chem. Ref. Data*, vol. 29(4), pp. 597–1048, 2000.

[99] M. Perryman, M. Cropper, G. Ramsay, F. Favata, A. Peacock, N. Rando, and A. Reynolds, "High-speed energy-resolved STJ photometry of the eclipsing binary UZ For," *Mon. Not. Roy. Astron. Soc.*, vol. 324, no. 4, pp. 899–909, 2001.

[100] M. Lissitski, D. Perez de Lara, C. R., M. Della Rocca, L. Maritato, and M. Salvato, "Progress in fabrication of high quality tantalum film absorber for STJ radiation detector," *Proceedings of LTD-10*, vol. 520, pp. 243–245, 2004.

[101] K. Watanabe, K. Yoshida, T. Aoki, and S. Kohjiro, "Kinetic inductance of superconducting coplanar waveguide," *Jpn. J. Appl. Physs.*, vol. 33, pp. 5708–5712, 1994.

[102] W. Chang, "Numerical-calculation of the inductances of a multisuperconductor transmission-line system," *IEEE Trans. Magnetics*, vol. 17, pp. 764–766, 1981.

[103] U. Fano, "Ionization yield of radiations 2: The fluctuations of the number of ions," *Phys. Rev.*, vol. 72, no. 1, pp. 26–29, 1947.

[104] J. Ward, *Observations of carbon monoxide in the starburst galaxy M82 with a 690 GHz-wide spectral bandwidth receiver.* PhD thesis, California Institute of Technology, 2002.

[105] J. Jackson, *Classical Electrodynamics.* John Wiley & Sons, 3rd edition ed., 1999.

[106] G. Stan, S. Field, and J. Martinis, "Critical field for complete vortex expulsion from narrow superconducting strips," *Phys. Rev. Lett.*, vol. 92, 2004.

[107] "http://www.weinschel.com/pdfiles/wmod8310.pdf."

[108] "http://www.rsd.de/."

[109] E. Ivanov, J. Hartnett, and M. Tobar, "Cryogenic microwave amplifiers for precision measurements," *IEEE Trans. Ultrasonics, Ferroelectronics, and Freq. Control*, vol. 47, pp. 1273–1274, 2000.

[110] L. Cutler and C. Searle, "Some aspects of the theory and measurement of frequency flucuations in frequency standards," *Proceedings of the IEEE*, vol. 54, pp. 136–154, 1966.

[111] W. Press, S. Teukolsky, W. Vetterling, and B. Flannery, *Numerical Recipies in C.* Cambridge University Press, second ed., 1992.

[112] M. A. Biondi and M. P. Garfunkel, "Millimeter wave absorption in superconducting aluminum. I. Temperature dependence of the energy gap," *Phys. Rev.*, vol. 116, pp. 853–861, November 1959.

[113] G. L. Wells, J. E. Jackson, and E. N. Mitchell, "Superconducting tunneling in single–crystal and polycrystal films of aluminum," *Phys. Rev. B*, vol. 1, pp. 3636–3644, May 1970.

[114] W. Phillips, "Two–level states in glasses," *Rep. Prog. Phys.*, vol. 50, pp. 1657–1708, 1997.

[115] S. Rogge, D. Natelson, B. Tigner, and D. Osheroff, "Nonlinear dielectric response of glasses at low temperature," *Phys. Rev. B*, vol. 55, no. 17, pp. 11256–11262, 1997.

[116] P. Santhanam and D. Prober, "Inelastic electron scattering mechanisms in clean aluminum films," *Phys. Rev. B*, vol. 29, no. 6, pp. 3733–3736, 1984.

[117] T. Klapwijk, P. van der Plas, and J. Mooij, "Electron-electron scattering in dirty three-dimensional aluminum films," *Phys. Rev. B*, vol. 33, no. 2, pp. 1474–1477, 1986.